



HAL
open science

Precipitation evolution in an Al-Zn-Mg alloy during non-isothermal heat treatments and in the heat-affected zone of welded joints.

Myriam Nicolas

► **To cite this version:**

Myriam Nicolas. Precipitation evolution in an Al-Zn-Mg alloy during non-isothermal heat treatments and in the heat-affected zone of welded joints.. Material chemistry. Institut National Polytechnique de Grenoble - INPG, 2002. English. NNT: . tel-00370436

HAL Id: tel-00370436

<https://theses.hal.science/tel-00370436>

Submitted on 24 Mar 2009

HAL is a multi-disciplinary open access archive for the deposit and dissemination of scientific research documents, whether they are published or not. The documents may come from teaching and research institutions in France or abroad, or from public or private research centers.

L'archive ouverte pluridisciplinaire **HAL**, est destinée au dépôt et à la diffusion de documents scientifiques de niveau recherche, publiés ou non, émanant des établissements d'enseignement et de recherche français ou étrangers, des laboratoires publics ou privés.

INSTITUT NATIONAL POLYTECHNIQUE DE GRENOBLE

N° attribué par la bibliothèque

/ _ / _ / _ / _ / _ / _ / _ / _ / _ / _ /

THESE

pour obtenir le grade de

DOCTEUR DE L'INPG

Spécialité: Science et Génie des Matériaux

préparée au **Laboratoire de Thermodynamique et de Physico-Chimie Métallurgiques**

dans le cadre de *l'Ecole Doctorale Matériaux et Génie des Procédés*

présentée et soutenue publiquement

par

Myriam NICOLAS

le 17 décembre 2002

Titre :

Evolution de l'état de précipitation dans un alliage Al-Zn-Mg lors de traitements thermiques anisothermes et dans la zone affectée thermiquement de joints soudés.

Directeurs de thèse :

Yves Bréchet
Alexis Deschamps

JURY

M. Øystein Grong,	Président
M. Roland Fortunier,	Rapporteur
M. Hugh Shercliff,	Rapporteur
M. Yves Bréchet,	Directeur de thèse
M. Alexis Deschamps,	Co-encadrant
M. Ole Runar Myhr,	Examineur

Titre en français

Evolution de l'état de précipitation dans un alliage Al-Zn-Mg lors de traitements thermiques anisothermes et dans la zone affectée thermiquement de joints soudés.

Résumé en français

Le soudage des alliages Al-Zn-Mg est de plus en plus utilisé dans l'industrie du transport. Les variations brutales de température induites par le soudage à l'arc provoquent des modifications importantes de la microstructure dans la zone dite affectée thermiquement.

Cette étude porte sur l'évolution de la précipitation suite à ce procédé de l'alliage 7108.50 présentant différentes microstructures initiales. Une caractérisation fine des précipités durcissants dans la zone affectée thermiquement a été menée par SAXS, MET et DSC juste après soudage et après traitements thermiques post-soudage. Afin de mieux cerner les mécanismes influençant la précipitation au cours de ce procédé anisotherme, des traitements thermiques contrôlés, de type réversion ou rampes de montée en température, ont également été étudiés.

Un modèle basé sur l'évolution d'une distribution en taille de particules a été développé afin de prédire l'état de précipitation après divers traitements thermiques, dont le soudage.

Mots-clé : précipitation - alliages Al-Zn-Mg – soudage - traitements anisothermes - modélisation de la précipitation

Titre en anglais

Precipitation evolution in an Al-Zn-Mg alloy during non-isothermal heat treatments and in the heat-affected zone of welded joints.

Abstract

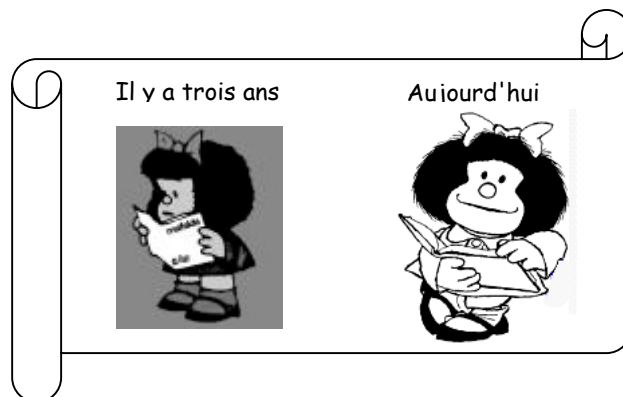
Welding of Al-Zn-Mg alloys is increasingly used in the transportation industry. The optimisation of the welding process requires a good understanding of the microstructures generated by the rapid temperature rise in the heat-affected zone.

This study deals with the evolution of the precipitation state after welding of the 7108.50 alloy in different initial tempers. A quantitative characterisation of the hardening precipitates in the heat-affected zone has been carried out by SAXS, TEM and DSC just after welding and after different post-welding heat treatments. To better understand the mechanisms involved in the precipitation evolution during this highly non-isothermal thermal cycle, controlled heat treatments, including reversion and continuous heating, have been studied.

Modelling based on the evolution of a particle distribution has been developed in order to predict the precipitation state after various heat treatments, including welding.

Key words: precipitation – Al-Zn-Mg alloys – welding – non-isothermal heat treatments – precipitation modelling

Remerciements



Je voudrais d'abord remercier ceux grâce à qui cette thèse a pu être entreprise:

- mes directeurs de thèse: Alexis et Yves,
- Ole Runar Myhr et Svein Skjervold, de Hydro Automotive Structures qui nous ont fourni le sujet d'étude ainsi que le matériau et avec qui nous avons entretenu une collaboration efficace malgré la distance,
- Claude Bernard et Jean-Marc Chaix, directeurs successifs du LTPCM où j'ai pu réaliser ce travail.

Au cours de cette thèse, j'ai également eu l'occasion de voyager. Merci notamment à Janos Lendvai et à son groupe pour leur accueil à Budapest.

Cette thèse a également pu bénéficier du soutien technique, théorique mais également l'accueil sympathique des gens du laboratoire. Merci donc à l'ensemble du groupe Physique du Métal et du LTPCM, et plus particulièrement:

- Alexis pour ses idées débordantes, sa présence et des discussions enrichissantes,
- Françoise, Frédéric L. et Jean-Paul ainsi que l'ensemble du personnel technique de la ligne D2AM pour leur efficacité lors des différentes expériences de petits angles sur la ligne et leurs dépouillements,
- Frédéric L. et Damien pour deux nuits de folie à l'ESRF,
- Béatrice et Patricia pour leur savoir-faire en microscopie électronique en transmission, notamment en faisceau convergent,
- Frédéric P. pour son assistance informatique,
- le personnel technique et administratif du laboratoire pour les dépannages fréquents, en particulier Michèle et Jean-Louis,
- Chris pour avoir relu et corrigé mon anglais,
- Frédéric P., Sophie, Fabien, Damien, Marc, Cécile, John, Chris et autres "juniors" du groupe et du laboratoire pour l'ambiance...

Enfin merci à mon David pour son soutien moral de chaque instant.

Table des matières

Table des matières.....	i
Résumé étendu.....	1
Introduction générale.....	13
Chapter I. Matériaux et techniques expérimentales.....	17
I.1. Matériaux.....	17
I.1.1. Composition.....	17
I.1.2. Traitements thermo-mécaniques.....	19
I.1.3. Paramètres de soudage.....	19
I.2. Techniques expérimentales.....	20
I.2.1. Microdureté.....	20
I.2.2. Microscopie optique.....	21
I.2.3. Calorimétrie Différentielle à balayage (DSC).....	21
I.2.4. Microscopie Electronique en Transmission (TEM).....	22
I.2.5. Diffusion centrale de rayons X (SAXS).....	27
I.2.6. Bilan.....	35
Chapter II. Caractérisation du matériau avant soudage	37
II.1. Revue bibliographique : précipitation dans les alliages Al-Zn-Mg.....	37
II.1.1. Description des alliages 7xxx.....	37
II.1.2. Phases dans les alliages 7xxx.....	40
II.1.3. Séquences de décomposition.....	46
II.1.4. Bilan.....	51
II.2. Caractérisation quantitative par mesures de SAXS.....	52
II.2.1. Interprétation des mesures de SAXS.....	52
II.2.2. Estimation de la fraction volumique à partir des mesures de SAXS.....	54
II.3. Recherche complémentaire par TEM et DSC.....	57
II.3.1. Nature des phases présentes.....	57
II.3.2. Mesure des distributions en taille de particules.....	60
II.3.3. TEM quantitatif: estimation de la fraction volumique.....	63

II.4. Du TEM au SAXS	68
II.4.1. Calibration du rayon	68
II.4.2. Calibration de la fraction volumique	70
II.5. Points-clé	72
Chapter III. Evolution de la précipitation au cours du soudage	73
III.1. Revue bibliographique: description du soudage	73
III.1.1. Techniques de soudage	73
III.1.2. Flux de chaleur et distribution de la chaleur dans la ZAT	74
III.1.3. Influence du soudage sur la microstructure et les propriétés de la ZAT	76
III.2. Calcul des profils thermiques	79
III.3. Structure granulaire	81
III.3.1. Matériau avant soudage	81
III.3.2. Structure granulaire après soudage	82
III.4. Effet du soudage sur la microstructure de précipitation	83
III.4.1. Profils de microdureté	83
III.4.2. Résultats des mesures de SAXS	84
III.4.3. Observations en TEM	87
III.4.4. Mesures de DSC	90
III.5. Traitements thermiques post-soudage	91
III.5.1. Maturation à l'ambiante	91
III.5.2. Traitements de revenu	96
III.6. Bilan et questions ouvertes	102
Chapter IV. Evolution de la précipitation au cours de traitements non-isothermes... 105	105
IV.1. Définition des traitements thermiques modèles	105
IV.2. Revue bibliographique: réponse d'un alliage 7xxx à un traitement contrôlé	106
IV.2.1. Séquence de décomposition au cours de rampes de température	106
IV.2.2. Traitements de réversion	111
IV.3. Evolution de la précipitation au cours de traitement de réversion	117
IV.3.1. Evolution générale	117
IV.3.2. Influence de la température	119
IV.3.3. Comparaison des comportements des états T6 et T7	121
IV.4. Rampes de montée en température	122
IV.4.1. Caractérisation en SAXS	122
IV.4.2. Mesures de DSC	125
IV.5. Bilan	129
Chapter V. Modélisation de l'évolution de la précipitation en situation non-isotherme	131
V.1. Revue bibliographique : modélisation de la précipitation	131
V.1.1. L'approche JMA	132
V.1.2. Théorie classique de germination, croissance, coalescence	132
V.1.3. Germination, croissance, coalescence en tant de mécanismes couplés	137

V.2. Modélisation de l'évolution d'une distribution de particules	138
V.2.1. Deux équations de base	138
V.2.2. Distribution en taille de particules	142
V.3. Calibration du modèle.....	144
V.3.1. Paramètres du modèle.....	144
V.3.2. Calibration de l'état T7	145
V.3.3. Calibration des états T6 et T4.....	148
V.4. Application aux traitements non-isothermes et au soudage	149
V.4.1. Rampes de montée en température	149
V.4.2. Soudage	152
V.5. Discussion.....	154
V.5.1. Evolution de la précipitation au cours de traitements isothermes.....	154
V.5.2. Evolution de la précipitation au cours de rampes de température.....	157
V.5.3. Evolution de la précipitation au cours du soudage	158
V.6. Modélisation de la limite d'élasticité	159
V.6.1. Considérations générales	159
V.6.2. Modélisation simple de la limite d'élasticité.....	160
V.6.3. Application à l'évolution de la microdureté dans la ZAT	161
V.7. Perspectives du modèle.....	162
V.8. Bilan.....	163
Conclusions et perspectives	165
Références bibliographiques	171

Table of contents

Table of contents.....	i
Résumé étendu.....	1
General introduction.....	13
Chapter I. Materials and experimental techniques	17
I.1. Materials	17
I.1.1. Composition	17
I.1.2. Thermomechanical treatment	19
I.1.3. Welding parameters	19
I.2. Experimental techniques.....	20
I.2.1. Microhardness	20
I.2.2. Optical microscopy	21
I.2.3. Differential Scanning Calorimetry (DSC).....	21
I.2.4. Transmission Electron Microscopy (TEM).....	22
I.2.5. Small-Angle X-ray Scattering (SAXS)	27
I.2.6. Summary	35
Chapter II. Characterisation of the material prior to welding	37
II.1. Literature review: precipitation in Al-Zn-Mg alloys	37
II.1.1. Description of 7xxx alloys	37
II.1.2. Phases in Al-Zn-Mg alloys	40
II.1.3. Decomposition processes.....	46
II.1.4. Relevant points for the present investigation	51
II.2. Quantitative characterisation by SAXS measurements	52
II.2.1. Interpretation of SAXS measurements.....	52
II.2.2. Estimation of volume fraction from SAXS measurements	54
II.3. Complementary investigations using TEM and DSC.....	57
II.3.1. Nature of present phases	57
II.3.2. Measurement of particle size distributions	60
II.3.3. Quantitative TEM: volume fraction estimation	63
II.4. From TEM to SAXS	68
II.4.1. Radius calibration	68
II.4.2. Volume fraction calibration	70

II.5. Key points 72

Chapter III. Precipitation evolution during welding and post-welding heat treatments
73

III.1. Literature review: description of welding 73
 III.1.1. Welding techniques 73
 III.1.2. Heat flow and temperature distribution in the heat-affected zone 74
 III.1.3. Influence of welding on HAZ microstructure and properties 76
 III.2. Calculation of the thermal profiles 79
 III.3. Grain structure 81
 III.3.1. Material prior to welding 81
 III.3.2. Grain structure after welding 82
 III.4. Effect of welding on the precipitation microstructure 83
 III.4.1. Microhardness profiles 83
 III.4.2. Results of SAXS investigation 84
 III.4.3. TEM observations 87
 III.4.4. DSC investigation 90
 III.5. Post-welding heat treatments 91
 III.5.1. Natural ageing 91
 III.5.2. Artificial ageing 96
 III.6. Summary and open questions 102

Chapter IV. Precipitation evolution during non-isothermal heat treatments..... 105

IV.1. Definition of model heat treatments 105
 IV.2. Literature review: response of a 7xxx alloy to a controlled heat treatment..... 106
 IV.2.1. Decomposition processes during continuous heating 106
 IV.2.2. Reversion heat treatments 111
 IV.3. Precipitation evolution during reversion heat treatments 117
 IV.3.1. General precipitation evolution 117
 IV.3.2. Temperature dependence 119
 IV.3.3. Comparison of T6 and T7 behaviours 121
 IV.4. Continuous heating 122
 IV.4.1. SAXS investigation 122
 IV.4.2. DSC investigation 125
 IV.5. Summary 129

Chapter V. Modelling of precipitation evolution during non-isothermal heat treatments 131

V.1. Literature review: precipitation modelling 131
 V.1.1. The JMA approach 132
 V.1.2. The classical nucleation, growth and coarsening laws 132
 V.1.3. Nucleation, growth and coarsening as coupled processes 137
 V.2. Modelling of particle distribution 138
 V.2.1. Two basic equations 138

V.2.2. Particle size distribution	142
V.3. Calibration of the model	144
V.3.1. Model parameters	144
V.3.2. Calibration for the T7 temper	145
V.3.3. Calibration for the T6 and T4 tempers.....	148
V.4. Application to non-isothermal heat treatments and welding	149
V.4.1. Continuous heating	149
V.4.2. Welding	152
V.5. Discussion.....	154
V.5.1. Precipitation evolution during isothermal heat treatments.....	154
V.5.2. Precipitation evolution during continuous heating	157
V.5.3. Precipitation evolution during welding.....	158
V.6. Modelling of the yield stress in the heat-affected zone	159
V.6.1. General considerations.....	159
V.6.2. Simple modelling of the yield stress.....	160
V.6.3. Application to microhardness evolution in the heat-affected zone	161
V.7. Future developments.....	162
V.8. Summary.....	163
Conclusions and future work	165
Bibliographic references	171

Résumé étendu

Introduction

Les alliages d'aluminium, notamment les alliages à durcissement structural, sont de plus en plus utilisés dans l'industrie automobile du fait de leur bon compromis densité/propriétés mécaniques. Or le soudage à l'arc reste une des techniques d'assemblage privilégiées dans ce domaine d'applications pour des raisons de coût. Ce procédé appliqué à des alliages à durcissement structural (alliages de la série 7xxx –Al-Zn-Mg– par exemple) a pour conséquence de modifier la microstructure du matériau de base et donc ses propriétés mécaniques. En effet, même si en dehors du cordon de soudure, le matériau ne subit pas la fusion, il est sujet à des changements de température qui vont modifier son état de précipitation (notion de zone affectée thermiquement). Différents processus peuvent alors avoir lieu: la dissolution des précipités, leur coalescence, voire des transformations de phase.

Le but de cette étude est de caractériser qualitativement et quantitativement l'évolution de l'état de précipitation à l'issue du procédé de soudage dans la zone affectée thermiquement en fonction de l'état initial du matériau. Afin de mieux comprendre l'évolution de la précipitation au cours de traitements anisothermes, une série d'études sur des traitements thermiques simples tels que des traitements de réversion ou des rampes de montée en température (à vitesse constante) a été entreprise. Enfin un modèle a été développé afin de prédire l'évolution d'une distribution donnée de précipités soumise à des variations de températures.

Matériau et techniques expérimentales

Le matériau de l'étude est un alliage commercial de la série 7xxx, le 7108.50 de composition Al-5wt%Zn-0.8wt%Mg(-Zr). Cet alliage nous a été fourni sous forme de plaques extrudées par Hydro Automotive Structures (Raufoss – Norvège) à l'état soudé. Trois états initiaux ont été étudiés: un état mûri à l'ambiante (T4), un état revenu au pic de durcissement obtenu à 140°C (T6) et un état sur-revenu à 170°C (T7).

Différentes techniques de caractérisation de la microstructure ont été mises en œuvre:

- des mesures de microdureté, en tant qu'indicateur des modifications de microstructure,
- des mesures en diffusion centrale de rayons X (SAXS) qui donnent accès à des valeurs moyennes de l'état de précipitation telles que la fraction volumique et le rayon moyen des particules,
- des observations en microscopie électronique en transmission (MET) qui permettent une observation locale de la distribution de précipités,

- des mesures en calorimétrie différentielle à balayage (DSC) qui permettent de définir les domaines de température correspondant aux changements de microstructure.

Caractérisation de la microstructure avant soudage

La séquence de précipitation dans les alliages Al-Zn-Mg est relativement complexe et fait intervenir à la fois des phases stables (notamment la phase d'équilibre η de composition $MgZn_2$) ainsi que des phases métastables telles que les zones de Guinier-Preston et la phase métastable η' . La séquence de précipitation est indiquée ci-dessus ainsi que la gamme de température d'existence de chacune des phases:

Solution solide sursaturée \rightarrow GP zones (20-150°C) \rightarrow η' (100-170°C) \rightarrow η (150-300°C)

Une étude détaillée en MET, SAXS et DSC a permis de déterminer la nature des phases présentes dans chacun des états de base étudiés (T4, T6 et T7) ainsi que leur distribution en taille, fraction volumique et rayon moyen (voir Figure 1).

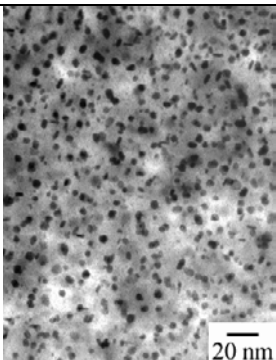
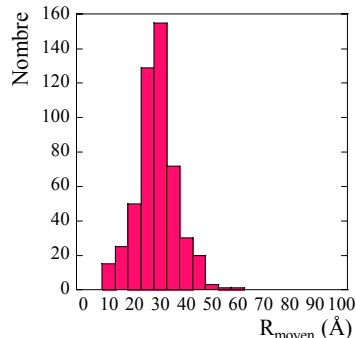
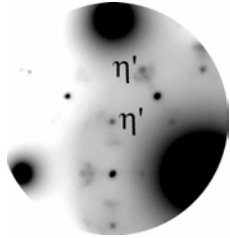
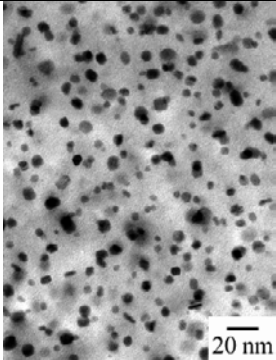
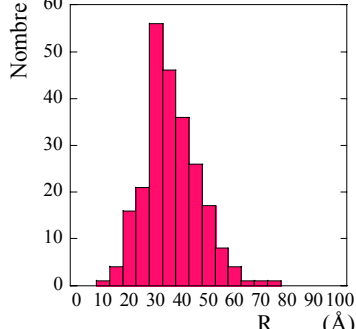
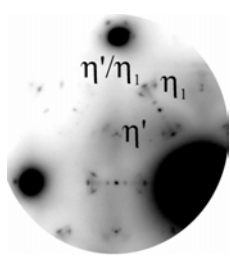
	Image en champ clair (MET)	Distribution en taille des précipités (MET)	Cliché de diffraction en axe de zone [111] (MET)	Résumé (SAXS couplé au MET)
T4				zones GP $R_{\text{moyen}} = 7.1 \text{ \AA}$ $f_v = 2.1 \%$
T6				principalement η' $R_{\text{moyen}} = 24.3 \text{ \AA}$ $f_v = 2.5 \%$
T7				mélange $\eta'+\eta$ $R_{\text{moyen}} = 38 \text{ \AA}$ $f_v = 2.6 \%$

Figure 1 : Caractérisation de la précipitation durcissante des états initiaux T4, T6 et T7.

Evolution de la précipitation au cours du soudage et de traitements post-soudage

L'état de précipitation à l'issue de l'opération de soudage a été caractérisé en détails par MET et SAXS.

Profils thermiques au cours du soudage

Au cours du soudage, chaque point de la zone affectée thermiquement subit un cycle thermique complexe dont les caractéristiques dépendent principalement de la distance au cordon de soudure. Les profils thermiques ont été calculés par le logiciel *Weldsim* et calibrés sur des mesures expérimentales par thermocouple (voir Figure 2).

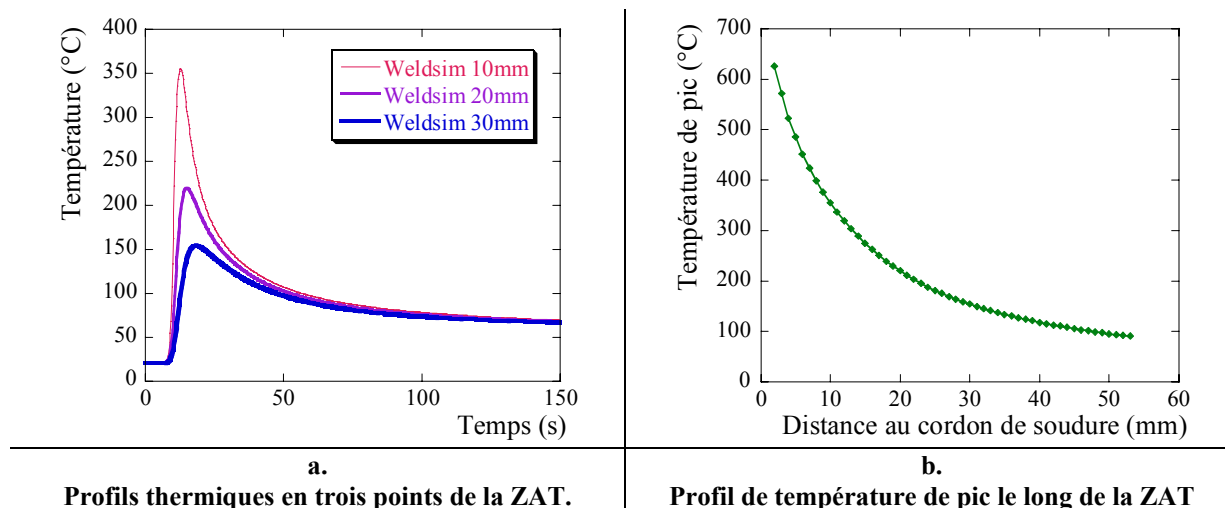


Figure 2 : Profils thermiques le long de la zone affectée thermiquement (ZAT) ainsi que le profil de température de pic résultant.

Caractérisation juste après soudage

Les microstructures après soudage ont été caractérisées par MET (micrographies et distribution en taille) et par SAXS (profils de fraction volumiques et rayon moyens) dans la zone affectée thermiquement; les résultats sont présentés sur les figures Figure 3 et Figure 4 pour les soudures T4 et (T6, T7) respectivement.

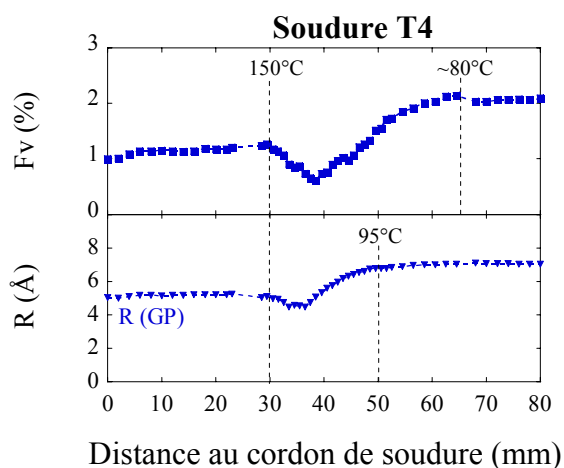


Figure 3 : Evolution de la fraction volumique F_v et du rayon moyen des précipités le long de la zone affectée thermiquement d'une soudure T4. Les températures indiquent les températures de pic.

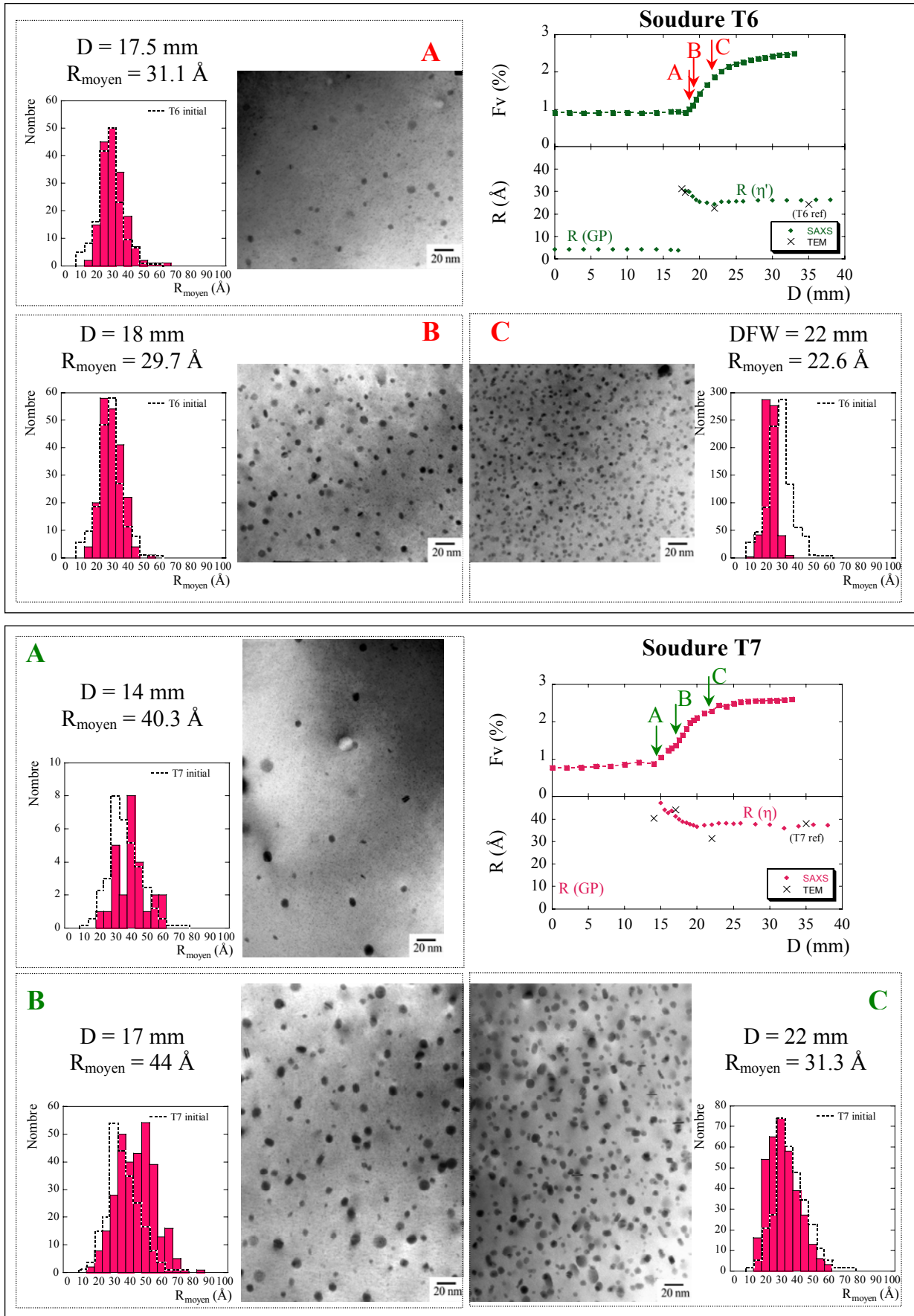


Figure 4 : Evolution de la fraction volumique F_v et du rayon moyen des précipités le long de la zone affectée thermiquement d'une soudure T6 et T7.

Pour les trois états, la microstructure peut être divisée en trois régions:

- une zone loin du cordon de soudure non affectée par le soudage dont les caractéristiques sont les mêmes que celles du matériau de base,
- une zone proche du cordon de soudure où la dissolution a été complète et où des zones GP ont re-précipité lors du refroidissement de la soudure ainsi qu'au cours du stockage à température ambiante,
- une zone intermédiaire où la dissolution n'est que partielle et où de la coalescence a pu être observée dans le cas des états T6 et T7.

Il faut noter que la coalescence n'affecte pas entièrement la zone de transition mais uniquement la zone où la température a été la plus élevée au cours du cycle thermique. Ceci suggère qu'une partie de la dissolution intervient sans changement significatif de la taille moyenne des particules.

Evolution de la précipitation au cours de traitements thermiques anisothermes

Pour mieux comprendre l'évolution de la précipitation au cours du procédé de soudage, le comportement d'un état précipité a été étudié au cours de traitements thermiques contrôlés. Deux types de traitements thermiques ont été réalisés in-situ au cours de mesures de SAXS:

- des traitements de réversion constitués d'un palier isotherme précédé d'une montée rapide en température (sur les matériaux T6 et T7),
- des rampes de montée en température à vitesse constante (sur les trois matériaux).

Traitements de réversion

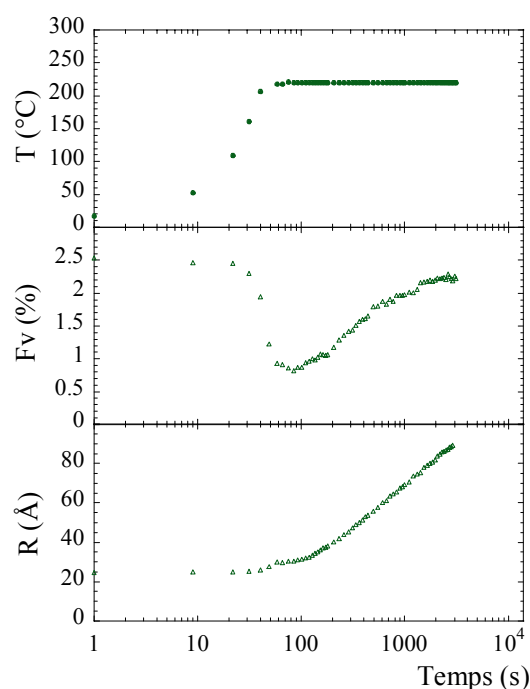


Figure 15 : Réversion T6-220°C: évolution de la température, de la fraction volumique et de la taille moyenne des précipités.

La Figure I5 montre l'évolution caractéristique de la fraction volumique et du rayon moyen des précipités au cours d'un traitement de réversion. Trois stades peuvent être distingués: d'abord une dissolution rapide caractérisée par une chute brutale de la fraction volumique accompagnée d'une faible variation du rayon moyen, puis la fraction volumique atteint un minimum avant de remonter vers une valeur d'équilibre, cette dernière étape s'accompagne d'une augmentation de la fraction volumique (coalescence).

L'évolution de ce comportement en fonction de la température est présentée pour les matériaux T6 et T7 sur la Figure 6. On peut observer que plus la température de réversion est élevée, plus le minimum de fraction volumique ainsi que la fraction volumique d'équilibre diminuent. De plus, en comparant le comportement des matériaux T6 et T7, on peut remarquer que la présence de phase plus stable (dont le solvus est plus élevé) limite la dissolution par rapport à la phase métastable η' .

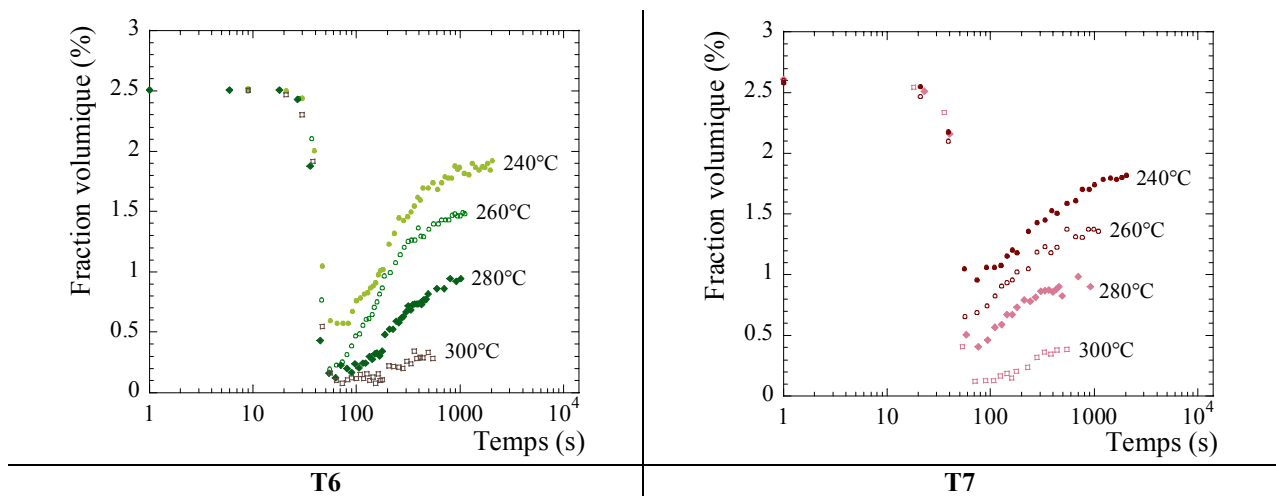


Figure 6 : Réversion – T6, T7: évolution du comportement de réversion en fonction de la température du palier isotherme pour les matériaux T6 et T7.

Rampes de montée en température

Le comportement au cours de rampes de montée en température pour les matériaux T6 et T7 est présenté sur la figure Figure 7.

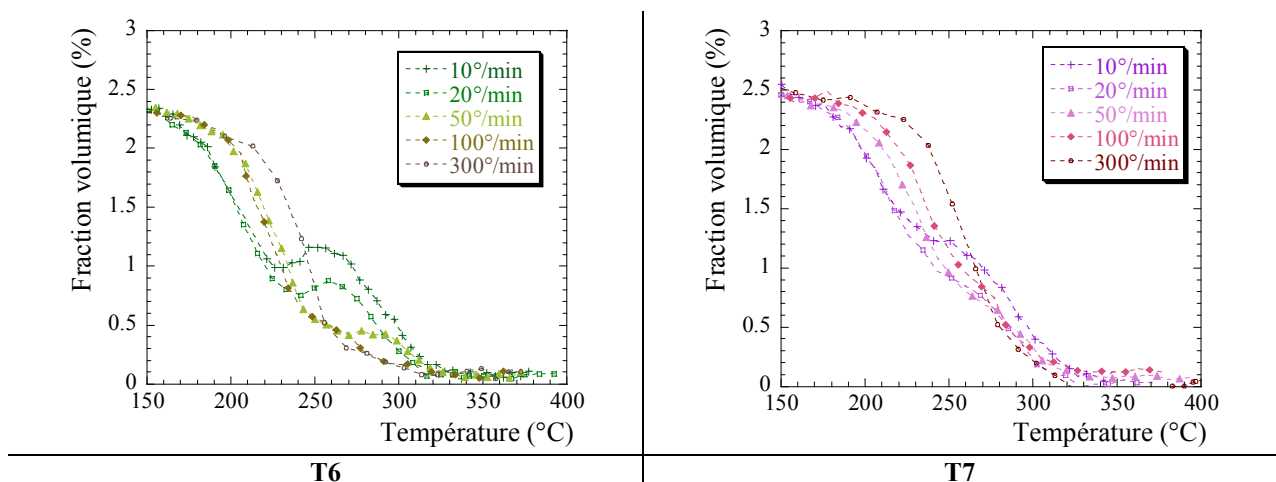


Figure 7 : Rampes – T6, T7: évolution de la fraction volumique au cours de rampes de montée en température pour des vitesses variant de 10°/min à 300°/min pour les matériaux T6 et T7.

Le mécanisme gouvernant ce type de traitement thermique est la dissolution caractérisée par une chute de la fraction volumique. Pour des raisons de cinétiques, plus la vitesse de montée en température est élevée, plus la dissolution est repoussée vers les hautes températures. De plus la gamme de température correspondant à la dissolution des précipités contenus dans l'état T7 est supérieure d'une vingtaine de degrés à celle du matériau T6. Ceci est dû à la nature des précipités contenus dans chacun des états: métastables et plus petits dans le cas du T6, ce qui favorisent leur dissolution à plus basse température.

Un fait marquant dans le cas du matériau T6 pour des faibles vitesses de montée en température est la présence d'une "anomalie" de dissolution, caractérisée par une remontée de la fraction volumique aux alentours de 250°C. Cette anomalie a été attribuée à la transformation de phase $\eta' \rightarrow \eta$. Il faut noter que ce comportement est décalé vers les plus hautes températures lorsque la vitesse de montée en température augmente puis tend à disparaître.

Dans le cas du matériau T7, aucune remontée n'est observée; par contre, dans la même gamme de température un point d'inflexion apparaît pour les faibles vitesses de montée en température. Ce point d'inflexion est-il également dû à la transformation des précipités η' présents dans l'état initial?

Les résultats obtenus pour le matériau T4 (voir Figure 8) montrent une rapide dissolution de l'ensemble des zones GP pour des températures inférieures à 150°C. A plus haute température (autour de 250°C) on peut observer une remontée de la fraction volumique, attribuée à la précipitation de la phase η .

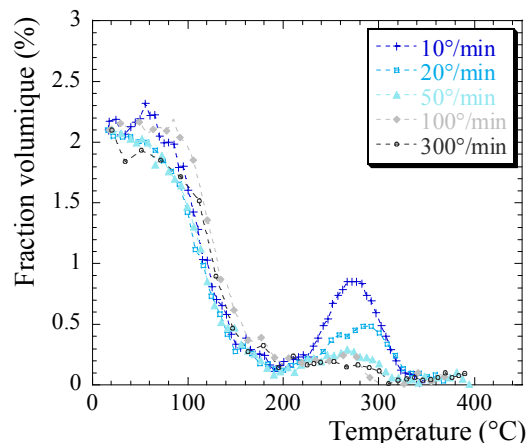


Figure 8 : Rampe – T4: évolution de la fraction volumique au cours de rampes de montée en température à des vitesses variant de 10°/min à 300°/min pour le matériau T4.

Enseignement vis-à-vis du soudage

Etant les vitesses de montée en température très rapides dans le cas du soudage (de l'ordre de 1000°/min), les transformations de phase ne sont pas supposées intervenir.

La dissolution à rayon moyen constant a été mise en évidence pour les traitements thermiques contrôlés.

Modélisation

Un modèle simple basé sur une loi d'évolution du rayon des particules appliquée à une distribution de précipités pré-existante a été développé dans le cas des alliages Al-Zn-Mg. Ce

modèle ne prend en compte qu'un seul type de précipités, et ne fait pas intervenir des phénomènes tels que la germination ou les transformations de phase.

Lois d'évolution

La loi classique d'évolution du rayon est utilisée:

$$v = \frac{dr}{dt} = \frac{\bar{C} - C_i(r)}{C_p - C_i(r)} \frac{D}{r}$$

où r est le rayon du précipité,
 \bar{C} est la concentration moyenne dans la matrice,
 $C_i(r)$ est la concentration à l'interface matrice-précipité,
 C_p est la concentration du précipité,
 D est le coefficient de diffusion.

L'effet de taille du précipité a été considéré à travers l'équation de Gibbs-Thompson appliquée au produit de solubilité:

$$K(r) = K^\infty \exp\left(\frac{2\sigma V_m}{rRT}\right)$$

où K^∞ est la concentration interfaciale d'un précipité infini,
 σ est l'énergie d'interface précipité-matrice,
 V_m est le volume molaire du précipité.

$C_i(r)$ est déterminé par le diagramme de phases et dans le cas ternaire par l'équilibre des flux à l'interface des deux espèces diffusantes.

Dans le cas du modèle de classes développé ici, ces lois sont appliquées à chacune des classes de taille de la distribution de précipités.

Application du modèle aux traitements thermiques contrôlés

Les résultats de la modélisation dans le cas de traitements thermiques simples tels que des traitements de réversion ou des rampes de montée en température ont été comparés aux résultats expérimentaux.

Les résultats expérimentaux obtenus au cours de traitements de réversion ont été utilisés de façon à calibrer les paramètres du système tels que le produit de solubilité, les coefficients de diffusion et l'énergie d'interface des précipités. Les résultats ainsi obtenus en réversion sur l'état T7 sont présentés sur la Figure 9. Les résultats de la modélisation sont satisfaisants tant en termes d'évolution de la fraction volumique que de l'évolution de la taille moyenne des précipités.

Le modèle prédit une dissolution à rayon moyen constant en début de réversion, observée expérimentalement. Le modèle permet d'expliquer ce comportement par l'évolution du rayon critique au cours du traitement. En effet lorsque la température est brutalement augmentée, le rayon critique devient très grand par rapport à la distribution de précipités; toutes les particules deviennent donc instables et se dissolvent, les plus petites se dissolvant plus vite que les grosses, aboutissant à un "écrasement" vertical de la distribution, d'où un rayon moyen constant. Du fait des forts rejets de solutés dans la matrice, le rayon critique diminue ensuite pour revenir à l'intérieur de la distribution. Au minimum de fraction volumique, le rayon

critique égale le rayon moyen et la croissance devient le phénomène prédominant et le système tend vers la fraction volumique d'équilibre.

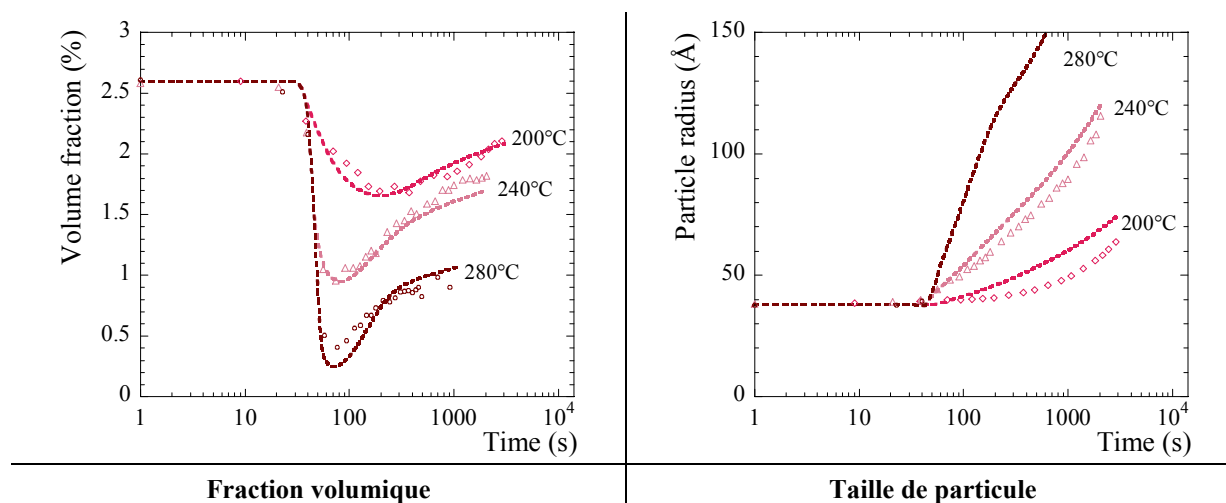


Figure 9 : Réversion – T7: évolution de la fraction volumique et de la taille des précipités en fonction du temps à 200, 240 et 280°C. Comparaison entre le modèle (pointillés) et les résultats expérimentaux (symboles).

Le modèle a ensuite été appliqué aux rampes de montée en température et comparé aux résultats expérimentaux (voir Figure 10). En comparant ces résultats aux résultats expérimentaux (voir Figure 7), on peut noter que la gamme de température où la dissolution se produit est bien reproduite ainsi que l'influence de la vitesse de montée en température.

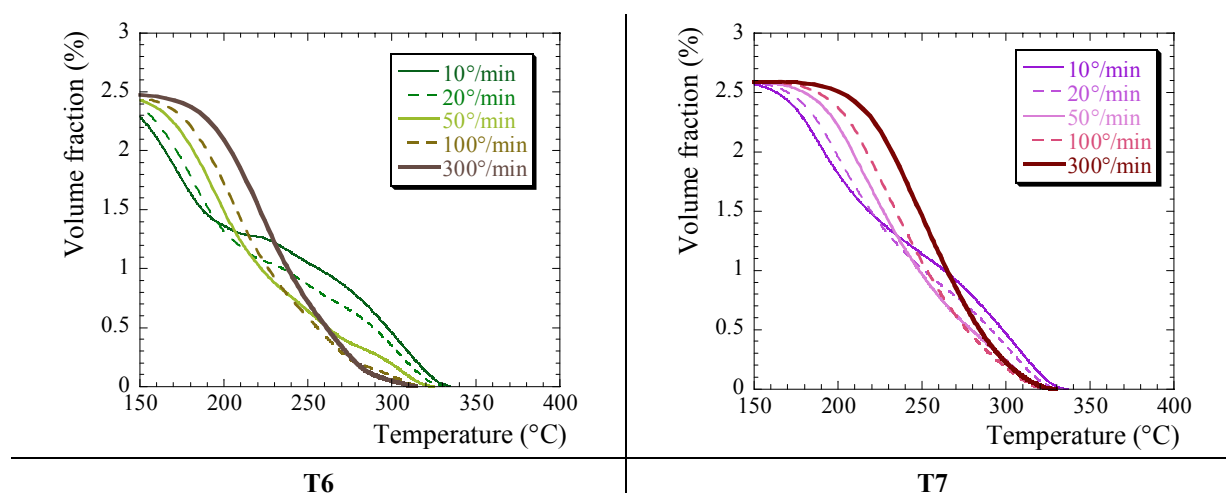


Figure 10 : Rampes – T6, T7, modèle: modélisation de l'évolution de la fraction volumique au cours de rampes de montée en température pour des vitesses de montée variant de 10°/min à 300°/min.

Dans le cas du matériau T6, l'anomalie de dissolution n'est pas reproduite par le modèle puisque celui-ci n'inclut pas de transformations de phases. Par contre, on peut noter un point d'inflexion, qui dans le cas du matériau T7, reproduit tout à fait le phénomène observé expérimentalement. Ce point d'inflexion n'est donc pas dû à la transformation de phase $\eta' \rightarrow \eta$. En fait, ce point d'inflexion doit être attribué à la compétition entre la dissolution des précipités et leur croissance qui devient effective pour de faibles vitesses de montée en température. Pour des vitesses plus élevées, la dissolution est le mécanisme prépondérant.

Application au soudage

Le modèle ainsi établi et validé vis-à-vis de traitements thermiques simples a été appliqué dans le cas du soudage. Le modèle a donc été appliqué aux profils thermiques calculés par le logiciel *Weldsim* (voir Figure 2) correspondant à différents points de la zone affectée thermiquement. La fraction volumique et le rayon moyen résultant du procédé de soudage sont présentés sur la Figure 11 pour les trois matériaux étudiés.

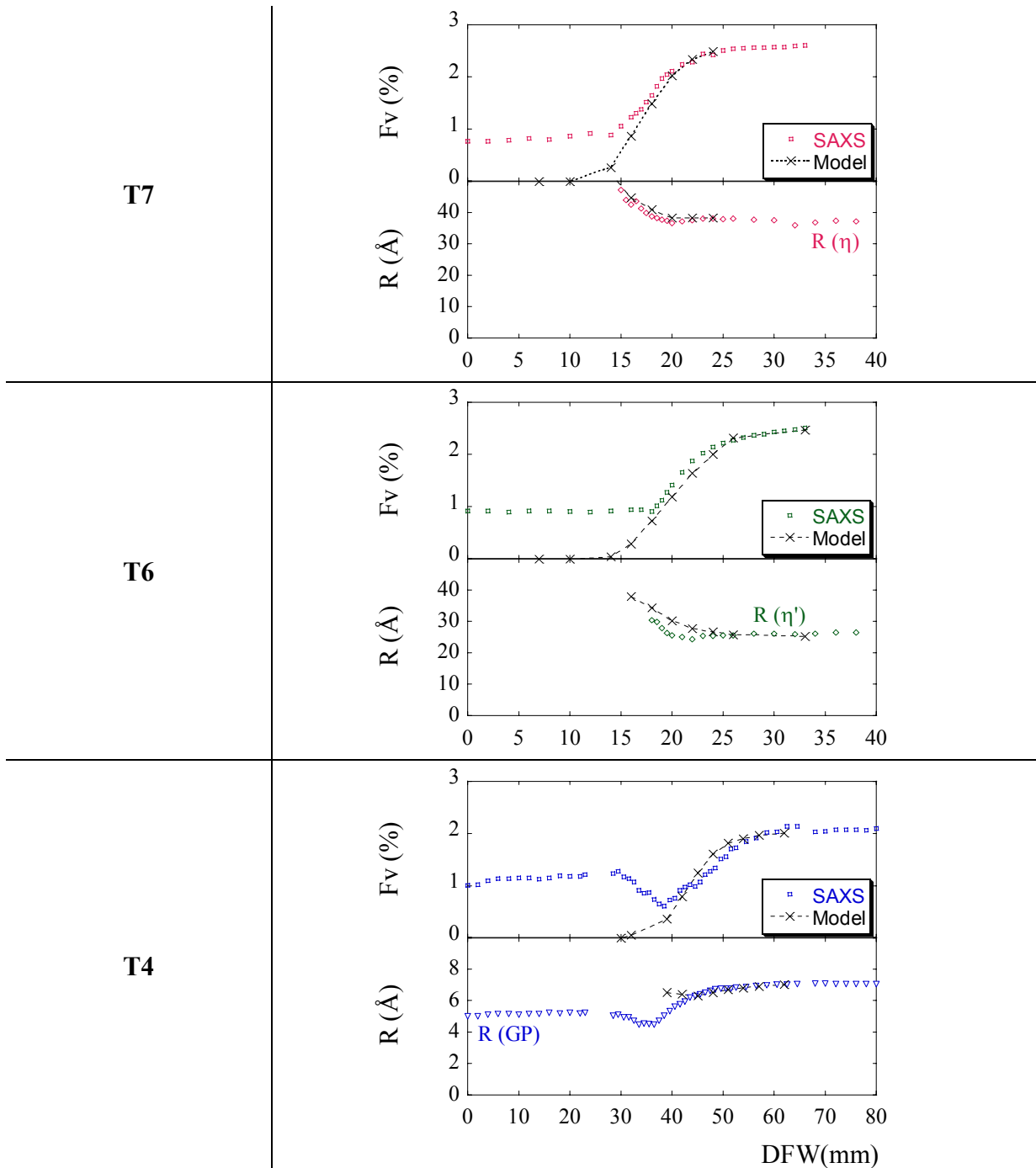


Figure 11 : Soudage – T7, T6, T4: application du modèle aux cycles thermiques du procédé de soudage, fraction volumique et taille des précipités résultant.

Le modèle reproduit de façon tout à fait satisfaisante les résultats expérimentaux dans la zone de transition. Dans la zone totalement révertie, le modèle prédit une fraction volumique nulle.

Il faut rappeler que la fraction volumique mesurée expérimentalement dans cette zone correspond à des zones GP précipités à basse température. Etant donné que le modèle n'inclut pas la germination, il ne pouvait reproduire ce phénomène.

Conclusion

Cette étude, visant à comprendre l'évolution de la précipitation durcissante au cours du traitement thermique complexe que constitue le procédé de soudage, a été divisée en trois parties:

- la caractérisation des états soudés pour différentes microstructures initiales,
- l'étude de traitements thermiques modèles (traitements de réversion et rampes de montée en température),
- la modélisation de l'évolution d'une distribution de précipités donnée au cours de traitements thermiques anisothermes.

L'étude menée a abouti à une meilleure compréhension des mécanismes gouvernant l'évolution d'un état précipité soumis à des changements de température.

General introduction

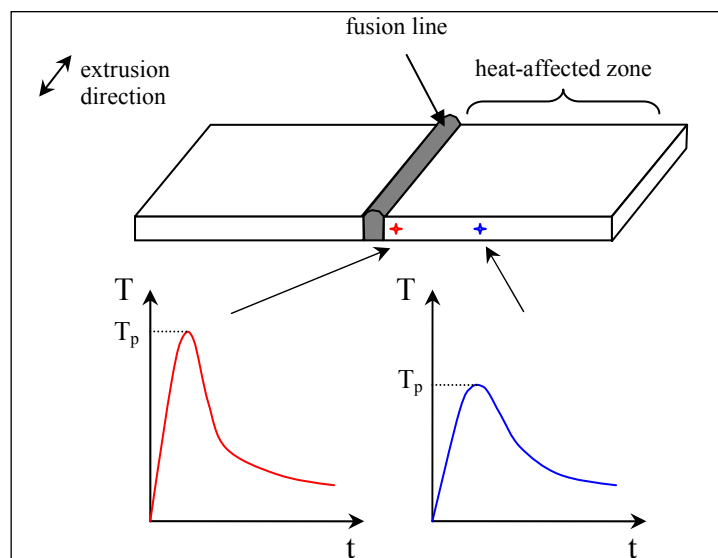
Industrial and scientific background

The use of light alloys, in particular aluminium alloys, is in expansion in the automotive industry due to their low density and good mechanical properties. One of the main issues for automotive applications consists in joining all individual elements. This is particularly problematic in case of precipitate hardening aluminium alloys, like 6xxx (Al-Mg-Si) or 7xxx (Al-Zn-Mg) series. For cost considerations the main joining process remains arc-welding.

This process is particularly detrimental for the mechanical properties for two main reasons:

- in the limits of the weld pool, the fusion deeply modifies the microstructure and then the mechanical properties, in addition to composition changes involved by the filler metal,
- out of the fusion zone, the base material properties are affected due to brutal temperature changes, which induce microstructural changes.

In this study we will focus on the second point, i.e. microstructural evolution, more precisely the evolution of the strengthening precipitation, outside the fusion zone. This region is called the heat-affected zone (HAZ), i.e. the region where the properties of the base material are affected by the thermal cycle of the welding process. In each point of the heat-affected zone, the thermal profile is different, as illustrated in the figure below.



Schematic thermal profiles along the heat-affected zone. T_p refers to the peak temperature.

The studied material is a commercial alloy of the 7xxx series: the 7108.50, which is used for the processing of car bumpers. Good mechanical properties (in particular the yield strength) of this alloy stem from precipitation strengthening. Submitted to high temperature changes, the precipitate microstructure may become unstable and will lose its beneficial effect on mechanical properties.

In Al-Zn-Mg alloys, the precipitation sequence is relatively complex and different states may be used for industrial applications. The decomposition sequence from the solid solution is basically:

Solid solution \rightarrow Guinier-Preston zones \rightarrow metastable η' \rightarrow equilibrium η

This involves metastable precipitates (like GP zones or η') and the stable η -phase which show very different solvus temperatures. Therefore, when submitted to a sudden temperature change, the precipitation state will be modified depending on:

- the nature of initially present precipitates,
- the temperature range and
- the duration of the heat input.

Different processes may be involved: dissolution, coarsening or phase transformation from metastable precipitates to a more stable phase.

Methodology

Study of the as-welded structures

We are interested in the precipitation microstructure along the heat-affected zone of the welded Al-Zn-Mg alloy 7108.50. We will study the influence of the initial precipitation state by using three different initial tempers: each state is characterised by a different precipitate microstructure, constituted of either GP zones (T4 temper), η' (T6 temper) or η -phase (T7 temper). These initial states need to be carefully characterised to serve as reference microstructural states.

To characterize the precipitation state in each point of the heat-affected zone, two complementary techniques have been used:

- Small-Angle X-ray Scattering (SAXS) which provides average features of the precipitation microstructure like the volume fraction and the mean particle size and
- Transmission Electron Microscopy (TEM) which provides quantitative local characterisation of the precipitation microstructure like the particle distribution.

Precipitation evolution during model non-isothermal heat treatments

To better understand the precipitation evolution during welding which is a particularly complex non-isothermal heat treatment, more simple thermal cycles have been investigated like reversion treatments and continuous heating. The evolution of the precipitation with time has been followed in-situ using two techniques:

- SAXS which provides volume fraction and mean radius evolution during the heat treatment (in-situ SAXS experiments) and

- Differential Scanning Calorimetry (DSC) which reveals the reactions occurring during the thermal cycle.

Modelling of precipitation evolution in non-isothermal situations

A model based on simple laws has been developed to describe the evolution of a given precipitate distribution submitted to temperature changes. To apply the modelling to the welding process, the thermal profiles experienced in each point of the heat-affected zone needs to be determined. This model will be confronted to experimental results.

Study

After a presentation of the materials and the investigation techniques employed to quantify the precipitation state (Chapter I), the three initial states will be extensively characterised in Chapter II to serve as reference precipitation states.

In Chapter III, the thermal cycles experienced in each point of the heat-affected zone will be calculated. The microstructure in the as-welded state will be characterised for the three initial tempers by means of SAXS and TEM. Moreover the capacity of the material to recover good mechanical properties through post-welding heat treatments will also be investigated.

Chapter IV will be dedicated to the characterisation of the precipitation evolution during controlled non-isothermal heat treatments. The aim of this chapter is to understand the mechanisms controlling the precipitation evolution during reversion treatments and continuous heating, leading to a better understanding of the precipitation changes during the welding process.

Finally modelling will be developed in Chapter V by means of simple laws applied to a precipitate distribution. The results are compared to experimental data obtained from controlled heat treatments and after welding.

Each chapter (except chapter I) is introduced by a literature review relative to the discussion developed in this section.

Chapter I. *Materials and experimental techniques*

This chapter is dedicated to the presentation of the materials studied in this work and of the investigation methods employed to quantify the precipitation evolution during welding and other non-isothermal heat treatments. Materials in the as-welded condition have been provided by Hydro Raufoss Automotive. Both transmission electron microscopy and small-angle X-ray scattering have been used to quantify the precipitation features in terms of size and volume fraction.

I.1. **Materials**

The alloy selected for this study is a commercial Al-Zn-Mg alloy: AA 7108.50. This alloy was provided by Hydro Raufoss Automotive as extruded thin plates, in the as-welded state. Three different initial states, i.e. three different tempers, have been welded: T4 naturally aged, T6 peak-aged and T7 an overaged state.

I.1.1. **Composition**

Nominal composition of the alloy is given in Table I.1.

	Zn	Mg	Cu	Mn	Ti	Cr	Zr	Fe	Si
wt %	5.5	0.80	0.016	0.010	0.008	0.002	0.16	0.17	0.05
at %	2.35	0.92	0.007	0.005	0.005	0.001	0.05	0.085	0.05

Table I.1: Composition of AA7108.50 alloy (in weight and atom %). Minor elements appear in gray.

This alloy possesses a relatively low content of solute elements compared to high-strength alloys (generally Al-Zn-Mg-Cu alloys). Consequently it has the advantage of a lower quench-sensitivity. This allows to limit precipitation of undesirable coarse particles, in particular on grain boundaries, during the cooling part of the welding process.

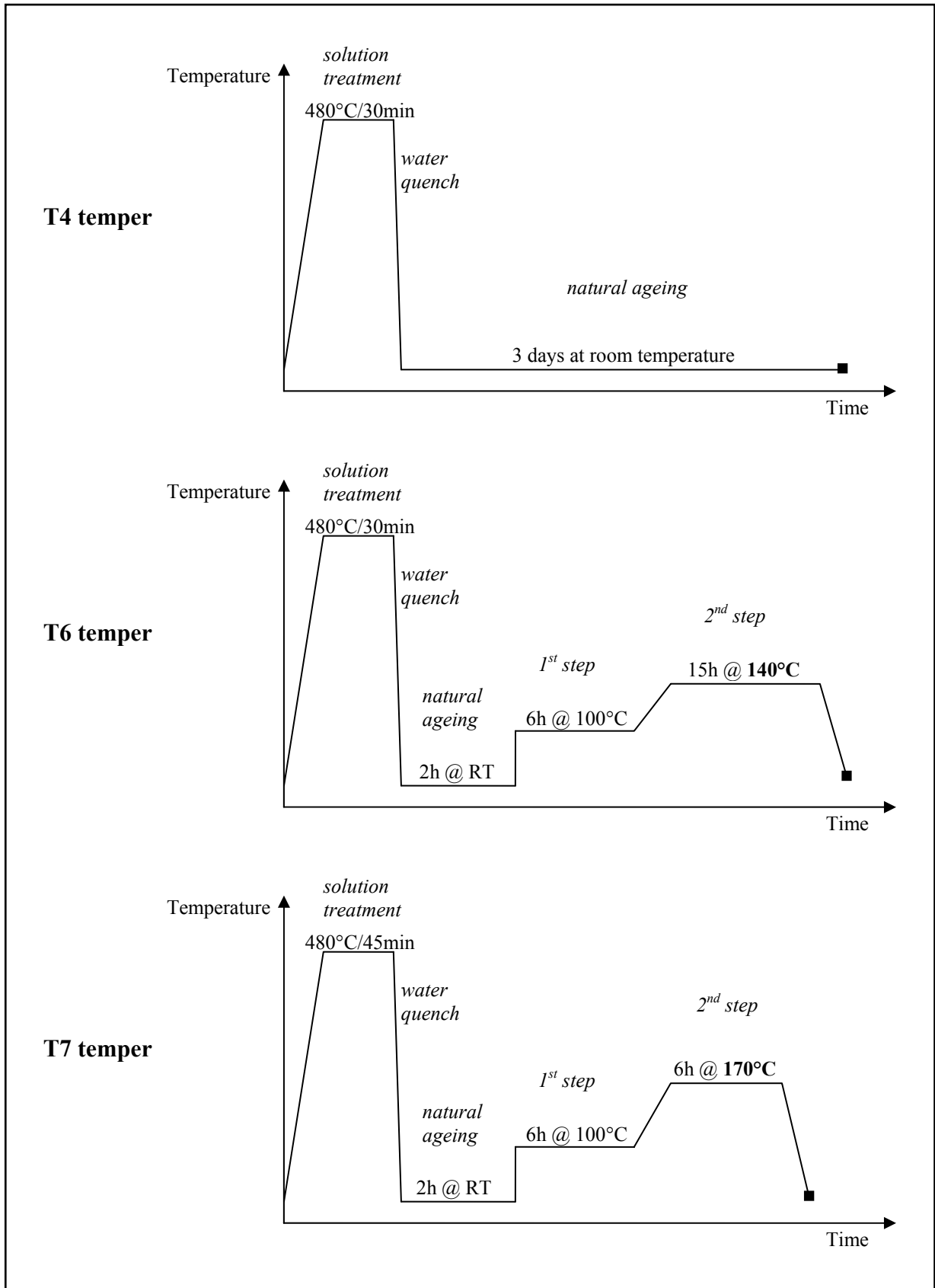
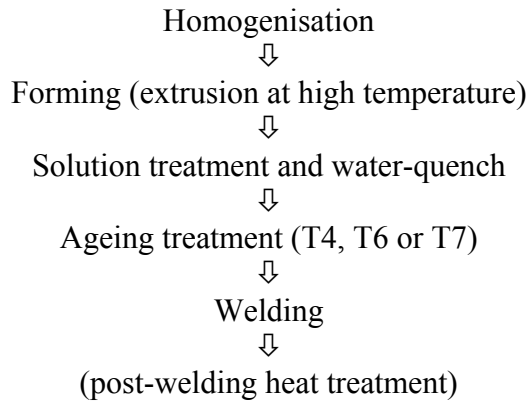


Figure I.1: Schematic representation of heat treatments used to perform T4, T6 and T7 tempers.

I.1.2. Thermomechanical treatment

The global thermomechanical treatment is as follows:



Three different tempers were welded: T4, T6 and T79 (called T7 in the following). Definitions of these tempers are given in Figure I.1. The T4 state is obtained by natural ageing, whereas the T6 and T7 states are the results of two-step ageings. The T6 temper corresponds to the peak-aged hardening condition (obtained at 140°C) and the T7 temper is an overaged state (obtained at 170°C).

I.1.3. Welding parameters

Welding experiments have been carried out at the Hydro Raufoss Automotive plant in Norway (Raufoss). The procedure consisted in welding together two extruded plates of the 7108.50 alloy, using MIG (Metal Inert Gas) process under argon (see Chapter III for more details about the welding process). The filler material is an Al-5wt%Mg alloy.

Sample geometry is shown in Figure I.2. Initial plate dimensions were 5mm*150mm*300mm. The welding process was performed by a welding robot, insuring the reproducibility of the procedure. To be sure to study steady-state welding, only the inner 100mm part of the welded plate was kept for investigation (see Figure I.2.a). The width of the weld nugget is about 8.5 mm as shown in Figure I.2.b.

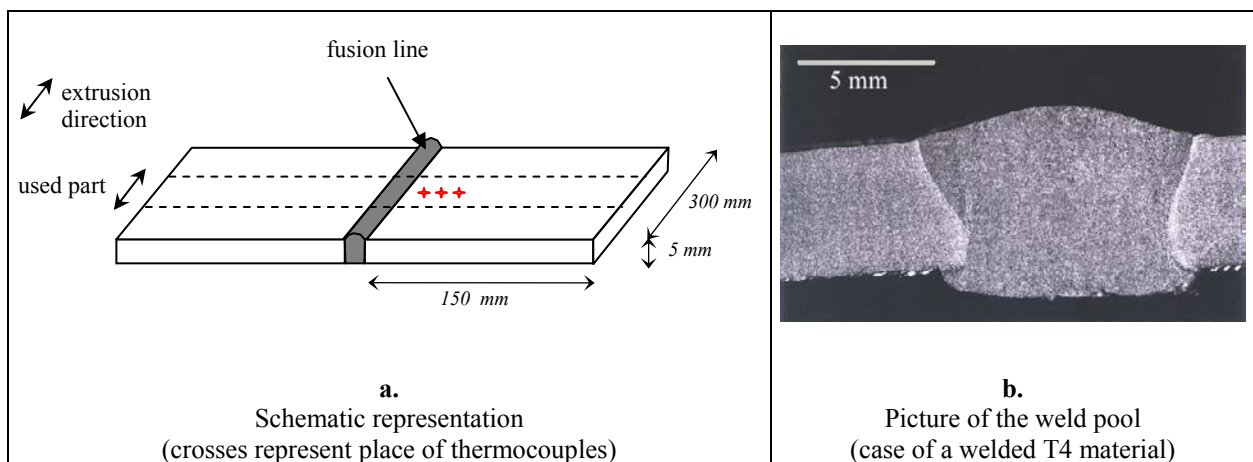


Figure I.2: Sample geometry.

During welding, the temperature profile during the thermal cycle was registered in three points at different distances from the fusion line: 10, 20 and 30mm (see crosses on Figure I.2.a). The temperature measurements were carried out by thermocouples. Welding parameters are given in Table I.2.

Current tension	Amperage	Wire speed	Welding speed
21.9 V	202 A	12 m/min	10 mm/s

Table I.2: Welding parameters.

After welding and cutting to reduce the size of the samples, welded parts were put into liquid nitrogen, experiencing a maximum of 10 minutes at room temperature after welding. The samples were received in the as-welded condition and stored during the whole duration of the Ph.D. work in liquid nitrogen to prevent the precipitation of GP zones at room temperature.

I.2. Experimental techniques

I.2.1. Microhardness

Microhardness measurements have been carried out to have a first insight of the evolution of mechanical properties after various heat treatments, including welding. This technique is particularly well suited to the study of welding since it is possible to measure microhardness profiles along the transverse axis of the welded material. Thus we can monitor the evolution of mechanical properties in each point of the heat-affected zone. It would be much more difficult to perform other mechanical testing in this zone as it would require preparation of very small-sized and thin samples parallel to the welding line.

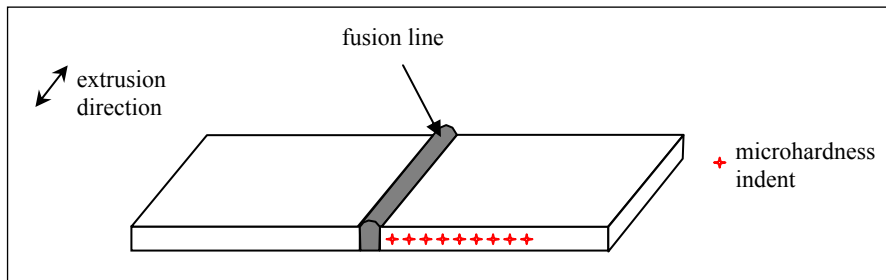


Figure I.3: Illustration of microhardness sample geometry.

Microhardness measurements have been carried out on a LEITZ apparatus. Preparation of samples consists in polishing down to 1 μm . The maximum load of 500g has been chosen to maximise precision of the results. In the case of welded samples, microhardness has been measured at numerous points along the heat-affected zone with spacings down to 0.5mm. Measurements have been carried out on a transverse section at mid-thickness of the plate. Figure I.3 shows the measurements conditions.

Vickers hardness can be directly calculated from the measurements of the two diagonals of the indent using the following relationship:

$$\text{Microhardness (HV}_{500\text{g}}) = \frac{189.F.10^3}{d^2} \quad (I.1)$$

where d is the mean value of diagonal measurements (in μm),
 F value is 4.903N corresponding to 500g load.

For the chosen load, the maximum size of the indent experienced during the various measurements performed during this work, was found to be around 150 μm . This is relatively small with regard to the extension of the heat-affected zone (of the order of 1 cm). This technique is therefore well adapted to our study.

I.2.2. Optical microscopy

Optical microscopy has been used to characterise the grain and sub-grain structure of the alloys in their initial state and after welding.

The grain structure has been revealed using electropolishing. Specimens were anodized in 5% HBF_4 (+ distilled water) at 28 volts for 2 minutes before optical microscopy investigations.

Sub-grain boundaries have been evidenced by chemical chromic etching. The solution consists of 1 ml HF, 16 ml HNO_3 , 84 ml chromic solution (30mg crystallised chromic anhydrite in 830 ml distilled water). Specimens are immersed in this solution during 15s to 2 minutes to reveal well-defined sub-grain boundaries.

I.2.3. Differential Scanning Calorimetry (DSC)

Differential scanning calorimetry has been used in two ways:

- to elucidate the nature of the precipitate phases formed during different heat treatments and to give some information about their relative volume fractions,
- to study dissolution and precipitation kinetics.

This technique is based on the measurements of exchanged heat during a transformation.

Samples for DSC analysis are prepared by manual polishing to obtain disk-shaped samples with a mass between 10 and 20mg. DSC measurements of the heat flow have been performed using the calorimeter in the constant heating mode (between 5 and 100 $^\circ$ /min). To increase the sensitivity of the measurements, a high purity aluminium disc (of mass approximately equal to that of the samples) was used as a reference. No thermal events are expected to occur in this reference sample over the range of investigated temperatures. In order to minimize oxidation, experiments have been carried out under a controlled atmosphere.

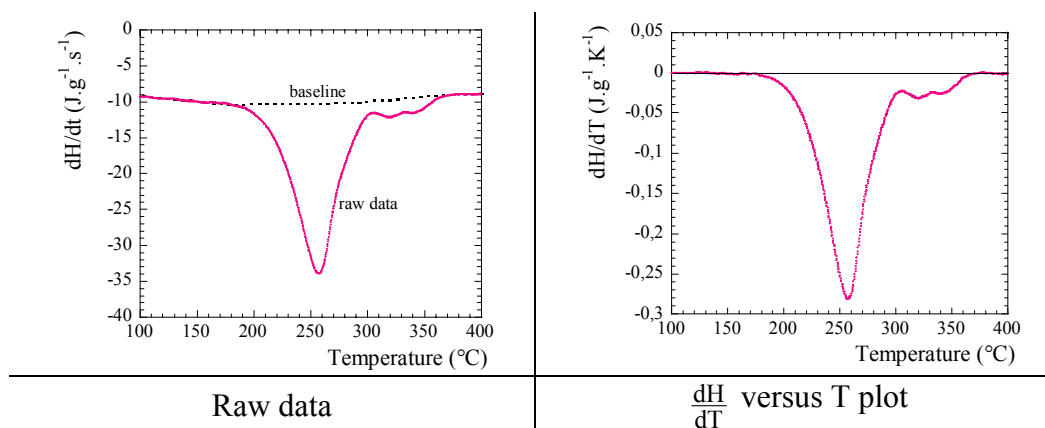


Figure I.4: DSC baseline correction.

After each run, a polynomial baseline was subtracted from the data (see Figure I.4). This baseline represents the temperature-dependent heat flow of the aluminium-rich solid solution and of insoluble precipitates. The remaining heat flow represents the heat associated with the solid state reactions which take place during the DSC run. Each dominant reaction can be characterised by a peak in the $\frac{dH}{dT}$ versus T plot.

DSC experiments have been carried out at Budapest (Hungary) at the Department of Physics of the Eötvös Loránd University on a Perkin-Elmer device under supervision of I. Groma and J. Lendvai.

I.2.4. Transmission Electron Microscopy (TEM)

Transmission electron microscopy has been first used to study qualitatively the precipitation microstructure of materials in their initial states or after welding. In a second part of the investigation, TEM was used in a quantitative manner, by measuring the thin foil thickness, which is necessary for a quantitative measure of the precipitate density.

We have focused our study on intra-granular precipitation, i.e. on hardening precipitation.

I.2.4.1. Conventional TEM

Fine-scale precipitation (strengthening precipitation) can be investigated by this technique. TEM is helpful in determining the nature of the particles, using diffraction mode, and the particle distributions, using imaging (plus image analysis) and thus particle sizes.

For all observations, except for thickness measurements, a Jeol 3010 TEM, operating at 300 KV has been used (see Figure I.5).

TEM samples have been prepared using the following procedure:

- manual grinding down to 100 μm ,
- electropolishing using a solution composed of $\frac{1}{3}$ nitric acid and $\frac{2}{3}$ methanol. Experimental conditions were -20°C and 15V-200mA.

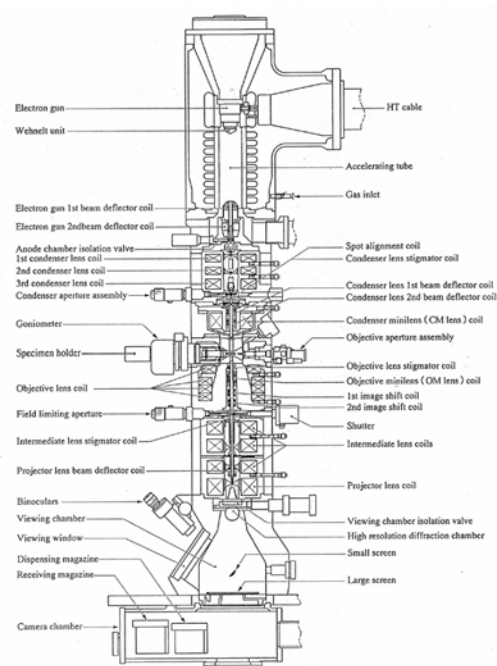


Figure I.5: Scheme of the Jeol 3010 TEM.

I.2.4.2. Quantitative TEM: measurement of precipitate volume fractions

Quantitative TEM can be used to determine the volume fraction of hardening precipitates. This technique proceeds in several steps [Donnadieu, 1999]:

- 1) Imaging of precipitates by conventional TEM in a selected area,
- 2) Image analysis to obtain the areal density of precipitates included in the investigated area taking into account the precipitate morphology,

- 3) Local thickness measurement of the investigated area, which allows to calculate the investigated volume,
- 4) Calculation of the volume fraction.

Local thickness determination of a crystal can be obtained using TEM in the Convergent-Beam Electron Diffraction (CBED) mode. This method is generally considered as the most accurate method of thickness measurement for crystalline materials [Williams, 1996]. A good review and methodology for thickness measurement by CBED method is given by Williams and Carter [Williams, 1996].

Background

CBED is a diffraction mode which differs from usual selected-area diffraction (SAD) (see Figure I.6). Actually in SAD mode, the incident electron beam on the specimen is parallel and relatively large ($\sim 1\text{-}10\mu\text{m}$) and forms point-shaped diffraction pattern. In the case of CBED, the beam is convergent (beam convergence semi-angle $\alpha > 10$ mrad) and relatively small ($\sim 10\text{-}100$ nm). This gives rise to a pattern constituted of diffraction disks that include local crystal information.

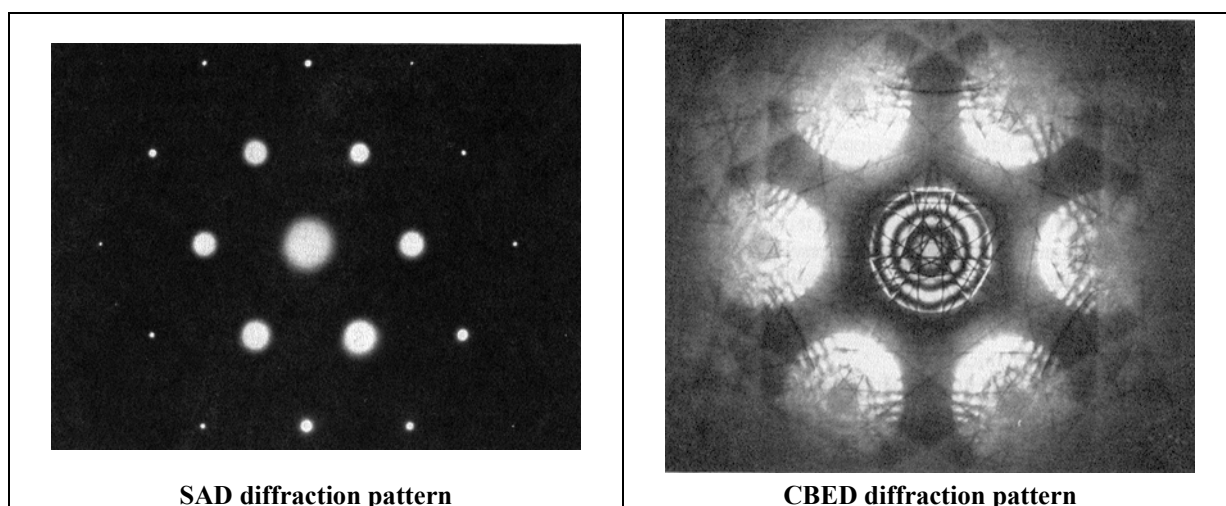


Figure I.6: SAD and CBED diffraction pattern obtained in the $[111]\text{Si}$ zone axis [Williams, 1996].

The size of the diffraction disk depends on the convergence semi-angle α , as shown on Figure I.7. The convergence angle can be modified by changing the C2 aperture size. The pattern of non-overlapping disks is called a Kossel-Möllentstedt (K-M) pattern.

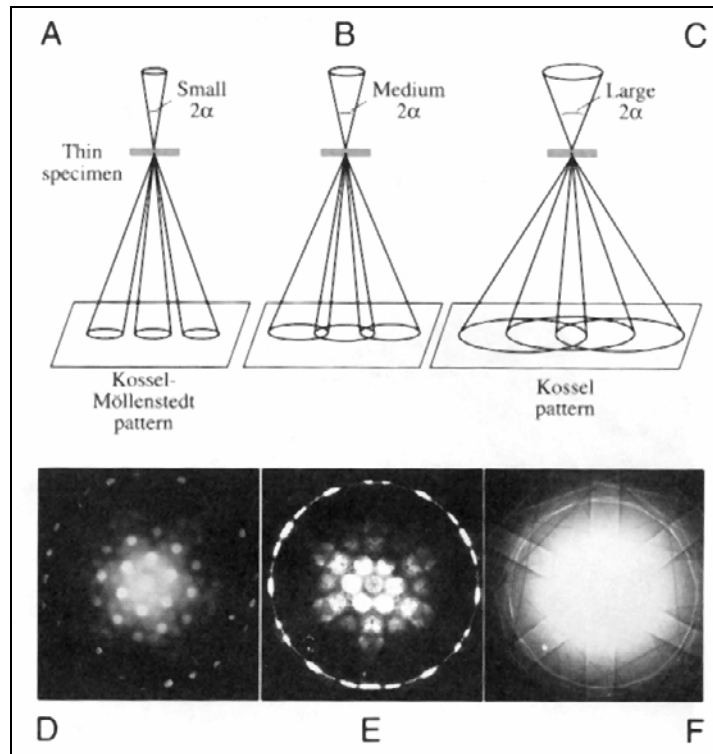


Figure I.7: (A)-(C) schematic electron paths show how increasing the convergence semi-angle α causes the CBED pattern to change from one in which individual disks are resolved to one in which all the disks overlap. In (D)-(F) are presented the experimental patterns on the TEM screen corresponding to (A)-(C) [Williams, 1996].

When one records a zone-axis pattern in these conditions, such as shown in Figure I.6, the 000 disk usually contains concentric diffuse fringes. When moving the specimen under the beam, the number of fringes changes: they become more numerous as the foil thickness increases. In fact, the number of fringes increases by one every time the thickness increases by one characteristic distance, called the extinction distance, ξ_g . ξ_g is a parameter related to the nature of the crystalline structure of the sample (via the interplanar distance of diffracting planes) and to the wavelength of the incident beam. If the specimen is less than one extinction distance thick, then no fringes are observed and the 000 disk is uniformly bright. Clearly these fringes contain thickness information. Moreover this foil thickness information is localised at the point in which the diffraction pattern is obtained.

In practice, to simplify the interpretation, thickness measurements are not made under zone-axis conditions but under two-beam conditions with only one strongly excited reflection. In this case, the CBED disks contain parallel rather than concentric intensity oscillations, as shown in Figure I.8. Again the number of fringes is related to the specimen thickness.

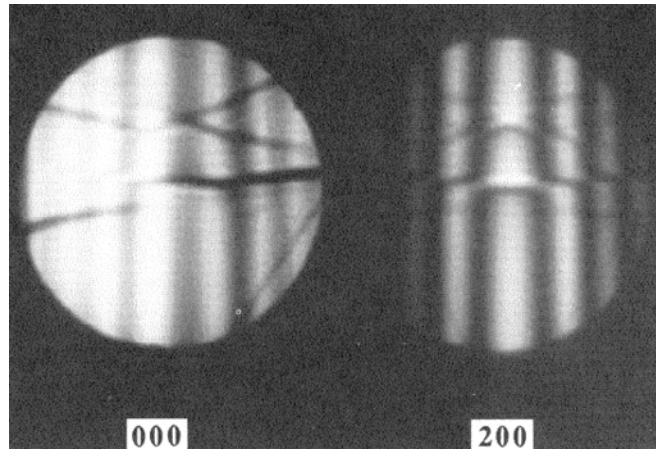


Figure I.8: Kossel-Möllenstedt fringes in a CBED pattern from pure Al taken under two-beam conditions with (200) strongly excited [Williams, 1996].

Under two-beam conditions, the theoretical diffracted intensity is given by [Morniroli, 1998]:

$$I_g = \left(\frac{1}{s\xi_g} \right)^2 \sin^2(\pi z s) \quad (I.2)$$

where z is the foil thickness,
 s is the deviation vector,
 ξ_g is the extinction distance.

In conventional imaging, under exact two-beam conditions, s is equal to 0 and z is varying. This gives rise to rocking-curve intensity oscillations which corresponds to the thickness fringes observed in a bright-field image (see Figure I.9). In CBED, thickness is constant and s is varying, giving rise to the previously observed oscillations in discs observed in the diffraction mode (see Figure I.9).

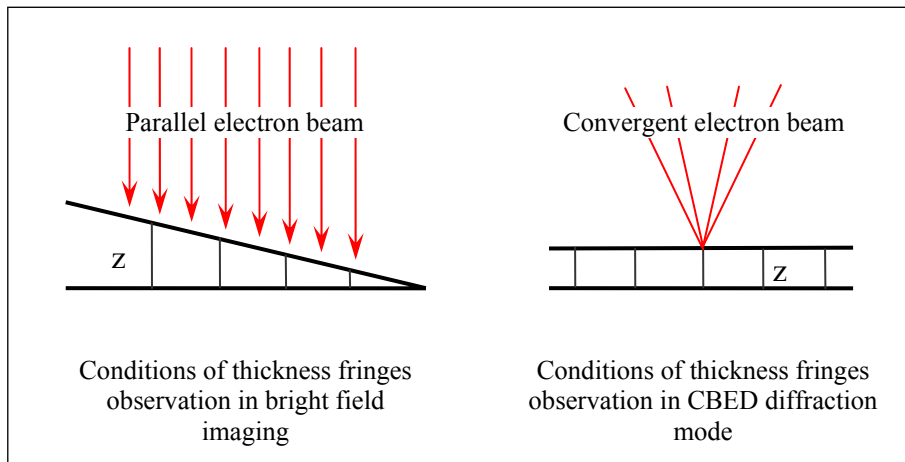


Figure I.9: Conditions of formation of thickness fringes by variation of z (bright field imaging) or s (CBED).

There are two potential drawbacks which can be encountered used CBED due to a very local incident beam:

- local intense contamination can occur which can cause localised stresses,
- the convergent beam may heat or damage the region of investigation.

Thickness determination

The procedure to extract the thickness from the fringe pattern was first described by Kelly *et al.* [Kelly, 1975] and developed in detail by Allen [Allen, 1981].

For a constant foil thickness (z), the positions of dark fringes in the diffracted hkl disk are correlated to a series of deviation values from the Bragg angle, s_i , corresponding to different incident angles of electrons within the convergent incident beam. Kelly *et al.* [Kelly, 1975] have shown that in the two-beam approximation, the following equation is verified:

$$\left(\frac{s_i}{n_i}\right)^2 + \left(\frac{1}{\xi_g n_i}\right)^2 = \left(\frac{1}{z}\right)^2 \tag{I.3}$$

where n_i is an integer corresponding to the i^{th} fringe (generally first fringe corresponds to $n_1=1$, and so on...
 ξ_g is the extinction distance,
 z is the foil thickness.

Each s_i is defined as:
$$s_i = \frac{\lambda Y_i}{2Rd_{hkl}^2} \tag{I.4}$$

where λ is the wavelength of the incident beam,
 Y_i corresponds to double the distance between the central bright fringe and the i^{th} dark fringe (see Figure I.10),
 R is the distance between the diffracted disk and the transmitted one (see Figure I.10),
 d_{hkl} is the hkl interplanar spacing.

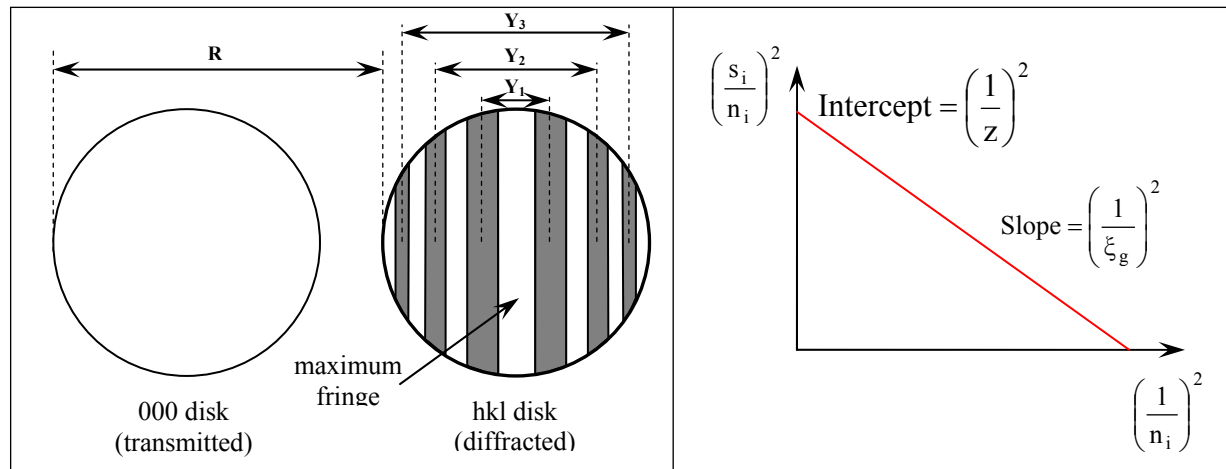


Figure I.10: Measurements and plot necessary to extract thickness (z) from Kossel-Möllenstedt fringes.

Therefore the plot $(s_i/n_i)^2$ versus $(1/n_i)^2$ is expected to be linear and extrapolation to the ordinate gives z^{-2} and hence the foil thickness z (see Figure I.10). If the plot is a curve and not a line, it means that $n_1=1$ was not a good assumption, i.e. the real first fringe is unobservable (blended with the central fringe); then repeat the procedure with $n_1=2$.

Similarly, bright fringes can give a series of s_k values. This series may give a straight line in a similar plot $(s_k/x_k)^2$ versus $(1/x_k)^2$ where x_k belongs to the following series: 1.431; 2.459; 3.471; 4.777...

Application of this procedure can be found in Chapter II.

I.2.5. Small-Angle X-ray Scattering (SAXS)

Small-Angle X-ray Scattering (SAXS) is a technique used to study the structural features of a distribution of particles. The presence of small particles embedded in a matrix, gives a characteristic response under an X-ray beam. This mechanism is comparable to the commonly observed phenomena of perihelion and the scattering of light in fog (see Figure I.11).

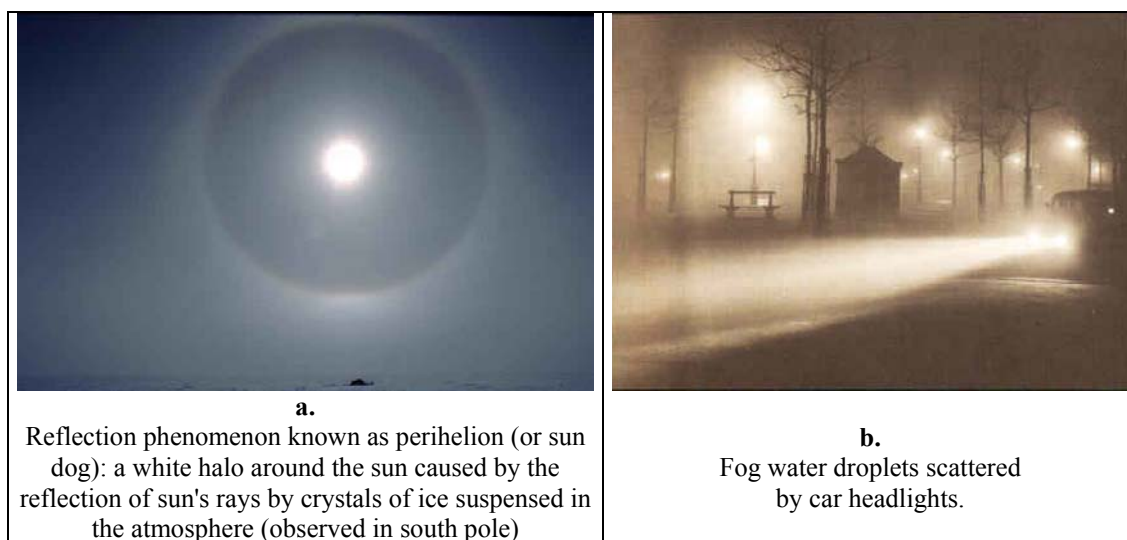


Figure I.11: Commonly observed scattering phenomena.

Since X-rays are primarily scattered by electrons, they are sensitive to electron density differences existing between particles and the matrix (basically the atomic number contrast). Like any other scattering process, SAXS is controlled by a reciprocity law which gives an inverse relationship between particle size and scattering angle. Therefore as particle sizes are considerably larger than X-ray wavelength, the scattering response is expected at small angle range.

I.2.5.1. General theory

A synthetic presentation of the basic theory, techniques and applications of SAXS can be found in Small-Angle X-ray Scattering edited by O. Glatter and O. Kratky [Glatter, 1982].

Diffraction is produced by the interference of waves scattered by an object. In the case of X-rays, every electron becomes the source of a scattered wave. The scattered waves are coherent. Coherence means that the amplitudes are added and the intensity is given by the absolute square of the resulting amplitude. If we assume that the system is isotropic, i.e. that the system exhibits spherical symmetry, amplitudes of the waves are equal in each direction and differ only by their phase. This phase only depends on the position of the electron in space.

Let us consider the path difference between two waves scattered in the same direction by two points separated by \mathbf{r} . It can be shown that the scattering response of an electron is given by:

$$I(\mathbf{q}) = \mathbf{e}^{-i\mathbf{q}\mathbf{r}} \quad (I.5)$$

\mathbf{q} is the scattering vector with the following magnitude:

$$q = \frac{4\pi \sin\theta}{\lambda} \quad (I.6)$$

where θ is the scattering semi-angle,
 λ is the wavelength.

The resulting amplitude in a defined direction (characterised by \mathbf{q}) is obtained by summing up the response of all electrons included in the investigated volume:

$$F(\mathbf{q}) = \iiint \rho(\mathbf{r}) e^{-i\mathbf{q}\cdot\mathbf{r}} dV \quad (I.7)$$

where ρ is the electron density.

The scattered intensity is then given by the absolute square of the resulting amplitude. In the case of small-angle scattering, this intensity can be written:

$$I(\mathbf{q}) = \int \tilde{\rho}^2(\mathbf{r}) \frac{\sin(\mathbf{q}\cdot\mathbf{r})}{qr} 4\pi r^2 dr \quad (I.8)$$

where $\tilde{\rho}^2(\mathbf{r})$ is the so-called autocorrelation function defined as:

$$\tilde{\rho}^2(\mathbf{r}) = \iiint \rho(\mathbf{r}) \rho(\mathbf{r} + d\mathbf{r}) dV \quad (I.9)$$

For the sake of simplicity, let us now consider a dilute solution of identical spherical particles of radius R_0 and electron density ρ_s , embedded in a matrix of electron density ρ_0 . This system can be entirely represented by the scattering of one single particle of radius R_0 and volume V .

The intensity scattered by one single spherical particle is given by:

$$I(\mathbf{q}) = (\rho_s - \rho_0)^2 V^2 \left[3 \frac{\sin(qR_0) - qR_0 \cos(qR_0)}{(qR_0)^3} \right]^2 \quad (I.10)$$

For a distribution of particles of different sizes, the intensity can be calculated as follows:

$$I(\mathbf{q}) = \int_0^\infty I(\mathbf{q}, R) f(R) dR \quad (I.11)$$

where $f(R)$ is the distribution function of the particles.

Invariant Q_0

It can be shown that the so-called integrated intensity Q_0 defined in the following way must be invariant, irrespective of size and shape of the particles:

$$Q_0 = \int_0^\infty I(\mathbf{q}) q^2 dq \quad (I.12)$$

In case of a two-phase system, this invariant Q_0 is directly related to the volume fraction and electron density difference, also called contrast:

$$Q_0 = 2\pi^2 (\rho_s - \rho_0)^2 f_v (1 - f_v) \quad (I.13)$$

where f_v is the volume fraction of particles.

Guinier approximation

Guinier showed that, for small q -values, a universal approximation for all morphologies of particles exists:

$$I(\mathbf{q}) = (\rho_s - \rho_0)^2 V^2 \exp\left(-\frac{q^2 R_g^2}{3}\right) \quad (I.14)$$

where R_g is called the Guinier radius.

R_g is also called radius of gyration as it is defined as the mean square distance from the particle centre of gravity, where the role of mass is played by electrons.

In the case of a monodisperse distribution of spheres, the Guinier radius can be directly related to the mean radius of particles R_0 :

$$R_0 = \sqrt{\frac{5}{3}} R_g \quad (I.15)$$

In the case of platelets, the Guinier radius (R_g) is related to the radius R and thickness (a) of the platelet through the relationship [Gomiero, 1990]:

$$R_g = R \sqrt{\frac{2 + \left(\frac{a}{R}\right)^2}{5}} \quad (I.16)$$

Porod's law

For high q -values, the intensity was shown to have an asymptotic response in q^{-4} , called Porod's law:

$$I(q) = \frac{K}{q^4} + I_{\text{Laue}} \quad (I.17)$$

where $K = \frac{Q_0 S}{\pi V}$ with S and V being the surface and the volume of the particle respectively,

I_{Laue} is a term corresponding to the response of the remaining supersaturation of solute atoms in the matrix.

In summary, from this theoretical background, two main features can be determined from the interpretation of SAXS measurements in the case of particles embedded in a matrix:

- the volume fraction using the integrated intensity Q_0 , assuming that the precipitate composition is known (i.e. the electron density),
- the Guinier radius, which can be correlated by calibration with some other technique like TEM to the mean particle size.

I.2.5.2. Preparation of samples and in-situ SAXS experiments

Experimental details are presented here concerning the preparation of the samples and the geometry of the furnace used to carry out in-situ heat treatments.

Sample preparation

Sample thickness has to be adjusted so that both the scattered intensity is high enough and the absorption effect is not too detrimental. This compromise is obtained with an optimal transmission of 0.37. The corresponding thickness is given using the following relationship between transmission tr and sample thickness e :

$$tr = \exp\left(-\left(\frac{\mu}{\rho}\right)_{\text{alloy}} \rho_{\text{alloy}} e\right) \quad (I.18)$$

where $(\mu/\rho)_{\text{alloy}}$ is the mass absorption coefficient of the alloy,
 ρ_{alloy} is the density of the alloy.

In the case of the 7108.50 alloy, the density (ρ_{alloy}) is 2800 Kg/m³ and the $(\mu/\rho)_{\text{alloy}}$ was estimated as 55.8 and 47.7 cm²/g for the two wavelengths used in this work ($\lambda=1.61\text{\AA}$ and $\lambda=1.48\text{\AA}$ respectively). These parameters give an optimum thickness around 75 μm .

To reach such a thickness, samples have been first mechanically polished down to 100 μm . They were then electropolished down to the optimum thickness in a cooled solution at 20°C of $\frac{2}{3}$ methanol, $\frac{1}{3}$ nitric acid under a potential of 15V.

In-situ heat treatments

A furnace has been developed in the laboratory by JC Werenskiold and was specially designed to perform experiments under an X-ray beam. Figure I.12 is a schematic representation of this furnace showing the position of the sample and of the beam. Heating is achieved by a heating resistor wire and controlled by a thermocouple positioned in the vicinity of the sample. Cooling is performed by circulation of a cooling liquid cooled at $\sim 10^\circ\text{C}$.

The maximum temperature obtained was around 500°C and the maximum heating rate which can be reached is 300°/min (5°/s).

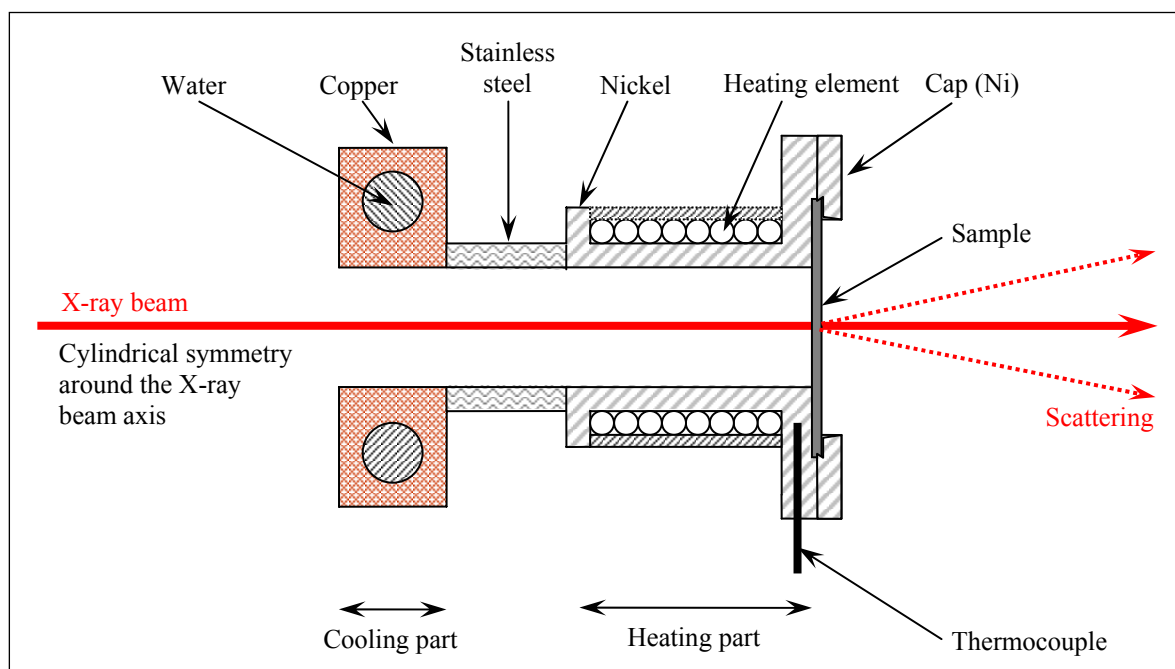


Figure I.12: Schematic representation of the furnace developed to carry out in-situ heat treatments under an X-ray beam.

I.2.5.3. Presentation of the ESRF beam-line

Since our SAXS experiments require:

- a good spatial resolution for scanning of the heat-affected zone in the case of welded structures and,
- a high X-ray flux for time-resolved in-situ experiments,

the D2AM (BM02) beam line at the European Synchrotron Radiation Facility (ESRF) (see Figure I.13) appeared as the most suited device.



Figure I.13: Aerial picture of the ESRF plant in Grenoble.

Each beam-line is composed of three different rooms (see Figure I.14):

- an optics hutch where the beam is transformed to a monochromatic beam at the desired wavelength focused on the sample,
- an experimental hutch where the SAXS device is located, including the sample holder and the 2D-CCD detector which collects the scattered X-rays,
- the control cabin from where the experiment is controlled.

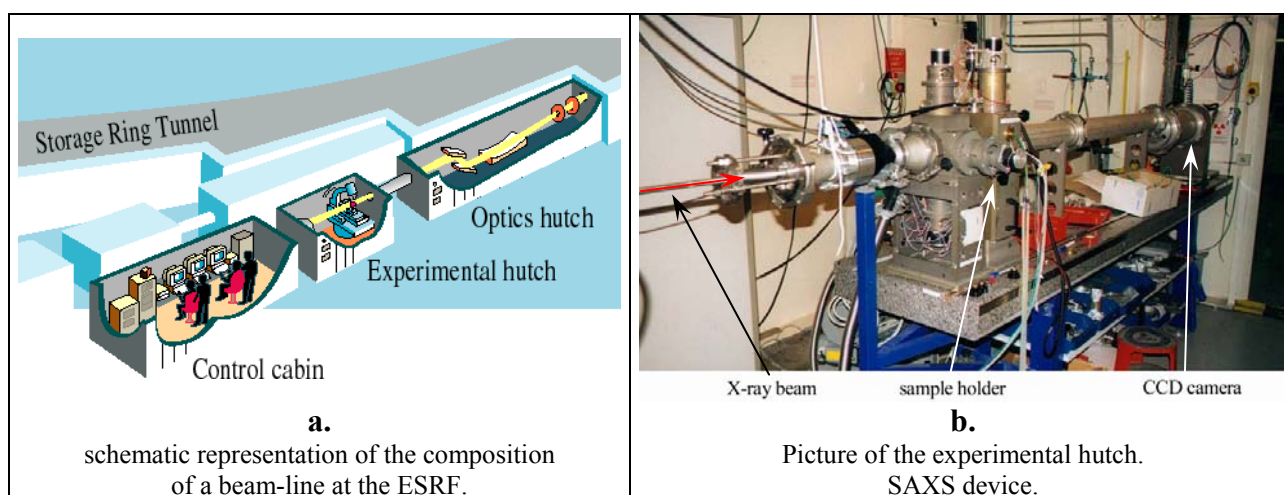


Figure I.14: Beam-line composition.

The SAXS device is sketched in Figure I.15. The dimension of the incident beam on the sample is $100\mu\text{m} * 200\mu\text{m}$, which allows a good spatial resolution of measurements. Photomultipliers (PM0 and PM1) are used to calculate the transmission of the sample and to normalise the signal during data interpretation. The sample holder is kept in vacuum to avoid scattering from air. A beam-stop is placed just in front of the detector on the way of the direct beam to avoid deterioration of the CCD camera.

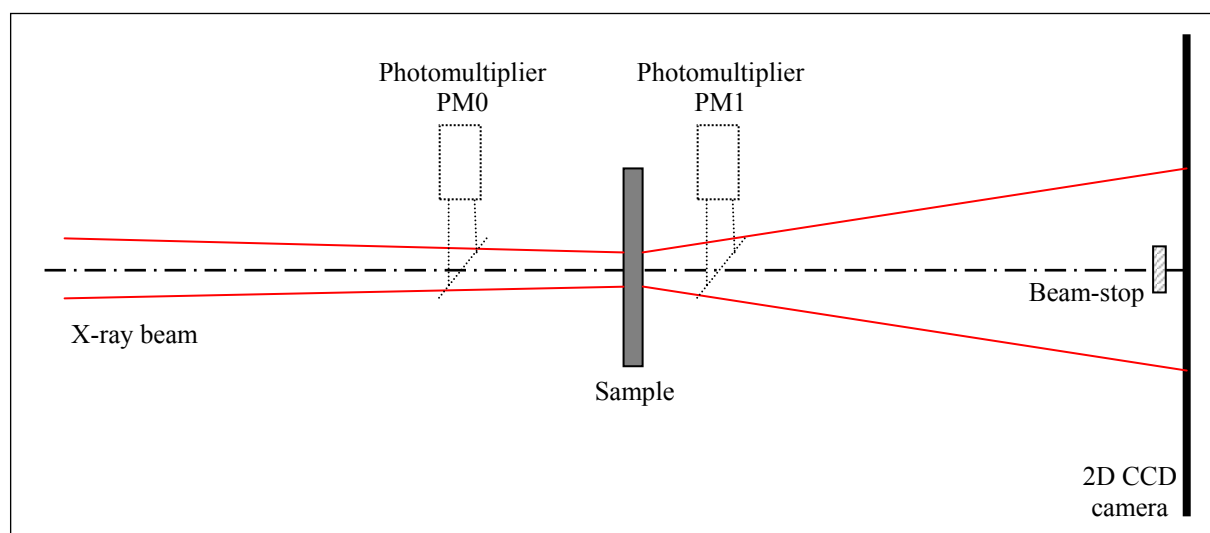


Figure I.15: Schematic representation of the D2AM beam-line device.

Two different sample-detector distances were used to study different sizes from a few Å to 150 Å (q -values included in the $[0.001;0.7]$ range). Moreover two wavelengths close in absolute values, have been used during the two different experiments performed at the ESRF: $\lambda=1.61\text{Å}$ and $\lambda=1.48\text{Å}$ respectively.

I.2.5.4. Data interpretation

Prior to data interpretation in terms of Guinier radius and integrated intensity, different data processing steps are necessary.

Data processing

Figure I.16 shows a typical SAXS spectrum acquired by the CCD camera. Different steps are necessary to correct this raw signal and to convert it to absolute values.

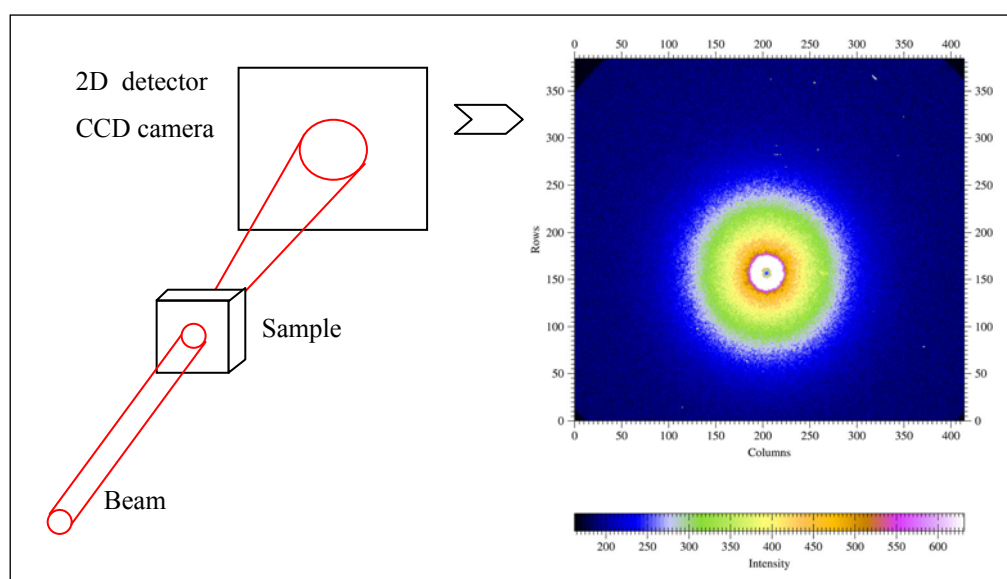


Figure I.16: Typical SAXS map collected by the CCD camera.

- 1) **Correction of the CCD camera defaults.** Subtraction of a signal obtained without the X-ray beam allows for correction of detector noise (called "dark"). Moreover the record of an isotropic scattering signal obtained from the fluorescence of a pure iron sample enables correction for the different collection efficiencies of each pixel of the CCD camera (called "flat" correction).
- 2) **Radial averaging.** An average of the signal intensity obtained at equal q -values (radial average from the centre of the incident beam) is calculated to get a spectrum I versus q .
- 3) **Background noise correction.** A measurement of the scattering of the direct beam without sample is performed and subtracted to suppress any parasite signal (essentially due to non-perfect collimation and diffraction from the slits and also scattering from particles remaining in vacuum, kapton windows, etc.)
- 4) **Intensity normalisation.** The normalised intensity is calculated using the following relationship:

$$I_{\text{norm}}(q) = \frac{I_{\text{corrected}}(q)}{f_{\text{corr}} \cdot \text{tr} \cdot e \cdot r_e^2 \cdot d\Omega} \quad (I.19)$$

where $I_{\text{corrected}}(q)$ is the obtained raw intensity after various corrections,
 f_{corr} is a correction factor obtained by measurement of a standard sample (here lupolen whose maximum intensity is calibrated at 6 cm^{-1} or 75.4 \AA^{-3}) [Russell, 1988],
 tr is the sample transmission,
 e is the sample thickness,
 r_e is the electron radius ($r_e = 2.81 \cdot 10^{-13} \text{ cm}$).

- 5) **Laue correction.** The Laue-term is a constant value corresponding to the scattering of the disordered solid solution and some fluorescence. It can be determined using the Iq^4 versus q^4 plot: the Laue intensity is given by the slope (see equation I.17).

Once all these corrections and treatments are correctly done, the data can be interpreted.

Data interpretation

Features of the microstructure can be determined from SAXS measurements in terms of integrated intensity Q_0 and Guinier radius R_g . These values, under certain conditions, can be converted into precipitate volume fraction and real mean radius, as will be explained in the next chapter.

In order to determine these values (Q_0 and R_g), two main plots have been used (see Figure I.17):

- $Iq^2=f(q)$ where Q_0 can be evaluated from the area under the curve and,
- $\ln(I)=f(q^2)$ where R_g is directly related to the slope of the linear part of the curve.

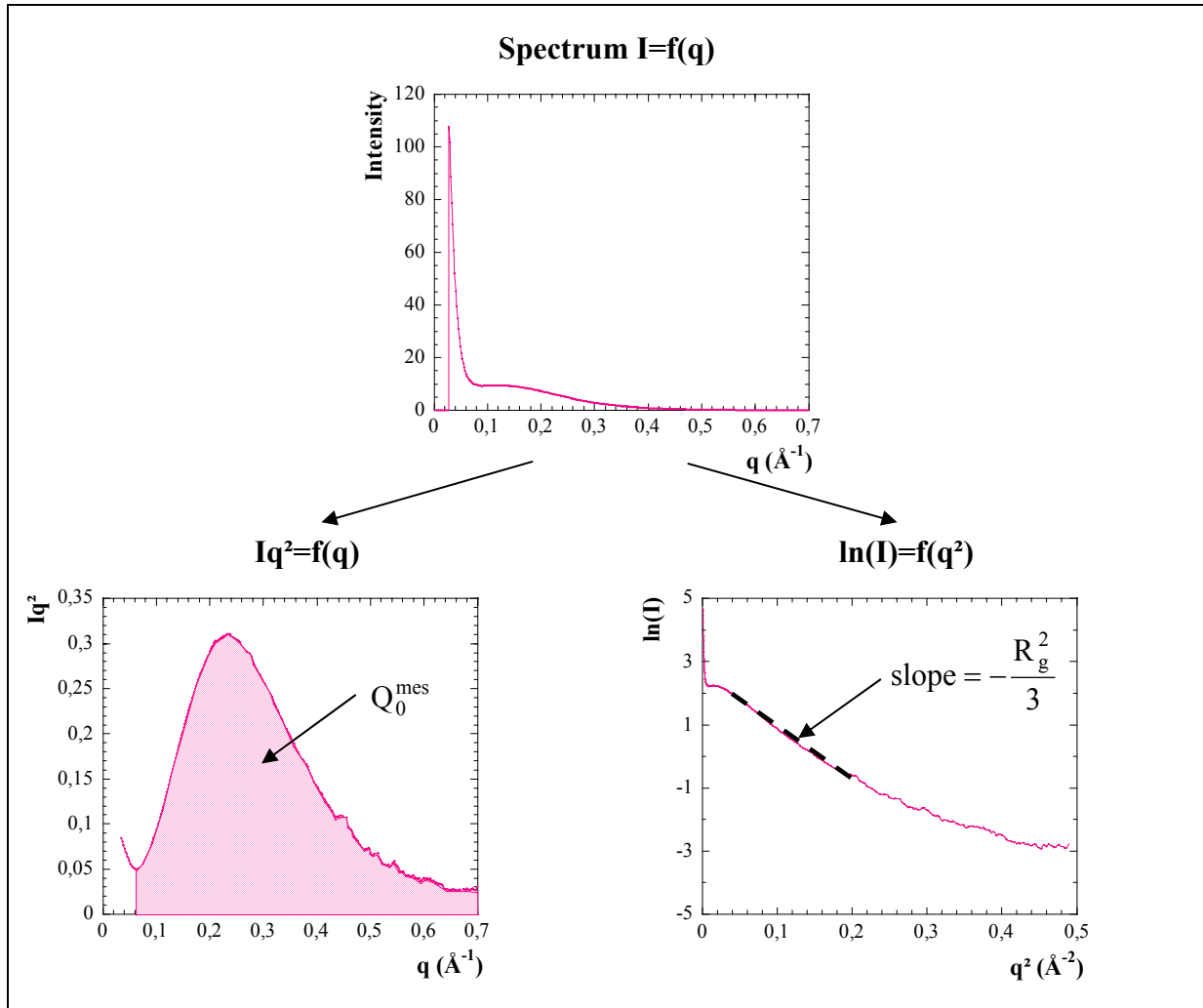


Figure I.17: Interpretation of SAXS data in terms of integrated intensity Q_0 and Guinier radius R_g . Example of a SAXS spectrum measured on a T4 material.

Qualitatively, the presence of a maximum in the Iq^2 versus q plot is related to the presence of a particle family characterised by a mean particle size. In this case, the q -value corresponding to this maximum is equal to $\frac{\sqrt{3}}{R_g}$.

The total scattered integrated intensity Q_0 corresponds to the area under the curve of the Iq^2 versus q plot in the $[0, +\infty]$ range. Naturally, the experimental spectrum is limited by two values, q_0 and q_∞ , making the measured integrated intensity truncated. Owing to the limits on the integral, the rigorous evaluation of Q_0 is accomplished by considering three different contributions [Russell, 1988]:

$$Q_0 = \int_0^{q_0} I(q)q^2 dq + \int_{q_0}^{q_\infty} I(q)q^2 dq + \int_{q_\infty}^{\infty} I(q)q^2 dq \quad (I.20)$$

The first term on the right-hand side covers the q -range from 0 to q_0 , where q_0 corresponds to the first data point. This integral is well approximated by the area of a triangle with base q_0 and height $I(q_0)q_0^2$. The second term is simply the area under the experimental spectrum in the q -range $[q_0; q_\infty]$. The third term can be given by the Porod' behaviour $I(q)=K/q^4$ (see

equation I.17) if this one is obeyed for q -values higher than q_∞ . Finally the total integrated intensity can be calculated as follows:

$$Q_0 = \frac{I(q_0)q_0^3}{2} + Q_0^{\text{mes}} + \frac{K}{q_\infty} \quad (I.21)$$

The Guinier radius can be estimated using the slope of the Guinier plot $\ln(I)$ versus q^2 which is equal to $-\frac{R_g^2}{3}$ (see Figure I.17). The Guinier approximation is valid for small q -values, as it is obtained by limited development close to zero (normally $qR_g \ll 1$). In practise, a well-defined linear behaviour has been observed in the $\ln(I)$ versus q^2 plot for higher qR_g values. The convergence of the Guinier plot was then applied to q -values included in the $[1.2R_g; 2.8R_g]$ q -range. This q -range was chosen to correspond to the maximum of the peak observed in the Iq^2 versus q plot. The procedure to determine the Guinier radius R_g consists in different steps:

- 1) first estimation of R_g using the q_{max} value corresponding to the maximum of the peak in the Iq^2 versus q plot $R_{g1} \approx \frac{\sqrt{3}}{q_{\text{max}}}$,
- 2) a first linear regression is performed in the $\ln(I)$ versus q^2 plot in the q -range $[1.2R_{g1}; 2.8R_{g1}]$, giving a new estimation of the Guinier radius R_{g2} .
- 3) this method is iterated until convergence is obtained.

I.2.6. Summary

In summary, differential scanning calorimetry, transmission electron microscopy and small-angle X-ray scattering appear as complementary techniques in the quantitative description of hardening precipitation in our alloys. They give access to the precipitate nature, morphology, particle distribution, mean size and volume fraction.

These techniques are also powerful tools for the study of precipitation kinetics, in terms of formation, dissolution or transformation from metastable phases to more stable ones.

Chapter II. Characterisation of the material prior to welding

In this chapter will be discussed the quantitative investigation of the studied material's precipitation microstructure prior to welding. First, a literature review will summarise the current understanding of precipitation in Al-Zn-Mg alloys. Two complementary techniques, SAXS and TEM, have been used to quantify hardening precipitates in the three different tempers of interest: T4, T6 and T7. This investigation will serve as a reference in the subsequent study.

II.1. Literature review: precipitation in Al-Zn-Mg alloys

Aluminium alloys having the strongest response to age hardening are based on the Al-Zn-Mg system (7xxx alloys). These alloys benefit from a good precipitation strengthening, through complex decomposition processes involving both stable and metastable phases.

II.1.1. Description of 7xxx alloys

In early stages of development of aluminium alloys, the binary Al-Zn system was believed to be promising. Actually zinc solubility in aluminium is large at high temperature and decreases down to 2% at room temperature, therefore this system was expected to have a good age hardening capacity. However the extent of hardening was relatively small because the precipitates formed were essentially pure zinc, and resulting in a limited hardening of the alloy [Polmear, 1957-1958].

In terms of age hardening, the benefit of a small addition of magnesium was clearly shown by Polmear *et al.* [Polmear, 1957-1958]. Magnesium additions modify notably the hardening phases, as seen in the phase diagram (see Figure II.1.a). A preferential interaction between small zinc atoms and large magnesium atoms on the aluminium lattice, involving some clustering (in order to reduce lattice strain energy), plays an important role in the decomposition processes during ageing.

II.1.1.1. The Al-Zn-Mg system

The aluminium-rich corner of the ternary Al-Zn-Mg phase diagram has been thoroughly investigated, one example of an isothermal section at 200°C is given in Figure II.1.a. Godard [Godard, 1999] made a review of the various published phase diagrams in the literature. These different phase diagrams were relatively coherent in terms of phases involved in the Al-rich corner but discrepancies remained in the details. In particular, the solvus of the $MgZn_2$ -phase, of great interest in dissolution-precipitation modelling of this phase, was subject to large differences, in particular for low and medium temperatures ($T < 300^\circ\text{C}$). Figure II.1.b shows a recent phase diagram presenting the solubility of zinc and magnesium in the aluminium solid solution, calibrated with numerous experimental data [Petrov, 2000].

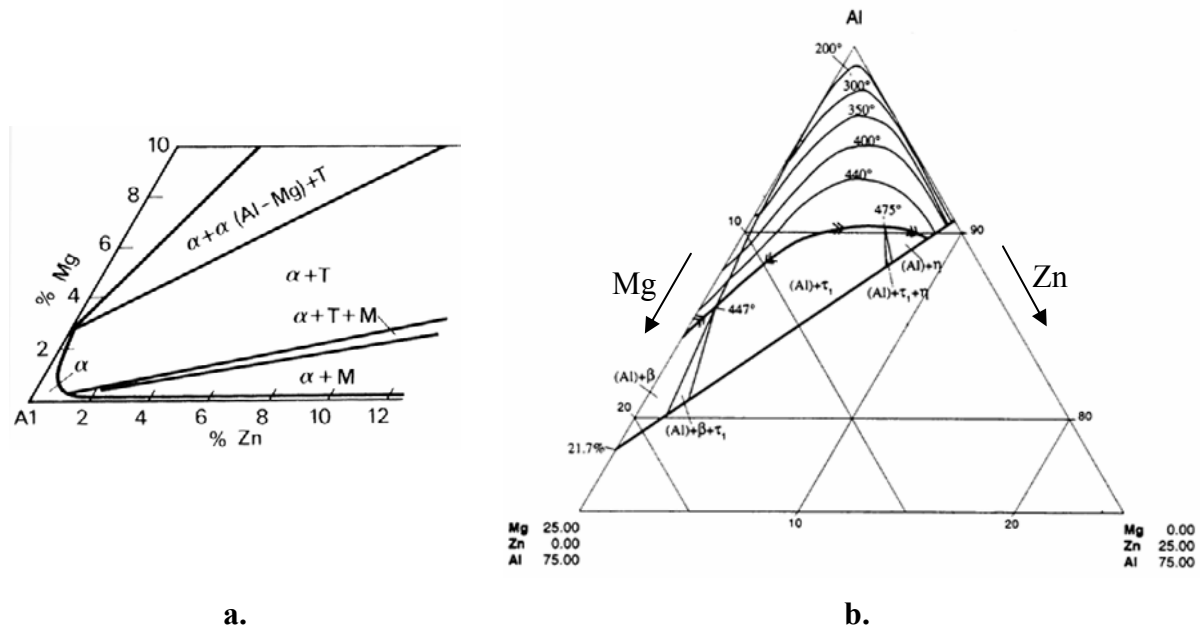


Figure II.1: The ternary Al-Zn-Mg phase diagram in the Al-rich corner
 a. Section at 200°C ($M = \eta = MgZn_2$; $T = Al_2Mg_3Zn_3$) [Polmear, 1995].
 b. Solvus at various temperatures (in at%) [Petrov, 2000].

Modern tools are now available to provide on-line phase-diagrams, isothermal sections, etc. Figure II.2.a shows the result of a calculated phase diagram at 300°C using the PANDAT database (for more information see <http://www.computherm.com>). The position of the η - $MgZn_2$ phase solvus boundary for various temperatures between 150°C and 300°C was also calculated (see Figure II.2.b).

Details of the solvus boundary of the η - $MgZn_2$ phase will be of great interest in the modelling part of this work concerning precipitation and dissolution of this phase during high temperature heat treatments.

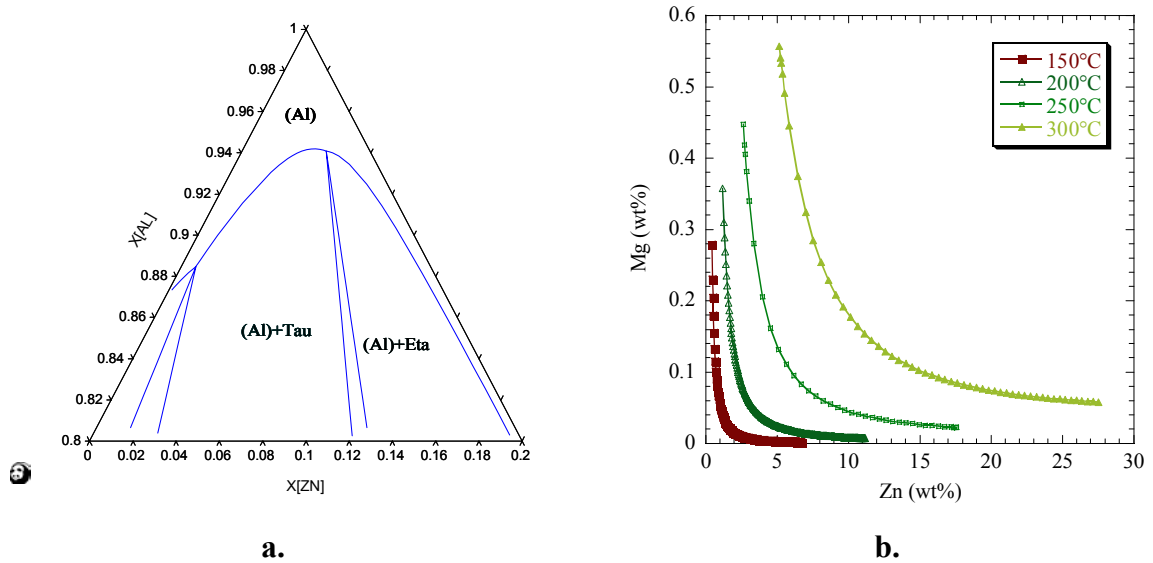


Figure II.2: Thermodynamic data obtained from the Pandat database
 a. Calculation of the Al-rich corner section at 400°C (in at%).
 b. Solvus of the η -MgZn₂ phase for various temperatures between 150°C and 300°C.

The quaternary Al-Zn-Mg-Cu system

For aircraft applications, Al-Zn-Mg-Cu alloys have been developed, leading to the high-strength 7xxx series. These alloys have generally higher solute contents and exhibit high age-hardening responses. The addition of copper is normally considered as favourable to reduce or prevent stress corrosion cracking. Unfortunately, copper may also contribute to the formation of low melting point phases at the grain boundaries in the high temperature regions of the weld. Because of this, Al-Zn-Mg-Cu alloys are usually considered to be non-weldable alloys. For applications that include welding, copper is either omitted or kept to a low level.

II.1.1.2. Influence of zirconium additions

Zirconium additions are used in 7xxx series alloys (both in weldable Al-Zn-Mg alloys and in high-strength Al-Zn-Mg-Cu alloys) in order to inhibit recrystallisation and thus to refine the grain size. Zirconium was preferred to other grain refiners like chromium or manganese because zirconium has the least deleterious effect on quench sensitivity (capacity to achieve a maximum supersaturation of alloying elements after quenching).

Zirconium forms small, insoluble particles of Al₃Zr, called dispersoids, during the casting and homogenisation treatment. These particles have a pinning effect on grain and sub-grain boundaries during annealing, partially inhibiting recrystallisation [Ryum, 1969]. The dispersoids are inhomogeneously distributed throughout the material in the form of bands (see Figure II.3) due to the initial dendritic segregation (Zr is a peritectic element) followed by high deformation during extrusion.

These dispersoids may act as potential sites for heterogeneous precipitation under conditions of slow quenching, creating a solute depleted zone around these particles [Deschamps, 1998].

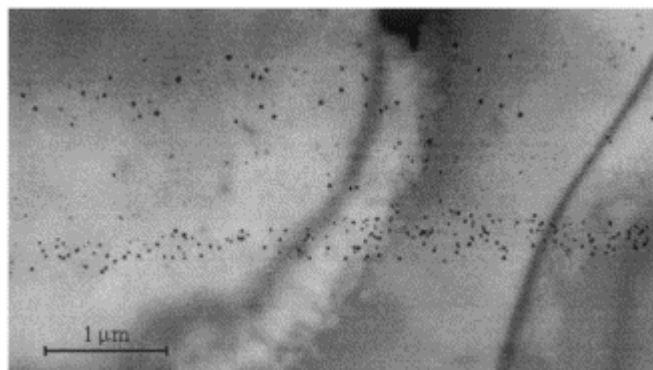


Figure II.3: Spatial distribution of Al_3Zr particles in an Al-6wt%Zn-2wt%Mg-0.1wt%Zr [Deschamps, 1998].

In general, a zirconium addition is considered to have no influence on precipitation behaviour. However some authors reported that zirconium slows down precipitation processes in Al-Zn-Mg alloys [Mukhopadhyay, 1994]. According to these authors, the number of free vacancies available after quenching would decrease as sub-grain boundaries and non-coherent portions of Al_3Zr/Al interfaces can act as vacancy sinks. This involves reduced nucleation and growth kinetics of GP zones after quenching which are nuclei for subsequent hardening precipitates.

II.1.2. Phases in Al-Zn-Mg alloys

The phases involved during usual heat treatments of Al-Zn-Mg alloys can be separated into two classes: equilibrium phases and metastable precipitates. The nature of these phases will first be presented in terms of their crystal symmetry and their orientation relationships with the matrix, before a review of the chemical composition of each phase is presented.

II.1.2.1. Stable equilibrium phases

In the aluminium-rich corner of the ternary Al-Zn-Mg phase diagram (see Figure II.1), two equilibrium phases can be observed:

- the η -phase ($MgZn_2$) which is the only stable phase observed in our alloy,
- the T-phase ($Al_2Mg_3Zn_3$) which is not commonly observed during usual heat treatments of commercial alloys [Löffler, 1983].

In the following, we will exclusively focus on the η -phase.

This phase is hexagonal with the following lattice parameters: $a=5.23\text{\AA}$ and $c=8.57\text{\AA}$. The η -precipitates are incoherent with the matrix. At least 11 different crystallographic orientation relationships have been reported in the literature [Löffler, 1983; Degisher, 1980] (see Table II.1). The most commonly observed are [Gjønnnes, 1970; Degisher, 1980]:

- η_1 -plates lying on $\{100\}_\alpha$ [Gjønnnes, 1970; Park, 1983] or on $\{112\}_\alpha$ [Degisher, 1980],
- η_2 -plates on $\{111\}_\alpha$,
- η_4 -rods along $\langle 110 \rangle_\alpha$.

As illustrated on Figure II.4, the shape of η -particles is quite difficult to define, depending on the orientation of the foil.

Type	Orientation relationships	
η_1	$(0001)_\eta // (110)_\alpha$	$(10\bar{1}0)_\eta // (001)_\alpha$
η_2	$(0001)_\eta // (1\bar{1}\bar{1})_\alpha$	$(10\bar{1}0)_\eta // (110)_\alpha$
η_3	$(0001)_\eta // (1\bar{1}\bar{1})_\alpha$	$(11\bar{2}0)_\eta // (110)_\alpha$
η_4	$(0001)_\eta // (110)_\alpha$	$(\bar{1}2\bar{1}0)_\eta // (1\bar{1}\bar{1})_\alpha$
η_5	$(30\bar{3}2)_\eta // (110)_\alpha$	$(\bar{1}2\bar{1}0)_\eta // (1\bar{1}\bar{1})_\alpha$
η_6	$(20\bar{2}1)_\eta // (1\bar{1}2)_\alpha$	$(\bar{1}2\bar{1}0)_\eta // (1\bar{1}\bar{1})_\alpha$
η_7	$(10\bar{1}4)_\eta // (110)_\alpha$	$(\bar{1}2\bar{1}0)_\eta // (1\bar{1}\bar{1})_\alpha$
η_8	$(0001)_\eta // (31\bar{1})_\alpha$	$(\bar{1}2\bar{1}0)_\eta // (1\bar{1}2)_\alpha$
η_9	$(0001)_\eta // (110)_\alpha$	$(\bar{1}2\bar{1}0)_\eta // (001)_\alpha$
η_{10}	$(0001)_\eta // (1\bar{1}\bar{1})_\alpha$	$(11\bar{2}0)_\eta // (1\bar{3}4)_\alpha$
η_{11}	$(0001)_\eta // (110)_\alpha$	$(10\bar{1}0)_\eta // (1\bar{1}\bar{1})_\alpha$

Table II.1: Reported orientation relationships of the η -phase [Degisher, 1980].

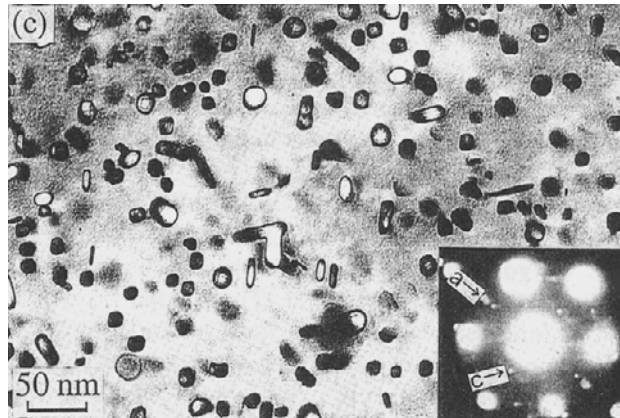


Figure II.4: Bright-field TEM image of precipitates aged at 200°C for 90 minutes in 7050 alloy (Al-6wt%Zn-2.2wt%Mg-2.2wt%Cu). The estimated mean size of η -precipitates is 10-30 nm. [Yamamoto, 1998]

The chemical composition of this phase is generally assumed to be $MgZn_2$. Even if this is certainly true for the bulk phase, there may be some deviations for small particles, as observed by Stiller [Stiller, 1999] (see II.1.2.3. Compilation of composition data).

II.1.2.2. Metastable phases

As η -particles are incoherent with the matrix (and have a relatively high interfacial energy), metastable precipitates, with a higher level of coherency (and lower interfacial energy), may be expected to form preferentially at low temperatures because of a lower activation barrier for nucleation. The most common metastable phases in the Al-Zn-Mg system are Guinier-Preston zones (GP zones) and η' -particles.

GP zones

GP zones form at low temperature, even at room temperature and are completely coherent with the aluminium matrix. They consist of layers parallel to the (100) matrix planes enriched in zinc and magnesium alternatively, due to the opposite size effect of the two alloying elements [Ringer, 2000]. In Al-Zn-Mg alloys, their shape is generally accepted to be spherical as observed in High-Resolution TEM images (see Figure II.5) [Hono, 1992; Mukhopadhyay, 1994; Maloney, 1999].

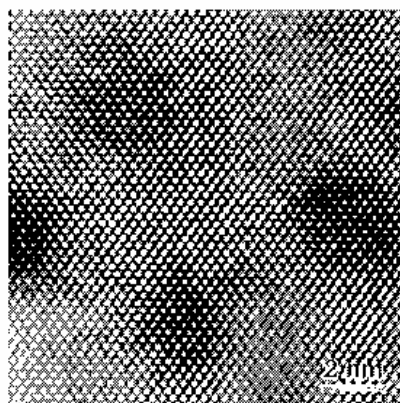


Figure II.5: $\langle 110 \rangle_{\alpha}$ bright field HRTEM image of an Al-4.5wt%Zn-1.5wt%Mg alloy aged 168h at 60°C [Maloney, 1999].

Their composition depends on the Zn/Mg ratio of the base material and is still difficult to determine, even with APFIM (Atom Probe Field-Ion Microscopy) measurements because of the fine scale of the particles (see II.1.2.3. Compilation of composition data).

A second type of GP zones (called GP(II)) have been reported in the literature. Their existence was first evidenced by small-angle scattering [Ungár, 1979b; Blaschko, 1982]: in fact two straight lines appeared in the Guinier plot, characteristic of two types of particles. GP(II) zones appear on $\{111\}_{\alpha}$ planes and are a few atomic layers thick [Stiller, 1999]. They form only after quenching from temperatures higher than 450°C.

The η' -phase

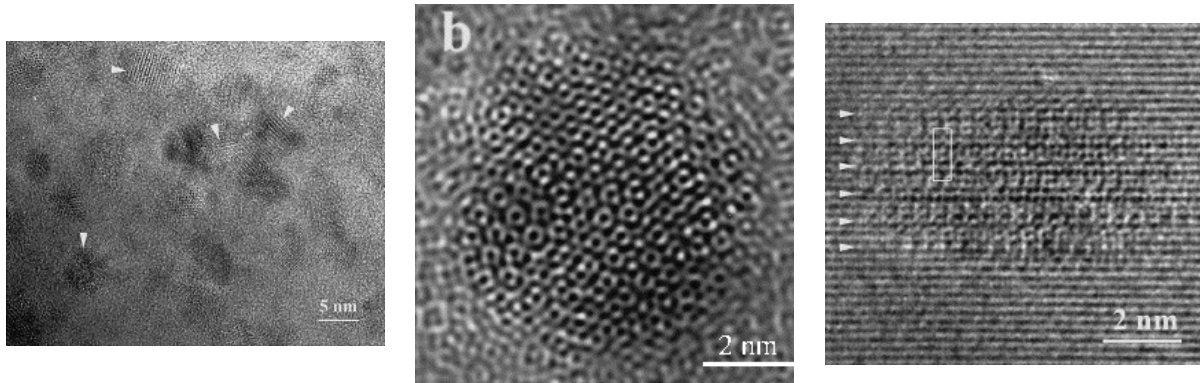
The high strength of Al-Zn-Mg alloys and their pronounced hardening response to heat treatment is generally associated with the η' -phase [Lendvai, 1996]. Hence, this is a well-studied but still controversial metastable phase. Significant disagreements exist especially regarding crystallographic structure, orientation and composition.

There is general agreement that η' -particles are plate-like precipitates on $\{111\}_{\alpha}$ [Gjønnnes, 1970] and are semi-coherent with the aluminium matrix: they are coherent on $\{111\}_{\alpha}$ planes and incoherent on the side of the plate. The shape of η' -particles was well defined using High Resolution Transmission Electron Microscopy (HRTEM) (see Figure II.6). Generally, they form and grow at temperatures between 100°C and 150°C [Park, 1983].

Li *et al.* [Li, 1999] definitely confirmed by means of HRTEM observations the hexagonal structure of η' -phase, first proposed by Graf *et al.* [Graf, 1956] and Auger *et al.* [Auger, 1974] with lattice parameters: $a = 4.96\text{\AA}$ and $c = 14.03\text{\AA}$. The following orientation relationship between η' and the aluminium matrix has been proposed by Auld and Cousland [Auld, 1974]:

$$(0001)_{\eta'} // (1\bar{1}\bar{1})_{\alpha}; (10\bar{1}0)_{\eta'} // (110)_{\alpha}$$

This is identical to the orientation relationship of η_2 (see Table II.1).



HRTEM image at low magnification along the $[111]$ zone axis

HRTEM image of η' -precipitate along the $[0001]$ zone axis

HRTEM image of η' -precipitate along the $[11.0]$ zone axis

Figure II.6: HREM imaging of η' -precipitates using different zone axis showing the plate-like shape of these particles [Li, 1999].

The structure for the η' -phase proposed by Auld and Cousland [Auld, 1974] is shown in Figure II.7 presenting a sketch of the basic Bravais lattice of the η' unit cell and the correspondence of the η'/α lattices on the $\{110\}_\alpha$ planes. In this model, the $\{111\}_\alpha$ planes are parallel to the $(0001)_{\eta'}$ and $(\bar{1}2.2)_{\eta'}$ planes. Other models were proposed by Gjønnes and Simensen [Gjønnes, 1970] and more recently by Li et al [Li, 1999]. Among the available models, that of Auld and Cousland is the more plausible as it exhibits a low lattice misfit across the precipitate and matrix; moreover total energy calculations performed by Wolverton [Wolverton, 2001] supported the validity of this model. The lattice parameters of the η' -phase is related to those of the aluminium matrix as:

$$d_{10.0; \eta'} = 3d_{220; \alpha}; \quad d_{00.1; \eta'} = 6d_{111; \alpha}$$

η' is commonly assumed to have the composition of MgZn_2 , equivalent to the equilibrium η -phase. There have been a number of studies on the composition of the η' -phase (see II.1.2.3. Compilation of composition data). A survey of these results suggests that there is some variation in the proposed precipitate compositions, although there is general agreement that the phase has a significant Zn deficit from the MgZn_2 composition first proposed [Mondolfo, 1956]. Some investigations found evidence for Al presence in the structure of η' -phase, however this is difficult to confirm even with 3-dimensional atom probe analysis [Brenner, 1991; Li, 1999]. Moreover it is difficult to assess the composition of this phase as the precipitate chemistry is expected to change during the ageing process [Ringer, 2000].

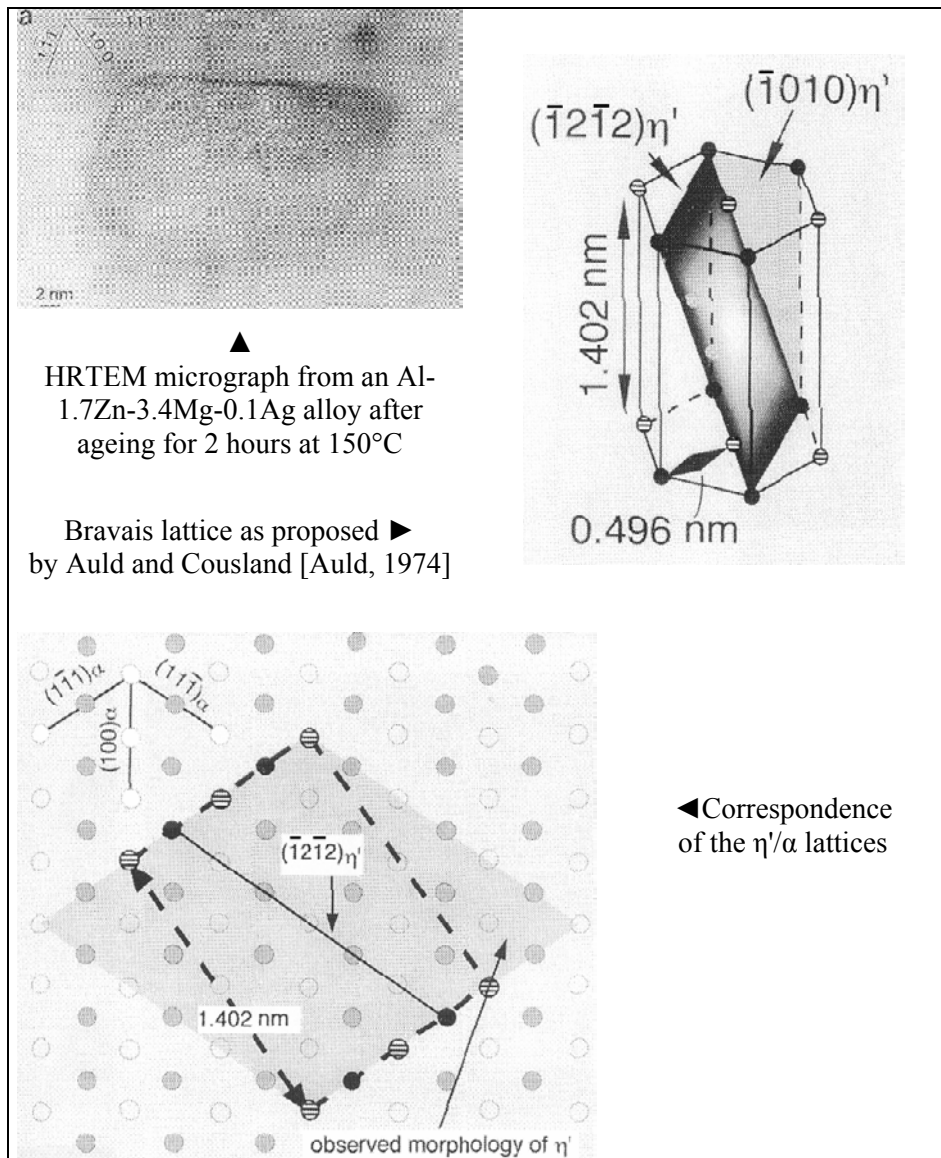


Figure II.7: Analysis of the η' -structure [Ringer, 2000]

II.1.2.3. Compilation of composition data

In Table II.2, Table II.3, and Table II.4 are tabulated the compositions of η , GP zones, and η' -phase respectively, reported in the literature. These references are relatively recent as new techniques such as the atom probe field-ion microscopy (APFIM), tomographic atom probe or 3-dimension atom probe developed. It should be noted that even using these techniques, the analysis of the Al content remains difficult since atoms from the matrix may interfere with measurements in the particles.

η-phase

<i>Author</i>	<i>Experimental conditions</i>	<i>η-composition</i>	<i>Zn-Mg ratio</i>
[Polmear, 1957-58]	Equilibrium	MgZn ₂	$\frac{Zn}{Mg} \approx 2$
[Maloney, 1999]	7108.50 (Al-4.5wt%Zn-1.5wt%Mg) TEM, 3DAP aged 45h/150°C		$\frac{Zn}{Mg} \approx 2.1$
[Stiller, 1999]	Al-2.3at%Zn-1.4at%Mg TEM, APFIM aged 5h/100°C + 6h/150°C		$\frac{Zn}{Mg} \in [1;1.6]$
[Deschamps, 2001]	Al-6wt%Zn-2.3wt%Mg SAXS, TAP aged 50h/160°C	53%Zn 32%Mg 15% Al	$\frac{Zn}{Mg} \approx 1.6$

Table II.2: Reported η composition (3DAP: 3-dimensional atom probe analysis; TAP: Tomographic Atom Probe).

GP zones

<i>Author</i>	<i>Experimental conditions</i>	<i>GP composition</i>	<i>Zn-Mg ratio</i>
[Ortner, 1988]	Al-7.3wt%Zn-2.6wt%Mg APFIM aged at 150°C/0.5-10h (is it GP zones ? [Hono, 1992])	Al ₆ ZnMg	$\frac{Zn}{Mg} \approx 1$
[Hono, 1992]	Al-2at%Zn-2at%Mg-0.2 or 0.5at%Cu APFIM aged at 120°C/48h	20-25at% Zn 15-20at%Mg 1-3at%Cu 64-52at%Al	$\frac{Zn}{Mg} \approx 1.3$
[Maloney, 1999]	7108.50 (Al-4.5wt%Zn-1.5wt%Mg) TEM, 3DAP aged at 60°C/168h; 90°C/168h		$\frac{Zn}{Mg}$ (GP) \approx $\frac{Zn}{Mg}$ (alloy)
[Stiller, 1999]	Al-2.3at%Zn-1.4at%Mg TEM, APFIM aged at 150°C/1.5h	84.5%Al 9%Zn 7.5%Mg	$\frac{Zn}{Mg} \approx 1.2$

Table II.3: Reported GP zone composition.

η' -phase

<i>Author</i>	<i>Experimental conditions</i>	η' - <i>composition</i>	<i>Zn-Mg ratio</i>
[Brenner, 1991]	7150 (Al-6.4wt%Zn-2.4wt%Mg-2.2wt%Cu) APFIM T6 (24h/120°C)	Mg(Zn,Cu,Al) ₂	$\frac{\text{Zn}}{\text{Mg}} \approx 1$
[Warren, 1992]	7150 APFIM, POSAP T6 (24h/120°C)	68%Al 13%Zn 19%Mg	$\frac{\text{Zn}}{\text{Mg}} \approx 0.7$
[Li, 1999]	AA7108 (Al-5.4wt%Zn-1.2wt%Mg) HRTEM, structural model T6 (5h/100°C + 6h/150°C)	Mg ₂ Zn _{5-x} Al _{2+x}	$\frac{\text{Zn}}{\text{Mg}} \approx 2.5$
[Maloney, 1999]	7108.50 (Al-4.5wt%Zn-1.5wt%Mg) TEM, 3DAP aged 45h/150°C	$\frac{\text{Zn}}{\text{Mg}} (\eta') \approx$ $\frac{\text{Zn}}{\text{Mg}} (\text{alloy})$	$\frac{\text{Zn}}{\text{Mg}} \approx 1.4$
[Stiller, 1999]	Al-2.3at%Zn-1.4at%Mg TEM, APFIM aged 5h/100°C + 6h/150°C	55-65at% Al	$\frac{\text{Zn}}{\text{Mg}} \approx 1$
[Deschamps, 2001]	Al-6wt%Zn-2.3wt%Mg TEM, SAXS, TAP heating up to 160°C at 30°/h	28%Zn 19%Mg 53%Al	$\frac{\text{Zn}}{\text{Mg}} \approx 1.5$

Table II.4: Reported η' composition
(POSAP: Position sensitive atom probe).

The assumption of MgZn₂ composition for the η -phase seems to be quite reasonable even if the Zn/Mg ratio may be smaller at the early stages of formation of this phase.

For GP zones and η' -precipitates, authors tend to agree about a Zn to Mg ratio contained in the [1;2] range. The only value higher than 2 [Li, 1999] relies on a structural model which has been shown to be irrelevant by Wolverton [Wolverton, 2001] and Ringer [Ringer, 2000].

II.1.3. Decomposition processes

II.1.3.1. Homogeneous precipitation

The sequence of precipitation in Al-Zn-Mg alloys strongly depends on the history of the material, including quenching conditions, natural ageing and further heat treatment. Löffler [Löffler, 1983] and Lendvai [Lendvai, 1996] have provided a good review of the decomposition processed taking place in Al-Zn-Mg alloys.

After a one-step ageing treatment, i.e. solution treatment and quench to the ageing temperature, direct precipitation will take place. Near room temperature (20°C < T < 100°C), the decomposition of the supersaturated solution (SSS) occurs by formation of GP zones [Lendvai, 1979]. At higher temperatures (120°C < T < 170°C), the formation of η' -precipitates is predominant and at still higher temperatures (170°C < T < 250°C) the nucleation and growth of the equilibrium η -phase occur [Radomsky, 1979].

In the case of a multi-step ageing (typically: quench at room temperature, natural ageing followed by the precipitation treatment), the decomposition processes become much more complex. This type of heat treatment is of great interest as it is generally used in the industry to improve mechanical properties. The benefit of a double ageing was well illustrated by Ryum [Ryum, 1975] (see Figure II.8). In fact, a direct quench leads to precipitation of coarse η' or η -particles, unable to strengthen efficiently the material, whereas multi-step ageing is characterised by a high density of precipitates. The marked benefit of double ageing can be attributed in a large extent to quenching effect and the role of the quenched vacancies in facilitating nucleation.

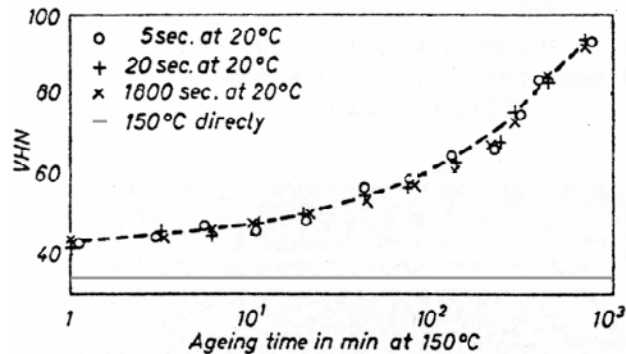


Figure II.8: Influence of pre-ageing time at 20°C (after quenching) on subsequent ageing at 150°C on an Al-6wt%Zn-1wt%MG [Ryum, 1975].

The main precipitation sequence reported in the literature during multi-step ageing [Lacom, 1980; Löffler, 1983; Zahra, 1981] is:



GP zones, formed at low temperature after quenching (typically room temperature), can act as nucleation sites for more stable precipitates. Quenched-in vacancies have been shown to directly influence the rate of GP zone formation by accelerating the diffusion process and possibly aiding their nucleation, as illustrated by Lacom *et al.* [Lacom, 1982] (see Figure II.9). Figure II.9 shows the influence of a reversion treatment at high temperature (200°C and 230°C) following quench at 0°C on subsequent heat treatment at 150°C; it can be observed that the precipitate density formed at 150°C is greatly reduced by the reversion treatment. The reversion reduces the concentration of mobile excess vacancies produced during the quench; therefore the nucleation rate of GP zones is decreased and the potential for nucleation of further precipitation at 150°C is then considerably reduced. The microstructure is expected to be similar to that following a direct quench at 150°C.

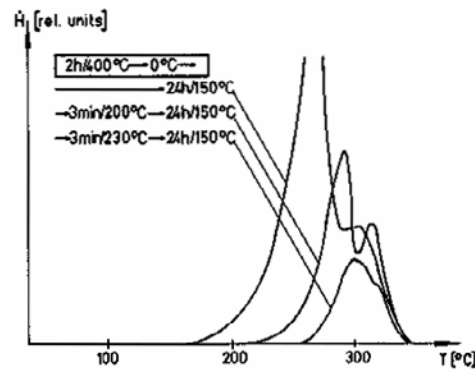


Figure II.9: DSC heat flow curves (Heating rate = 20°/min) showing the influence of reversion treatment at 200°C and 230°C (vacancy annealing) on subsequent 24h ageing at 150°C, to compare with 2-step ageing on an Al-5wt%Zn-1wt%Mg [Lacom, 1982].

Another precipitation sequence has been reported [Ryum, 1975; Lacom, 1980] involving vacancy-rich clusters (VRC) which form during the quench or short room temperature ageing:



The VRC have been showed to be closely related to GP(II), either as the same phase or as a precursor to GP(II) [Berg, 2001]. VRC are formed during or immediately after quenching, they are reported to be remarkably stable up to ageing temperatures around 180°C but they disappear during long-term ageing near room temperature [Löffler, 1983].

As a consequence, for long pre-ageing times at low temperature, the GP zone decomposition process is predominant. On the contrary, in the case of a short pre-treatment, there is insufficient time to form GP zones [Polmear, 1957-1958] and the VRC sequence becomes active. Industrial heat treatments generally involve a sufficiently long room temperature pre-ageing to form a large amount of GP zones. Consequently, in the following, we will only discuss the sequence involving GP zones.

When the temperature is increased from the pre-ageing temperature up to the ageing temperature, dissolution of GP zones occurs. This dissolution, called reversion, can be partial: in this case, overcritical-sized GP zones can directly act as nuclei of the η' -phase [Lorimer, 1966]. Mukhopadhyay [Mukhopadhyay, 1994] observed by HRTEM the nucleation of η' on GP zones. When the ageing temperature is higher than the reversion temperature, the GP zone dissolution is complete. In spite of this complete reversion, ageing can still result in a fine distribution of η' -particles. In that case, it is assumed that concentration fluctuations rich in zinc and magnesium are left behind by GP zones which can play an important role in the formation of the η' -phase.

Little is known about the η' to η transition. It has been proposed that a $\eta' \rightarrow \eta$ transformation may occur at the existing η' -precipitates and progresses spontaneously rather than through dissolution and reprecipitation [Gjønnnes, 1970]. Some authors [Gjønnnes, 1970; De Ardo, 1973; Degisher, 1980; Zahra, 1981; Park, 1989; Yamamoto, 1998] proposed a different precipitation sequence depending on the orientation type of the formed η -particle:

- η_1 particles are not formed from η' but are directly nucleated from the supersaturated solid solution,
- η' transform to η_2 ; this is in good agreement with orientation relationships,
- η_4 mainly precipitates on defects such as grain and sub-grain boundaries as well as dislocations.

II.1.3.2. Heterogeneous precipitation

Microstructure in the vicinity of grain boundaries

The grain boundary microstructure can be characterised by two characteristic features: precipitates heterogeneously nucleated on grain boundaries, and the so-called precipitate free zones (PFZ). Both are of major importance in fracture mechanisms of precipitation hardening alloys [Vasudévan, 1987].

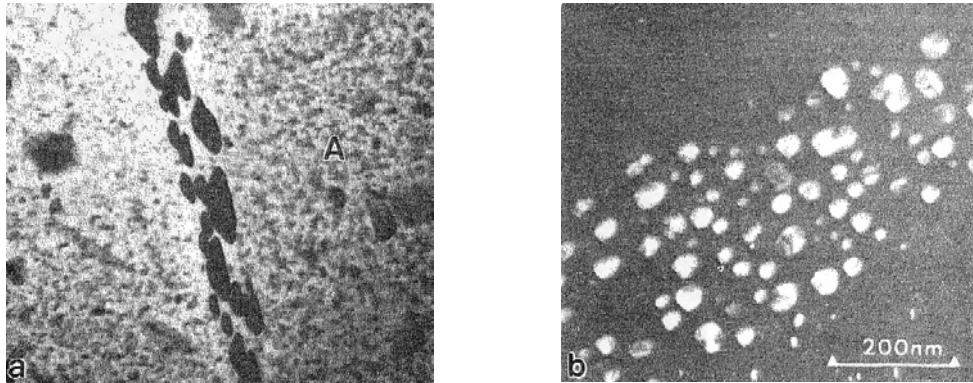


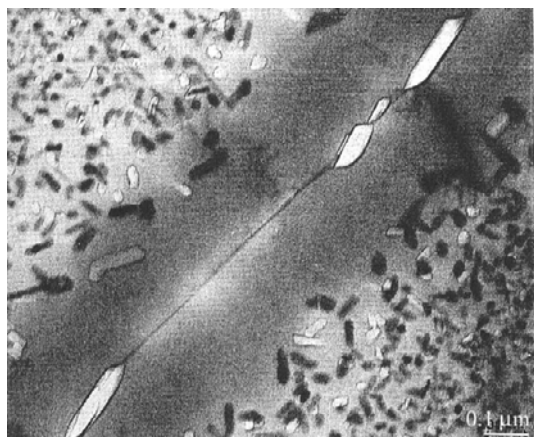
Figure II.10: Precipitates at a high (a) and a low (b) angle grain boundary (same scale) in a commercial 7075-T73 alloy [Park, 1986].

Precipitation at grain boundaries has been studied in detail by Park [Park, 1986]. In particular he looked at low and high angle grain boundaries, both present in extruded and rolled microstructures. The precipitates were identified as the equilibrium η -phase for both types of grain boundaries. Low angle grain boundaries contain copious quantities of η -precipitates with plate-shaped morphologies, whereas high angle grain boundaries contain a smaller number of large and thick particles (see Figure II.10), indicating an earlier precipitation in the quenching history.

The formation of PFZ has been well characterised by Raghavan [Raghavan, 1980]. A TEM micrograph of a PFZ formed in an Al-2.2at%Zn-4.7at%Mg is shown in Figure II.11. In earlier investigations, PFZ formation was generally attributed to either solute depletion or vacancy depletion. Raghavan explained the formation of PFZ in Al-Zn-Mg alloys in the following way (see Figure II.11):

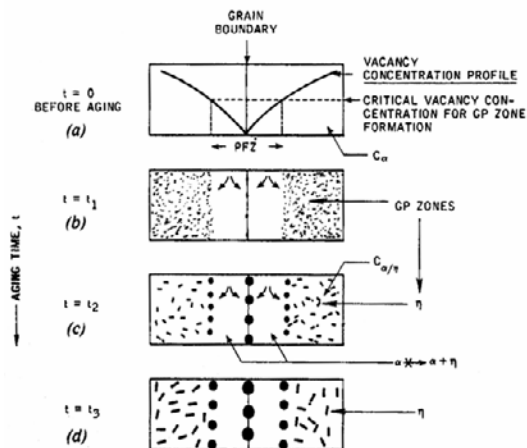
- During the initial quench from the solution treatment temperature, a vacancy concentration profile is developed near the grain boundaries (grain boundaries act as vacancy sinks).
- During natural aging at room temperature, as a critical vacancy concentration is necessary to nucleate the transient Guinier-Preston zones, GP zones do not form in the vicinity of grain boundaries.
- During subsequent aging, due to the absence of GP zones which normally provide nucleation sites for the formation of hardening η' - or η -phases, hardening precipitates do not form.

Due to the diffusion of solute towards the grain interior, the precipitates at the limit of the PFZ coarsen. Similarly, the grain boundary precipitates grow as a result of solute diffusion towards the grain boundaries. This process continues until the solute concentration of the matrix is uniform across the PFZ.



a.

Bright field image showing the PFZ, precipitates in the grain interior and grain boundary in an Al-2.2at%Zn-4.7at%Mg [Raghavan, 1980]



b.

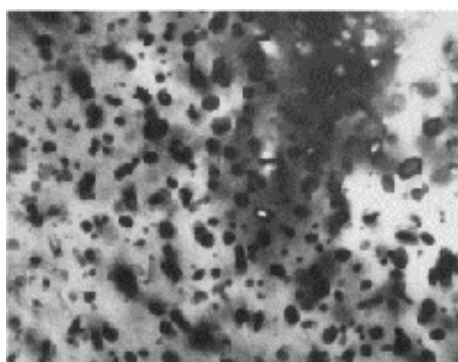
Schematic illustration of the formation of PFZ in Al-Zn-Mg alloys [Raghavan, 1980]

Figure II.11: Precipitate free zones in Al-Zn-Mg alloys.

Precipitation on dislocations

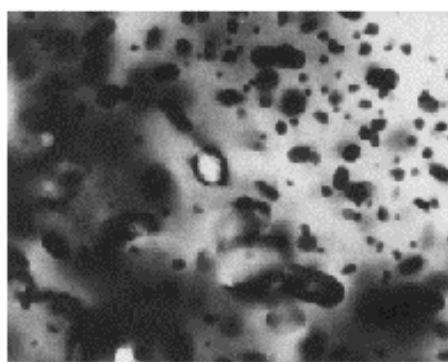
Precipitation on dislocations has been investigated in the study of the influence of pre-straining on mechanical properties [Deschamps, 1999]. A plastic deformation step ($\epsilon \sim 2\%$) is generally performed after quenching in the industrial thermomechanical processing to relieve quench-induced internal stresses.

Dislocations are favourable nucleation sites for precipitates, and short-circuit diffusion paths for solutes. This results in faster and coarser precipitation on dislocations of stable precipitates. On the other hand, the interaction between dislocations and solutes results in a solute depleted zone around dislocations. Therefore a lower solute fraction is available for bulk precipitation. Dislocations act also as vacancy sinks, disturbing the global precipitation sequence of homogeneous precipitation, as illustrated in Figure II.12.



a.

Undeformed material



b.

Material predeformed 10%

Figure II.12: TEM micrographs of an Al-6.1wt%Zn-2.3wt%Mg alloy aged 50h at 150°C [Deschamps, 1999].

TEM analysis shows that η -precipitates formed on dislocations are mainly of the η_2 -type, whereas in the undeformed material, η -precipitates are mostly in the η_1 and η_4 orientation. It

can be observed that size and spatial distribution of precipitates during ageing is also modified by the presence of dislocations.

Precipitation on dispersoids

Dispersoids (Al_3Zr) may also act as potential sites of heterogeneous nucleation during quenching, as observed in Figure II.13 [Deschamps, 1998]. This is most commonly observed in quench-sensitive Al-Zn-Mg-Cu alloys, resulting in an heterogeneous distribution of these precipitates in the form of bands (see II.1.1.2. Influence of zirconium additions).

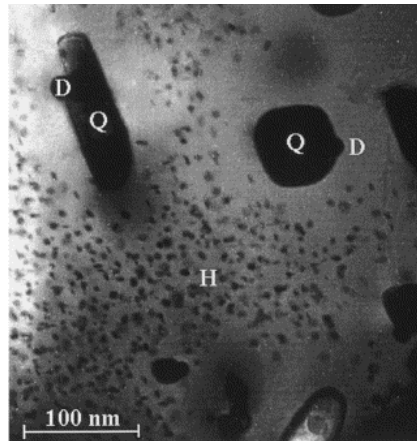


Figure II.13: TEM micrograph of an Al-6.1wt%Zn-2.3wt%Mg alloy after solution treatment, air quench, 3 days natural ageing and 2 h at 160°C (heating rate 30°C h⁻¹), showing the presence of a precipitate-free zone surrounding quench-induced precipitates. Al₃Zr dispersoids are marked (D), quench-induced precipitates are marked (Q) and homogeneously nucleated precipitates are marked (H) [Deschamps, 1998].

As in the case of precipitation on dislocation, precipitates heterogeneously nucleated on dispersoids are also surrounded by a precipitate-free zone, due to the local solute depletion.

II.1.4. Relevant points for the present investigation

In this study, three different tempers will be investigated: T4, obtained after natural ageing, T6, peak-aged hardened (obtained at 140°C) and T7, an overaged state obtained at 170°C. Based on previous literature review, we can debate about the nature of the hardening precipitates contained in each state.

T4 temper is expected to contain exclusively spherical GP zones, 5-10 Å in size.

Park [Park, 1983] and Viana [Viana, 1999] studied the precipitate microstructure of 7075 alloy (Al-6.5wt%Zn-2.7wt%Mg-1.5wt%Cu) contained in T6 (aged for 24h at 120°C) and T7 (aged 24h at 165°C) tempers. Both concluded that T6 temper contains mainly η' -phase, 3-10 nm large, whereas T7 temper contains essentially η -particles, in its η_1 and η_2 morphologies, with some presence of η' -precipitates.

Although the compositions of 7108.50 and 7075 are very different, equivalent precipitation states are expected in our alloy. To summarize:

- T4 → GP zones
- T6 → η'
- T7 → η + small amounts of η'

II.2. Quantitative characterisation by SAXS measurements

Small-Angle X-ray Scattering (SAXS) is a powerful technique for obtaining average features of a microstructure containing nano-scale precipitates. Under certain conditions, it can give quantitative measurements of precipitate size and volume fraction. This section is devoted to the evaluation of these quantities in the three investigated initial states: T4, T6 and T7.

II.2.1. Interpretation of SAXS measurements

Small-angle scattering spectra *intensity versus scattering vector* ($I=f(q)$) obtained for the three investigated tempers of 7108.50 alloy are presented in Figure II.14. Plots of interest in the determination of the integrated intensity Q_0 and Guinier radius R_g are also presented.

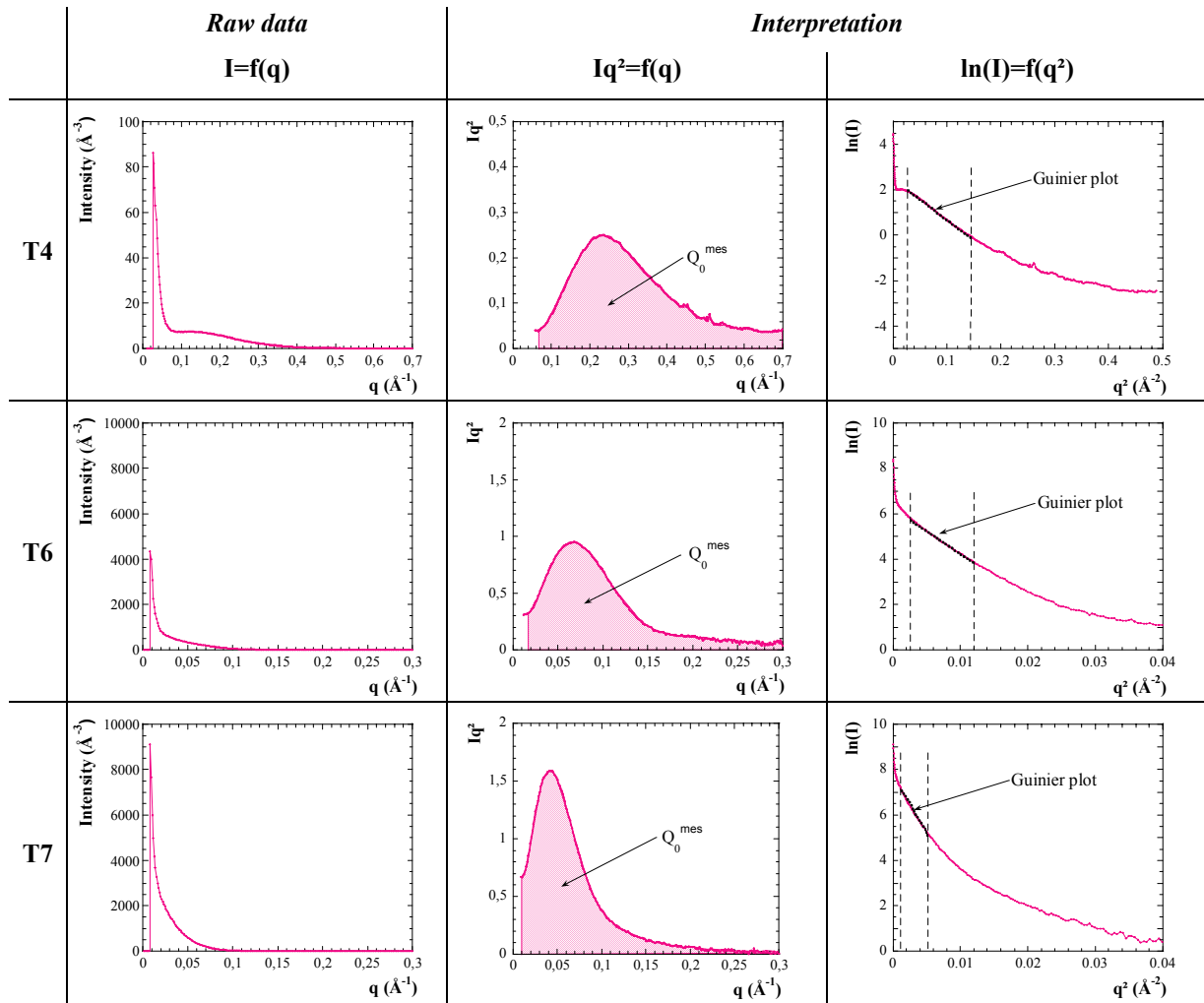


Figure II.14: SAXS results obtained from T4, T6 and T7 materials. Different plots used in the interpretation are presented. For T6 and T7 states, the same scale was applied. Note the huge intensity differences between T4 and T6-T7 tempers.

II.2.1.1. Guinier radius

The Guinier radius is calculated using the slope of the $\ln(I)$ versus q^2 plot, which is characterised by a straight line in a defined q -range in the presence of a single family of precipitates. The slope is equal to $-\frac{R_g^2}{3}$ (see Chapter I).

The determination of the Guinier radius for the three materials is given in Table II.5. Uncertainties are given with regards to deviations to the mean Guinier radius obtained from several samples measured for each state (~ 10 per state).

	Guinier radius
T4	$7.5^{\pm 0.2} \text{ \AA}$
T6	$25.6^{\pm 0.5} \text{ \AA}$
T7	$40^{\pm 1} \text{ \AA}$

Table II.5: Guinier radius (R_g) obtained for T4, T6 and T7 initial states.

II.2.1.2. Integrated intensity

In the determination of the total integrated intensity, measurement of the area under the curve Q_0^{mes} of the Iq^2 versus q plot have to be completed by including two additional terms. These terms correspond to the behaviour close to zero and to infinity respectively (see equations I.20 and I.21). The global expression of Q_0 is recalled here:

$$Q_0 = \frac{I(q_0)q_0^3}{2} + Q_0^{\text{mes}} + \frac{K}{q_1} \quad (\text{II.1})$$

where q_0 is the first data point,

q_1 is the last data point,

K is a constant defined in the Porod's law (see equation I.17), representing the origin ordinate of the Iq^4 versus q^4 plot in the high q -range.

Figure II.15 illustrates the way to determine the constant K using the Iq^4 versus q^4 plot for large q -values.

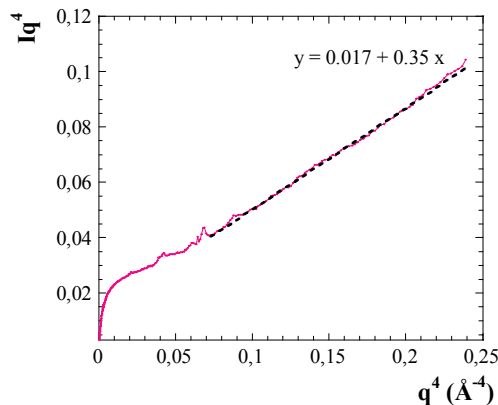


Figure II.15: Determination of the K constant in the Iq^4 versus q^4 plot. K is the origin ordinate and Laue the slope of the Porod's behaviour. Example of T4 initial state which illustrates particularly well the Porod's law.

Table II.6 presents the estimation of the complete integrated intensity by adding the three terms, as discussed in equation II.I.

	$Q_0^{\text{mes}} = \int_{q_0}^{q_\infty} Iq^2 dq$	q_0 (\AA^{-1})	$\frac{I(q_0)q_0^3}{2} = \int_0^{q_0} Iq^2 dq$	q_∞ (\AA^{-1})	K	$\frac{K}{q_\infty} = \int_{q_\infty}^{\infty} Iq^2 dq$
T4	$0.072^{\pm 0.005} \text{\AA}^{-6}$	0.05	0.001	0.6	0.017	$0.028^{\pm 0.002}$
T6	$0.102^{\pm 0.005} \text{\AA}^{-6}$	0.01	0.003	0.3	0.0046	$0.015^{\pm 0.002}$
T7	$0.112^{\pm 0.005} \text{\AA}^{-6}$	0.01	0.003	0.3	0.0029	$0.010^{\pm 0.002}$

Table II.6: Estimation of the three terms involved in the calculation of the total integrated intensity.

	Q_0 (\AA^{-6})
T4	$0.101^{\pm 0.01}$
T6	$0.12^{\pm 0.01}$
T7	$0.125^{\pm 0.01}$

Table II.7: Total integrated intensity obtained for the three states investigated.

Table II.7 is a summary of the calculated integrated intensity Q_0 obtained by summing up the three different terms determined in Table II.6. On the basis on these results, volume fraction estimations can be made, which will be done in the next section.

II.2.2. Estimation of volume fraction from SAXS measurements

The integrated intensity is directly related to the volume fraction f_v and composition of the precipitates. In the case of a two-phase model, the relationship is relatively simple (see equation I.13):

$$Q_0 = 2\pi^2(\rho_p - \rho_m)^2 f_v(1 - f_v) \quad (II.2)$$

where ρ_p and ρ_m are the precipitate and matrix electron density respectively (in $e.\text{\AA}^{-3}$).

For small volume fractions of precipitates, as observed in our study, equation II.2 can be approximated by:

$$Q_0 = 2\pi^2(\rho_p - \rho_m)^2 f_v = \alpha f_v \quad (II.3)$$

where α is a composition-dependent constant.

The electron density is related to the atomic concentration of each element constituted either the precipitate or the matrix:

$$\rho_p = \frac{f_{\text{Zn}} C_{\text{Zn}}^p + f_{\text{Mg}} C_{\text{Mg}}^p + f_{\text{Al}} C_{\text{Al}}^p}{V_{\text{at}}^p} \quad (II.4)$$

$$\rho_m = \frac{f_{\text{Zn}} C_{\text{Zn}}^m + f_{\text{Mg}} C_{\text{Mg}}^m + f_{\text{Al}} C_{\text{Al}}^m}{V_{\text{at}}^m} \approx \frac{f_{\text{Al}}}{V_{\text{at}}^m} \quad (II.5)$$

where f_i is the atomic scattering factor of the element i ,

C_i^p and C_i^m are the atomic concentration of element i in the precipitate and the matrix respectively,

V_{at}^p and V_{at}^m are the precipitate and matrix atomic volume respectively (in \AA^3).

In a first approximation, i.e. when the X-ray wavelength is far from an absorption edge of the species, the atomic scattering factor f_i is equal to the atomic number Z_i . For wavelengths used during our experiments, only zinc atomic scattering factor f_{Zn} needs to be slightly corrected:

$$f_{Zn} = Z_{Zn} + f'_{Zn} + if''_{Zn} \quad (II.6)$$

where f'_{Zn} and f''_{Zn} are energy-dependent corrective factors (tabulated values). For the wavelength studied ($\lambda \sim 1.55 \text{\AA}^{-1}$), f'_{Zn} is negligible and f''_{Zn} is evaluated to -1.6. Table II.8 is a summary of the atomic scattering factors of aluminium, magnesium and zinc and of the respective atomic volumes.

$f_{Al} = Z_{Al}$	13
$f_{Mg} = Z_{Mg}$	12
$f_{Zn} = Z_{Zn} + f'_{Zn}$	28.4
V_{at}^p	$1.10^{-5} \text{ m}^3 \cdot \text{mol}^{-1} = 16.6 \text{\AA}^3$
V_{at}^m	$1.10^{-5} \text{ m}^3 \cdot \text{mol}^{-1} = 16.6 \text{\AA}^3$

Table II.8: Atomic scattering factors and atomic volumes necessary in the determination of the volume fraction.

Although spectra of three initial states T4, T6 and T7 are completely different (see Figure II.14), the variations in terms of integrated intensity are relatively small (refer to Table II.7). Small Q_0 -variations from one state to another can then be explained in two ways:

- if all precipitates have the same composition, the three tempers have very similar volume fractions,
- or the volume fractions are significantly different and the compositions are varying from one state to another in such a way that Q_0 fluctuates weakly.

II.2.2.1. MgZn₂ assumption

Under the hypothesis of a constant composition for all precipitates (GP zones, η' - and η -phase) involved in the T4, T6 and T7 tempers, the most relevant composition is MgZn₂. This composition corresponds indeed to the equilibrium composition of the η -phase. This assumption implies that no aluminium is present in the constitution of the precipitates. The atomic concentration of zinc and magnesium are then:

$$C_{Zn}^p = \frac{2}{3} \quad ; \quad C_{Mg}^p = \frac{1}{3}$$

We can then estimate the volume fractions for the three initial states: T4, T6 and T7 using the following relationship:

$$fv = \frac{Q_0}{7.07} \quad (II.7)$$

Table II.9 shows the results in terms of volume fraction under the assumption of equal composition for all precipitates.

	$Q_0 (\text{\AA}^{-6})$	$f_v (\%)$
T4	$0.101^{\pm 0.01}$	$1.43^{\pm 0.1}$
T6	$0.12^{\pm 0.01}$	$1.70^{\pm 0.1}$
T7	$0.125^{\pm 0.01}$	$1.77^{\pm 0.1}$

Table II.9: Volume fraction calculated from SAXS integrated intensity in the $MgZn_2$ assumption.

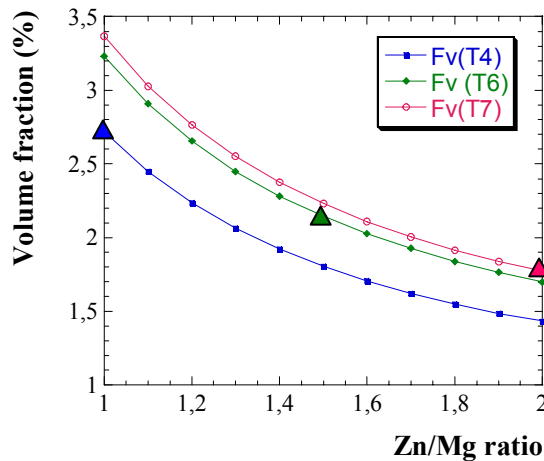
Considering the literature data reviewed (see II.1.2.3. Compilation of composition data), the assumption of a constant precipitate composition must be considered questionable. In fact, using new techniques it appears that precipitates in Al-Zn-Mg alloys, even η -particles, have a Zn/Mg ratio smaller than 2. The presence of aluminium in metastable precipitates, especially η' -phase, is also proposed (see Table II.4).

II.2.2.2. Influence of composition changes

According to the literature, the Zn/Mg ratio is generally assumed to be in the range [1;2]. Moreover, the Zn/Mg ratio is expected to increase with stability of precipitates. Schematically, the Zn/Mg ratio is (see II.1.2.3. Compilation of composition data):

- ~1 for GP zones
- ~1.5 for η' -precipitates
- ~2 for η -phase.

Figure II.16 illustrates the influence of the Zn/Mg ratio on the determination of the volume fractions. The reported compositions for GP zones, η' - and η -phase are displayed by triangles on the T4, T6 and T7 curves respectively.



	Precipitates	Zn/Mg ratio	$f_v (\%)$
T4	GP zones	1	2.72
T6	η'	1.5	2.14
T7	η	2	1.77

Figure II.16: Influence of Zn/Mg ratio on the estimation of the volume fraction for T4, T6 and T7 states. Triangles mark more relevant composition of precipitates contained in each state, corresponding values are reported in the table.

No aluminium was included in the composition of the precipitates.

It can be observed that in this case, the T4 material presents the higher volume fraction followed by T6 and finally T7 states. This is completely the reverse situation as compared to the previous $MgZn_2$ hypothesis, where the following order was respected $f_v(T7) > f_v(T6) > f_v(T4)$. But volume fraction values remain in a reasonable range, in comparison with previous studies [Deschamps, 2001].

Let us now consider the presence of aluminium in the composition of precipitates. When attempts have been made to quantify aluminium content in precipitates of Al-Zn-Mg alloys, up to more than 50% Al has been reported. Let us take into account such amounts of aluminium (~50%) in GP zones and η' -particles, together with more relevant Zn/Mg ratios, as defined before. Therefore, the compositions of precipitates contained in the T4 and T6 initial states would be:

- 50%Al – 30%Zn – 20%Mg for η' -precipitates,
- 50%Al – 25%Zn – 25%Mg for GP zones.

The corresponding volume fractions of the T4 and T6 materials become 10.9% and 8.6% respectively. These large values are unrealistic, it can thus be stated that aluminium contents in the order of 50% or more are not plausible.

In summary, volume fraction calibration is greatly complicated by the uncertainties in phase composition. Table II.10 gives a summary of calculated Guinier radii and estimated volume fractions using the two most relevant composition assumptions developed earlier.

	Precipitates	R_g (Å)	Zn/Mg ratio	f_v (%)	Zn/Mg ratio	f_v (%)
T4	GP zones	7.5 ± 0.2 Å	2	1.43 ± 0.1	1	2.72 ± 0.1
T6	η'	25.6 ± 0.5 Å	2	1.70 ± 0.1	1.5	2.14 ± 0.1
T7	η	40 ± 1 Å	2	1.77 ± 0.1	2	1.77 ± 0.1

Table II.10: Summary of resulting Guinier radius and volume fraction for two more relevant composition assumptions.

II.3. Complementary investigations using TEM and DSC

Transmission electron microscopy and DSC have been used as complementary techniques to SAXS. It allowed us:

- to determine the nature of phases present in the investigated materials using diffraction pattern indexing and DSC,
- to measure the particle distributions in tempers T6 and T7,
- to determine the volume fraction using a geometrical approach.

II.3.1. Nature of present phases

Two techniques have been carried out to determine the nature of phases present in our different tempers. Analysis of extra-spots in our diffraction patterns allowed us to detect the

presence of different phases and also to distinguish between the different η -orientations. DSC was used as a way to identify and quantify each phase.

II.3.1.1. Diffraction pattern analysis

Figure II.17 is a summary of the different diffraction spots induced by η' - or η -phases in the $[111]_{Al}$ zone axis. These extra-spots can be used as detectors of the presence of these phases in the studied material.

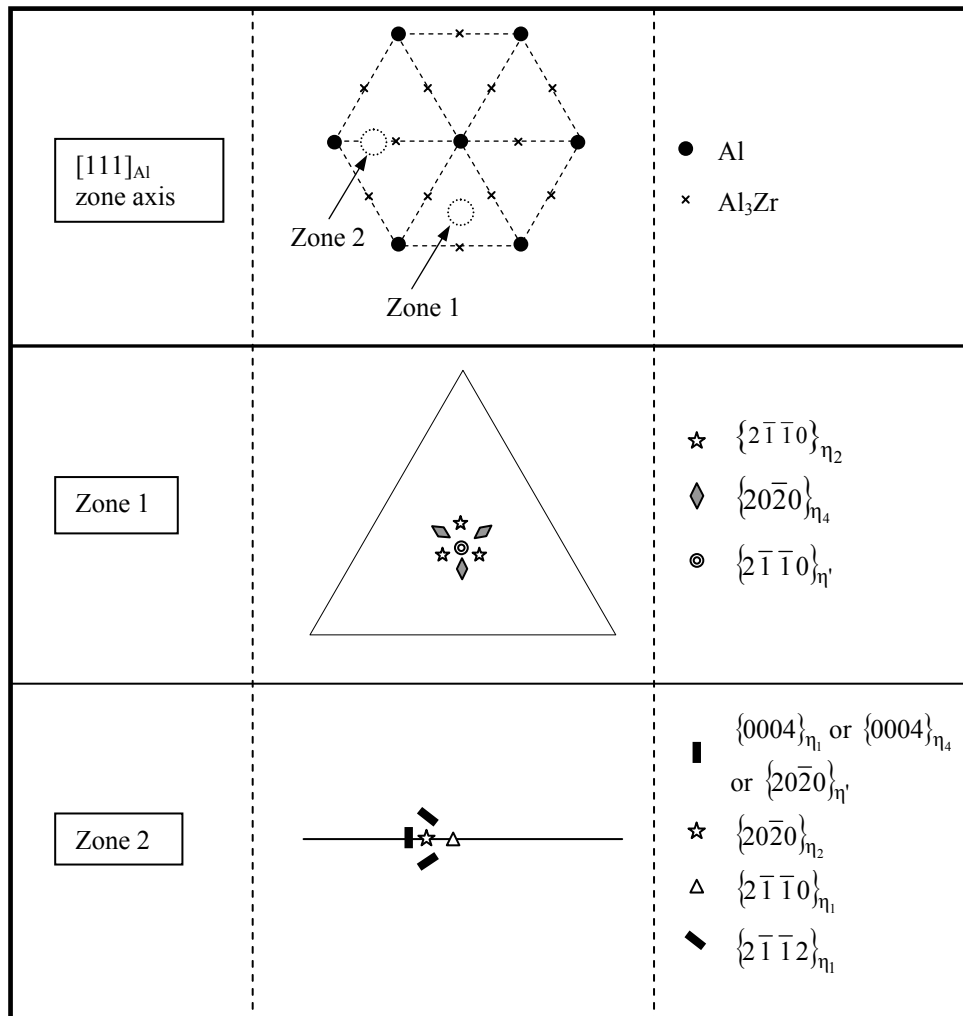


Figure II.17: Schematic representation of diffraction extra-spots from η' - and η -phases in the $[111]_{Al}$ zone axis [Deschamps, 1997].

T6 and T7 $[111]_{Al}$ zone axis diffraction patterns are shown in Figure II.18. It can be seen that both T6 and T7 initial states contain η' - and η -precipitates. However η' -spots are more intense in the T6 material than in the T7 temper. Moreover diffraction from η_1 -orientation is more abundant in the diffraction pattern of the T7 state.

The T6 temper, as expected, is mainly constituted of η' -precipitates. Surprisingly, the T7 state is not only composed of η -precipitates but is a mixture of η' - and η_1 -particles.

The respective proportions of η' - and η -phases in the two states can not be obtained quantitatively from the direct analysis of these diffraction patterns.

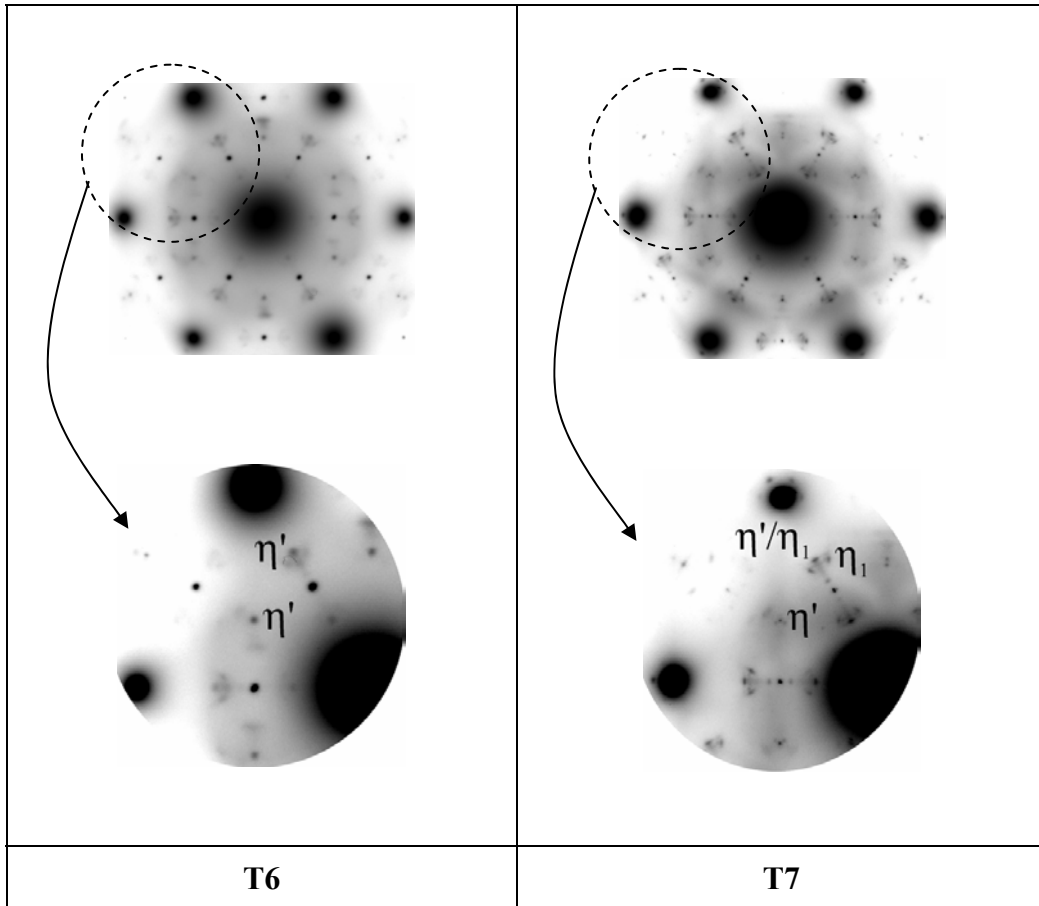


Figure II.18: $[111]_{Al}$ zone axis diffraction patterns obtained by TEM on T6 and T7 tempers.

II.3.1.2. DSC study

Figure II.19 shows dissolution peaks registered for T4, T6 and T7 tempers at a high heating rate ($100^{\circ}/\text{min}$). This heating rate was chosen to avoid transformation reactions which may occur during slow heating. Actually slow heating promotes the apparition of peaks other than the interesting dissolution peak of initially present phases.

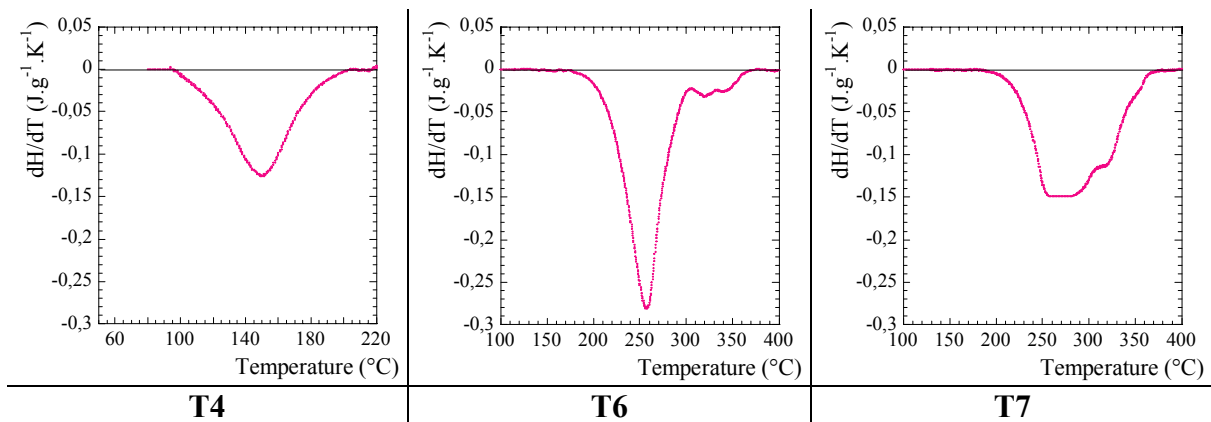


Figure II.19: DSC scans of T4, T6 and T7 initial states (heating rate = $100^{\circ}/\text{min}$).

It can be observed that for the T4 and T6 tempers, the dissolution peak appears as a single peak, whereas the T7 response seems to be the superposition of at least two dissolution peaks. Regarding the temperature ranges involved for each temper, we can conclude that:

- the T4 state is constituted of GP zones which dissolve between 100°C and 190°C,
- the T6 temper contains essentially η' -particles with a corresponding dissolution peak temperature around 250°C; possibly relatively small and unstable η -precipitates may dissolve in the same temperature range,
- the T7 state is a mixture of η' (the dissolution begins at the same temperature as in T6) and of more stable η -precipitates which dissolve at higher temperatures (around 300°C).

It should be noted that, due to the high heating rate (100°/min), dissolution temperatures are somewhat higher than the generally reported dissolution temperature ranges (typical heating rates of 5-20°/min).

Donoso [Donoso, 1985] proposed to relate the area of a dissolution peak ΔH_r with the volume fraction f_v of precipitates involved in the dissolution mechanism in such a way that:

$$\Delta H_r = C f_v \quad (II.8)$$

where C is a constant depending on the nature of involved particles. It should be noticed that C has been calibrated using SAXS measurements reported in the literature.

He reported the following C -values for GP zones and η' :

$$C = 281 \text{ J.g}^{-1} \text{ for GP zones}$$

$$C = 400 \text{ J.g}^{-1} \text{ for } \eta'.$$

This procedure was applied to T4 and T6 dissolution peaks to determine the volume fractions of GP zones and η' -particles respectively contained in these tempers. Table II.11 shows the results of such an analysis. Accuracy of this method relies on the reliability of the C value, which we are not able to estimate. It can however be concluded that results are of the same order of magnitude as those obtained from SAXS, although with slightly higher values.

	T_{start}	T_{end}	Dissolution peak area	C	f_v
T4 (GP zones)	80°C	210°C	5.71 J.g ⁻¹	281 J.g ⁻¹	2.03%
T6 (η')	150°C	300°C	13 J.g ⁻¹	400 J.g ⁻¹	3.25%

Table II.11: Quantification of GP zones and η' -particles respectively contained in the T4 and T6 tempers obtained by estimation of the area under the dissolution peak.

II.3.2. Measurement of particle size distributions

In this section and following one, we will introduce a new temper, called T7+, which has the advantage of exhibiting a coarser precipitate microstructure than all the other tempers and therefore is easier to observe and analyse. This temper is based on the T7 temper but its second step heat treatment at 170°C is 2 hours longer. SAXS results obtained on the T7+ temper are displayed in Table II.12.

	R_g	Q_0
T7+	49 ^{±1} Å	0.12 ^{±0.01} Å ⁻⁶

Table II.12: SAXS results obtained on T7+ temper.

Typical images of these three tempers are shown in Figure II.20. Size differences are obvious. Quantitative measurements of the size distributions of hardening precipitates contained in the T6, T7 and T7+ tempers have been carried out by image analysis.

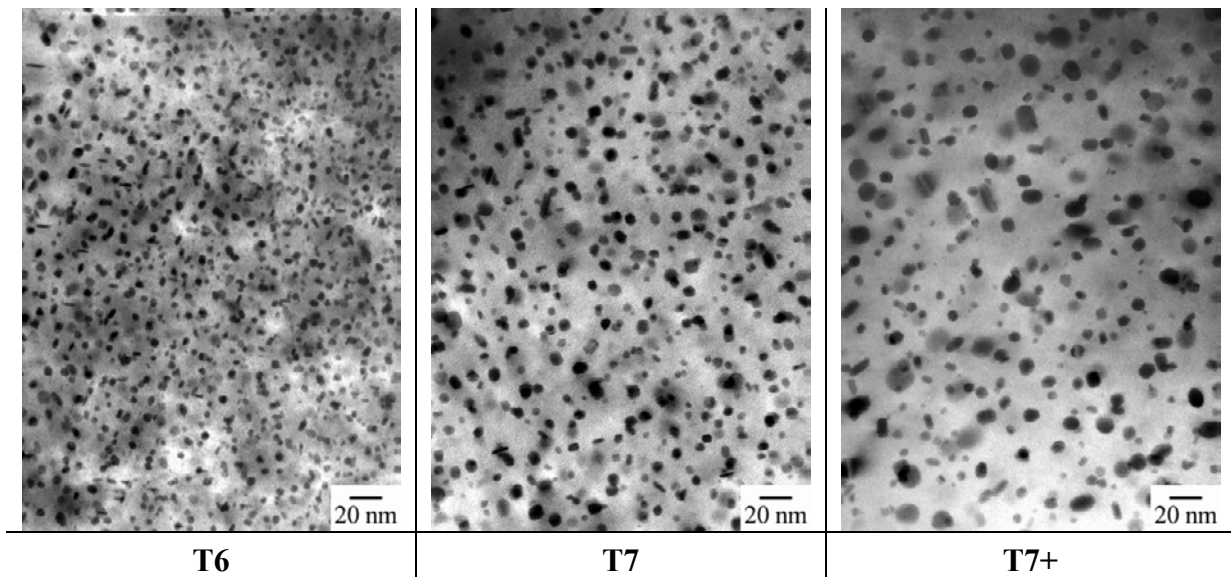


Figure II.20: Characteristic T6, T7 and T7+ bright-field images. Observation conditions are described below.

The procedure occurs in different steps:

- 1) **Imaging of particles.** Conditions to image hardening particles in bright-field mode are particularly restrictive. Good images have been obtained in oscillations of thickness fringes in two-beam $(111)_{Al}$ conditions close to a $[110]_{Al}$ zone axis (see Figure II.21). Equivalent conditions have been used by Park [Park, 1988]. Dark-field images have not been used due to the required precision of the aperture position to consider only one family of precipitates. Comparison between dark-field and bright-field analysis have been carried out by Park who concluded that both approaches give similar results. To ensure a good reproducibility of the results all images were performed at the same magnification ($\times 300\,000$) which had been calibrated.

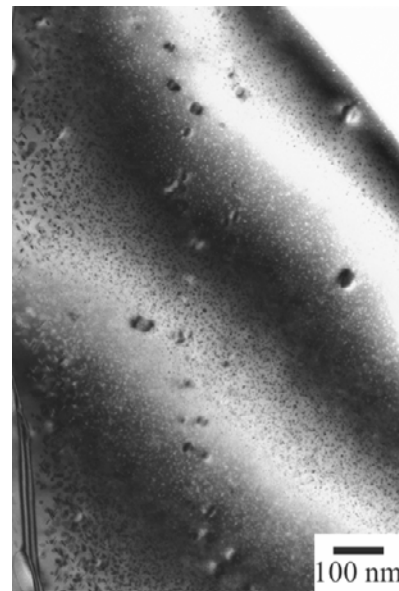


Figure II.21: Conditions of bright-field observations of hardening precipitates in the oscillations of thickness fringes in two-beam $(111)_{Al}$ conditions close to a $[110]_{Al}$ zone axis.

- 2) **Manual surrounding of particles.** This laborious method has been carried out manually because simple tools of automatic analysis were not accurate enough. Due to contrast variations within a TEM image, tested commercial softwares tend to lose very small particles. Images resulting from manual surrounding are shown in Figure II.22. Due to overlapping of some particles, the use of several layouts has been necessary.
- 3) **Image analysis.** The free software *ImageTool* has been used to perform image analysis. After thresholding (see Figure II.22), particles have been analysed. Different parameters have been retained: major axis length, minor axis length and elongation.

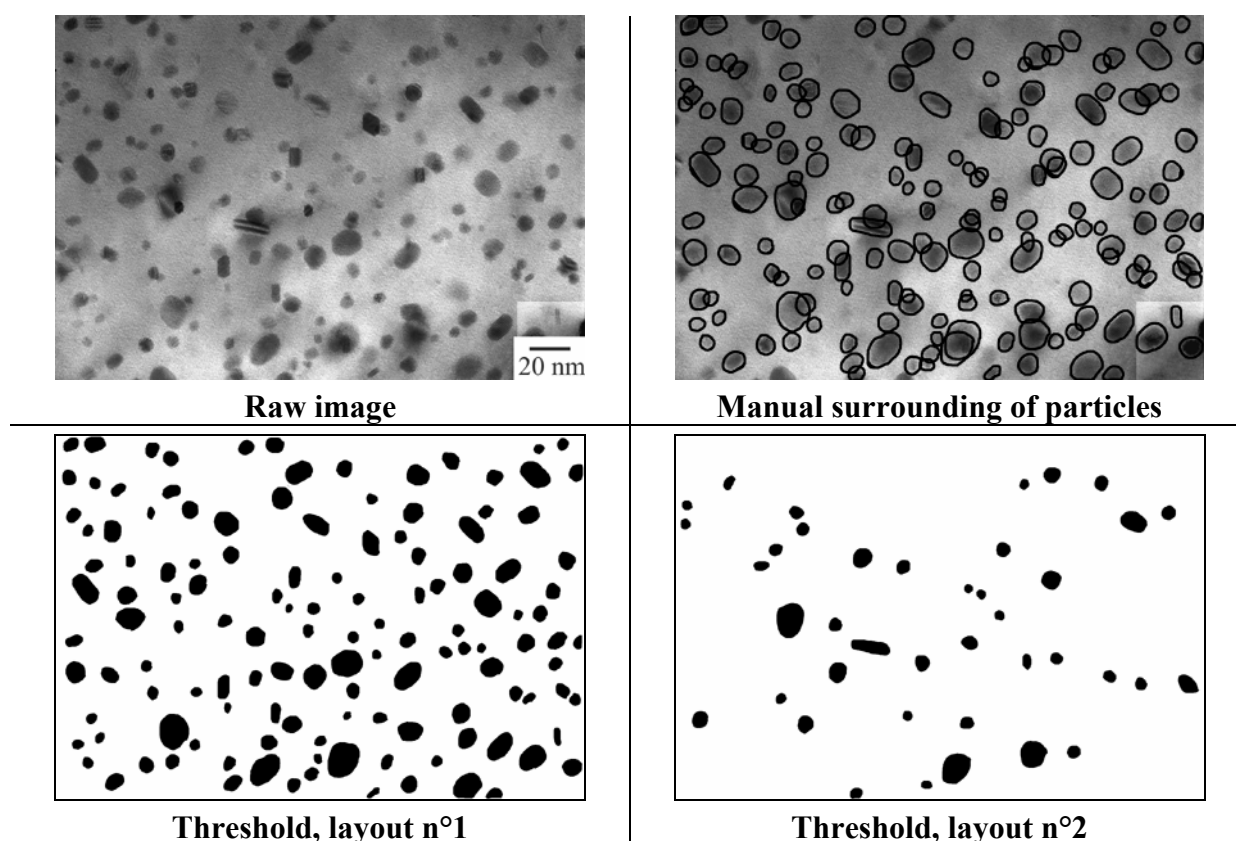


Figure II.22: From the raw image to the image analysis. Two layouts have been necessary because of overlapping of some particles. Example is an image obtained for the T7+ temper.

In order to get a statistically significant result, the analysis has been performed on approximately 300-500 particles. One should note that no correction treatment, as proposed by Hilliard [Hilliard, 1962], has been performed to take into account artefacts of the technique. Edge effects have been neglected considering the small precipitate numbers concerned as compared to the total precipitate numbers included in the image. Moreover surface effects (preferential removal of some particles due to etching) are expected to be small as the thickness is large compared to the size of the particles (particles 4nm in size to compare with 50nm thickness). Finally, overlapping has been taken into account by using several layouts.

The analysis results of T6, T7 and T7+ images are presented in Figure II.23 in terms of particle size distributions. The parameter used is the average between the maximum and minimum axis length of particles, divided by two, to be converted into a radius.

It can be observed that, as expected, the T6 temper presents the smaller mean particle size, followed by the T7 and T7+ states. Moreover, the size distribution enlarges as the mean particle radius increases (see standard deviations in Figure II.23).

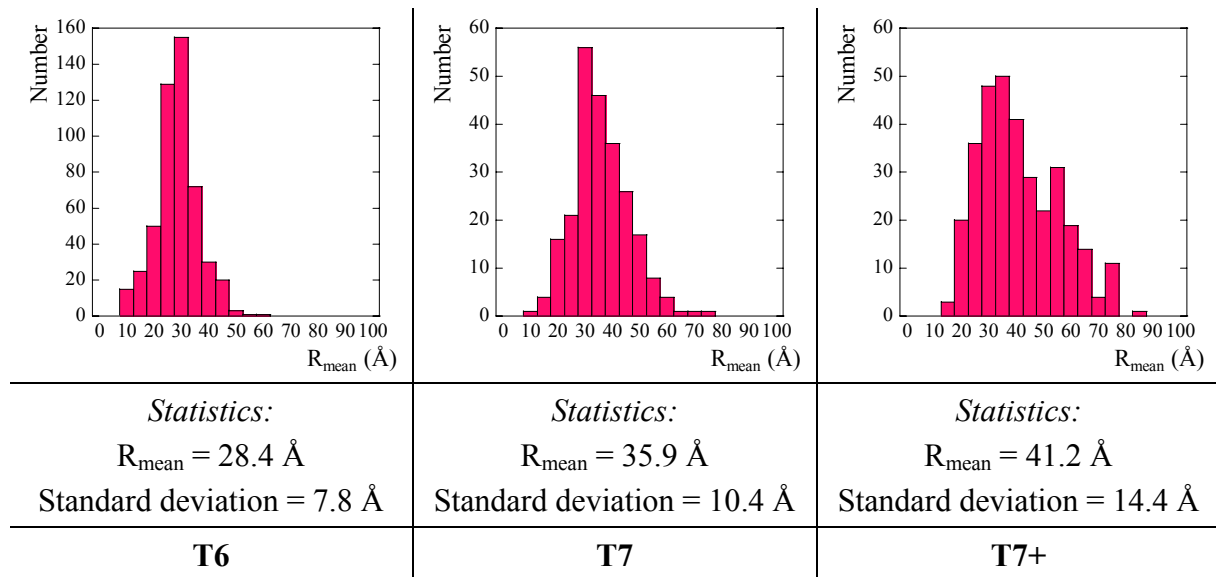


Figure II.23: T6, T7 and T7+ size distributions determined by TEM image analysis and corresponding statistics.

II.3.3. Quantitative TEM: volume fraction estimation

Quantitative TEM has been performed to estimate the precipitate volume fraction in the T6, T7 and T7+ tempers. This technique is entirely geometric, on the contrary to SAXS which is also sensitive to precipitate composition. This analysis proceeds in two steps:

- determination of the volume investigated, corresponding to the material volume where particles are imaged,
- calculation of the total volume of precipitates observed in each image.

II.3.3.1. Determination of the investigated volume

For determination of the investigated volume, both the area of the micrograph and the thickness are necessary. The area can be easily calculated using the dimensions of the image. For thickness measurements, convergent-beam technique has been used (see Chapter I for details concerning this technique).

Normally, thickness should be measured in exactly the same position as the micrograph used for image analysis. However, due to the relatively large volume fractions concerned ($\sim 2\%$), good imaging conditions could only be reached in very thin areas ($\leq 50\text{nm}$), where the convergence of the TEM used (2000FX) did not allow thickness measurements. Therefore the previous method was not applied. Another technique has been developed: thickness profiles (*thickness versus distance from the hole*) have been measured in several points of one single grain for each temper. Micrographs have been taken in the same grain and distance from the hole has been measured for each image. It should be noted that no tilt effect has been taken into account. Figure II.24 shows a series of points at different distances from the hole where thickness measurements have been carried out.

CBED patterns have been taken under $(220)_{Al}$ two-beam conditions. Actually, in aluminium alloys, these conditions allow to reach the smallest measurable thickness, as compared to other two-beam conditions [Allen, 1981].

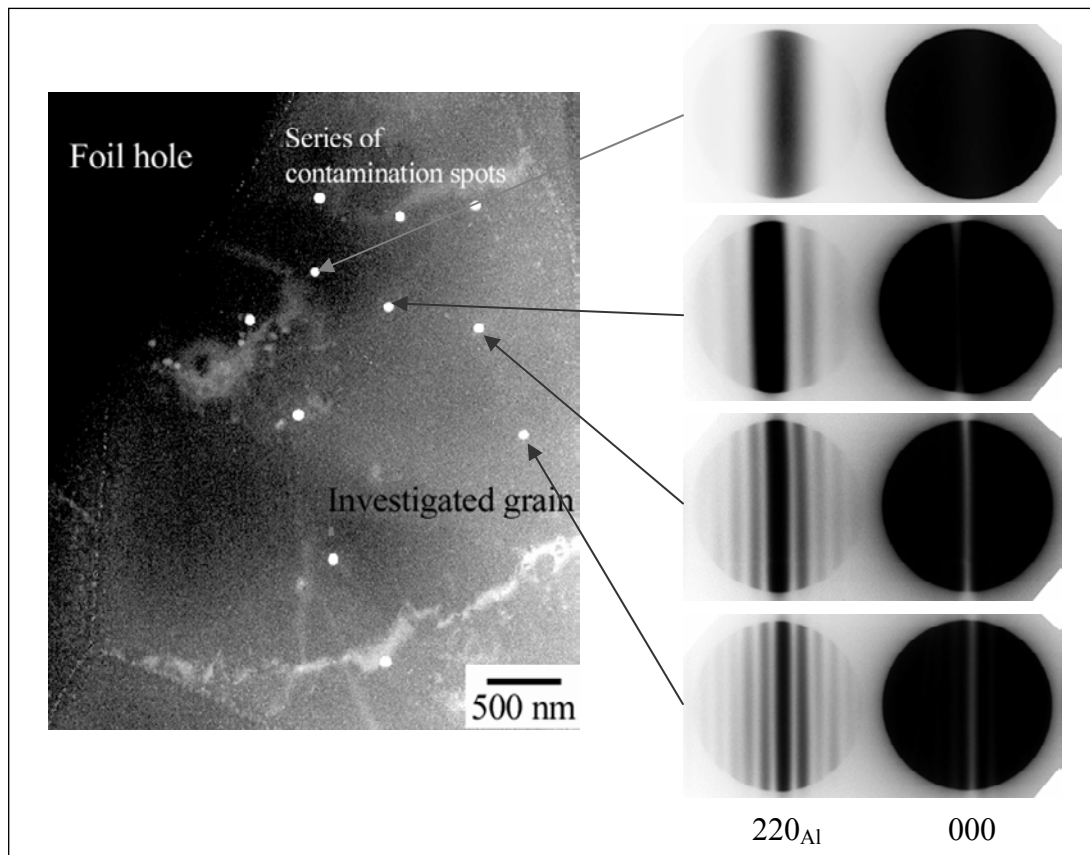


Figure II.24: Series of diffraction patterns corresponding to different points placed at different distances from the foil hole, as indicated on the micrograph.

Each diffraction pattern gives rise to the measure of a series of s_i and s_k values, corresponding to bright and dark fringes respectively. Note that we are working with negatives; thus bright fringes appear as dark fringes and inversely. It is then possible to evaluate the thickness using a linear regression in the $(s_i/n_i)^2$ versus $(1/n_i)^2$ plot (together with the $(s_k/x_k)^2$ versus $(1/x_k)^2$ plot), as shown on Figure II.25.a. As detailed in Chapter I, the ordinate at the origin of the straight line is directly related to the local thickness where the diffraction is performed (characterised by a contamination spot in Figure II.24).

Once all diffraction patterns were analysed, the thickness profile through the investigated grain could be drawn. Figure II.25.b shows the results obtained for the T6 investigation. The resulting plot shows that locally the foil corner can be considered as a wedge; actually the curve can be precisely approximated by a linear regression. Two different linear regressions are presented here: one optimising the fit, the other one going through the origin. In the case presented here the difference is very small between both; in others cases difference can lead up to 10 nm thickness deviation for points corresponding to imaging conditions. The first one has been used to calculate the investigated volume as it is not obvious that for very small thicknesses ($< 20\text{nm}$) the profile remains linear.

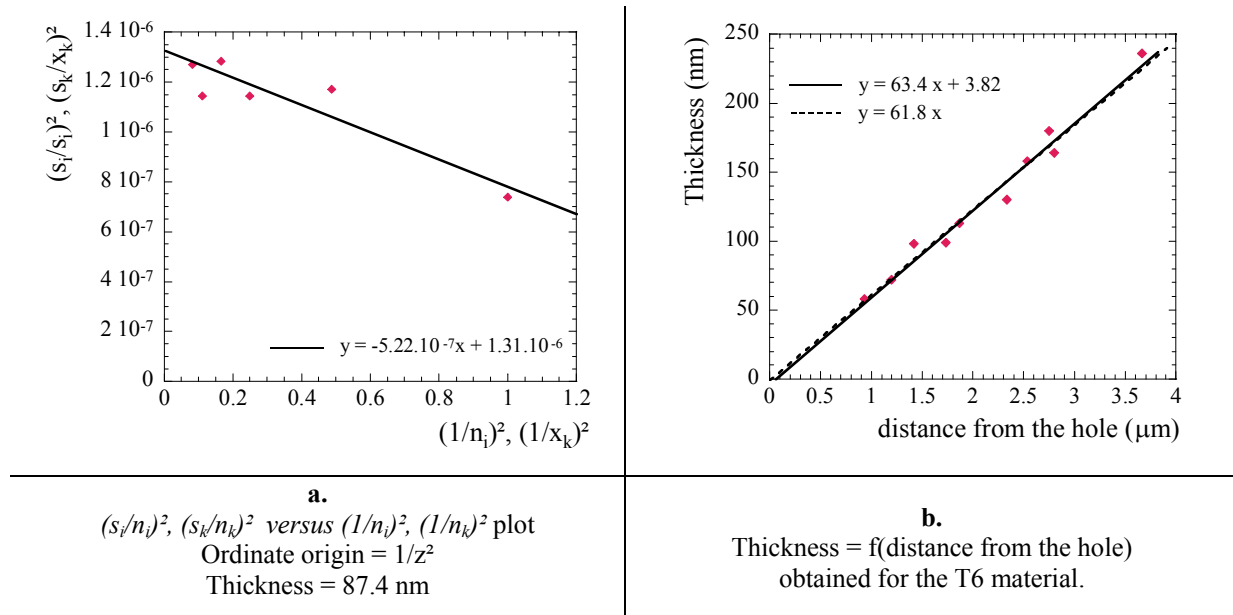


Figure II.25: Thickness determination (a) and thickness profile along a grain close to the foil hole.

If the distance between the hole edge and the image centre is known, the investigated volume can finally be calculated as follows:

$$V_{\text{tot}} = d.L.z \tag{II.9}$$

where d and L are the dimensions of the image (see Figure II.26),

z is the thickness corresponding to the centre of the image (see Figure II.26).

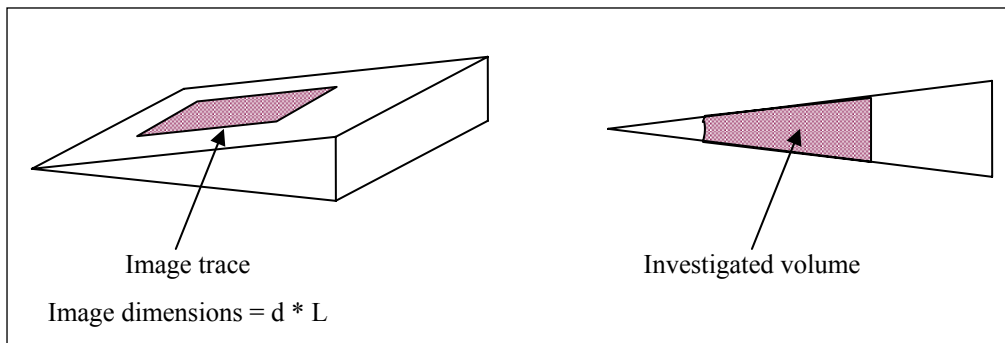


Figure II.26: Foil corner geometry showing how to calculate the investigated volume assuming a wedge shape.

II.3.3.2. Volume of precipitates included in the investigated volume

Regarding particle analysis, the same procedure as described in the preceding section has been applied. Then it remains to calculate the volume of precipitates included in the investigated volume from parameters estimated by image analysis. It should be noted that the particles observed in an image are only viewed via their 2-D projection.

For the T7 and T7+ materials, only rounded particles have been observed. For the T6 temper (see Figure II.27), another family of particles can clearly be observed in the micrographs: these ones have a platelet morphology, seen edge on (characterised by a high elongation > 2).

In the case of rounded particles, i.e. particles presenting an elongation smaller than 2, the shape has been assumed to be a sphere of radius R_{mean} . R_{mean} is the radius corresponding to the average of major and minor axis lengths, parameters obtained from image analysis. The areal density of precipitates is then calculated by adding the area of all particles.

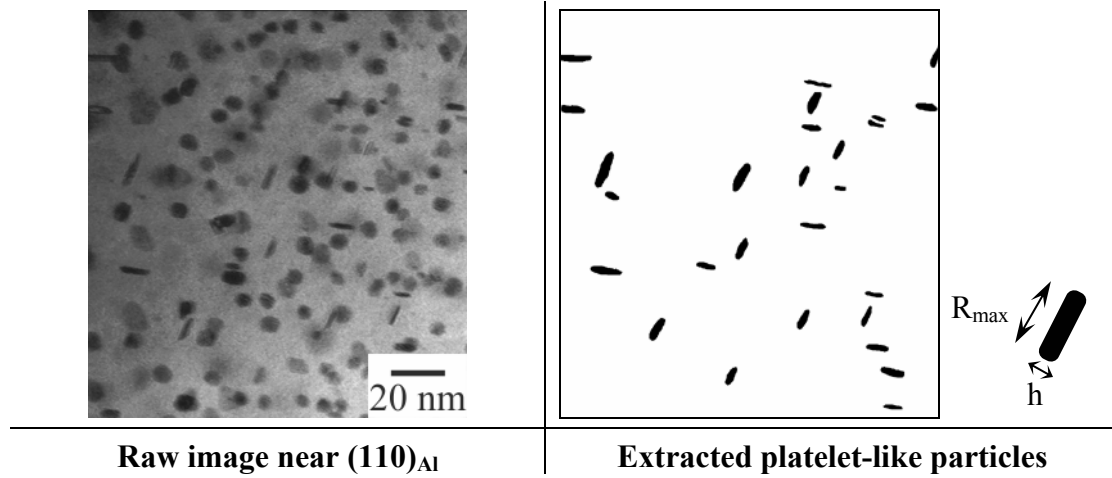


Figure II.27: Imaging showing the presence of platelet-like particles in the T6 temper.

When platelets are present, generally two families are observable, making an angle of approximately 70° . Actually these particles are expected to be η' -particles which are known to be platelets on $(111)_{\text{Al}}$. Since images are taken close to $(110)_{\text{Al}}$ zone axis, two families of $(111)_{\text{Al}}$ planes lie perpendicular to the beam. Therefore two families of η' -platelets can be observed, that is to say half of the real platelets contained in the investigated volume. Platelets which lie on the two $(111)_{\text{Al}}$ planes inclined to the electron beam will be observed as disks and are then included in the calculation of the volume of rounded particles, also present in the image. To calculate the resulting volume of particles, the following procedure has been performed:

- 1) Calculation of the volume of observed rounded particles, V_{sphere} ,
- 2) Calculation of the volume of observed platelets ($\pi R_{\text{max}}^2 * h$), $V_{\text{platelets}}$,
- 3) Estimation of corrected volume due to misoriented platelets counted as rounded particles, $V_{\text{correction}}$,
- 4) Calculation of total particle volume, $V_{\text{particles}}$, using the following formula:

$$V_{\text{particles}} = V_{\text{sphere}} + 2 V_{\text{platelets}} - V_{\text{correction}} \quad (II.10)$$

II.3.3.3. Calculated volume fractions

Results of the evaluation of the volume fraction of hardening precipitates for T6, T7 and T7+ tempers are displayed in Table II.13.

	Volume fraction
T6	$3.22 \pm 0.3 \%$
T7	$2.54 \pm 0.3 \%$
T7+	$2.18 \pm 0.3 \%$

Table II.13: T6, T7 and T7+ volume fraction estimations obtained by quantitative TEM. Accuracy is given in regards to different estimations obtained on 3 images for each state.

It can be concluded that the T6 volume fraction is markedly higher than that of the T7 and T7+ states, which can be considered as equivalent. Actually, T7+ temper is obtained by overaging the T7 state which contains already mostly the stable phase; volume fraction is then expected either to increase or to remain constant as coarsening occurs. One should note that the result obtained for the T6 temper by quantitative TEM is very close to that obtained by the simple approach using DSC (see Table II.11).

Is it surprising to obtain a smaller volume fraction for stable precipitates than for metastable ones? Two factors are playing a role which may explain this behaviour: the temperature effect and a composition effect.

Let us consider the simple case of a two-phase diagram, as shown on Figure II.28. We will deal with simple mass balance approaches for both stable and metastable phases, assuming that the equilibrium is reached. As activation energy barriers are smaller for metastable precipitates (lower interfacial energy due to higher coherency), the solvus of metastable phases is expected to be as illustrated on Figure II.28. A basic example is Al-Cu metastable phases (GP zones, θ'' , θ') as compared to the stable θ -phase [Porter, 1981].

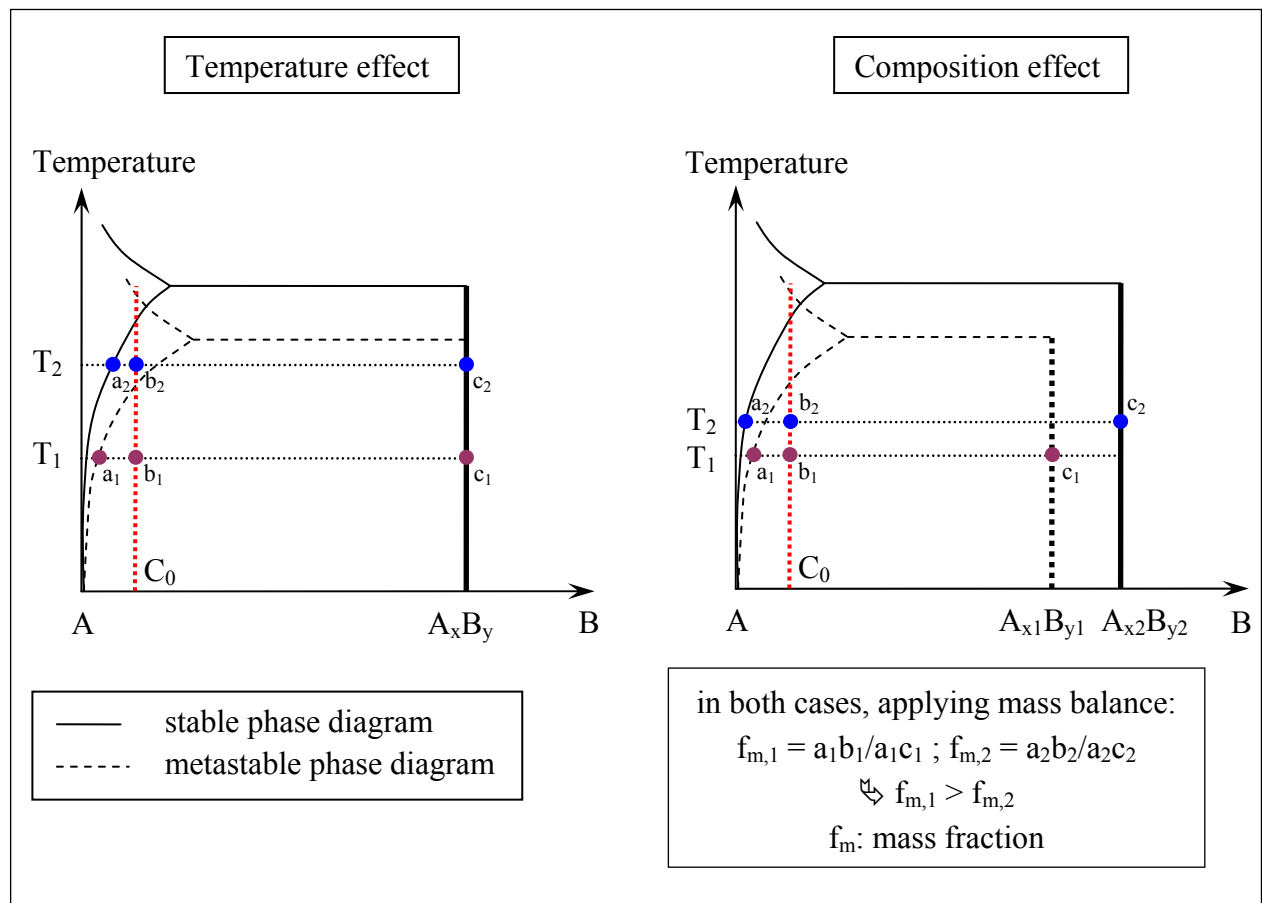


Figure II.28: Schematic representation of a two-phase diagram including stable and metastable phases showing how to explain why: $f_v(T6) > f_v(T7 \text{ or } T7+)$.

If the difference between ageing temperatures T_1 and T_2 (in our case 140 and 170°C) to obtain respectively metastable and stable precipitates is large enough, then this simple factor can explain the higher volume fraction of metastable phases (see Figure II.28).

If the difference between T_1 and T_2 is small, then the previous explanation is no longer valid, due to the shape of the metastable solvus. In this case, the higher volume fraction of metastable precipitates can be explained by a composition change between metastable and stable phases, as illustrated in Figure II.28. To be valid, the stable precipitates should have higher solute content than metastable one. A well-known illustration of this hypothesis is the case of steels, where the volume fraction of metastable cementite (Fe_3C) is much higher than that of the stable phase graphite.

Table II.14 is a summary of results obtained by quantitative TEM on the three different tempers: T6, T7 and T7+ in terms of mean radius and volume fraction.

	Precipitates	R_{mean} (Å)	f_v (%)
T6	η'	28.4 Å	3.22 ± 0.3 %
T7	$\eta' + \eta$	35.9 Å	2.54 ± 0.3 %
T7+	η	41.2 Å	2.18 ± 0.3 %

Table II.14: Summary of quantitative TEM results obtained on T6, T7 and T7+ tempers in terms of mean radius R_{mean} and volume fraction f_v .

II.4. From TEM to SAXS

In the work that follows, a quantitative study has been mainly undertaken by SAXS measurements. Previous study on initial states which have been investigated in depth using both SAXS and TEM, will be useful in the calibration of subsequent SAXS results, i.e. Guinier radius and integrated intensity, to convert them into mean radii and volume fractions of particles.

II.4.1. Radius calibration

The results obtained from TEM (see Table II.14) are of the same order of magnitude as the corresponding Guinier radius obtained from SAXS experiments (see Table II.10). These results are used to calibrate the Guinier radius in order to get a good approximation of the real radius of particles.

We recall here (see Chapter I equation I.15) that in the case of a monodisperse distribution of spherical particles of mean radius R , the ratio R/R_g was shown to be equal to $\sqrt{5/3}$ (≈ 1.29).

We can calculate the R_{mean}/R_g ratio for the T6, T7 and T7+ tempers from Guinier radius determined by SAXS and mean size of particles determined by TEM image analysis:

$$\text{for T6: } \frac{R_{mean}}{R_g} = \frac{28.4}{25.6} = 1.11$$

$$\text{for T7: } \frac{R_{mean}}{R_g} = \frac{35.9}{40} = 0.90$$

$$\text{for T7+ : } \frac{R_{\text{mean}}}{R_g} = \frac{41.2}{48.6} = 0.85$$

This ratio is smaller from that of a homogeneous distribution of spherical particles due to distribution and morphology effects.

From now on, the Guinier radius will be converted into mean radius of the particles using a corrective factor equal to the average of previous R_{mean}/R_g values, as follows:

$$R_{\text{mean}} = K.R_g = 0.95.R_g$$

Spectrum calculation

A simulation of a SAXS spectrum obtained from the particle distribution determined by TEM has been carried out.

The SAXS response of a sphere of radius r is (see Chapter I; equation I.10):

$$I(q) = KV^2 \left[3 \frac{\sin(qr) - qr\cos(qr)}{(qr)^3} \right]^2 \quad (II.11)$$

where $I(q)$ is the scattered intensity at the scattering vector q ,
 K is a constant depending on the composition of the particle,
 V is the volume of the particle.

The total intensity scattered by a distribution of spheres is then:

$$I(q) = \int_0^\infty I(q,r)f(r)dr \quad (II.12)$$

where $f(r)$ is the size distribution of the scattering particles, obtained by TEM image analysis.

Assuming that particles are spheres of radius R_{mean} calculated earlier, the spectrum *intensity I versus scattering vector q* has been calculated for the T6 and T7 materials, as shown in Figure II.29.

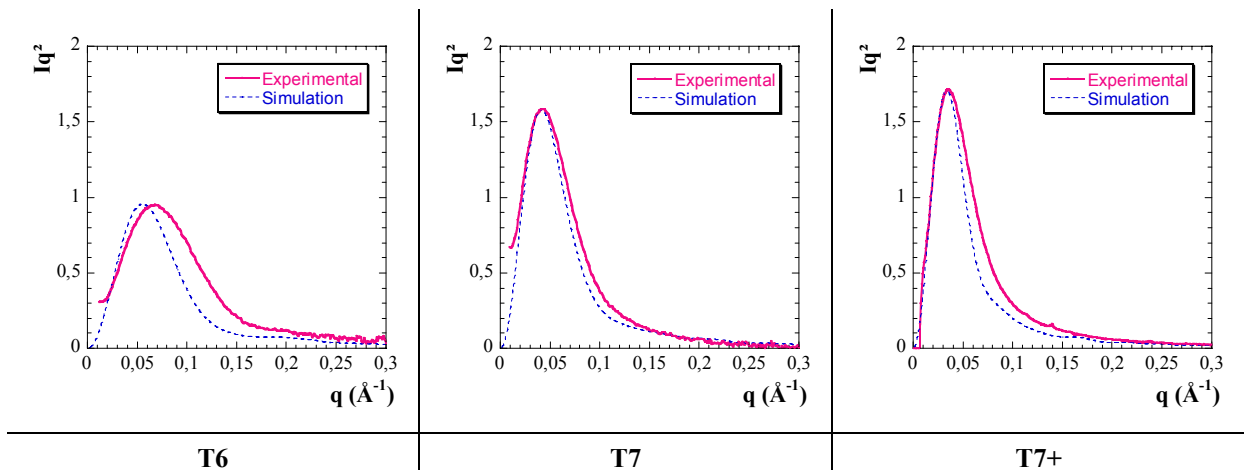


Figure II.29: Calculation of spectra for T6, T7 and T7+ states using the distribution obtained from TEM image analysis.

The obtained results are in good agreement with the experimental data, especially for the T7 and T7+ tempers. The position of the peak is particularly satisfying. It should be kept in mind

that the position of the peak in the Iq^2 versus q plot is closely related to the size of the particles. We can then conclude that the mean radius of the particles is a good estimation. The difference in the general shape is probably due to the shape of the particles which are not perfectly spherical, as observed by TEM.

The larger difference observed for the T6 material may be due to the shape of particles which are far from spheres. The simulation is made using the average distance of major and minor axis lengths of particles. This approximation is particularly wrong in the case of platelets. We can however conclude that the proposed mean particle size is overestimated as the position of the maximum is shifted towards smaller q -values.

II.4.2. Volume fraction calibration

II.4.2.1. Composition considerations

Considering the results obtained from quantitative TEM (see Table II.14), we can deduce some information concerning the chemistry of the phases present in the different states.

Since Mg and Al components have approximately the same atomic scattering factors ($Z_{Mg}=12$ and $Z_{Al}=13$) (see Table II.8), these two elements have an equivalent influence on the Q_0 value. An equivalent plot as presented in Figure II.16 can be drawn taking into account the $Zn/(Mg+Al)$ ratio. Figure II.30 displays the curve showing the influence of composition on volume fraction determined by SAXS for the T6 and T7 states. Quantitative TEM allowed us to identify the real volume fraction present in both tempers, and therefore we can deduce the composition range of precipitates contained in the T6 and T7 materials.

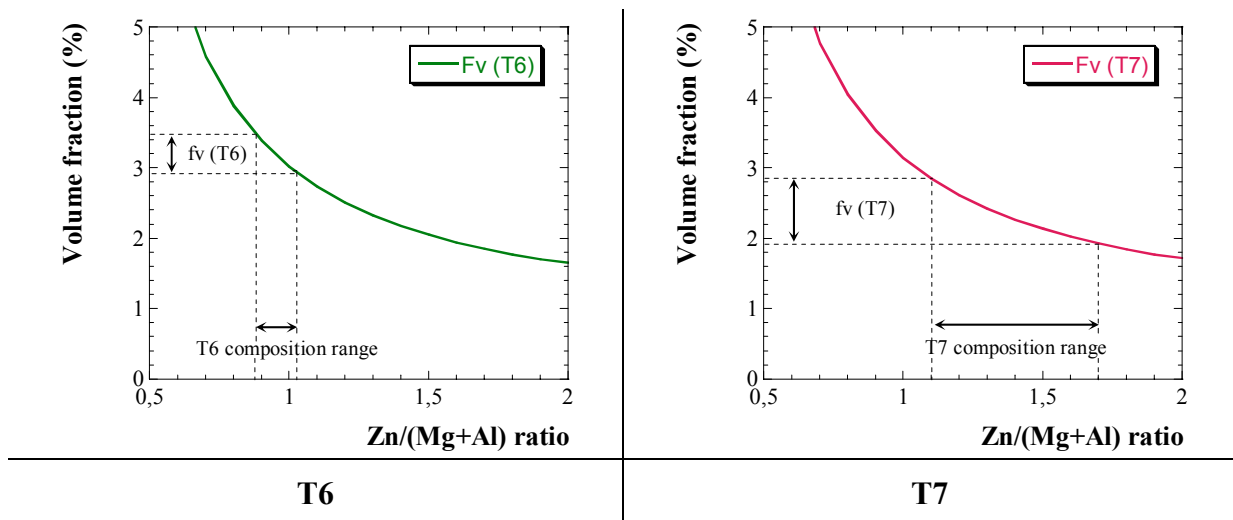


Figure II.30: Composition effect. TEM volume fraction results are used to deduce composition ranges, using Q_0 SAXS results. Note that T7 volume fraction range is given taking into account T7+ results.

We can thus propose the following composition for η' and $(\eta' + \eta)$ precipitates contained respectively in the T6 and T7 tempers. The results are displayed in Table II.15.

	Precipitates	$\frac{\text{Zn}}{\text{Al} + \text{Mg}}$	Average composition
T6	η'	0.9 - 1	$(\text{Mg,Al})_1\text{Zn}_1$
T7	$\eta' + \eta$	1.1 - 1.7	$(\text{Mg,Al})_1\text{Zn}_{1.4}$

Table II.15: Composition of η' and $(\eta'+\eta)$ precipitates deduced from complementary techniques: quantitative TEM and SAXS.

As it is generally accepted that the Zn/Mg ratio is close to 1.5 (refer to Table II.4), a reasonable composition for the η' -phase in view of our results is then (in atomic percent):

50% Zn
25% Mg
25% Al

Concerning the T7 material, which is a mixture of η' and η -precipitates, its Zn content is higher than in the T6 state which only contains the η' -phase. Actually, the η -phase composition is expected to be closer to the equilibrium MgZn_2 and to contain less aluminium (refer to Table II.2).

II.4.2.2. How to calibrate volume fraction?

In the following, quantitative investigations will be performed by SAXS measurements. It is then necessary to be able to convert integrated intensity Q_0 into volume fraction. This requires the application of a composition calibration. One major problem will appear, concerning particularly controlled in-situ heat treatments. During such heat treatments, phase transformations are expected to occur and compositional variations will occur during the heat treatments. As it is impossible to determine the nature and proportions of precipitates at each moment of the heat treatment, it is not possible to deal with compositional variations.

In the following work, we will assume a fixed composition for all precipitates, even for GP zones. The average value 1.2 of $\text{Zn}/(\text{Mg}+\text{Al})$ ratios obtained for the T6 and T7 states has been chosen as the most representative.

Finally, the volume fraction will be deduced from integrated intensity using the following relationship:

$$f_v = \alpha \cdot Q_0 = 0.209 \cdot Q_0$$

As a consequence, the T7 volume fraction will be slightly overestimated whereas the T6 one will be underestimated. However for the sake of simplicity this approximation appears to be a good compromise.

In summary, TEM and SAXS are complementary techniques which allowed us to reach a good knowledge of precipitates contained in materials prior to welding in terms of:

- nature of precipitates (including their chemistry),
- particle distribution,
- mean size,
- volume fraction.

II.5. Key points

Figure II.31 is a summary of the precipitate microstructure of the different materials prior to welding.

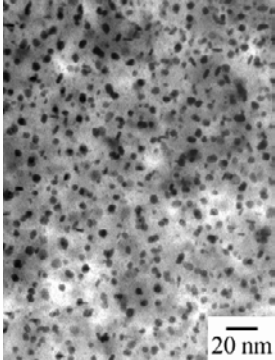
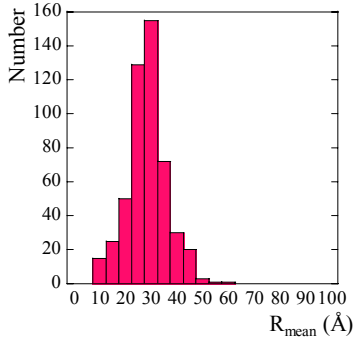
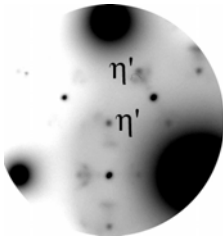
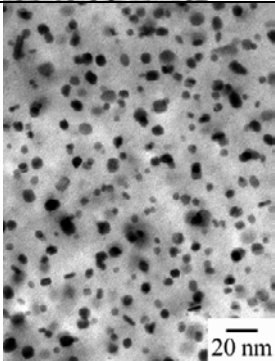
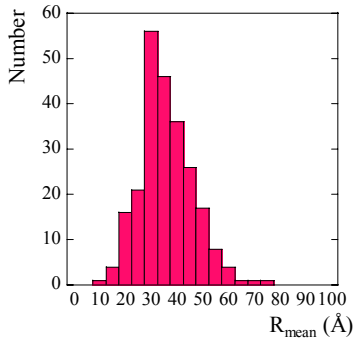
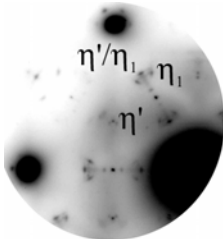
	Bright-field imaging (TEM)	Particle distribution (TEM)	[111] zone axis diffraction pattern (TEM)	Summary (SAXS coupled with TEM)
T4				GP zones $R_{\text{mean}} = 7.1 \text{ \AA}$ $f_v = 2.1 \%$
T6				mainly η' $R_{\text{mean}} = 24.3 \text{ \AA}$ $f_v = 2.5 \%$
T7				$\eta' + \eta$ $R_{\text{mean}} = 38 \text{ \AA}$ $f_v = 2.6 \%$

Figure II.31: Summary of precipitate microstructure of material prior to welding.

Remark: The lower T6 volume fraction, as compared to T7 temper, is an artefact due to the composition assumption (refer to II.4.2.2. How to calibrate volume fraction?).

Chapter III. Precipitation evolution during welding and post-welding heat treatments

Welding is a complex non-isothermal process. Each point of the material undergoes a specific thermal cycle. After a literature review concerning welding processes, the thermal profiles will be calculated at each point of the heat-affected zone, which is the key factor affecting the precipitation microstructure. We will then focus our investigation on the evolution of the strengthening precipitates in the as-welded state of three initial states: T4, T6 and T7 tempers. Finally we will discuss the response of the material to post-welding heat treatments, which aim at recovering the initial mechanical properties.

III.1. Literature review: description of welding

After a short review of existing welding processes, focusing mainly on the Metal Inert Gas (MIG) technique, we will examine the temperature profiles involved during welding. Indeed, in case of small distortions, only the temperature history needs to be considered to explain the microstructural evolution within the heat-affected zone (HAZ). Finally, a literature survey of the evolution of microstructural features and properties will be presented.

III.1.1. Welding techniques

Numerous welding processes are now available for aluminium alloys, from traditional arc-welding to more sophisticated techniques like laser [Mayer, 1996] or friction-stir welding [Thomas, 2002]. In the case of automotive applications, a low-cost process is needed, favouring the arc-welding process. Therefore, arc welding has been preferred to other techniques in automotive industry, and more precisely gas-shielded arc welding for joining of aluminium alloys. In this category, two main techniques have been developed:

- Metal Inert Gas (MIG) also called Gas-Metal Arc (GMA),
- Tungsten Inert Gas (TIG) also called Gas-Tungsten Arc (GTA).

These gas-shielded techniques prevent the electrode, weld puddle, arc and adjacent areas of the base metal from atmospheric contamination. For the MIG process, the heat for welding is

generated by an arc between a consumable electrode and the work metal, whereas for TIG welding, the electrode is non-consumable. These two processes are illustrated in Figure III.1.

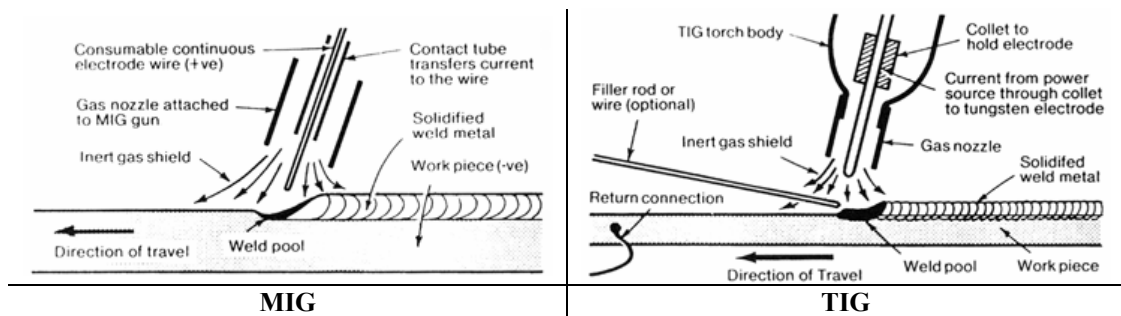


Figure III.1: Main features of MIG and TIG welding processes [Polmear, 1996].

Because the electrode is non-consumable, a TIG weld can be made by fusion of the base material without adding filler metal. However, in some cases a filler metal may be used depending on the requirements. TIG is especially well-suited to the welding of thin sheets. MIG is generally favoured for industrial production. The main advantage of MIG over TIG processes stems from the fact that the MIG consumable electrode can support a high current density. In the case of TIG, the current is limited by the melting temperature of the tungsten electrode. Therefore higher welding speeds can be reached during MIG welding [Welding and Brazing, 1971].

Filler metals are selected with regard to the composition of the base material and its ability to produce crack-free welds with maximum strength. Most suitable filler metals for welding of the 7xxx series are based on Al-Mg alloys.

III.1.2. Heat flow and temperature distribution in the heat-affected zone

The temperature history is the key factor determining the microstructural evolution of MIG welded plates since distortions induced by this process are relatively small [Welding and Brazing, 1971].

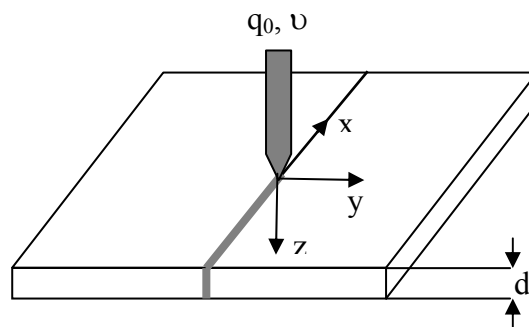


Figure III.2: Welding configuration and definition of ordinates.

Solutions to the heat-flow equations of a moving point heat-source were given by Rosenthal in 1935 [Easterling, 1992]. The differential equation of heat flow can be expressed (in the co-ordinate system defined in Figure III.2):

$$\frac{\partial T}{\partial t} = a \left(\frac{\partial^2 T}{\partial x^2} + \frac{\partial^2 T}{\partial y^2} + \frac{\partial^2 T}{\partial z^2} \right) \quad (III.1)$$

where T is the temperature (K)
 t is the time (s)
 a is the thermal diffusivity ($\text{mm}^2 \cdot \text{s}^{-1}$).

Let us now consider the simplified case of a fast moving high power source in a thin plate. In the following we will assume that the speed and the net power supplied by the source are constant. Under such conditions, a simplified solution (model after Rykalin) of the previous differential equation can be written as [Grong, 1996]:

$$T(y) - T_0 = \frac{q_0 / \nu d}{\rho c \sqrt{4\pi a t}} \exp\left(-\frac{y^2}{4at}\right) \quad (III.2)$$

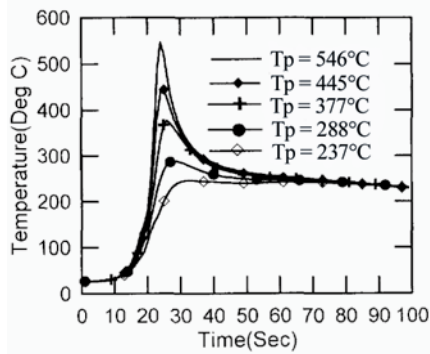
where T is the temperature at the transverse distance y ,
 T_0 is the initial temperature,
 q_0 is the net power received by the weld (W),
 ν is the welding speed ($\text{mm} \cdot \text{s}^{-1}$),
 d is the plate thickness (mm),
 ρc is the volume heat capacity ($\text{J} \cdot \text{mm}^{-3} \cdot \text{K}^{-1}$),
 a is the thermal diffusivity ($\text{mm}^2 \cdot \text{s}^{-1}$),
 t is the time (s),
 y is the transverse dimension (mm) (see Figure III.2).

In this simplified model, the solution is one-dimensional and isotherms are parallel to the welding direction x (see Figure III.2). This model can be practically applied when q_0/d is greater than $0.5 \text{ KW} \cdot \text{mm}^{-1}$. It will be shown below that the condition for the validity of this assumption is met in our study.

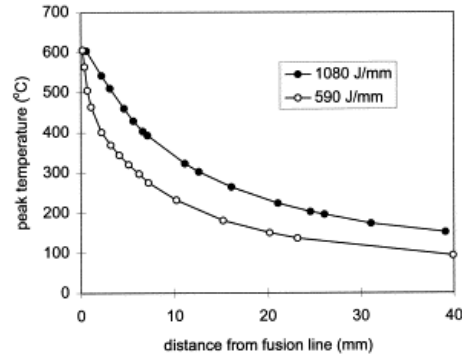
The net power received by the weld can be either measured by calorimetry or estimated from the welding parameters: the current I (A) and the arc voltage U (V) through an efficiency factor η :

$$q_0 = \eta * UI \quad (III.3)$$

For MIG welding of aluminium alloys under argon, η is estimated to be 0.7 [Grong, 1996].



a.
Thermal history in different points of the HAZ



b.
Peak temperature profile along the HAZ for two heat inputs

Figure III.3: a. Measured thermal cycles in the HAZ of a TIG welded 7075-T6 in different points of the HAZ [Hwang, 1998]. The closer to the fusion line, the higher the peak temperature T_p .

b. Relationship between the peak temperature and the distance from the fusion boundary for two heat inputs (590 and 1080 J/mm) [Ma, 1999].

Using the welding parameters displayed in Table I.2, q_0/d can be calculated and is equal in our case to $0.62 \text{ KW} \cdot \text{mm}^{-1}$. The previous simplified model can thus be applied to estimate the temperature history at each point of the heat-affected zone.

Finally, depending on its position, each point of the heat-affected zone undergoes a specific thermal cycle characterised by a peak temperature and a specific heating rate. Such thermal histories at different points of the HAZ are displayed in Figure III.3 together with the peak temperature profile along the heat-affected zone.

III.1.3. Influence of welding on HAZ microstructure and properties

Welding of age-hardenable alloys like 7xxx or 6xxx alloys is greatly detrimental to the initial properties of the material. In fact, the sudden high input of temperature involves radical changes of the existing microstructure, in particular of the precipitates responsible for the strengthening of the alloy. Many studies have already been carried out to better understand the influence of arc welding on the heat-affected zone properties and microstructure.

III.1.3.1. Mechanical properties

Hardness profiles

Welding of age-hardenable alloys is characterised by a large softening in the heat-affected zone, due to precipitation evolution during the heat input. Figure III.4 illustrates hardness profiles along the heat-affected zone and after prolonged natural ageing in the case of an Al-Mg-Si alloy, characterised by a similar precipitation sequence as in Al-Zn-Mg alloys.

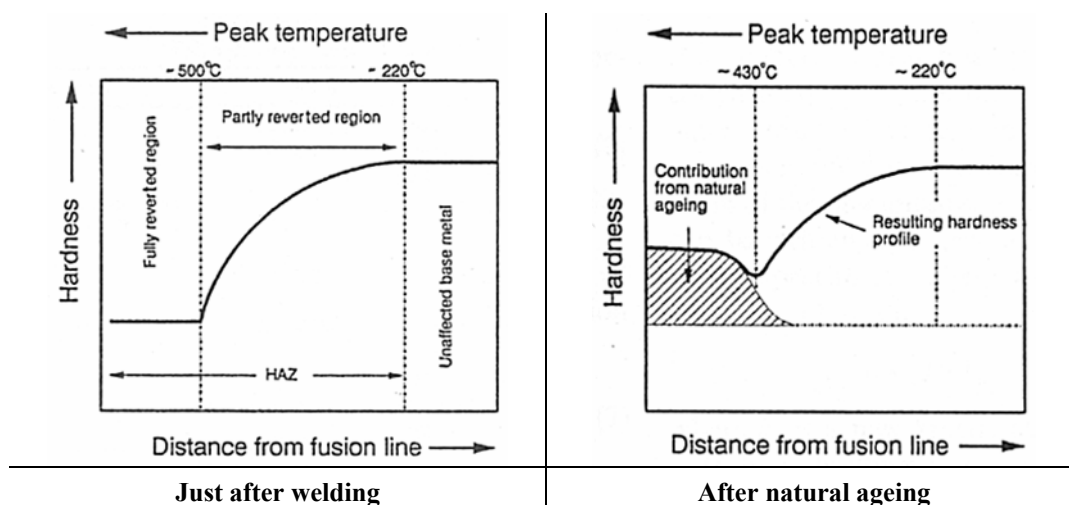


Figure III.4: Schematic diagrams showing the hardness distribution in the HAZ of 6082-T6 aluminium welds, just after welding and after prolonged room temperature ageing [Myhr, 1991a].

During natural ageing at room temperature, the solute left by precipitate dissolution in the vicinity of the fusion zone can lead to re-hardening by nucleation and growth of GP zones.

Thermal stability of strengthening precipitates in the Al-Zn-Mg system, η or η' -precipitates, is lower than for Al-Mg-Si alloys. Thus the peak temperature range corresponding to the hardness drop in the case of alloys of the 7xxx series is expected to be in the $200\text{--}350^{\circ}\text{C}$ range, as observed by Myhr *et al.* [Myhr, 1998] in the study of 7108-T6 welds. However recovery by re-precipitation is much more efficient in this system and it is expected that most of the strength loss can be recovered after a long period (3-5 months) of natural ageing.

Bjørneklett *et al.* [Bjørneklett, 1999] compared the typical hardness profiles for Al-Zn-Mg and Al-Mg-Si alloys welds after prolonged natural ageing, including both the heat-affected zone and the weld metal (see Figure III.5). In the case of Al-Mg-Si welds, the minimum HAZ strength level controls the overall resistance capacity of the joint. On the contrary for Al-Zn-Mg alloys, the metal in the weld nugget is the limiting factor due to the better ageing response of this system. However it should be noted that the recovered microstructure has a poorer thermal stability since it is composed of GP zones. Development of new filler materials is now in progress to improve the resistance of the global structure.

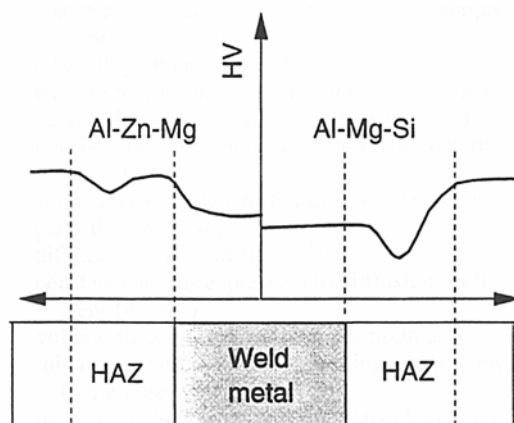


Figure III.5: Schematic diagram showing typical hardness profiles for Al-Zn-Mg and Al-Mg-Si welds following prolonged natural ageing [Bjørneklett, 1999].

Fracture

One limitation in the design of Al-Zn-Mg weldments lies in their high susceptibility to solidification cracking. During welding, liquid films form at grain boundaries adjacent to the fusion boundary (designed as white zone). These liquid films lead to the formation of microscopic intergranular cracks after welding which may provide paths for subsequent brittle intergranular fracture [Bjørneklett, 1996; Lu, 1996; Kim, 1996].

Fatigue strength of aluminium alloy welds are also of particular interest considering the structural applications of Al-Zn-Mg alloys. Fatigue performance is significantly affected by the level of residual stress and stress concentrations present in the material. If tensile residual stresses are present then crack initiation is accelerated resulting in a reduction of the fatigue life of the weld. During welding a complex distribution of residual stresses is produced by solidification shrinkage, local thermal expansion and induced plastic deformation.

III.1.3.2. Corrosion resistance

Two aspects of the microstructure have been pointed out to influence the corrosion resistance of Al-Zn-Mg welds:

- the concentration gradient in the partially reverted region of the heat-affected zone [Bjørneklett, 1999],
- the influence of precipitates at grain boundaries [Benedetti, 2000].

The steep concentration gradient of Zn and Mg in the partially reverted region of the HAZ will contribute to a change in the chemical potential across the heat-affected zone, reducing the corrosion resistance of this part of the weld [Bjørneklett, 1999].

III.1.3.3. Grain microstructure

The heat-affected zone can be divided into a number of sub-zones (depending on the base material). Figure III.6 is an illustration of such a division in the case of a 0.15wt%C steel. Each sub-zone refers to a different type of microstructure and consequently to different mechanical properties.

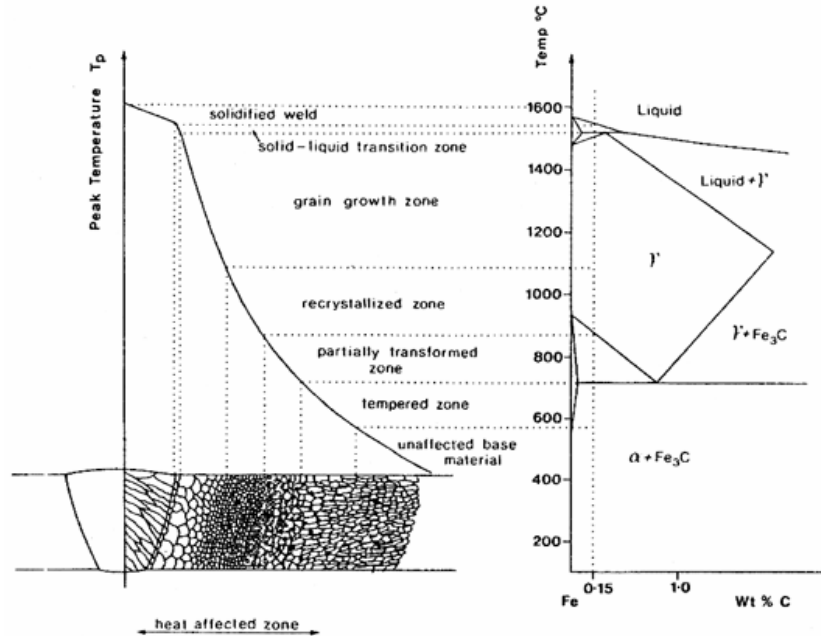


Figure III.6: Schematic diagram of the various sub-zones of the heat-affected zone of steel containing 0.15wt%C indicated on the Fe-Fe₃C phase diagram [Easterling, 1992].

A detailed analysis of the grain structure relevant to our Al-Zn-Mg alloy will be displayed in section (III.3. Grain structure). It has been shown that in the case of age-hardenable aluminium alloys, grain growth plays a minor role in strength changes [Ma, 1999].

III.1.3.4. Precipitation

We will now focus on precipitation evolution during welding. More precisely only the precipitation state after welding has been investigated due to the practical difficulties of following the evolution of precipitation features in-situ. The modification of the precipitate microstructure is the key factor influencing the strength in the case of heat-treatable aluminium alloys.

The pre-existing precipitation state can be modified in the following different ways:

- dissolution of precipitates,
- growth or coarsening of pre-existing precipitates,
- transformation of metastable phases to more stable forms,
- nucleation of new particles.

Ma and den Ouden [Ma, 1999] divided the heat-affected zone into two sub-zones: the dissolution zone, where dissolution is complete, and the overageing zone, where growth and coarsening of pre-existing particles occur. In the case of the 7020-T6 alloy (Al-5wt%Zn-1.5wt%Mg) the boundary between the two sub-zones corresponds to a peak temperature of about 350°C. The overageing zone covers the peak temperature range between 230 and 350°C.

Hwang and Chou [Hwang, 1998] studied more precisely the nature of the resulting precipitates in a welded 7075-T6 alloy using DSC. Initially present metastable η' -precipitates were found to transform gradually into the more stable η -phase as the peak temperature is increased. In particular for a 290°C peak temperature, the microstructure is composed of a mixture of $\eta'+\eta$ particles, whereas for a peak temperature of 380°C, no more η' -particles can be detected.

Lech-Grega *et al.* [Lech-Grega, 2001] proposed a quantitative analysis of FEG SEM images giving particle distributions in 7020 alloy subjected to a heat treatment simulating the welding process. Significant quantitative changes in the size and distribution of particles as a function of the heat treatment temperature have been observed, characterised by coarsening of observed particles. However it should be noted that the mean size of the studied particles does not correspond to strengthening precipitates and is more representative of coarse particle sizes (heterogeneous η -precipitation on grain boundaries for example). This means that not only the nano-scaled strengthening precipitates are affected by welding but also coarse particles located on grain boundaries.

III.2. Calculation of the thermal profiles

Thermal profiles were calculated by Hydro Automotive Structures using the finite element model *Weldsim* [Myhr, 1999]. This simulation has been performed using the weld parameters (welding speed, current, voltage, efficiency, steel table) and thermal material properties (fusion heat, specific heat capacity, thermal conductivity). Table III.1 is a summary of the different parameters used in the simulation.

Welding speed	0.01 m/s	
Current	101 A	
Voltage	21.9 V	
Net heat efficiency	0.8	
Density	2780 Kg/m ³	
Fusion heat	396 J/g	
Specific heat capacity	875 J/KgK	
Thermal conductivity	140 W/mK	
Liquid fraction	20 °C	0
	475 °C	0
	605 °C	0.1
	615 °C	0.2
	622 °C	0.3
	638 °C	0.7
	641 °C	1
Heat transfer coefficient to air	$\Delta T=10$ K	4 W/m ² K
	$\Delta T=100$ K	7.5 W/m ² K
	$\Delta T=600$ K	12 W/m ² K
Heat transfer coefficient between aluminium and steel	2500 W/m ² below the weld metal 200 W/m ² further from the weld zone	

Table III.1: Parameters relevant for the simulation.

The program solves the three dimensional, time dependent heat conduction equation by a finite element technique. The heat provided by the welding arc is represented by an ellipsoid volume distributed source. The simulation has been calibrated on experimental temperature

profiles measured in three different points: 10mm, 20mm and 30mm from the fusion line. The computational domain and the mesh are shown in Figure III.7 .

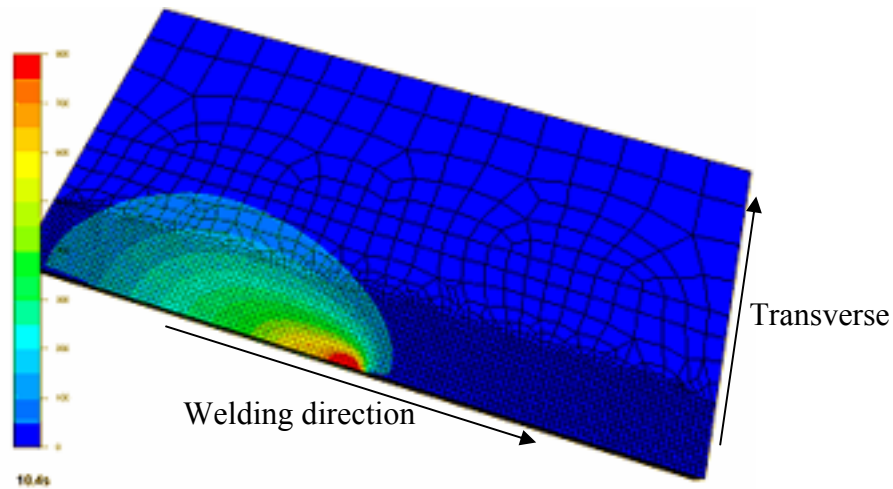


Figure III.7: Computational domain and mesh.

This simulation gives access to the thermal profile undergone during welding in each point of the heat-affected zone. The comparison between simulated and measured thermal profiles during welding is shown in Figure III.8.a. It can be concluded that the agreement between simulated and measured values is satisfying. The temperature at the end of the cooling part is overestimated, probably because of the difficulty to estimate the thermal influence of the steel table on the structure cooling. Another issue is the overestimation of the heating rate for points far from the weld. Nevertheless the calculated profiles should capture most of the microstructural changes: the peak temperature, as well as the time at high temperatures are correctly described. The resulting peak temperature distribution along the heat-affected zone is displayed in Figure III.8.b.

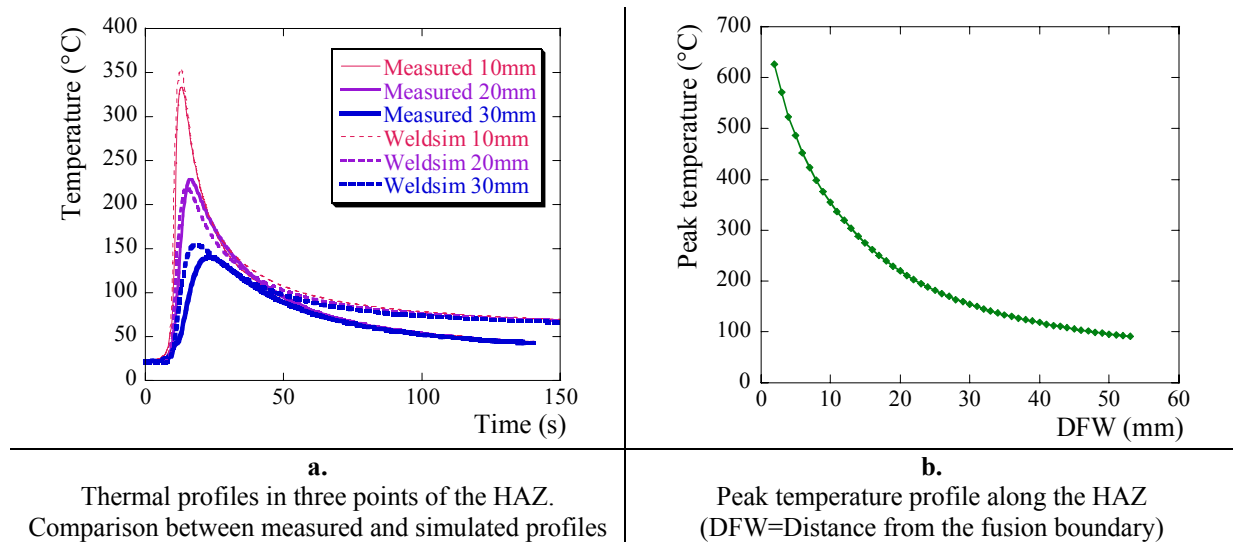


Figure III.8: Calculated thermal profiles (a) and resulting peak temperature profile along the heat-affected zone (b).

III.3. Grain structure

III.3.1. Material prior to welding

The grain structure of the initial plates in the normal plane, observed by optical microscopy, is shown in Figure III.9.

It can be observed that the grain structure is highly heterogeneous in the vicinity of the surfaces and sides of the plate. This may be due to heterogeneities in the deformation path (rate and mode) experienced during the extrusion process. In the core of the plate, the grain structure consists of elongated flat grains ($\sim 10 \times 100 \mu\text{m}^2$) as displayed in Figure III.9. Numerous subgrains can also be observed in the inner part of the plate, typical of a dislocation subgrain structure obtained after hot deformation processing.

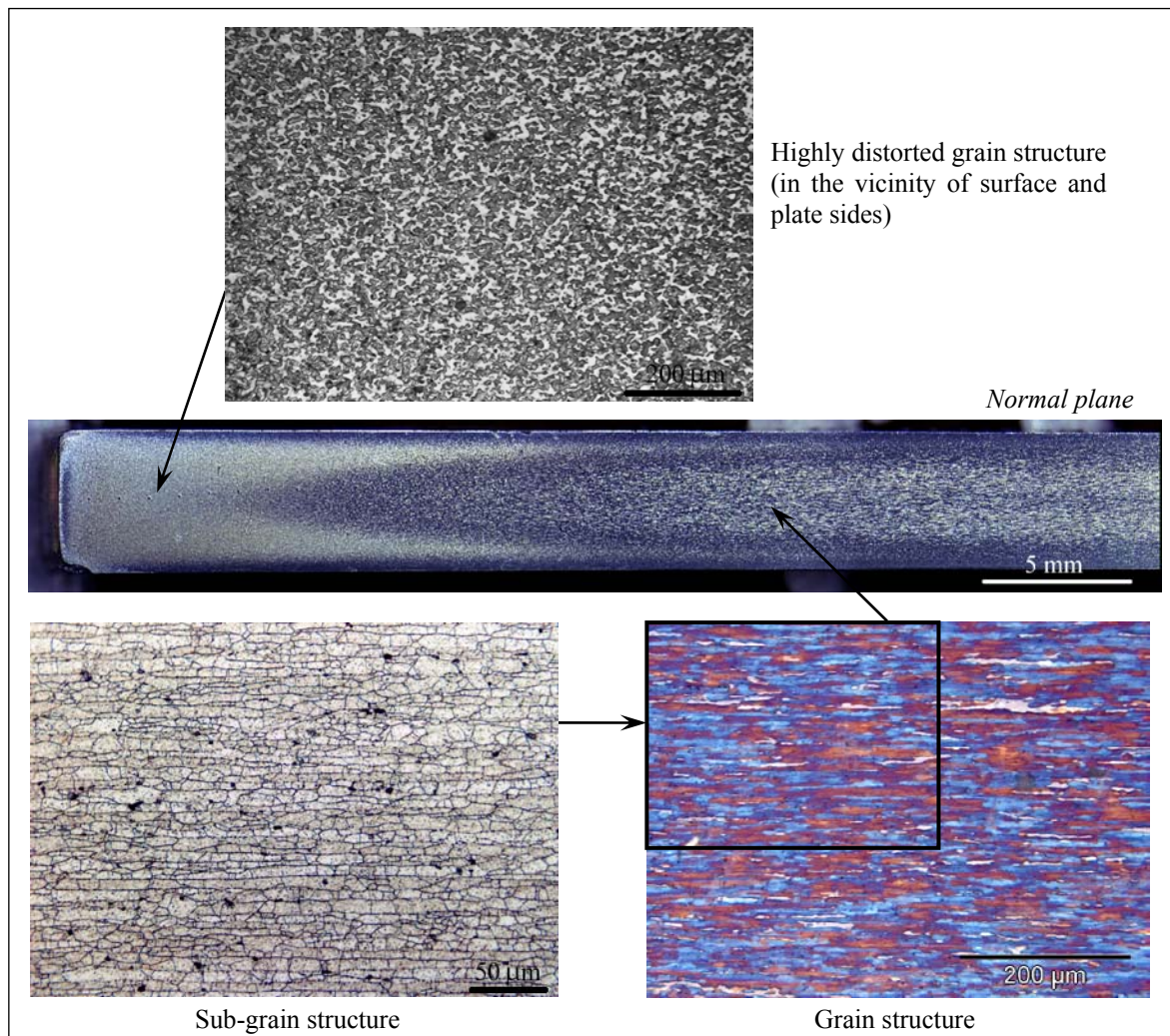


Figure III.9: Grain structure of initial plates in the normal plane observed by optical microscopy.

Sørensen [Sørensen, 1997] studied in detail the grain morphology of 7108 alloy in the as-extruded 5mm thick sheet state. He also observed heterogeneity in the grain structure:

- In the centre part of the plate, grains have a pancake-like shape; moreover the alloy 7108 has a non-recrystallised grain structure after extrusion and also after subsequent solution heat treatment (due to the high Zr-content – ~0.15wt%).
- Close to the surface, the grain structure was observed to be more fragmented; he explained this as a recrystallised grain layer formed at the surface.

In the normal plane, recrystallised grains can give rise to the distorted morphology observed close to the surface and plate sides.

III.3.2. Grain structure after welding

Plates were welded side to side, without specific preparation: neither the surface nor the sides have been removed, no special finishing. Figure III.10 shows that the initial grain morphology has been retained after welding. It can be observed that the side of the plate has been completely included in the fusion zone during welding. We will see in the following that the part of the heat-affected zone of special interest in this study (zone of partial dissolution) is located more than 10 mm away from the fusion boundary. Thus, the grain structure can be considered as homogeneous: only the non-recrystallised zone will be investigated.



Figure III.10: Optical micrograph of the welded material, observed in the normal plane.

Figure III.11 shows the grain structure close to the fusion boundary. The formation of a pool of molten metal directly below the heat source is inherent to the welding process. This pool is a mixture of both the filler metal and molten base material. The resulting microstructure is governed by solidification processes [Grong, 1996]. Columnar grains develop from the partly melted base material which acts as seed crystals. Moreover an equiaxed zone may develop in the centre of the casting if the conditions for nucleation of new grains are favourable. This is exactly what is observed in the weld pool in Figure III.11.

The fusion boundary consists of a band of recrystallised grains (see Figure III.11) where grain boundary liquation occurs during welding. This liquation phenomenon has been the subject of several microstructural investigations [Hepples, 1992; Cordier, 1977] due to the associated embrittlement phenomena [Bjørneklett, 1996; Lu, 1996]. This interfacial region is commonly known as the "white zone" due to its behaviour when etched by nitric acid [Cordier, 1977].

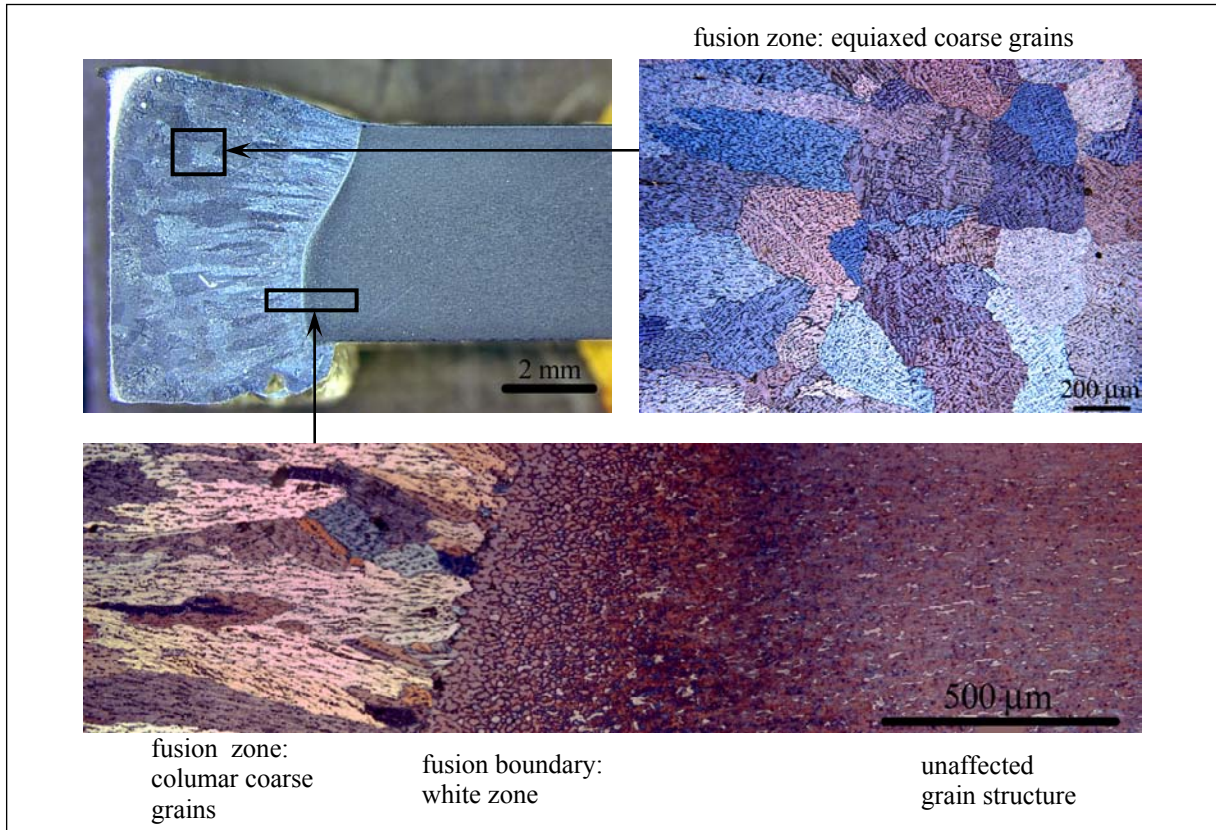


Figure III.11: Grain structure in the weld nugget and adjacent area.

III.4. Effect of welding on the precipitation microstructure

III.4.1. Microhardness profiles

Figure III.12 displays the microhardness profiles just after welding along the heat-affected zone of T4, T6 and T7 welds. Samples have been prepared taking care to minimize the time spent by the samples at room temperature in order to limit the precipitation of GP zones (this preparation sequence is given in Figure III.12 for each sample).

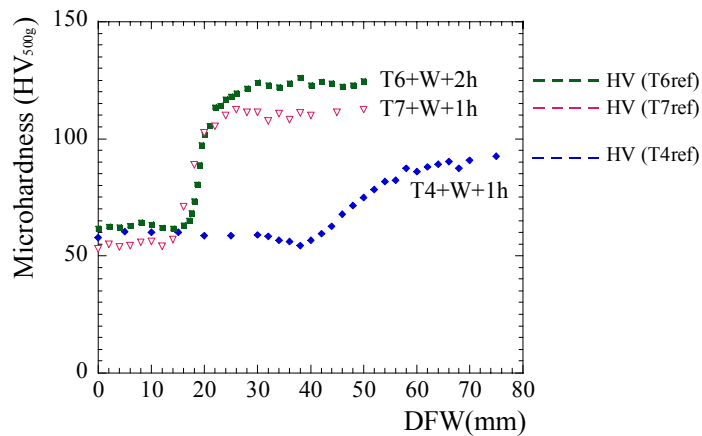


Figure III.12: Microhardness profiles along the heat-affected zone just after welding for the three initial states: T4, T6 and T7. (DFW=Distance from the fusion boundary).

As mentioned above (see III.1.3.1. Mechanical properties), the welding process results in a softening of the material evidenced here by hardness measurements.

The heat-affected zone can be divided into three parts:

- Far from the fusion zone (called III in the following): the unaffected base material characterised by a hardness typical of the T4, T6 and T7 tempers. As expected, the T6 state possesses the highest hardness level.
- Close to the fusion zone (I): a region where the hardness level is low, constant and equivalent for the three tempers. The extent of this zone depends on the initial state, from the narrowest one to the widest one: $T7 < T6 < T4$.
- Between (I) and (III): a transition zone (II) characterised by a hardness drop. This zone is particularly steep in the case of the T6 and T7 tempers, T4 presenting a wider transition zone.

In age-hardenable alloys, the hardness level is determined by strengthening precipitate characteristics like size and volume fraction. Consequently, we will now focus on the description of the precipitation microstructure to explain the hardness changes during welding.

III.4.2. Results of SAXS investigation

The results of SAXS investigation on the three welded tempers: T4, T6 and T7 are displayed in Figure III.13. The nature of the three zones revealed by microhardness can then be clarified:

- Zone (I) corresponds to a completely reverted zone where only GP zones are present. These have been formed either during the cooling stage of the welding process or during the preparation of the samples.
- Zone (II) is a transition zone where dissolution of the precipitates initially present is only partial.
- Zone (III) is the unaffected region where the microstructure remained stable during the welding process.

Zones (I) and (II) constitute the so-called heat-affected zone (HAZ), i.e. the region of the material where the precipitation state is affected by the thermal history of welding. Table III.2 presents some characteristic distances of this heat-affected zone.

	T4	T6	T7
HAZ extent	70 mm	30 mm	25 mm
Extent of Zone (I)	30 mm	17.5 mm	14.5 mm
Extent Zone of (II)	40 mm	12.5 mm	10.5 mm
Extent of the coarsening zone	—	2.5 mm	5.5 mm

Table III.2: Characteristic distances of the heat-affected zone.

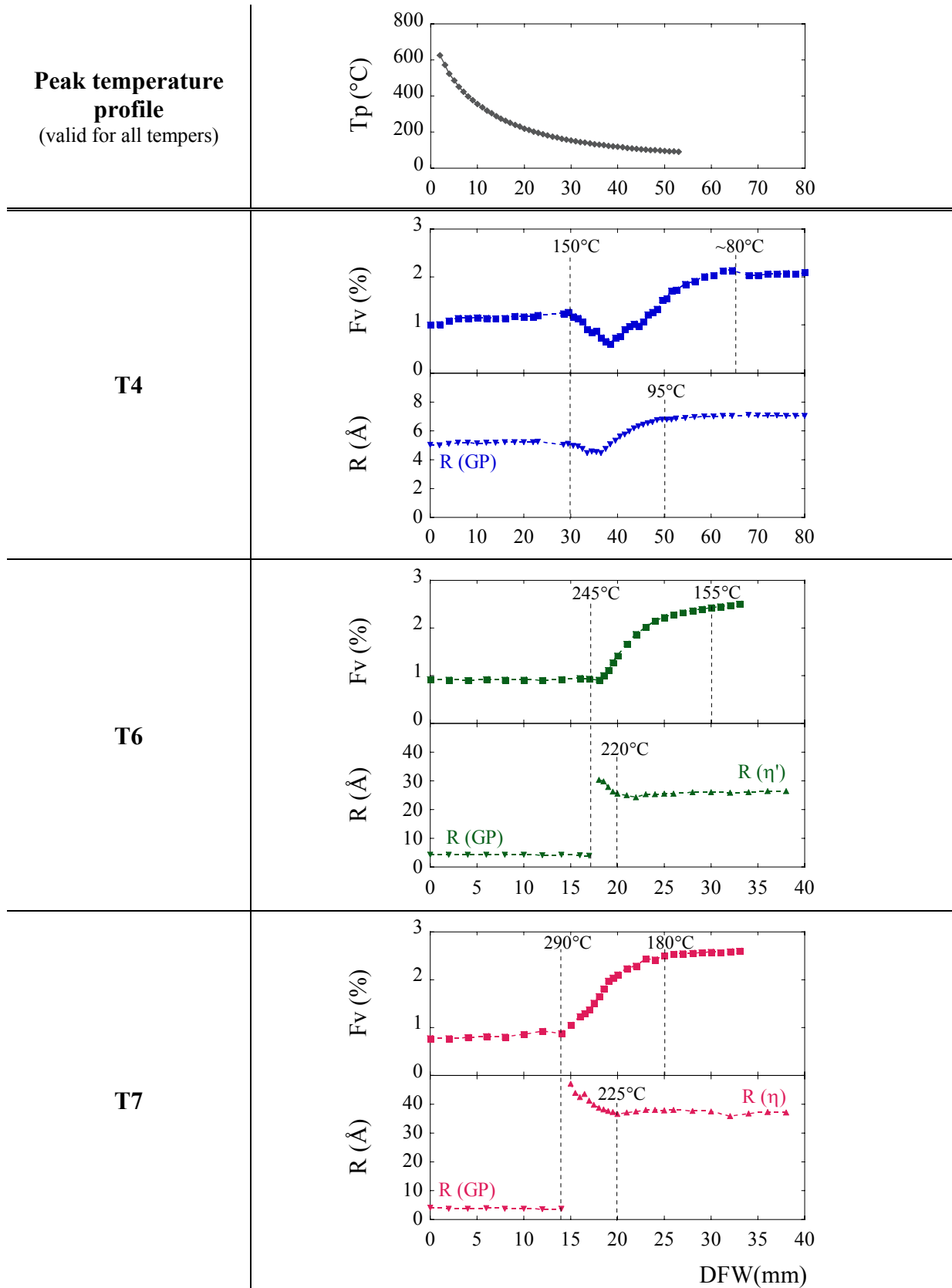


Figure III.13: Evolution of the volume fraction and particle size along the heat-affected zone. (DFW=Distance from the fusion boundary).

HAZ dimensions

The extent of the HAZ decreases with increasing stability of the precipitates:

$$\text{HAZ}_{T7} < \text{HAZ}_{T6} < \text{HAZ}_{T4}$$

This corresponds to the fact that metastable precipitates can be dissolved at lower temperatures (see Figure III.14), i.e. further from the fusion line.

The volume fraction drop is steeper in the T7 state than in the T6 state, which is itself steeper than in the T4 state, although its temperature range for dissolution is wider (180-290°C for T7 compared with 155-245°C for T6 and 80-150°C for T4). The explanation lies in the peak temperature profile which is very abrupt for high temperatures and becomes smooth for low temperatures (see Figure III.14). The dissolution temperature range for the T7 state is condensed in a very small section whereas for the T4 temper the dissolution temperature range extends along a large distance.

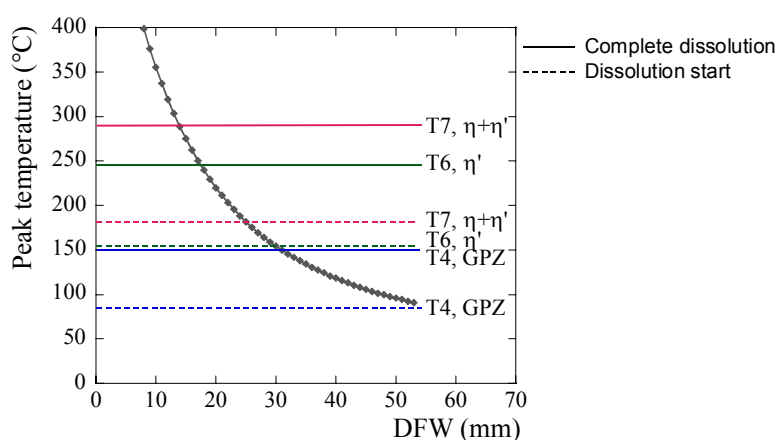


Figure III.14: Peak temperature ranges for dissolution of precipitates contained in T4, T6 and T7 materials during welding.

It should be noted that the extent of the transition zone is underestimated. In fact the precipitation of new GP zones during cooling or preparation of the samples masks the end of the volume fraction decrease, as schematised in Figure III.4. As a consequence the true boundary between partial and complete dissolution occurs for a somewhat higher peak temperature.

Coarsening of the T6 and T7 states

In contrast to the description of Ma and den Ouden [Ma, 1999] concerning the overageing zone (refer to III.1.3.4. Precipitation), who sustained that this zone is characterised by growth and coarsening of initially present particles, it can be seen that size changes do not affect the whole transition zone. In fact only around one half of zone (II) is characterised by an increase of the particle size (called coarsening) in the case of the T6 and T7 states, corresponding to the highest peak temperature region. This means that for relatively low temperatures, dissolution may occur with relatively small mean size variations. We will come back later to the explanation of this phenomenon.

Furthermore the T7 temper appears to be more affected by coarsening than the T6 material. This is probably due to the fact that η' -particles are metastable precipitates. When the temperature is raised, η' -precipitates need to transform to the stable η -phase before they can

coarsen to larger sizes. Since this transformation takes time, the overall size increase is smaller as compared to the T7 state, which already contains stable η -precipitates. Since during welding the temperature input is very rapid, phase transformation is difficult, or even prohibited; coarsening occurs but in a smaller extent than in the case of η -particles.

T4 behaviour

The T4 weld does not present any coarsening behaviour; on the contrary, the size tends to decrease simultaneously with the volume fraction. This means that all particles dissolve, without favouring larger ones. An important feature of this temper lies in the fact that re-precipitation and pre-existing precipitation are of the same nature: GP zones. Moreover for coherency reasons, GP zones are not expected to coarsen easily. Thus the recovery of initial properties in terms of hardness or volume fraction is expected to be as fast in the transition zone as in the completely reverted zone. However, it can be seen in Figure III.13 that recovery is less important in the transition zone. The particular behaviour of this temper after welding will be re-visited in the next section III.5. Post-welding heat treatments.

III.4.3. TEM observations

Figure III.15 and Figure III.16 display the results of TEM investigations of the evolution of the precipitation microstructure in the T6 and T7 welds respectively.

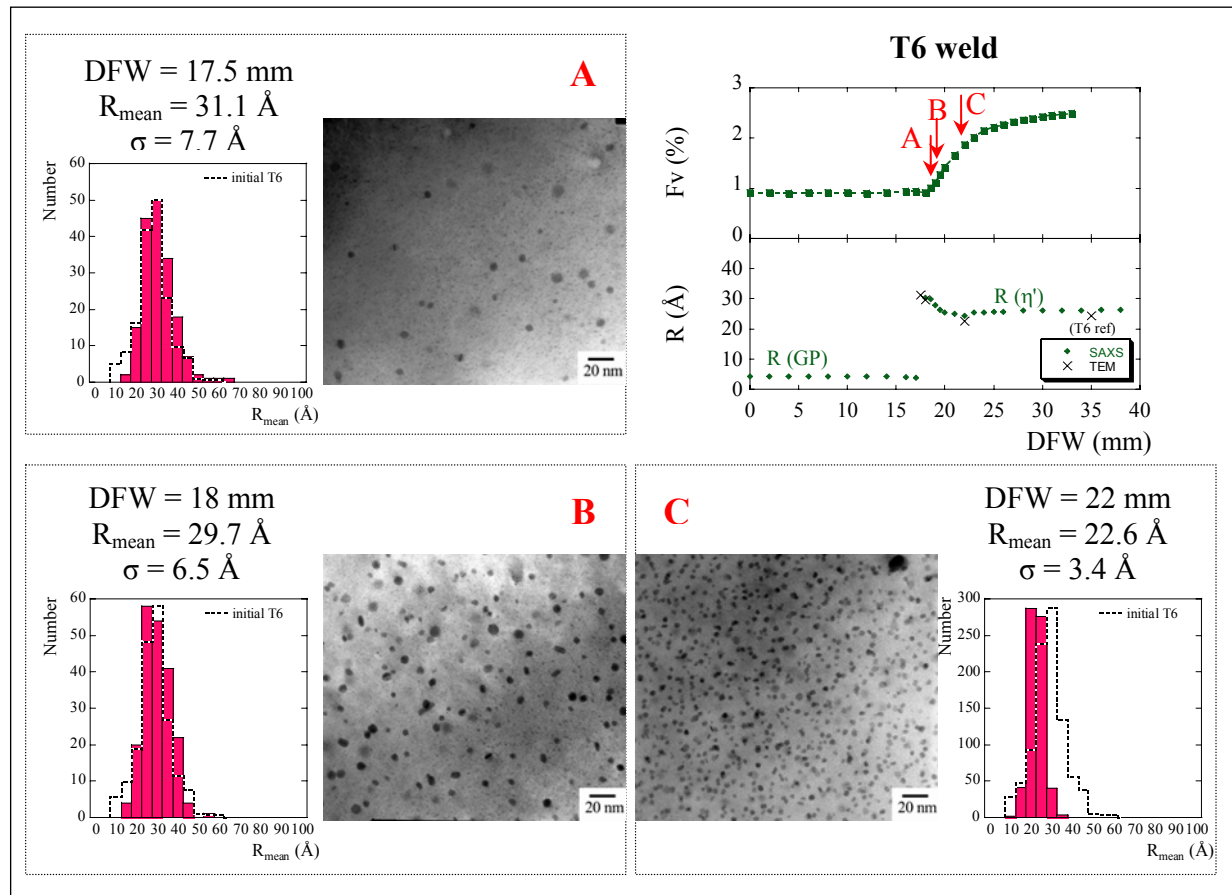


Figure III.15: Microstructural changes along the HAZ transition zone and corresponding particle distribution in a T6 weld. σ is the standard deviation.

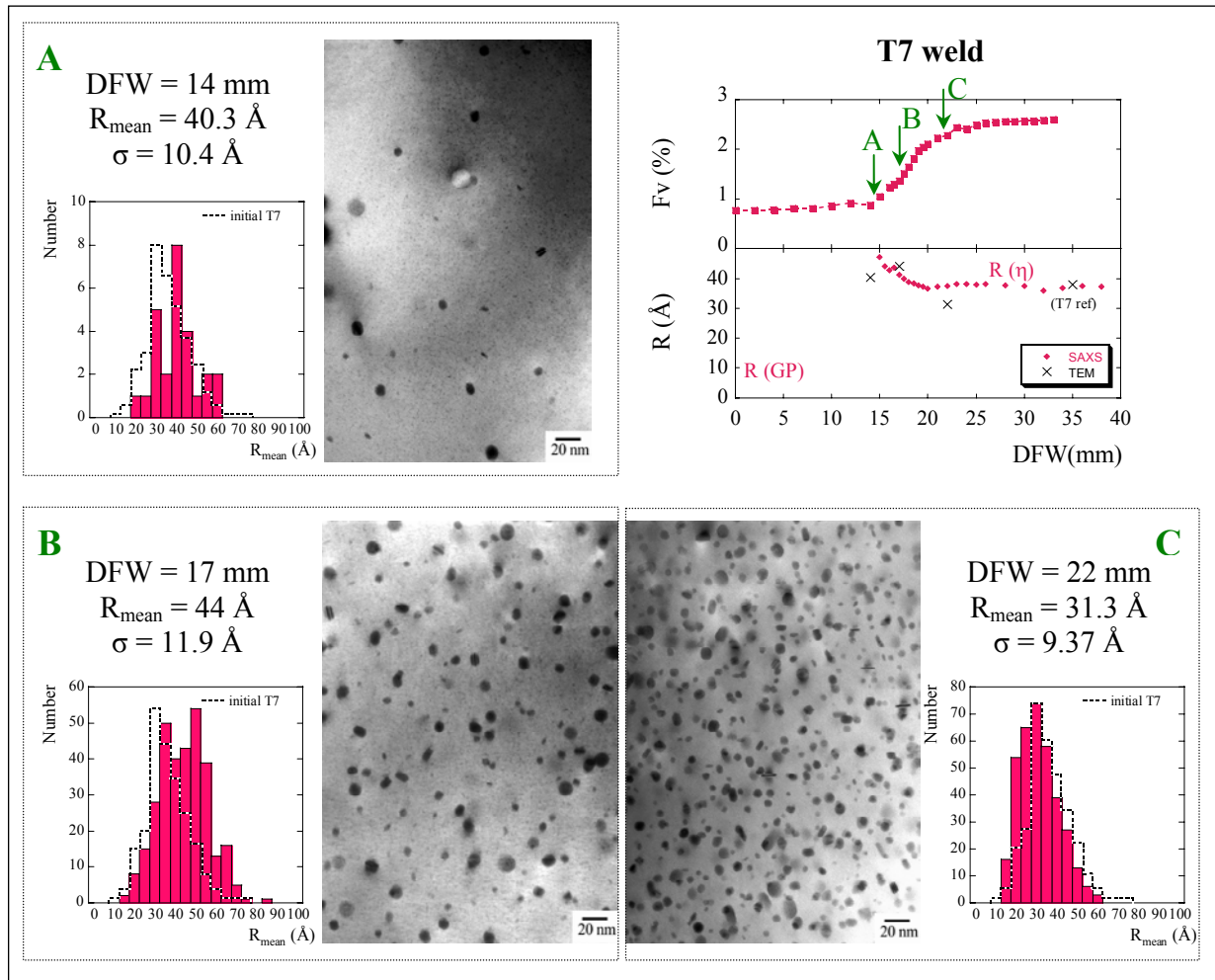


Figure III.16: Microstructural changes along the HAZ transition zone and corresponding particle distribution in a T7 weld. σ is the standard deviation.

Despite the non-constant foil thickness between the different micrographs which can be misleading, it is clear, at least qualitatively, that the precipitate volume fraction is decreasing as we move closer to the fusion line. The correlation between SAXS and TEM radius estimations is satisfying in the case of the T7 weld, and quite remarkable in the case of the T6 weld, as shown in the *radius versus distance from the fusion boundary* plot in Figure III.16 and Figure III.15. Moreover, as already mentioned in the SAXS investigation, coarsening is not observed in the whole transition zone but only in the part submitted to higher peak temperatures.

TEM image analysis gives information concerning the particle distribution. It can be seen that in the part where no size increase is observed (see T7–22mm and T6–22mm), the whole distribution is characterised by dissolution, even coarse particles. In fact no enlargement of the distribution is noticed in comparison with the initial T6 or T7 distribution (refer to Figure II.31). In other words all particles have dissolved with equivalent dissolution rates without favouring coarse particles. However, at points where coarsening has been observed (see T7–17mm, T6–18mm and T6–17.5mm), the particle distribution is wider than the initial one and extends to larger particle sizes (90 Å for T7–17mm and 70 Å for T6–17.5mm).

Moreover no sign of new small particles has been observed, that is to say that nucleation is not expected to be a significant process during welding. However when looking carefully at

TEM micrographs taken where substantial dissolution occurred like in the T7–14mm and T6–17.5mm specimens, very small particles can be observed, as shown in Figure III.17. These small particles are believed to be GP zones grown during natural ageing.

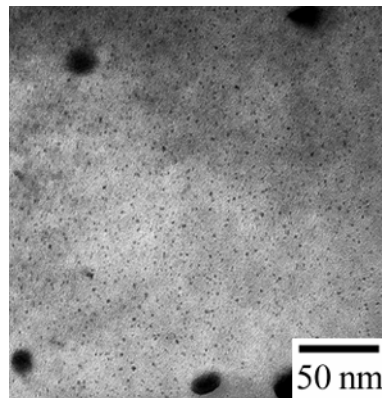


Figure III.17: GP zones observed as small dots in TEM micrographs of the T7–14mm sample.

The evolution of precipitates on grain boundaries has also been investigated, and representative examples are shown in Figure III.18. It can be seen that no significant changes of the precipitation on grain boundaries is observed in the transition zone, even if some dissolution appears for the sample 14mm from the fusion boundary. However, the micrographs presented here correspond to points of the heat-affected zone located in the transition zone, where peak temperatures are of the order of 250-300°C. Grain boundary particles are coarse η -precipitates, therefore they are very stable, much more so than the strengthening precipitates. Consequently these particles are expected to dissolve at higher peak temperatures, thus their evolution should occur in zone (I). One sample located at 5mm from the fusion boundary was examined and precipitation on grain boundaries was no longer observed.

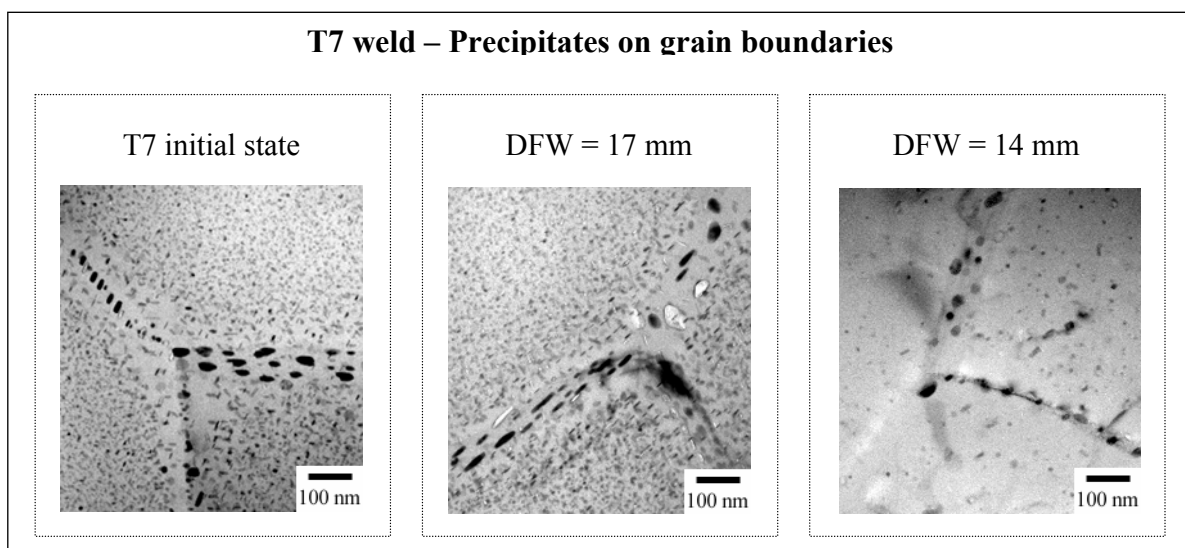


Figure III.18: Grain boundary microstructure: evolution of precipitates along the heat-affected zone of a T7 weld.

III.4.4. DSC investigation

In order to identify the nature of precipitates remaining after welding, and to clarify whether some phase transformation can occur during welding, a DSC scan of a sample taken in the transition zone of a T6 weld has been carried out. It is actually in the T6 material that a phase transformation of the precipitates is the most likely to occur. Moreover this is expected to occur in the high peak temperature range. The sample was taken at 20mm from the fusion boundary, i.e. in the middle of the transition zone. This appears to be a good compromise between a strong DSC signal (reasonable volume fraction) and a reasonable probability for phase transformation. A high heating rate (100°C/min) has been chosen to limit reactions during the scan.

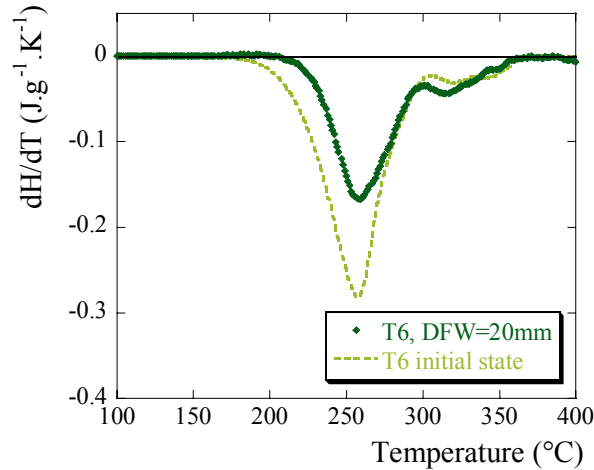


Figure III.19: DSC scan of a T6 sample (DFW=20mm) just after welding, to compare with the T6 initial state.

Figure III.19 compares the DSC response of this T6 sample (DFW=20mm), performed just after welding and the T6 initial state. As expected the intensity is smaller after welding due to the lower volume fraction. As the area under the curve can be related to the volume fraction (see equation II.8), the ratio of areas can be calculated and compared to volume fraction results obtained by SAXS. This is done in Table III.3. The agreement between both techniques is relatively good.

	DSC	SAXS
T6, DFW=20mm	$\Delta Hr_1 = -9.1 \text{ J.g}^{-1}$	$Fv_1 = 1.4 \%$
T6, initial state	$\Delta Hr_0 = -14.5 \text{ J.g}^{-1}$	$Fv_0 = 2.5 \%$
Ratio	0.63	0.56

Table III.3: Comparison of SAXS and DSC results in terms of remaining volume fraction. ΔHr is the integrated area of the DSC signal between 100°C and 400°C. Ratio refers respectively to the ratio of $\Delta Hr_1 / \Delta Hr_0$ for DSC and Fv_1 / Fv_0 for SAXS.

The main information from DSC lies in the fact that the global shape and temperature ranges are identical. This means that the nature of the precipitates of the two samples is the same, i.e. mainly η' -phase. A small second peak can be observed which can be correlated with η -phase dissolution. This peak is more pronounced after welding, indicating that some transformation can occur but to a very small extent.

III.5. Post-welding heat treatments

The capacity of the different tempers of 7108.50 alloy to recover good mechanical properties after welding have been investigated. Both the response to natural ageing and artificial ageing based on T6 and T7 tempers subsequent to welding has been studied.

III.5.1. Natural ageing

Where solute has been rejected in solid solution after dissolution of pre-existing precipitates, GP zones are expected to nucleate and grow at room temperature. As GP zones have a good hardening potential, hardness properties can be naturally recovered at room temperature.

III.5.1.1. Microhardness evolution

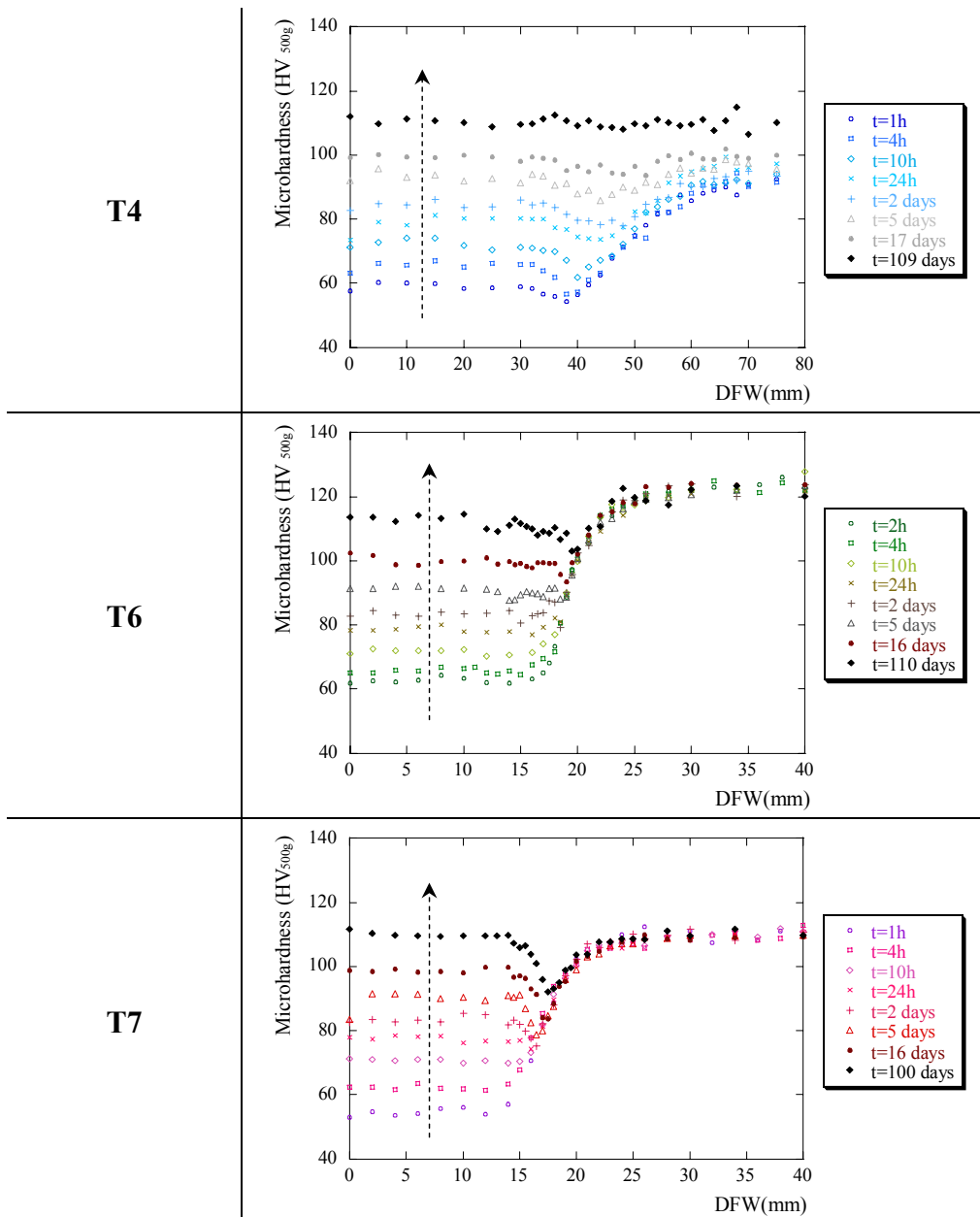


Figure III.20: Microhardness evolution during natural ageing subsequent to welding of T4, T6 and T7 materials. The arrow indicates increasing room temperature ageing times.

The microhardness evolution with time at room temperature is presented in Figure III.20 for the three different initial states: T4, T6 and T7.

Recovery of hardness by natural ageing is very efficient in zone (I), corresponding to the complete dissolution region. The hardness increase of the three initial states is exactly the same in this zone (see Figure III.21.a), confirming that the microstructure in the fully reverted zone is not dependent on the initial temper.

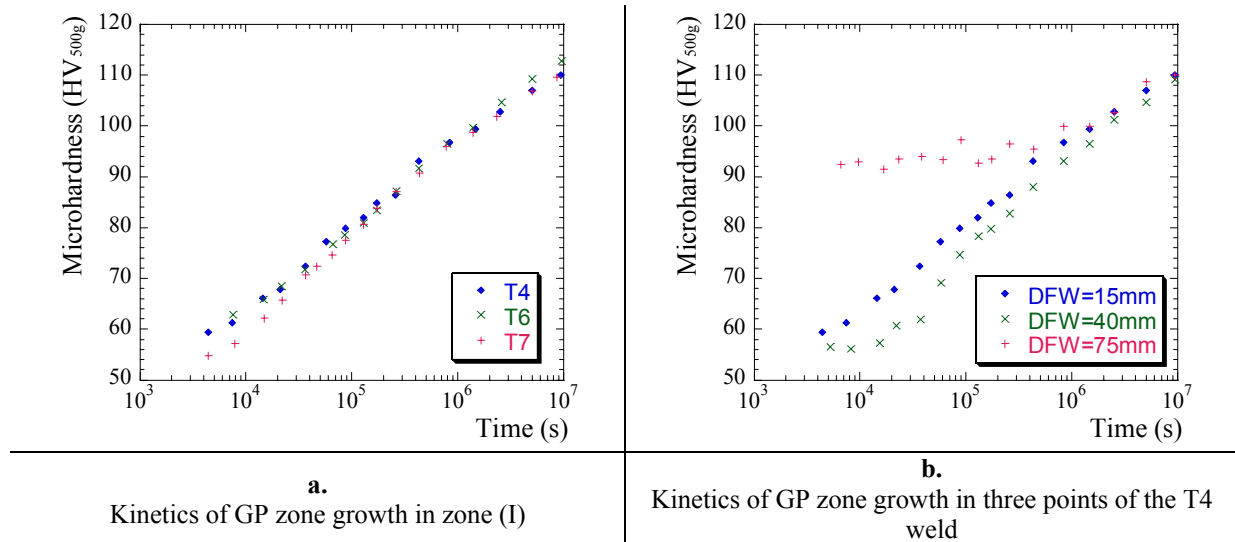


Figure III.21: Kinetics of GP zones growth. Comparison of the three tempers in zone (I) (a) and in different points of the heat-affected zone of the T4 weld (b).

However in the transition zone, some trace of welding history remains as observed for the T6 and T7 materials as a V-shaped curve. A critical solute content is necessary to nucleate new GP zones. This leads to a softened region located at a distance of the order of 10mm from the fusion zone.

In the case of the T4 material, this influence tends to disappear with time (see Figure III.21.b). Far from the fusion boundary, the hardness increase is slowed down due to the low solute content available in the solid solution. At the other end of the spectrum, the hardness increases very rapidly in zone (I) due to the high supersaturation. In the transition zone (DFW~40mm), an incubation time for precipitation can be observed. Finally, for long times ($t \geq 17$ days) the hardness properties become homogeneous along the whole heat-affected zone.

III.5.1.2. SAXS characterisation

The quantitative data on the precipitation microstructure will help us to further interpret these results. Figure III.22 shows the volume fraction and particle size evolution along the heat affected zone of the T4, T6 and T7 welds during natural ageing as measured by SAXS.

Behaviour in zone (I)

As expected, the hardness increase in zone (I) is attributed to nucleation and growth of new GP zones. Both increase together and no separate nucleation and growth regimes can be distinguished. The hardening potential of GP zones is increasing with size and volume fraction. In fact, full precipitate dissolution during the high temperature stage of welding

enables efficient GP zone formation. Some GP zones may nucleate during the cooling part of the welding process but the large development of this precipitation occurs during the room temperature storage of the welded structures. An interesting point in zone (I) is that the precipitation kinetics does not depend on the distance from the fusion boundary. Thus, in this zone one can expect that the large differences in thermal history do not result in significant changes of the vacancy concentration for instance.

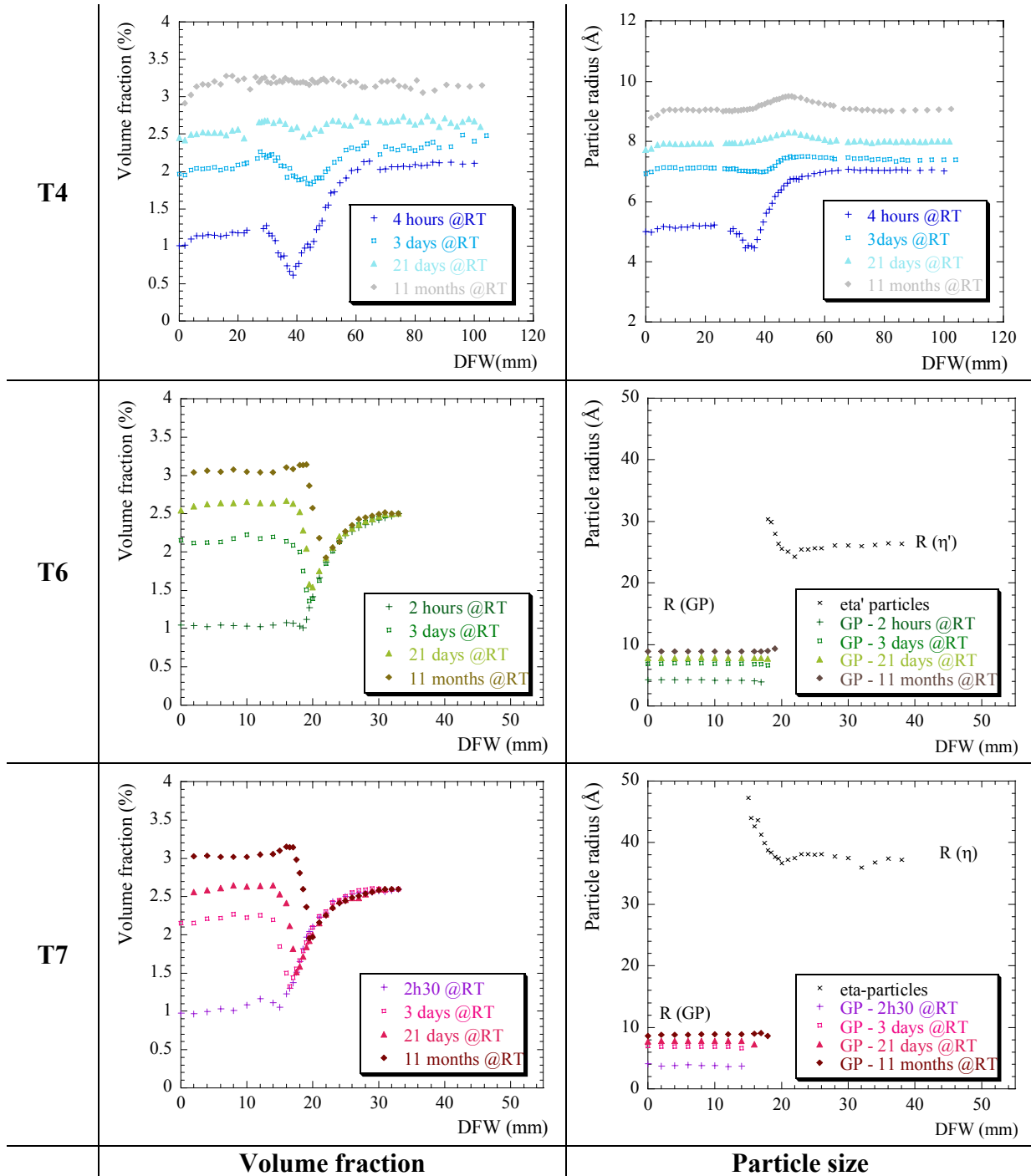


Figure III.22: Volume fraction and particle size evolution of T4, T6 and T7 materials stored at room temperature during few hours up to several months after welding.

T6 and T7 behaviour in the transition zone

The incomplete dissolution of particles in the transition zone means that less solute in solid solution is available for precipitation of GP zones. Therefore their nucleation rate is lower in this region as compared to the completely reverted zone. It seems that the volume fraction of remaining particles is the key factor influencing the formation rate of GP zones and not their size. Actually coarsening is not very detrimental for the formation of GP zones as coarsening occurs in a region characterised by a low volume fraction, thus a high supersaturation. Moreover the T6 and T7 welded materials, characterised by a similar volume fraction with different particle sizes, show the same behaviour, i.e. the same kinetics of GP zone formation.

When the volume fraction of remaining precipitates is $\sim 2\%$, GP zone formation is completely suppressed. The corresponding solid solution is thus the critical value below which the driving force is too small to enable nucleation of GP zones. This dependence of the GP zone formation rate on the supersaturation (and thus on volume fraction of remaining precipitates) is very abrupt, as seen in Figure III.22.

Discussion of T4 behaviour

In the T4 material, the variations of volume fraction and particle size in the heat-affected zone tend to disappear after 3 days at room temperature, when newly formed GP zones reach the characteristics of the pre-existing ones. After 3 days, zone (I) has the same precipitation state as the initial material. In the transition zone, the nucleation kinetics and growth of GP zones are initially slower, but after long times all differences disappear. We will discuss in the next paragraph the possible reasons for increasing the incubation time for GP zone formation in the transition zone. Finally, in the region of the transition zone where a small amount of dissolution occurred (beginning of the transition zone), larger particles are formed after long natural ageing times as observed on the *R versus DFW* plot of the T4 weld. Actually in this region partial dissolution has resulted in a too small solute release to the solid solution to promote new GP zone nucleation, thus the extra solute participate in the growth of the undissolved particles and the resulting precipitate size is larger.

In the case of the T4 initial state, two points still need to be clarified:

- Why can we observe a drop in volume fraction between zone (I) and (II)? This means that towards the end of the dissolution zone, new GP zones have difficulties to form upon cooling from the heat input.
- Why does the same zone experiences an incubation time upon natural ageing and finally reaches the same values of particle size and volume fraction after long natural ageing?

Different hypothesis can be formulated:

- 1) Some coarse particles may form during the high temperature stage of welding which may remove solute elements from the solid solution, which in turn will no longer be available for GP zone formation during natural ageing. This assumption is not very plausible as, in this case, the GP zone formation potential would be lowered even for long times.
- 2) The nucleation rate during natural ageing may be lowered due to different thermal histories. During the cooling stage of welding, each point of the heat-affected zone undergoes a different thermal history, which may lead to different precipitation kinetics, and thus to a different microstructure in the as-welded state. However as seen

in the thermal profiles (refer to Figure III.8.a), the low temperature part ($T < 120^{\circ}\text{C}$ corresponding to the temperature range for GP zone reversion) is identical for all points of the heat-affected zone. This explanation would lead to a continuous decrease of the GP zone formation potential along the heat-affected zone, including zone (I). It can be observed that in zone (I) GP zone volume fraction is constant.

- 3) GP zone kinetics is greatly influenced by the vacancy concentration [Asano, 1976]. If the vacancy concentration is lowered, then the GP zone formation rate should be altered. As the vacancy concentration is influenced by both the solutionizing and the quenching conditions, it can be assumed that parameters like the peak temperature and the cooling rate may act on the vacancy concentration. The higher the peak temperature, the higher the vacancy concentration is expected to be. However, once again the GP zone characteristics would be expected to decrease gradually along the zone (I) and not only in the transition zone.
- 4) However another factor can affect the vacancy concentration: the presence and movement of dislocations during the welding process, which are known to be efficient vacancy sinks. Local yielding has been noticed by Myhr *et al.* [Myhr, 1998] in the transition zone of AA7108-T6 welds, which occurs during the cooling leg of the thermal cycle. This last explanation is checked below against TEM observations.

III.5.1.3. TEM observations

In this part we will focus on the TEM observations in different points along the heat-affected zone of the T4 welds. TEM is expected to give some insight into the microstructural features able to explain the particular behaviour observed in the transition zone of the T4 welds.

Figure III.23 illustrates the dislocation structure evolution along the heat-affected zone of a T4 weld. Zone (I) and unaffected material are characterised by a low, similar density of random dislocations located in the grain interiors. In contrast, the dislocation microstructure in the transition zone is completely different, showing very few random dislocations, but numerous dislocation pile-ups (see T4-40mm).

This observation tends to support the last assumption made to explain the kinetics of T4 recovery in the transition zone, i.e. dislocations act as vacancy sinks. Actually to form these sub-grain boundaries, dislocations should move through the grains and may then decrease the vacancy concentration.

In a more advanced study it would be necessary to prove the validity of the hypothesis but this assumption appears to be the most reliable. One interesting consequence of this behaviour is that the effect of vacancies on the GP zone formation appears to be limited to the very first stage of the GP zone formation: at long times the GP zone microstructure is independent on the initial state.

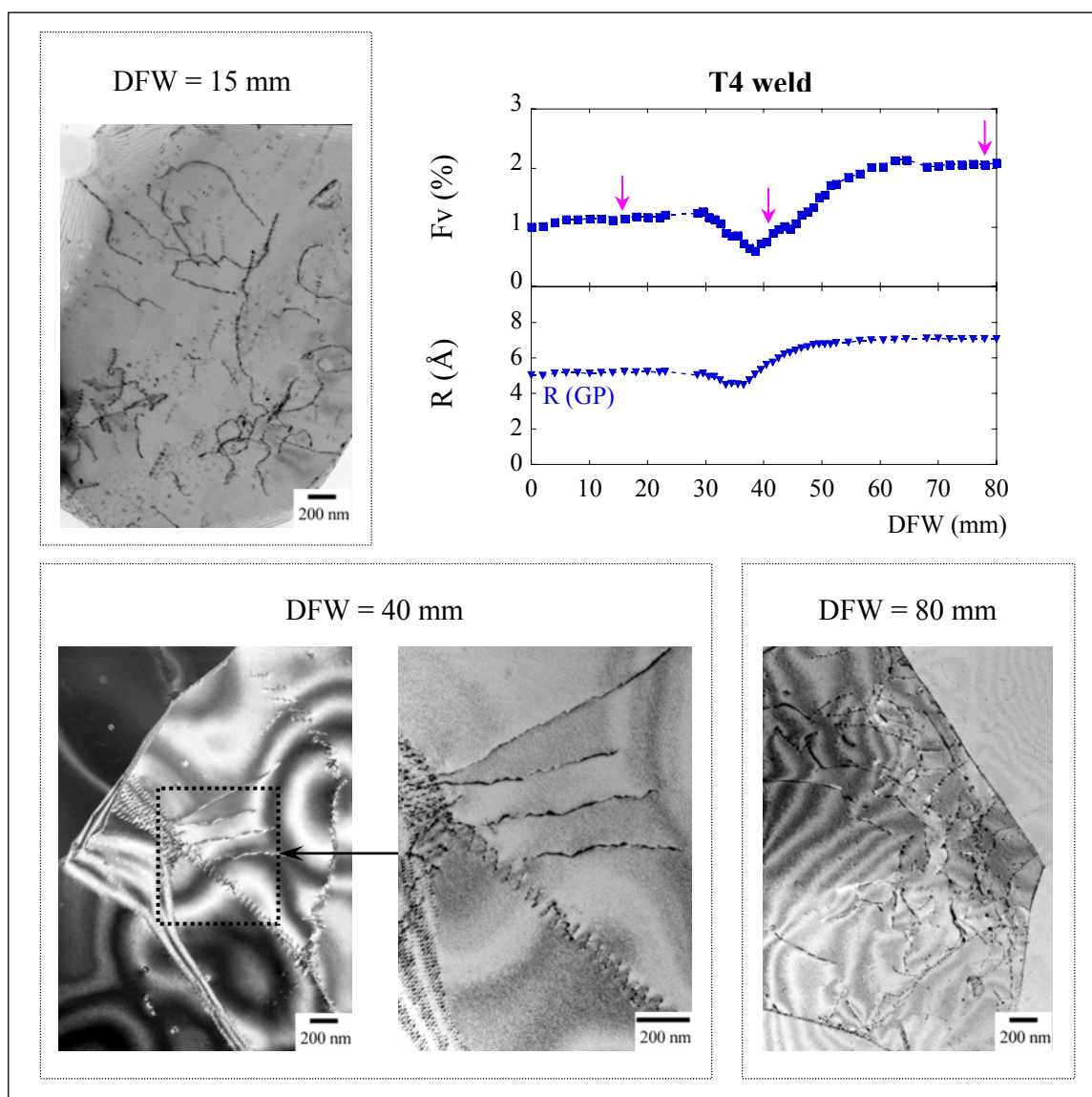


Figure III.23: Dislocation structure within the heat-affected zone of a T4 weld.

III.5.2. Artificial ageing

For the three initial states, post-welding heat treatments based on the T6 and T7 tempers have been carried out after welding of T4, T6 and T7 materials. For example, the entire history of a so-called T6+W+T7 sample is:

- T6 temper,
- welding process,
- T7 heat treatment (except the solution treatment at 480°C).

We will now discriminate between the T4 temper and the two others (T6 and T7 tempers) due to its different potential for microhardness and microstructure recovery, as shown by natural ageing.

III.5.2.1. T6 or T7 initial states

Microhardness evolution

Figure III.24 shows the resulting hardness profile along the heat-affected zone after T6 or T7 heat treatments performed on the T6 or T7 welds.

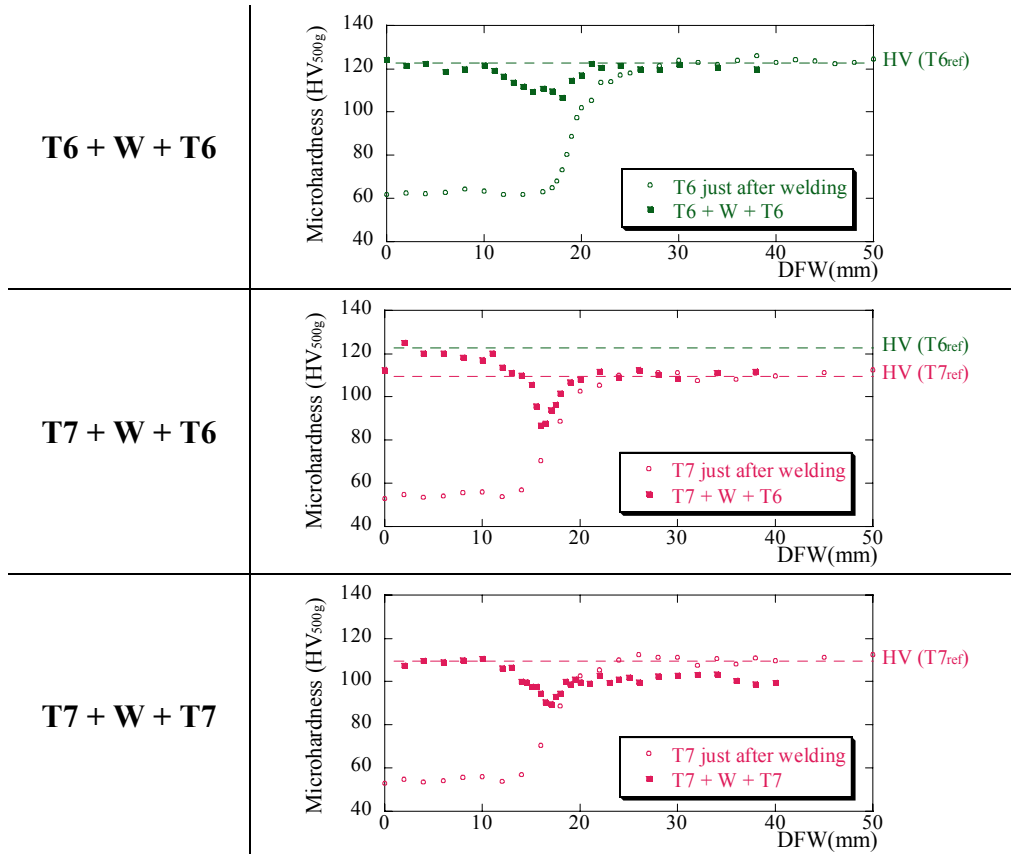


Figure III.24: Microhardness evolution after T6 or T7-type post-welding heat treatments on T6 or T7 welds.

One can see that the recovery of hardness typical for T6 or T7 tempers can be achieved in the fully reverted zone. In the region corresponding to the unaffected material (zone (III)), the hardness level remains constant when a T6 artificial ageing is carried out, whereas, when a T7 post-welding heat treatment is performed, a slight decrease of the hardness level is obtained (see T7 + W + T7). Finally, the transition zone is characterised by a hardness drop. Moreover this loss of mechanical properties is more marked in the case of initial T7 temper than for the T6 initial state.

SAXS investigation

Figure III.25 shows the evolution of the precipitation microstructure after the T6 or T7 post-welding heat treatments.

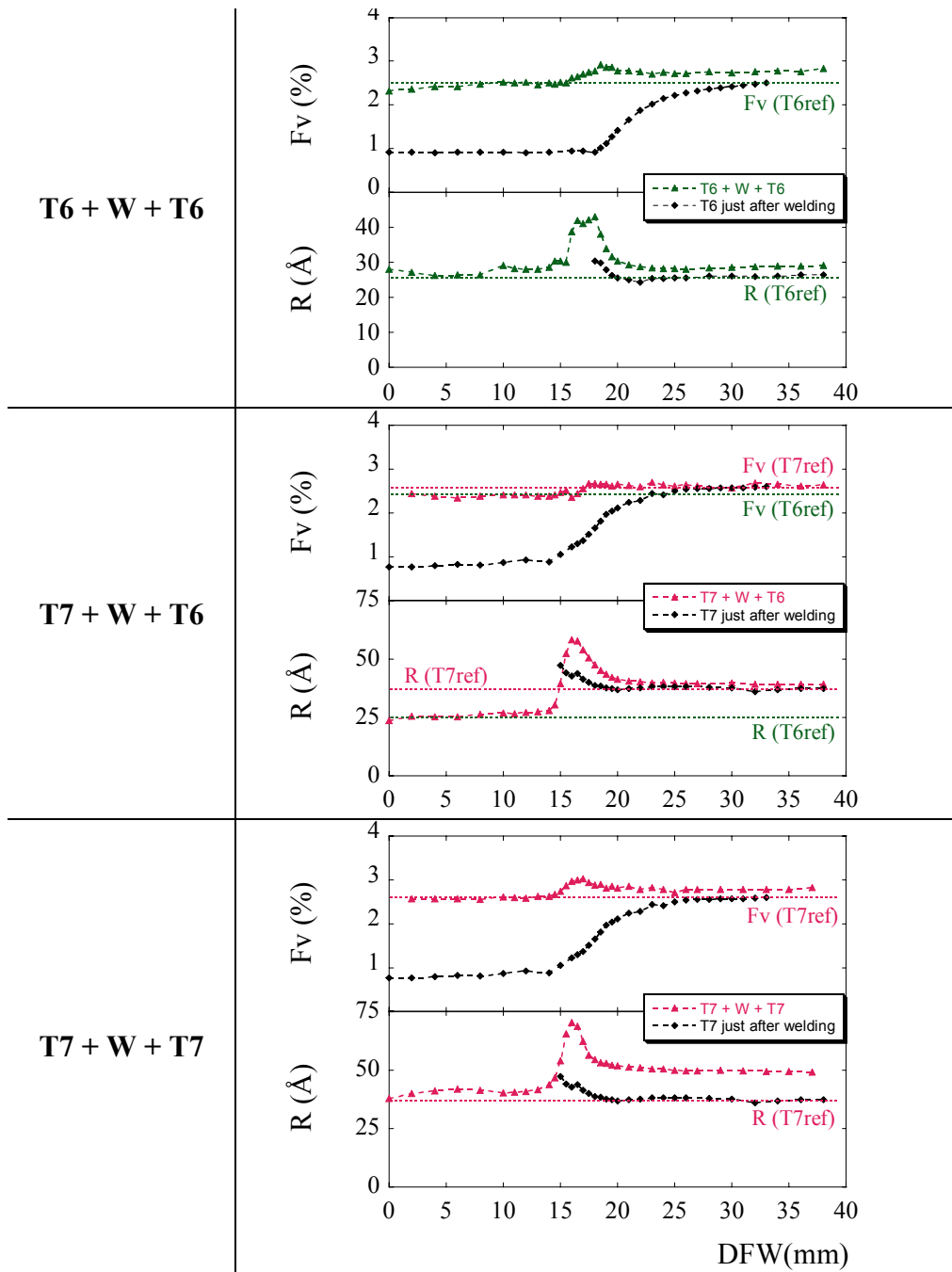


Figure III.25: Volume fraction and particle size along the heat-affected zone of T6 and T7 welds submitted to T6 or T7-type post-welding heat treatments.

It can be observed that for zone (I), corresponding to the completely reverted zone, the final microstructure is identical to that of the same heat treatment performed after a solution treatment and quench. Zone (III), corresponding to the unaffected material, is subjected to overageing during the post-welding heat treatment. This overageing is very small for T6+W+T6: the complementary treatment is not sufficient to induce a significant hardness loss, probably due to the flatness of the hardening curve (*hardness versus time*) close to the peak strength. It is negligible for the T7+W+T6 sample, as expected. It is highest in the case of the T7+W+T7 sample and explains the above hardness loss.

Concerning the transition zone, the behaviour of the region affected only by dissolution is similar to that of zone (III) and recovers good mechanical properties. However, the region affected by both dissolution and coarsening during the welding heat treatment is characterised by the presence of coarse particles. This results in a decrease of the mechanical properties, as has been noticed in Figure III.24. Furthermore, the behaviour of the initial T7 temper is more detrimental than the initial T6 state (larger maximum size in the HAZ). Actually, as observed earlier, the T7 welds are subjected to a larger extent of coarsening than the T6 welds. This phenomenon follows its course during subsequent artificial ageing.

Finally the extent of loss of mechanical properties of the T6 and T7 welds after post-welding heat treatments does not correspond to the entire transition zone but to the region submitted to coarsening during welding. The phenomenon is amplified during subsequent heat treatment resulting in a loss of hardness in this region, whereas in the region only affected by dissolution (no coarsening), mechanical properties can be recovered.

TEM observations

Figure III.26 shows TEM micrographs taken in the heat-affected zone of a T6 weld submitted to a subsequent T6 heat treatment.

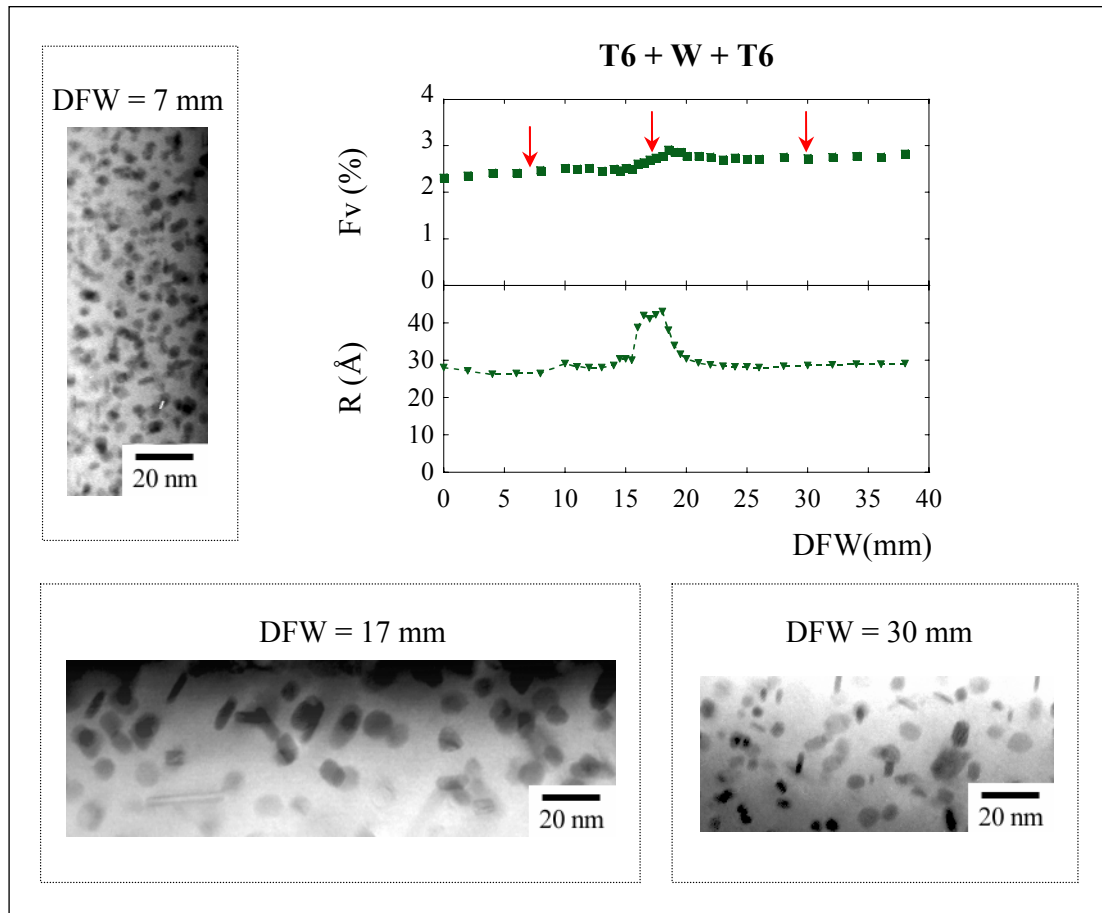


Figure III.26: TEM observations along the heat-affected of a T6+W+T6 sample.

It can be seen that the precipitate size at the point located 17mm from the fusion boundary is markedly coarser than in the rest of the material. This is in good agreement with the above SAXS measurements.

III.5.2.2. T4 initial state

Since it was observed that the T4 welds have a good capacity to precipitate GP zones as compared to T6 and T7 welds in the whole heat-affected zone, they are expected to have a better potential to erase the welding history after a post-welding heat treatment. Both T6 and T7 tempers have been carried out on T4 welds. The influence of storage time at room temperature before subsequent artificial ageing has also been studied, since it is known that a well-developed GP zone structure is favourable for the nucleation during artificial ageing. Moreover, it has been found that time is required to achieve a homogeneous microstructure at room temperature.

Microhardness evolution

Microhardness results are presented in Figure III.27.

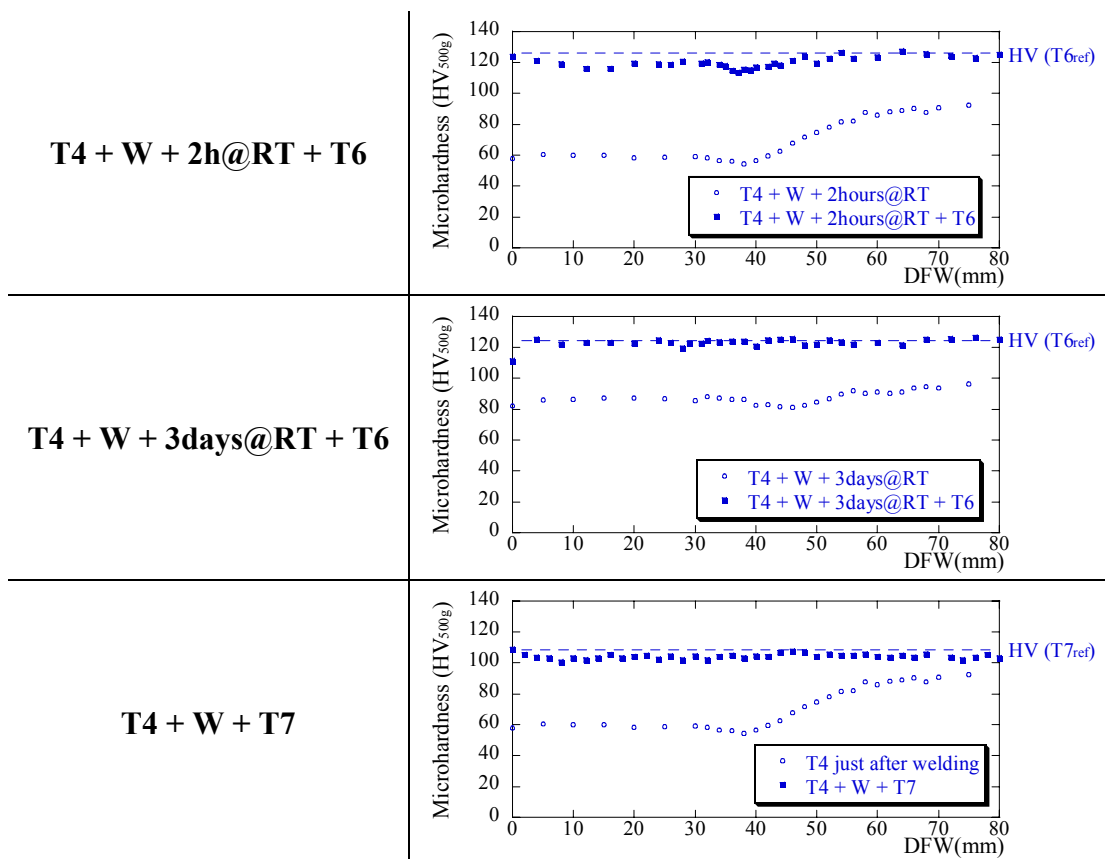


Figure III.27: Microhardness measurements after T6 or T7-type post-welding heat treatments performed on T4 welds. The influence of natural ageing after welding has also been investigated.

It can be seen that if sufficient time at room temperature is allowed, the hardness of a T6 or T7 material can be obtained in the whole heat-affected zone by artificial ageing of a T4 weld. However if the T6 treatment is carried out immediately after welding, recovery of T6 hardness is not complete in the heat-affected zone. One should note that the T7 temper is less sensitive to storage time at room temperature.

SAXS investigation

Figure III.28 shows corresponding volume fraction and particle size as measured by SAXS.

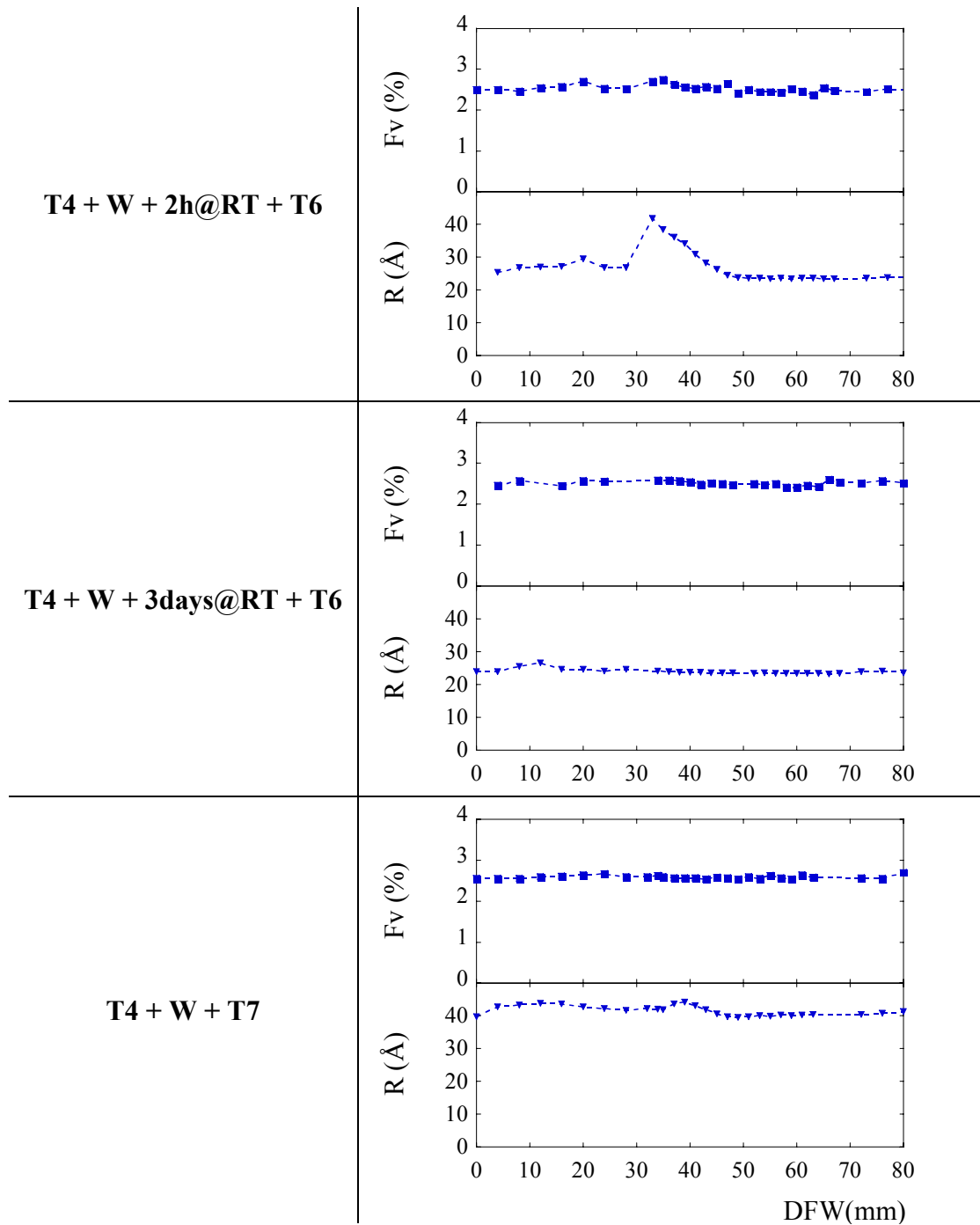


Figure III.28: Effect of post-welding heat treatments on volume fraction and particle size of T4 welds.

The homogeneity of hardness observed earlier can be correlated to a homogeneous microstructure obtained after post-welding heat treatment of a naturally aged T4 weld.

When storage time at room temperature is not long enough, coarser particles can be observed in the transition zone. We have already seen that in this region a larger incubation time is necessary to form new GP zones. Thus when the T6 post-welding heat treatment is carried out immediately after welding, fewer GP zones are present to serve as nucleation sites for η' -

particles, resulting in a smaller precipitate density and larger final size of particles with a lower strengthening effect. In the case of the T7 temper, the lower sensitivity is due to the fact that the microstructure is the result of overageing, which is less sensitive to the nucleation conditions.

III.6. Summary and open questions

Figure III.29 is a schematic representation of the precipitate evolution in the heat-affected zone of T4, T6 or T7 welds, as observed in the previous study.

Moreover it has been seen that it is possible to recover a homogeneous microstructure by using post-welding heat treatments under relevant conditions of initial state and storage time.

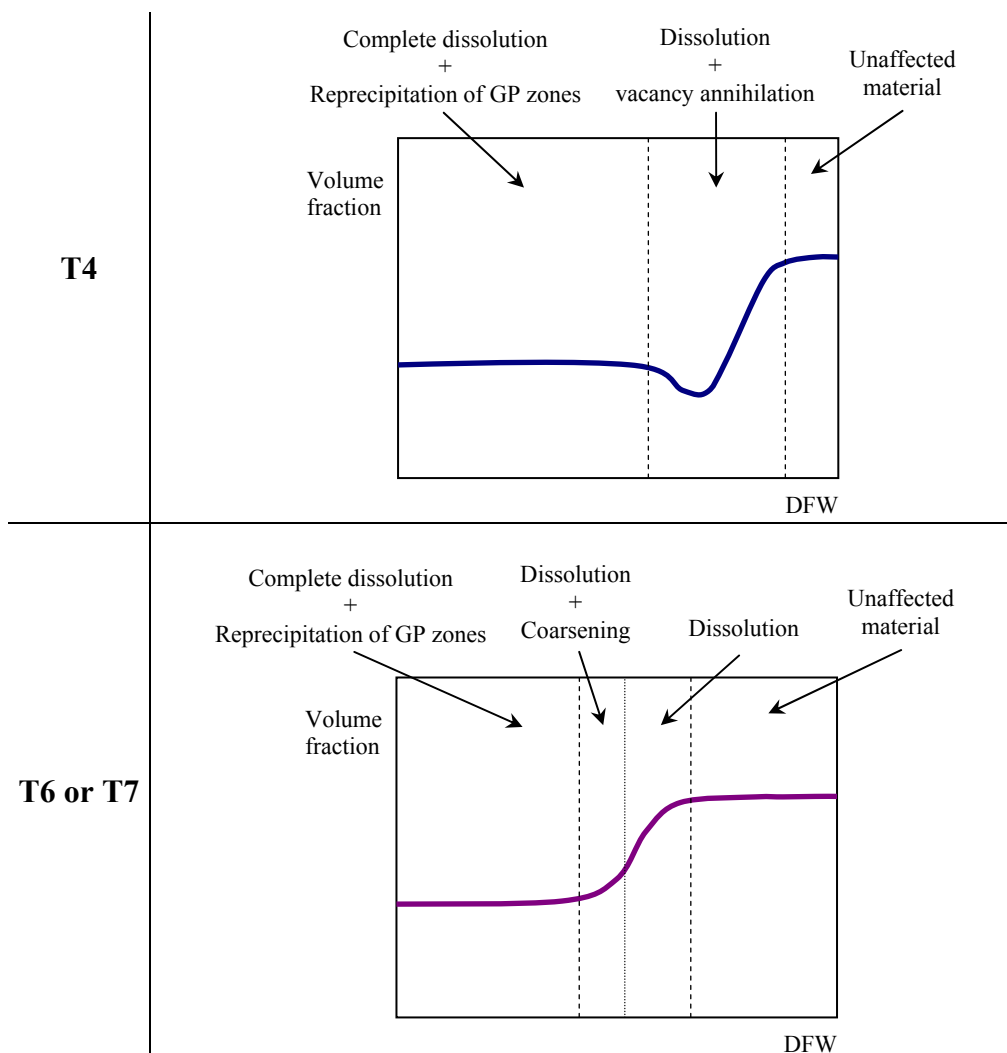


Figure III.29: Schematic representation of the precipitate evolution along the heat-affected zone.

At the end of this chapter, some questions remain open which we will try to answer in the following chapters, both by experimental evidence and by modelling.

- We have shown that the main phenomena leading to the precipitation microstructure evolution are dissolution and coarsening. In which conditions is it possible to neglect the influence of nucleation and phase transformations?
- We have observed that the dissolution processes can have a complex range of behaviours: in many cases (T6 and T7), dissolution occurs at constant mean radius up to a large reverted fraction; for larger reverted fractions, coarsening takes place; in some cases (T4) dissolution occurs with a decreasing mean size. This will be qualitatively studied along simple non-isothermal heat treatments (Chapter IV) and quantitatively modelled (Chapter V).
- From a modelling point of view, classical models, working on a system characterised by an average precipitate size and a volume fraction, will not be able to describe this dissolution at constant mean radius. Moreover coarsening has to be described by an additional equation. In order to model welding it is then necessary to take into account the particle distribution effect, i.e. interaction between particles of different sizes.

In the next chapters, we will try to answer these questions by conducting controlled heat treatments (isothermal and non-isothermal heat treatments). Moreover a process model based on simple laws applied to a particle distribution will be developed in the case of Al-Zn-Mg alloys.

Chapter IV. Precipitation evolution during non-isothermal heat treatments

Non-isothermal heat treatments have been studied in order to better understand the mechanisms controlling the precipitation microstructure changes occurring during complex thermal cycles. After a literature review dealing with the response of an Al-Zn-Mg alloy submitted to various heat treatments, results of in-situ investigations using both SAXS and DSC will be presented. Both reversion treatments and continuous heating have been carried out.

IV.1. Definition of model heat treatments

Three different kinds of experiments have been performed on the three initial tempers (T4, T6 and T7) to monitor in-situ the behaviour of precipitates submitted to controlled heat treatments.

- Reversion heat treatments were monitored in-situ by SAXS measurements: the temperature of an isothermal plateau is reached with the maximum heating rate of the furnace ($\sim 300^\circ/\text{min}$).
- Continuous heating was monitored in-situ by SAXS measurements: a constant heating rate is used to heat from room temperature up to 400°C . The range of available heating rates is $5^\circ/\text{min}$ up to $300^\circ/\text{min}$.
- Continuous heating was monitored by DSC: the experiment is equivalent to the above SAXS experiments and heating rates from $10^\circ/\text{min}$ up to $100^\circ/\text{min}$ (maximum heating rate of the device) have been investigated.

The heating rates which can be reached using these in-situ techniques are relatively low as compared to the heating rate involved during welding (see Figure IV.1). However the heating rate dependence can help us to better understand the precipitation changes involved during non-isothermal heat treatments and thus during welding.

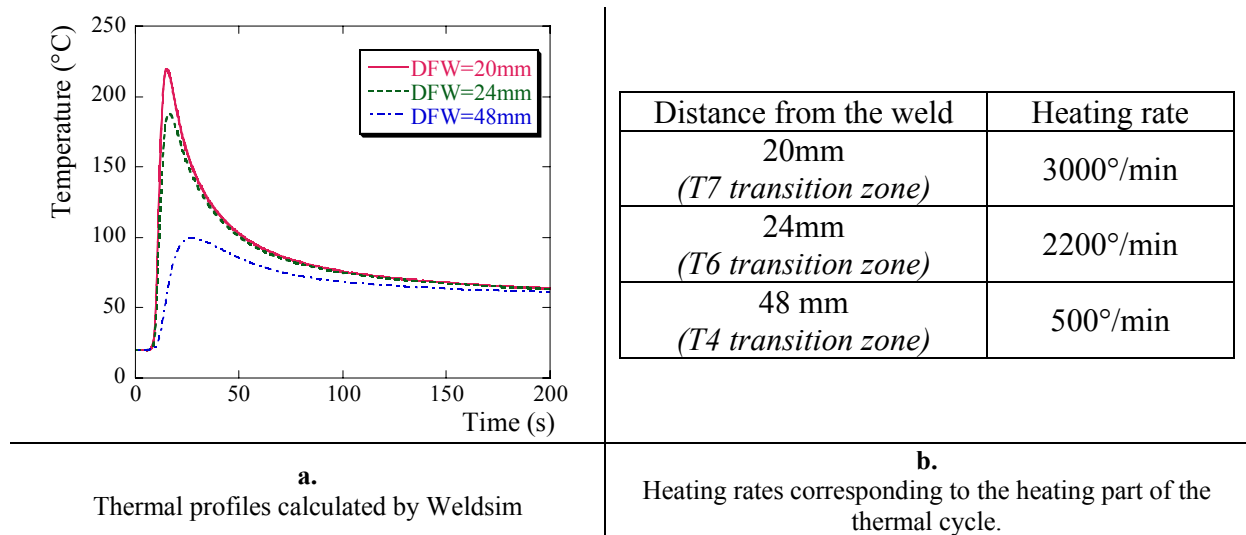


Figure IV.1: Thermal profiles (a.) and heating rates estimated in three points of the heat-affected zone corresponding to the middle of the transition zone of T4, T6 and T7 welds.

The next section summarises the reported results from the literature concerning precipitation evolution during comparable heat treatments.

IV.2. Literature review: response of a 7xxx alloy to a controlled heat treatment

The aim of this section is to compile a literature survey of the behaviour of a given initial precipitated microstructure submitted to a controlled heat treatment. Such treatments can be iso-rate treatments (i.e. at constant heating rate), typically differential scanning calorimetry (DSC) performed on different initial microstructures containing either GP zones, or η' - or η -precipitates. This leads to a better understanding of the microstructural evolution during continuous heating, a simple but meaningful non-isothermal heat treatment. Isothermal heat treatments have been extensively studied, generally to better understand two-step ageing treatment. As a consequence, the initial state is generally composed of GP zones and the investigated temperature ranges are relatively low ($\sim 150^\circ\text{C}$). Another rich topic within isothermal investigations is the so-called retrogression and re-ageing treatment which consists in heating a peak-aged state (T6) for a relatively short time at temperatures around 220°C followed by a new T6 temper. These studies, especially retrogression, can be of considerable interest in the study of microstructure evolution as it deals with the response of a T6 initial state to a medium-temperature heat treatment.

IV.2.1. Decomposition processes during continuous heating

Iso-rate heat treatment experiments (such as DSC or in-situ SAXS) are powerful investigative tools for studying the decomposition of alloys. However, because of the complex decomposition processes taking place in Al-Zn-Mg alloys, the results need to be carefully interpreted.

Many studies have been carried out on Al-Zn-Mg(-Cu) alloys. Hereafter we will give a schematic description of the microstructural changes during isorate heat treatments depending on the nature of initially present particles: GP zones, η' and η .

IV.2.1.1. GP zones as initial state

Typical DSC scans obtained from a material containing exclusively GP zones are shown on Figure IV.2. Schematically, these scans are characterised by two main endothermic peaks called D1 and D2 and one exothermic peak designed as P2. The first peak is directly related to the dissolution of pre-existing particles, i.e. GP zones. Peak (P2) is due to the formation of more stable phases, and peak D2 is the result of the dissolution of these phases.

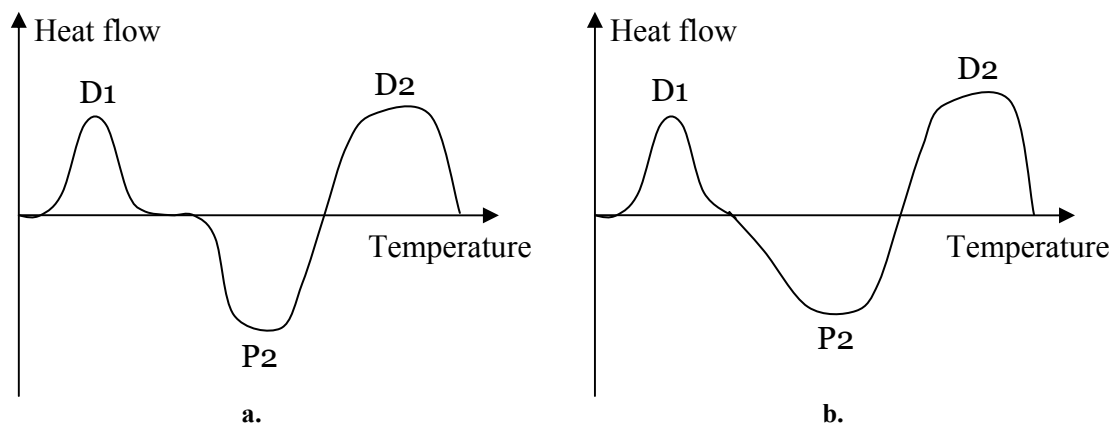


Figure IV.2: Schematic DSC scans for a material containing GP zones.

- Complete dissolution of GP zones before formation of more stable precipitates.
- Partial dissolution of GP zones before formation of more stable precipitates.

Two types of behaviour can be observed concerning the dissolution of GP zones and the subsequent precipitation of more stable precipitates. Lendvai [Lendvai, 1979], working on an Al-4.8wt%Zn-1.1wt%Mg alloy after 24 hours natural ageing (heating rate=40°/min), observed the complete dissolution of GP zones before any other precipitation event, as shown in Figure IV.2.a. Radomsky [Radomsky, 1979] studied the behaviour of two solute-rich alloys Al-4.5at%Zn-2 and 3at%Mg after 50 days pre-ageing at room temperature by DSC and in-situ SAXS and observed the direct transition from the endothermic to the exothermic reaction at ~190°C as illustrated in Figure IV.2.b. Figure IV.3 shows the corresponding changes in the SAXS integrated intensity during continuous heating as measured by Radomsky [Radomsky, 1979]. These are directly related to the volume fraction of precipitates. Similar results were also obtained by Ungár [Ungár, 1979a]. In that case, the reversion of GP zones is only partial, i.e. not all the GP zones dissolve before the formation of the metastable η' -phase starts. The formation of η' is in fact responsible for the increase of the integrated intensity around 190°C. Ungár [Ungár, 1979a] proposed a way to unify the different viewpoints related to GP zone dissolution. Based on the study of numerous Al-Zn-Mg alloys ($1 < \text{Zn} < 4.5\text{at}\%$, $1 < \text{Mg} < 3.3\text{at}\%$), first solution treated, water quenched and then aged at room temperature for two months, Ungár concluded that the chief factor is the bulk Zn content of the alloy. If $C_{\text{Zn}} < 2.5\text{at}\%$ the reversion of GP zones is complete, the formation of η' is inhibited in this temperature range because of a low supersaturation. If $C_{\text{Zn}} > 2.5\text{at}\%$, the formation of η' can start before the dissolution of GP zones can be completed and then the reversion of GP zones is only partial. Surprisingly, the magnesium content seems to be less important than the zinc content.

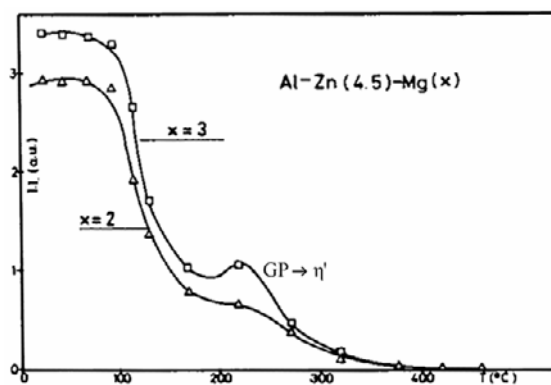


Figure IV.3: Changes of the integrated intensity of SAXS during continuous heating of two Al-Zn-Mg alloys (Al-4.5at%Zn-2at%Mg and Al-4.5at%Zn-3at%Mg) (heating rate=10°/min), as measured by Radomsky [Radomsky, 1979].
Integrated intensity is directly related to the precipitate volume fraction.

We will now discuss the influence of different parameters affecting the stability of GP zones: the ageing temperature and the ageing time. Lendvai [Lendvai, 1979] observed that the peak temperature for dissolution of GP zones was shifted towards higher temperatures (from 120 to 160°C) as the ageing temperature used to generate the GP zones was increased from 20°C to 60°C (the ageing time was 24 hours in both cases). Figure IV.4 presents the results obtained by Jiang [Jiang, 2000] on an Al-5.5wt%Zn-1.15wt%Mg alloy aged at room temperature for different times. The first endothermic peak becomes larger with increasing time as the volume fraction of GP zones formed at room temperature is enhanced. Moreover this peak is moved towards higher temperatures with increased ageing time. Actually the peak temperature is an indication of the stability of pre-existing precipitates [De Iasi, 1977] and during room temperature ageing GP zones nucleate, grow and become more stable. The same interpretation is available when increasing the ageing temperature. The mean size of metastable particles determines their stability and therefore their solvus temperature, whereas the volume fraction affects the area of the dissolution peak.

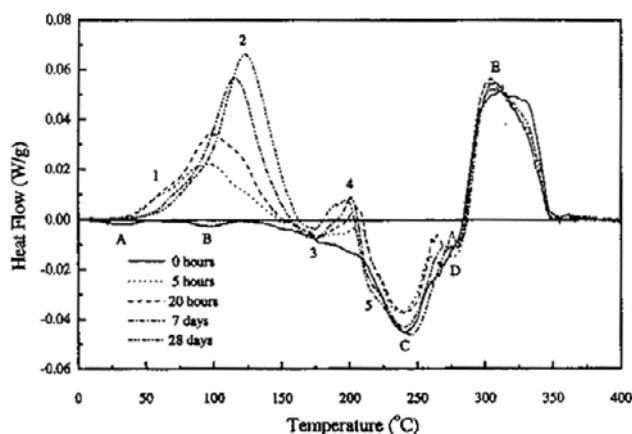


Figure IV.4: DSC thermograms of Al-5wt%Zn-1wt%Mg after ageing at room temperature for different times (heating rate=20°/min), as measured by Jiang [Jiang, 2000].

Due to the complex precipitation sequence involved in the Al-Zn-Mg system, temperature ranges for dissolution of metastable precipitates and formation of more stable ones may overlap. Therefore the peaks in a DSC scan are often not single peaks but are seen as two or even three overlapping peaks (for example: [Viana, 1999]). In a schematic point of view:

- Peak D1 is mainly due to dissolution of GP zones which may appear as a double peak in the presence of both GP(I) and GP(II) [Jiang, 2000]; it may overlap with η' -formation [Lendvai, 1979].
- Peak P2 is due to the formation of more stable particles: η' and η , generally giving rise to a doublet. A third peak may appear but its origin is still controversial: is it due to the nucleation of the T-phase or to the two-step formation of η (in that case second peak comes from the formation of η_1 from η' and the third is related to homogeneous precipitation of η_2) [Park, 1989]? The coarsening of η -precipitates via the Ostwald ripening was also proposed to cause this third peak [Viana, 1999] but this proposition seems questionable since Ostwald ripening should occur continuously with the formation of the η -phase.
- Peak D2 is related to the dissolution of the η -phase (and other phases present if relevant).

IV.2.1.2. η' as initial state

When the ageing temperature is around 100°C it becomes difficult to presume of the type of precipitates initially present in the microstructure, as illustrated by Jiang [Jiang, 2000] in Figure IV.5.a. It gave rise to a major controversy between Park [Park, 1989], Danh [Danh, 1983], Baldantoni [Baldantoni, 1985] and Papazian [Papazian, 1986] about DSC scan interpretation of the peak-aged condition of the commercial alloy 7075 obtained after ageing 24 hours at 120°C. Danh, Baldantoni and Papazian assumed that the initial precipitate population consists of GP zones, whereas Park, on the basis of a detailed TEM study [Park, 1983] considered η' -particles as responsible for age hardening in this temper. This illustrates the need for complementary techniques like TEM to complete the DSC characterisation of precipitation to better identify the nature of initially present phases, e.g. [Yamamoto, 1998].

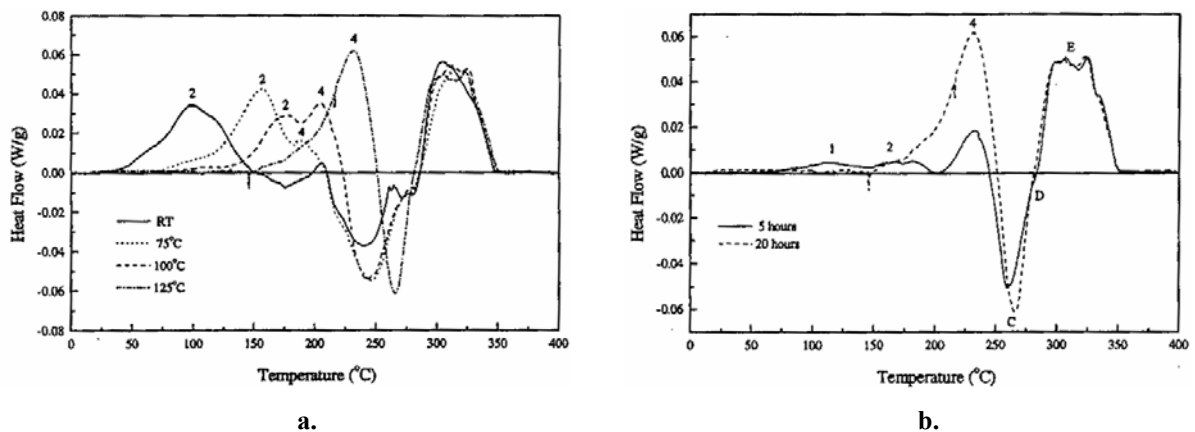


Figure IV.5: Thermograms of Al-5wt%Zn-1wt%Mg alloy (heating rate=20°/min), as measured by Jiang [Jiang, 2000]

- after ageing for 20 hours at different temperatures
- after ageing for 5 and 20 hours at 125°C.

Typical DSC scans of an Al-5.5wt%Zn-1.15wt%Mg alloy artificially aged at 125°C for 5 and 20 hours are shown on Figure IV.5.b [Jiang, 2000]. The predominance of η' -precipitates was illustrated by selected-area electron diffraction. These thermograms are characterised by three peaks: the first one is related to the presence of the initial η' -precipitates, which dissolve and then transform into η -phase giving the second peak; finally, the dissolution of η gives rise to the third broad peak.

García-Cordovilla [García-Cordovilla, 1990] studied the kinetics of η' -dissolution in an 7075 alloy in the T6 temper by DSC at different heating rates. He observed that the dissolution peak was shifted towards higher temperatures by $\sim 40^\circ\text{C}$ with increasing heating rates from 10 to $50^\circ/\text{min}$ due to kinetics effects.

IV.2.1.3. η as initial state

The continuous heating of a microstructure containing exclusively η -particles involves only the dissolution of these precipitates, giving a broad peak at high temperatures (see Figure IV.2).

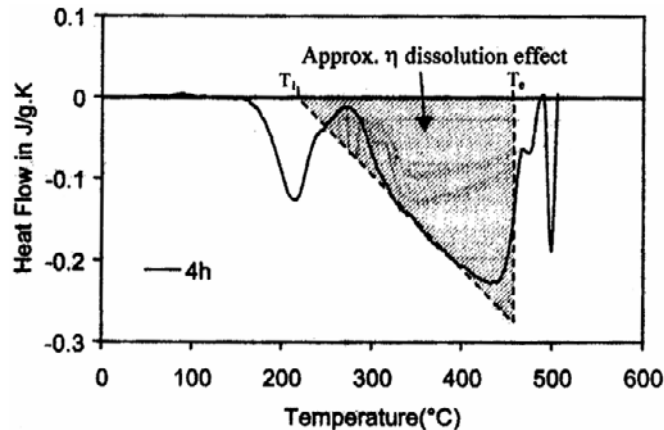


Figure IV.6: DSC curve of an Al-6wt%Zn-2.3wt%Mg-1.8wt%Cu in an overaged temper [Li, 2000].

One should note that in the case of an overaged microstructure (T7) [Adler, 1977; Park, 1989, Yamamoto, 1998; Viana, 1999], the resulting particles are generally η -particles but not exclusively; in fact this state contains also, in a smaller amount, η' -precipitates. This results in a two-peak thermogram due to the dissolution of η' and η -particles respectively.

IV.2.1.4. Summary

Table IV.1 is a summary of the temperature ranges for precipitation and dissolution of GP zones, η' - and η -particles during continuous heating, assuming low heating rates (typically $10\text{--}20^\circ/\text{min}$). These temperature ranges are approximate as they widely depend on the alloy composition. These are based on results obtained by Jiang [Jiang, 2000] who studied a ternary alloy (Al-5.5wt%Zn-1.15wt%Mg) whose composition is relatively close to the 7108.50 alloy.

	Precipitation peak	Dissolution peak
GP zones	$T < 50^\circ\text{C}$	$50^\circ\text{C} < T < 150^\circ\text{C}$
η'	$150^\circ\text{C} < T < 200^\circ\text{C}$	$200^\circ\text{C} < T < 250^\circ\text{C}$
η	$250^\circ\text{C} < T < 300^\circ\text{C}$	$300^\circ\text{C} < T < 350^\circ\text{C}$

Table IV.1: Summary of precipitation and dissolution temperature ranges during continuous heating at low heating rate (typically $10\text{--}20^\circ/\text{min}$), based on [Jiang, 2000].

The influence of various parameters like the heating rate and the ageing time and temperature, on a dissolution peak is schematised on Figure IV.7. The dissolution peak is shifted towards

higher temperatures with increasing heating rates due to kinetics effects: time is necessary to allow transformation. When the time or the temperature of ageing is increased, the particles formed are coarser and thus more stable, their dissolution consequently occurs at higher temperatures. In fact the peak temperature is an indication of the stability of the precipitates.

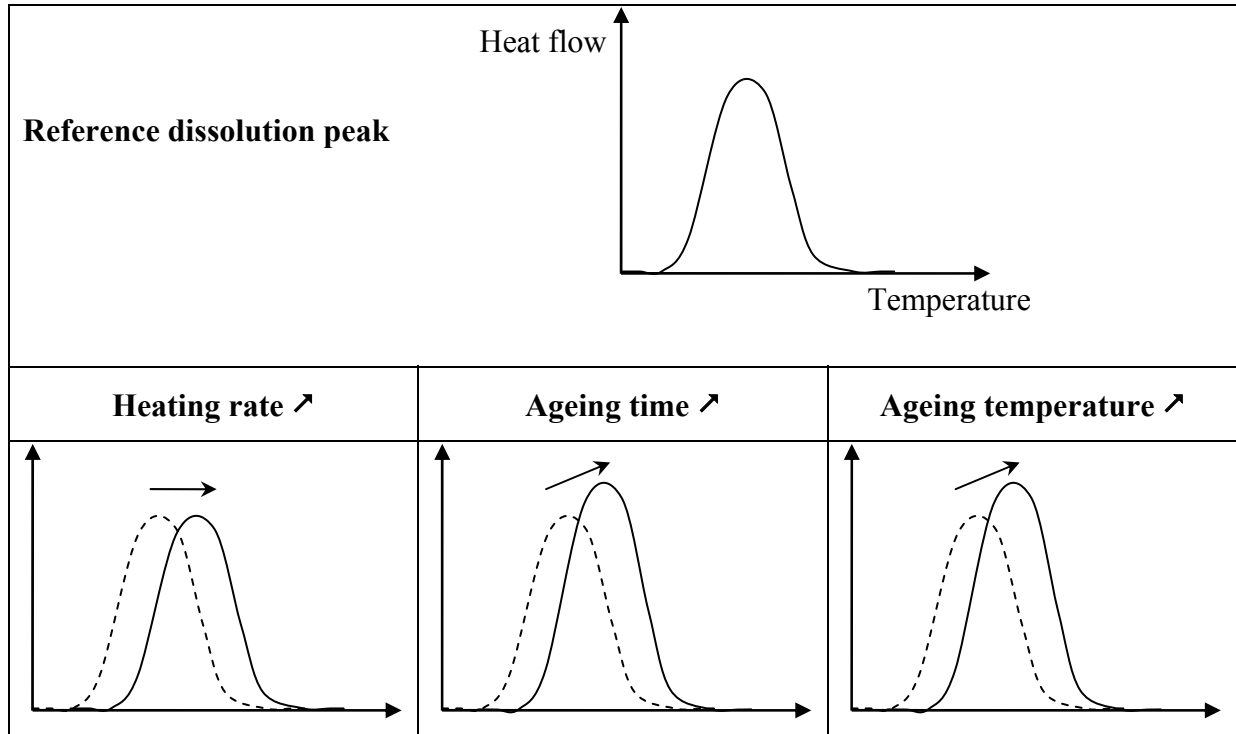


Figure IV.7: Influence of different parameters on the displacement of a dissolution peak.

IV.2.2. Reversion heat treatments

IV.2.2.1. Reversion of GP zones

The response of a precipitated state submitted to an isothermal heat treatment in the range of medium temperatures ($T < 200^\circ\text{C}$) is investigated here. GP zone reversion has been extensively studied in the literature due to its key role in two-step ageing. Previous studies can be divided into two main classes: ex-situ studies or in-situ investigations of the evolution of microstructural features. The first type gives an indication of what happens in terms of the phase transformations whereas in-situ studies are helpful to understand the general behaviour during the heat treatment.

The results of Gueffroy [Gueffroy, 1981a; Gueffroy, 1981b] will be presented to give a good overview of the evolution of size and volume fraction of particles during a reversion treatment. He studied the reversion behaviour at 180°C of an Al-4.5wt%Zn-2wt%Mg alloy (see Figure IV.8) by means of SAXS measurements as a function of the size of the precipitates grown at 100°C (radius between 1.2 and 2.7nm), assumed to be GP zones (is it still relevant when dealing with particles 2.7nm large?).

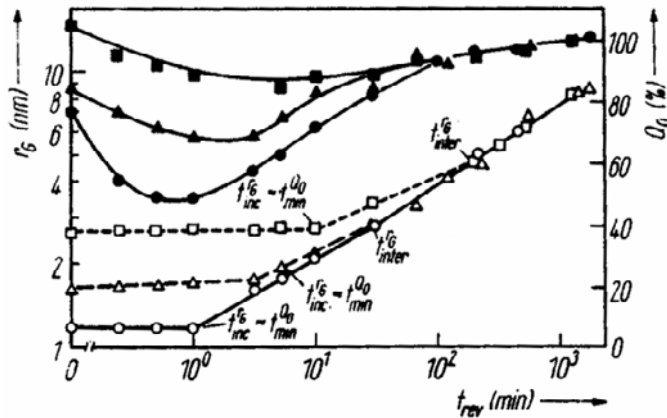


Figure IV.8: Evolution of Guinier radius (r_G open symbols) and integrated intensity (Q_0 in full symbols) versus the reversion time (t_{rev}) at $T_{rev}=180^\circ\text{C}$ starting with precipitates grown at 100°C to sizes 1.2nm (circles), 1.7nm (triangles) and 2.7nm (squares) respectively [Gueffroy, 1981a].

During the reversion treatment three stages relative to the growth of the precipitates can be distinguished:

- Stage 1 ($t < t_{inc}$): the radius (here the Guinier radius r_G) stays approximately constant up to t_{inc} (designated as an incubation time t_{inc}), which corresponds approximately to the minimum of Q_0 ; the volume fraction (here the integrated intensity Q_0) is decreasing, due to the dissolution of the unstable zones.
- Stage 2 ($t_{inc} < t < t_{inter}$): both the size and the volume fraction of the precipitates are increasing, characteristic behaviour of the growth of the particles.
- Stage 3 ($t > t_{inter}$): the volume fraction remains fairly constant and the size of particles increases according to a growth rate independent of pre-history. The chief process is the coarsening of the precipitates by Ostwald ripening.

It should be noted that no phase transformation could be evidenced by the author as SAXS, in principle, does not allow such observations. It is however expected that, at the end of the reversion treatment at 180°C , that the precipitates are either η' or η .

By TEM post-mortem investigations, Stiller [Stiller, 1999] observed the microstructure of an Al-2.3at%Zn-1.4at%Mg alloy first aged at 100°C for 5 hours and then aged for 6 hours at 150°C (typical industrial two-step ageing). After 1.5h at 100°C , TEM revealed two different clusters, GP(I) and type II. After two-step ageing, precipitates of η' , η and retained particles of type II were observed. This post-mortem study gives an indication of the phase transformations taking place during reversion.

Using in-situ SAXS experiments, Gomiero [Gomiero, 1994] followed the evolution of the Guinier radius R_g and integrated intensity Q as a function of ageing time at 120°C of the commercial 7150 alloy (Al-6wt%Zn-2.4wt%Mg-2.1wt%Cu) after 4 months natural ageing (see Figure IV.9).

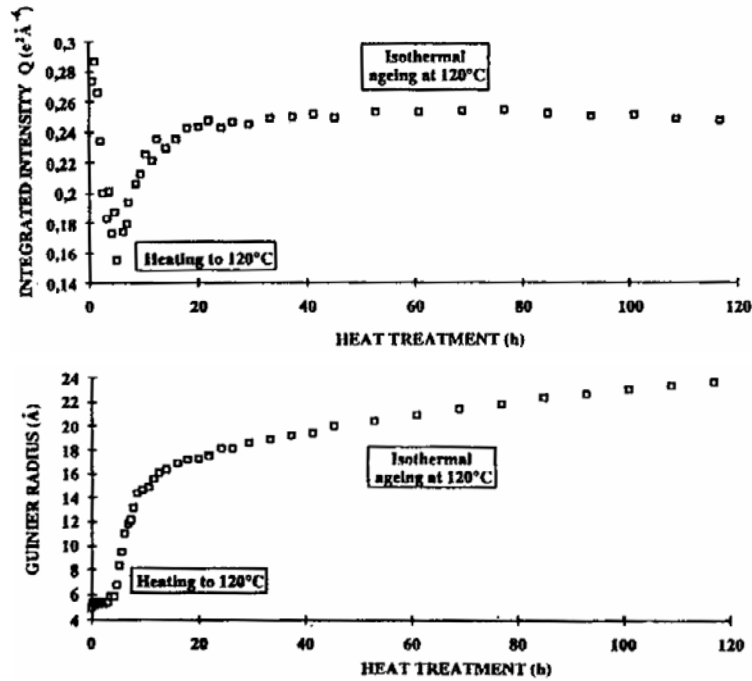


Figure IV.9: Variation of the integrated intensity Q and the Guinier radius as a function of ageing time at 120°C of 7150 after 4 months at room temperature [Gomiero, 1994]. The Guinier radius can be related to the mean radius of the particles and the integrated intensity to the volume fraction of particles.

The sharp decrease in Q observed during heating from 20°C to 120°C is attributed to the reversion of the GP zones formed during room temperature maturation. One can note that the radius remains unchanged during the reversion process. The subsequent increase of Q is due to the precipitation of the η' phase, confirmed by post-mortem TEM observations.

Ferragut [Ferragut, 1996] observed the evolution of hardness and positron lifetime in an Al-6wt%Zn-2wt%Mg-1wt%Cu alloy during isothermal artificial ageing at 150°C , after 5 days pre-ageing at room temperature after solution treatment and quenching (see Figure IV.10). During room temperature pre-ageing, metastable equilibrium was reached: GP zones formed, removing the supersaturation and vacancy-rich clusters completely dissolved. The evolution of hardness and positron lifetime was explained as follows:

- $t < 8\text{min}$: dissolution of smallest GP zones and coarsening of the largest ones occurs until coherency becomes energetically unfavourable,
- $t = 8\text{min}$: the transformation GP zones $\rightarrow \eta'$ begins, nucleation of η' is likely to occur on large GP zones [Ferragut, 1999],
- $t > 8\text{min}$: coarsening of η' , and eventually transformation $\eta' \rightarrow \eta$ are the main processes.

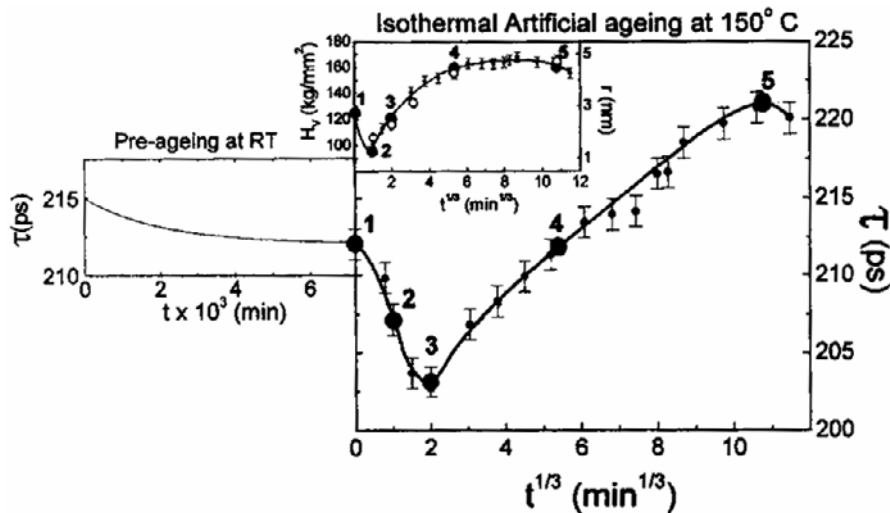


Figure IV.10: Evolution of the positron lifetime τ during isothermal artificial ageing at 150°C, after 5 days pre-ageing at room temperature. The evolution of τ during pre-ageing is shown in the middle left-hand figure. For the same heat treatment, Vickers microhardness H_V data are represented in the insert. The open symbols correspond to the mean precipitate size determined by TEM [Ferragut, 1996].

IV.2.2.2. Retrogression and reageing

The so-called retrogression and reageing (RRA) treatment has been extensively investigated during the 80s and 90s as a potential method to obtain a good compromise between high strength and good corrosion resistance. This heat treatment procedure has been devised for the 7xxx system alloys by Cina [Cina, 1974]. The retrogression and reageing treatment has been shown to produce a very high resistance to stress corrosion cracking typical of overaged tempers, while maintaining the very high strength of the peak-aged tempers [Park, 1988]. The RRA treatment is applied to materials in the peak-aged T6 condition and consists of the following steps:

- (1) a short-time anneal (from 5s to 30min) in the temperature range 200-280°C,
- (2) reageing under the same conditions used for the original T6 temper.

This special heat treatment can be of great interest in the understanding of welding as it deals with the evolution of a pre-precipitated microstructure (containing hardening precipitates, generally η') submitted to a high reversion temperature ($T > 200^\circ\text{C}$). Moreover the behaviour of a re-aged microstructure can be correlated with the microstructure developed during post-welding heat treatments.

The study of RRA was generally carried out on the 7075 alloy, widely used for aircraft structural materials. But this material is prone to stress corrosion cracking especially when aged to the maximum strength. Stress corrosion is thought to be closely related to grain boundary particles. The conventional method of solving this problem has been to overage the materials, involving a strength loss of 10-15%. Therefore, the 7075-T6 appeared as a good candidate for the study of RRA.

Retrogression

The effect of retrogression at 200°C and retrogression plus re-ageing (120°C / 24 hours) on yield strength of 7075-T6 is summarized in Figure IV.11.a. During retrogression, the strength falls very sharply toward a minimum value before increasing to a “secondary” peak and then decreasing at long times. The influence of the retrogression temperature has been largely reported by Park [Park, 1988] and can be seen in Figure IV.11.b. One should note that Habiby [Habiby, 1987] does not observe the secondary peak using both hardness and yield strength measurements for retrogression temperatures from 180°C to 240°C; but this is probably due to the time scale (of the order of the minute) which is quite large. In particular at 230°C, the minimum is expected to occur at around 20s (see Figure IV.11.b).

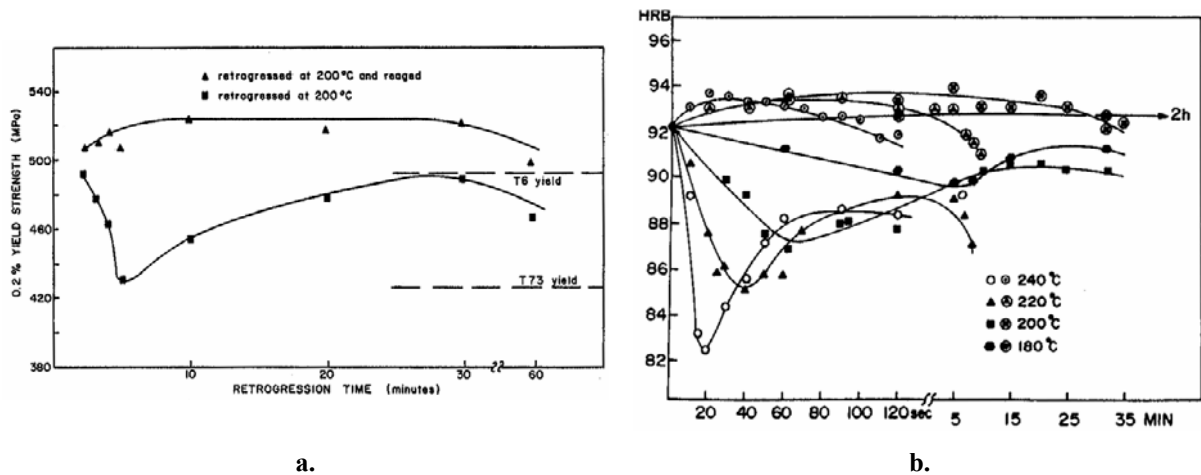


Figure IV.11: Changes in yield strength and hardness during retrogression and reageing.
 a. Retrogression temperature = 200°C [Danh, 1983].
 b. Retrogression temperature between 180°C and 240°C [Park, 1988].

The evolution of microstructure during such RRA heat treatments has been studied by many authors using various investigation techniques:

- TEM (transmission electron microscopy) [Danh, 1983; Park, 1984; Habiby, 1987; Park, 1988; Viana, 1999],
- DSC (differential scanning calorimetry) [Baldantoni, 1985; Papazian, 1986; Park, 1989; Gazda, 1997; Viana, 1999],
- Electrical resistivity [Gazda, 1997]
- SAXS (small-angle X-ray scattering) [Meng, 1990; Meng, 1997],
- APFIM (atom-probe field-ion microscopy) [Brenner, 1991; Warren, 1992].

The authors agree in the general interpretation of the hardness evolution during retrogression in three stages:

- (1) the first drop is due to the partial dissolution of initially present precipitates; indeed hardening particles constituting the initial T6 temper become unstable during the retrogression treatment since the retrogression temperature is significantly higher (>200°C) than the ageing temperature (generally 120°C),
- (2) the subsequent increase in hardness can be related to the transformation from metastable precipitates to more stable ones followed by growth of these new particles, which leads to the second hardness peak,

- (3) the last decrease in hardness is due to the coarsening of precipitates by Ostwald ripening and to the transition from shearing to by passing of dislocations.

However, there still remains a controversy, opposing principally Danh and Park in the 80s, concerning the identity of involved precipitates. This is mainly related to the characterisation of the initially present particles in the peak-aged T6 temper obtained for the 7075 alloy at 120°C. As a consequence, Danh [Danh, 1983; Danh, 1985] maintains that stage (1) can be attributed to the reversion of GP zones and therefore stage (2) is characterised by the formation and growth of η' -particles. On the other hand, Park [Park, 1984; Park, 1988; Park, 1989] attributes stage (1) to the partial dissolution of η' -particles followed by the transformation $\eta' \rightarrow \eta_2$ and last stage is then due to the coarsening of η -phase. A detailed identification of the precipitates contained in 7075-T6 material carried out by Warren [Warren, 1992], using diffraction pattern analysis and by Viana [Viana, 1999] using DSC, concluded that the main type of precipitate in this material was η' . This provides strong support to Park's interpretation.

Retrogression and reageing

The re-ageing treatment is generally performed on retrogressed material for a time corresponding to the minimum in hardness. The good performance of the RRA treatment in terms of strength and corrosion resistance can be explained in the following way [Park, 1988, Viana, 1999]:

- (1) Initial T6 temper promotes a fine distribution of hardening particles leading to the peak-strength and the precipitation of numerous η -particles on grain boundaries, which are thought to cause the poor corrosion resistance of the T6 temper.
- (2) During retrogression for short times partial dissolution of hardening precipitates and coarsening of grain boundary precipitates occurs.
- (3) Reageing promotes the re-precipitation of η' and subsequent coarsening of grain boundary precipitates, which is thought to be beneficial for corrosion resistance [Park, 1984].

As a result, inside the grains the microstructure is similar to that of the T6 temper and the final grain boundary microstructure is similar to that of the overaged T7 temper, and therefore less prone to stress corrosion cracking.

Moreover it was found that the precipitation microstructure inside the grains after RRA treatment is slightly different from that of the initial T6 state. In fact, RRA treatment leads to a microstructure slightly coarser and more stable in nature [Danh, 1983; Viana, 1999]. During the retrogression treatment, dissolution of the smaller η' -particles and coarsening of the larger η' -precipitates occurs as well as a partial transformation of the larger η' -particles to η -phase. Upon reageing further growth of the η -particles, subsequent growth of incompletely dissolved η' -particles and precipitation of new η' -precipitates [Meng, 1990; Meng, 1997] occurs to give a fine dispersion of precipitates [Warren, 1992].

RRA studies are able to provide useful information concerning the evolution of a microstructure containing hardening precipitates submitted to a high-temperature heat treatment for short times. Moreover re-ageing studies give an indication of the capacity of the material to recover its initial properties in terms of hardness or yield strength in dependence with the retrogression time.

IV.2.2.3. Summary

A schematic illustration of the behaviour of a pre-precipitated microstructure containing either GP zones or η' -particles when submitted to a further reversion heat treatment is shown in Figure IV.12.

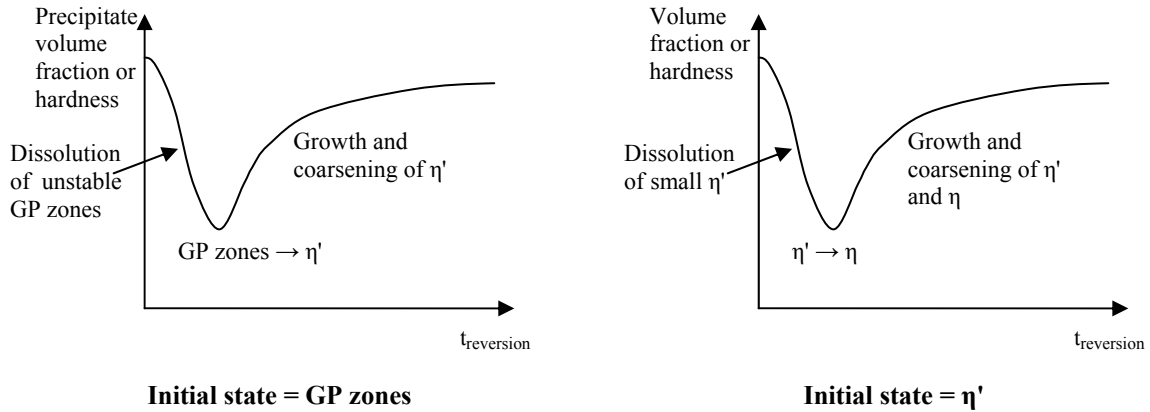


Figure IV.12: Schematic behaviour of precipitation evolution of a pre-precipitated microstructure containing either GP zones or η' -particles during a reversion heat treatment.

It should be noted that a minimum in hardness or volume fraction is always associated with a phase transformation. The transformation does not correspond exactly to the minimum but there a competition between dissolution and phase transformation and the transformation is assumed to become predominant around the minimum of hardness. We will discuss further the possible correlation between this minimum and a phase transformation by means of experimental results and modelling.

IV.3. Precipitation evolution during reversion heat treatments

Reversion treatments consisting of an initial fast heating at 300°/min followed by an isothermal holding at the desired temperature have been performed in-situ during SAXS measurements. A furnace was specially designed to carry out such experiments under the X-ray beam. This allowed us to monitor the volume fraction and mean radius during the whole treatment. Reversion treatments have been performed on the T6 and T7 initial states.

IV.3.1. General precipitation evolution

Figure IV.13 displays the evolution of microstructural features (volume fraction and particle size) during a typical reversion treatment, here at 220°C. The temperature profile during the treatment is also shown. These experiments and results are comparable to those of Gueffroy [Gueffroy, 1981a], as presented in Figure IV.8.

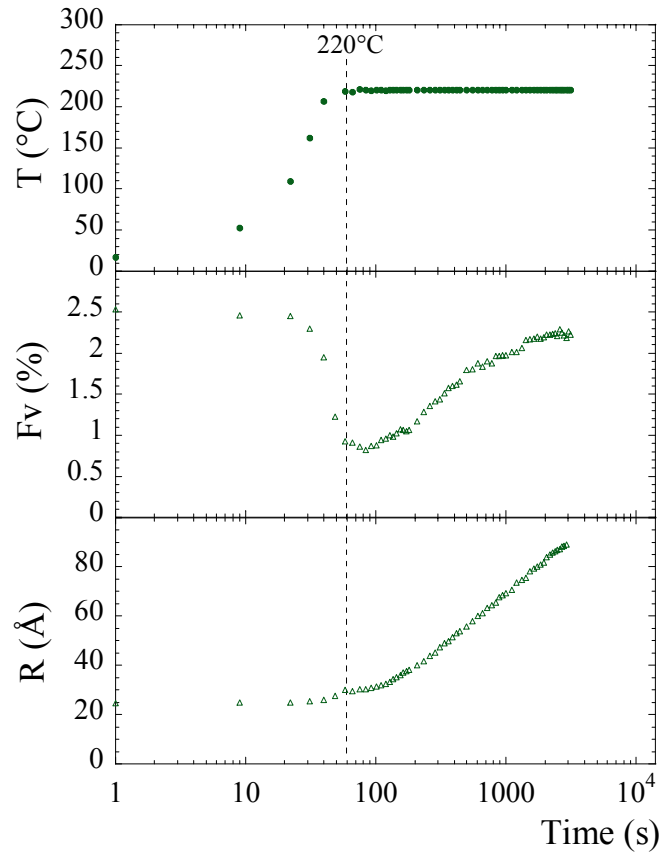


Figure IV.13: Evolution of the volume fraction and particle size during a reversion treatment at 220°C of a T6 sample. The temperature profile during the experiment is also presented. The dashed line indicates the limit of the initial heating.

The classical dissolution behaviour followed by coarsening can be observed. The volume fraction of precipitates first decreases, defining the dissolution process and then increases, characterising the so-called coarsening regime. It should be noted that most of the dissolution occurred during the heating stage of the reversion treatment. Therefore this type of heat treatment can not be simply considered as an isothermal treatment.

As mentioned by Gueffroy [Gueffroy, 1981a], the average particle radius remains relatively constant during the major part of the dissolution stage. This phenomenon has also been observed during welding. The underlying mechanism is not clear since it would be expected that smaller particles (less stable) first dissolve whereas the bigger ones remain unaffected, leading to an overall increase of the average size. This can be interpreted in two ways. Either the dissolution rate does not depend significantly on the size of the precipitates; each size class of the particle distribution will dissolve at the same rate. Or, as the small particles decrease in size, the bigger ones grow, resulting in a larger particle distribution but with the same mean radius. Of course these explanations are extreme cases and the reality probably lies somewhere in between.

During the coarsening stage, the particle size increases. The kinetics of the radius evolution during the isothermal part of the reversion treatment can be compared to classical laws of coarsening predicted by the Lifshitz-Slyozov-Wagner (LSW) theory. The LSW theory predicts a linear behaviour of $(R-R_0)^3$ versus $(t-t_0)$. This is plotted in Figure IV.14. It can be concluded that the coarsening stage is well represented by the LSW theory. Similar

observations were made by Dorward [Dorward, 1999] who studied the overageing kinetics of the 7050 alloy at intermediate temperatures (157-182°C).

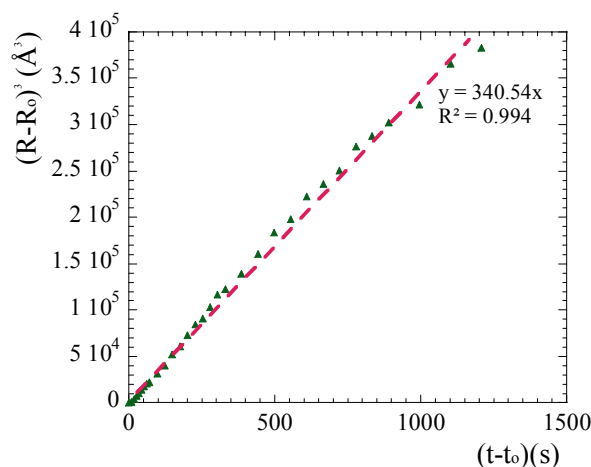


Figure IV.14: Comparison between experimental radius evolution and LSW theory on a reversion treatment at 220°C performed on a T6 initial state. Reference time, t_0 , has been taken equal to 100s, corresponding to the beginning of the coarsening stage. Moreover radius range has been limited to sizes smaller than 75 Å to ensure a good reliability of Guinier radius determination.

IV.3.2. Temperature dependence

The temperature dependence of the precipitation evolution during reversion treatments is shown in Figure IV.15 for both the T6 and T7 materials.

Volume fraction evolution

At 300°C, the dissolution is complete for the two tempers and no significant subsequent transformation is observed. At lower temperatures, dissolution is followed by an increase in the volume fraction. In most of the investigated cases, this dissolution is only partial and is followed by an increase in the volume fraction. This can be explained by the coarsening of pre-existing precipitates and perhaps a contribution from the nucleation and growth of new particles. In the case of the T6 state reverted at 280°C, the dissolution is complete and is followed by a subsequent increase in the volume fraction. This is exclusively due to the precipitation of new particles. These new particles are expected to belong to a phase different from that constituting the initial precipitation microstructure (here η' -precipitates are replaced by the η -phase). This behaviour is not observed for the T7 temper which already contains the η -phase.

At all temperatures higher than 220°C, the dissolution stage is very rapid, resulting in a rapid drop in the volume fraction. The time corresponding to the minimum volume fraction is then more or less identical. At lower temperatures, it increases as the temperature decreases.

During the coarsening stage, the volume fraction tends to a saturation level at long times, corresponding to the equilibrium volume fraction. This can be related to the remaining supersaturation which decreases as the volume fraction increases. Once the equilibrium concentration of the solid solution is reached, the volume fraction remains constant. This asymptotic volume fraction decreases with increasing temperature, in accordance with the shape of the α/η solvus boundary.

Moreover the time to reach the saturation increases as the reversion temperature decreases due to lower diffusion kinetics.

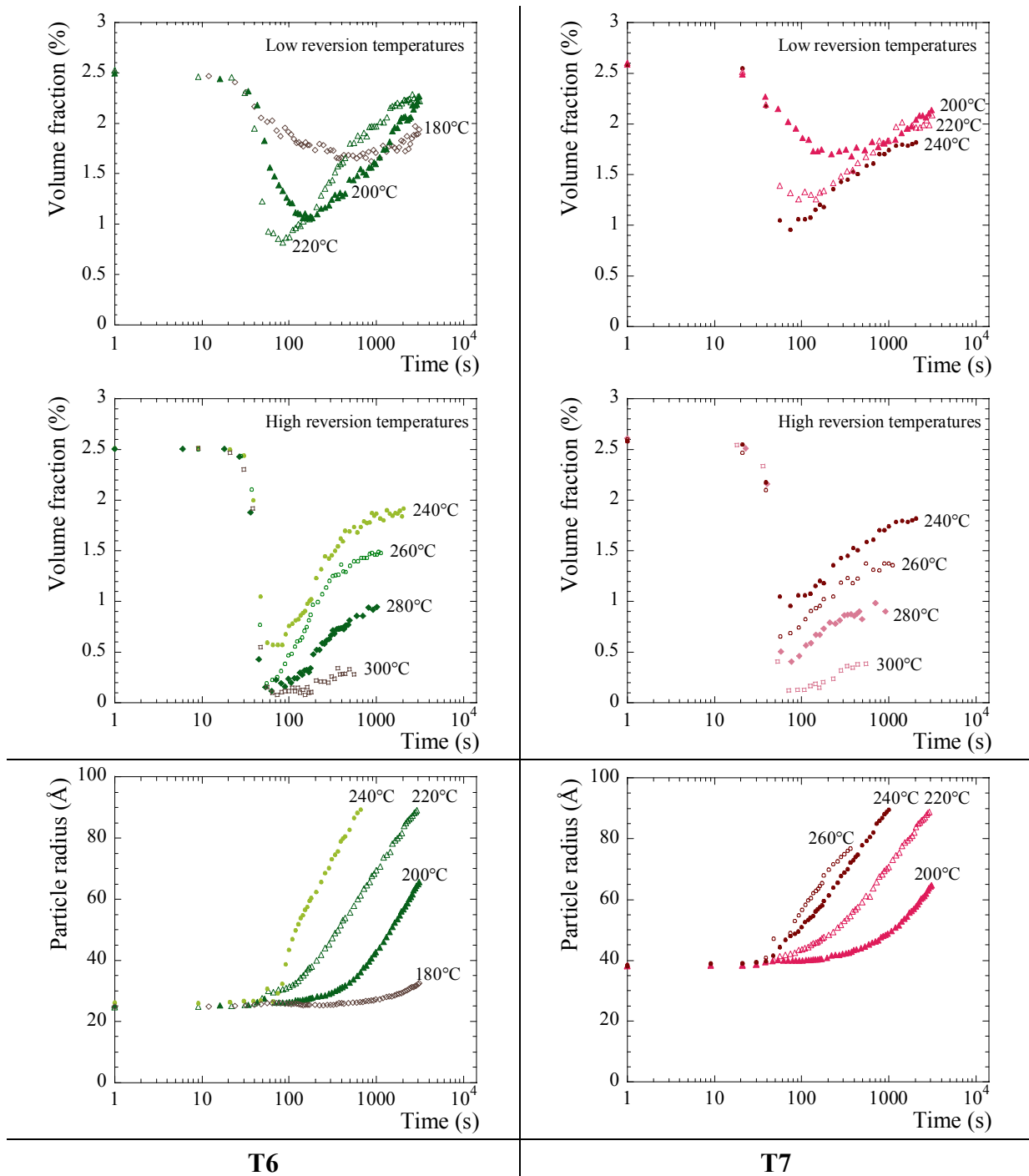


Figure IV.15: Evolution of volume fraction and particle size for various reversion temperatures applied to T6 and T7 materials. No radius can be determined for 280°C (and T6–260°C) because only radius smaller than $\sim 100\text{\AA}$ can be measured.

Particle size evolution

As it has already been observed for the T6–220°C experiment, the mean particle size remains constant during the major part of the dissolution stage. This phenomenon can now be considered to be the standard behaviour for particle size during dissolution.

During the coarsening stage the evolution of the particle size is monotonous and is not affected by the saturation of the corresponding volume fraction, as expected for the classical Ostwald ripening.

IV.3.3. Comparison of T6 and T7 behaviours

The drop in volume fraction is always more important for the T6 initial state than for the T7 state (see Figure IV.15). The T6 temper is less stable due to the nature of the precipitates constituting the microstructure. η' -precipitates, contained in the T6 material, are metastable precipitates (presenting a lower interfacial energy) whereas the T7 temper mainly contains equilibrium η -precipitates. Furthermore T7 particles are larger than those contained in the T6 state and are therefore more stable, resulting in a better "resistance to dissolution".

When the results of the T6 and T7 precipitate evolution are compared at the same reversion temperature (see Figure IV.16), the volume fractions are seen to become very close at long ageing times. Furthermore the T6 and T7 particle sizes also become identical at long times. This behaviour has been observed for all investigated reversion temperatures.

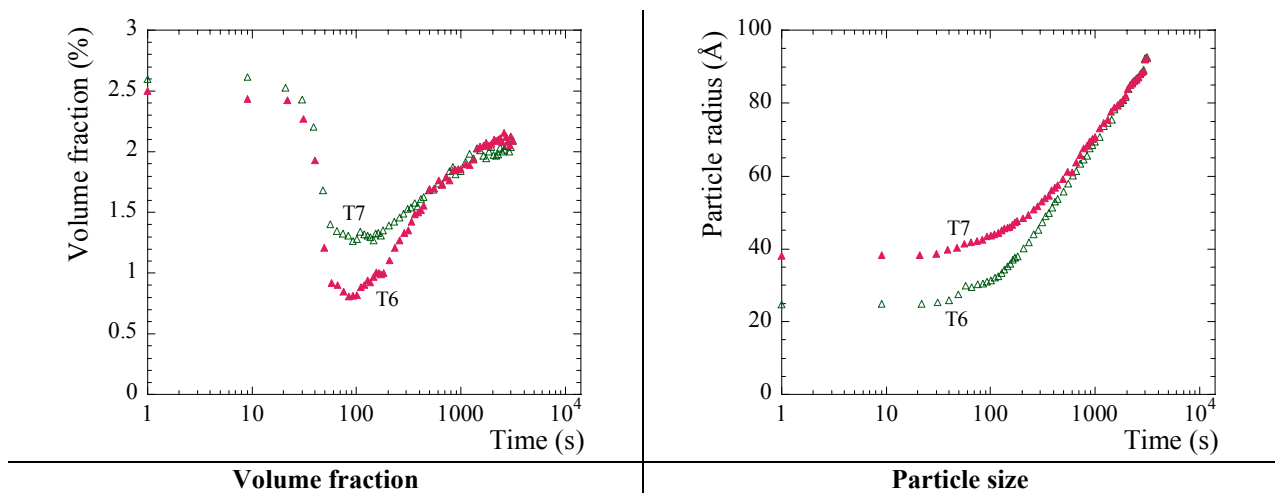


Figure IV.16: Comparison of T6 and T7 volume fraction and particle size evolution during a reversion treatment at 220°C.

These results suggest that the T6 and T7 materials submitted to a high temperature reversion treatment tend to the same microstructural state in terms of volume fraction, radius and certainly also in terms of precipitate nature. This implies that some phase transformation from metastable η' -particles to equilibrium η -phase should occur in the T6 state and also in the T7 state which also contains some η' -particles during the reversion treatment. Is it directly correlated to the minimum in volume fraction as proposed by several authors (see IV.2.2.3. Summary)? We will discuss this point in the next chapter (V. Modelling).

This systematic reversion study helped us to better understand precipitation evolution during isothermal heat treatments and also to quantify microstructural features during such heat treatments. These results will be useful in the calibration of thermodynamical parameters in the following modelling (Chapter V. Modelling).

IV.4. Continuous heating

To better understand the history of precipitation evolution during welding, in-situ non-isothermal experiments have been carried out. The most studied non-isothermal heat treatment is continuous heating. Both SAXS and DSC have been used to measure the microstructural changes during such heat treatments.

IV.4.1. SAXS investigation

Continuous heating experiments have been carried out in-situ during SAXS measurements using different heating rates ranging from $10^\circ/\text{min}$ to $300^\circ/\text{min}$ for the three initial states.

Figure IV.17 shows the results obtained on the T6 and T7 materials submitted to continuous heating at $20^\circ/\text{min}$. The predominant phenomenon is the dissolution of the precipitates (decrease of the volume fraction). The first half of the dissolution occurs at constant mean radius, as already observed during reversion treatments. Afterwards, the mean radius increases rapidly up to the complete dissolution. We will discuss in the section devoted to the influence of the initial state, the existence of an anomaly of dissolution observed in the T6– $10^\circ/\text{min}$ sample.

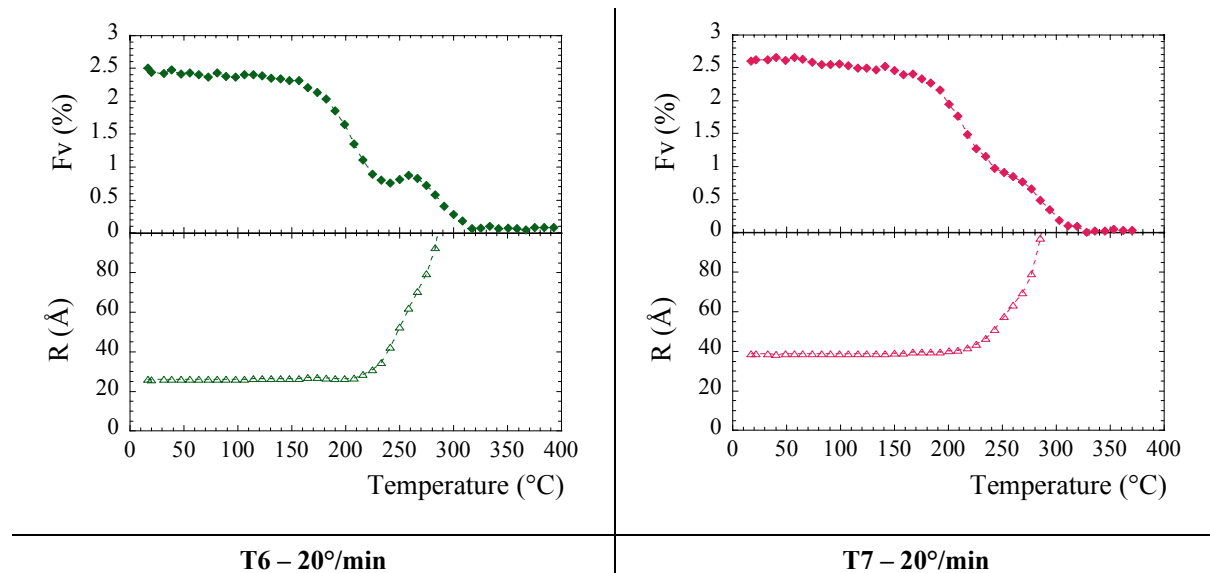


Figure IV.17: Evolution of volume fraction and particle size of T6 and T7 microstructures submitted to continuous heating at $20^\circ/\text{min}$.

Influence of the heating rate

Figure IV.18 displays the results obtained for the different heating rates for both the T6 and T7 initial states. A higher heating rate tends to shift the dissolution curve towards higher temperatures. A shift of 30°C can be observed between $10^\circ/\text{min}$ and $300^\circ/\text{min}$. This kinetic effect is particularly well-known in differential scanning calorimetry.

The same effect is observed in the precipitate radius evolution. However one should note that coarsening seems to be much more sensitive to the temperature than to the heating rate. The kinetics of the radius evolution *versus* temperature is the same for all heating rates. In both the T6 and T7 materials, coarsening begins at a temperature around 220°C . Above this temperature, a drastic increase of the particle radius is observed.

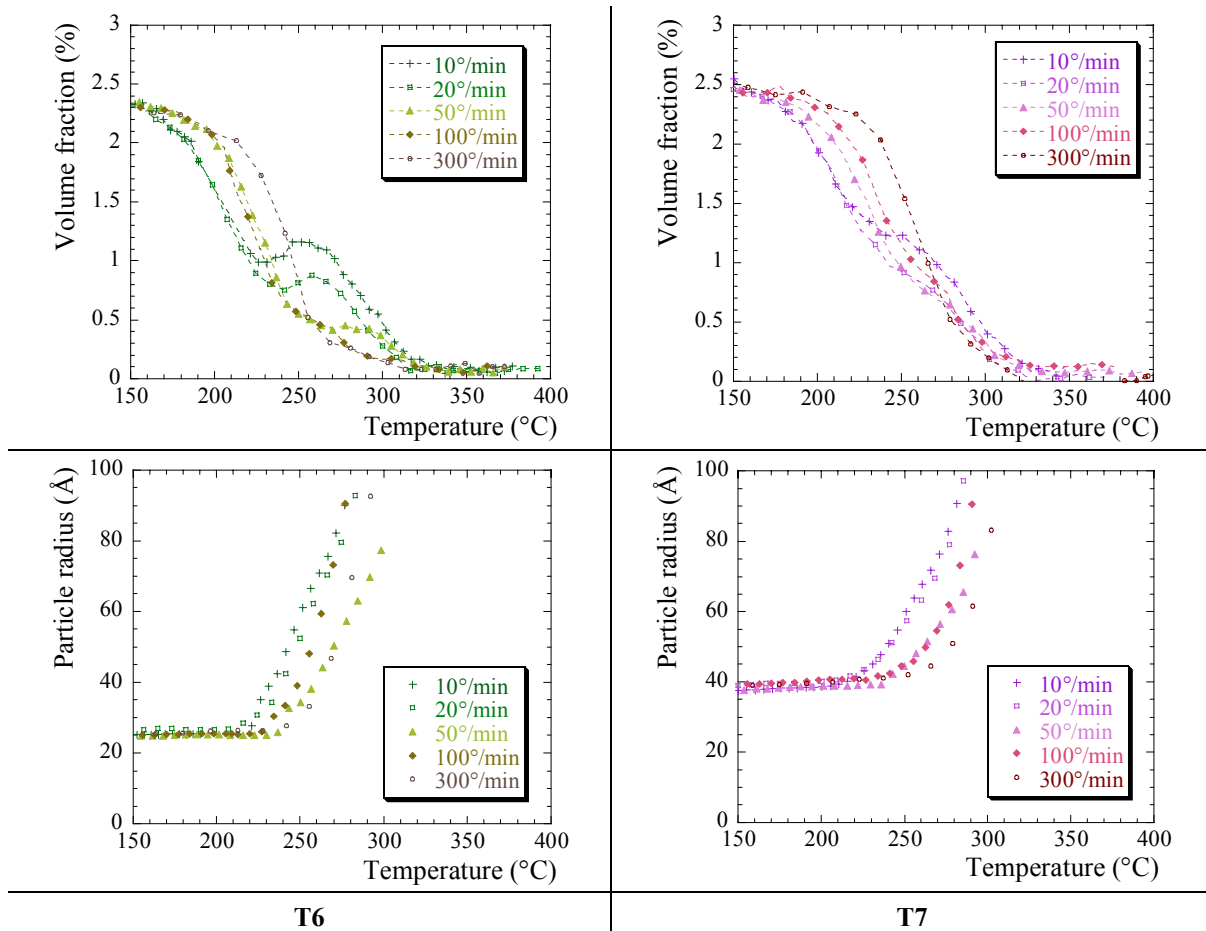


Figure IV.18: Evolution of the volume fraction and particle size of T6 and T7 materials during in-situ continuous heating experiments from 10°/min up to 300°/min.

Influence of the initial state

As can be seen in Figure IV.18, dissolution begins earlier for the T6 material than for the T7 state: 160°C at 10°/min to 190°C at 300°/min for T6 compared with 180°C at 10°/min to 210°C at 300°/min for T7. This is due to the lower stability of the η' -phase compared with the equilibrium η -phase and to the smaller T6 particle size which depresses the stability due to capillarity effects.

An important feature is the presence of a temporary interruption of the dissolution observed mainly in T6-curves at low heating rates (see T6–10°/min, T6–20°/min and T6–50°/min). This phenomenon can be attributed to the transformation $\eta' \rightarrow \eta$. The transformation to a more stable phase results in an increase of the equilibrium volume fraction at a given temperature. This transformation is observed at heating rates up to 50°/min. When increasing the rate, the volume fraction decreases and the temperature at which the $\eta' \rightarrow \eta$ transformation occurs increases: from 260°C to 290°C for 10°/min and 50°/min respectively. This reflects the competition between dissolution and transformation. When the heating rate is too high, there is insufficient time for transformation and the dissolution process dominates. However when the heating rate is low, the materials have for a sufficient time at intermediate temperature for the $\eta' \rightarrow \eta$ transformation to occur.

This transformation can also be observed in the T7 material at 10°/min but it appears as an inflexion point because of the smaller volume fraction of η' -particles contained in this state.

The behaviour of the T4 material submitted to continuous heating is different from that of the T6 or T7 initial states, as can be seen in Figure IV.19. In fact, the dissolution of GP zones is complete at 150°C for all heating rates and is fairly rate-independent. Afterwards, a volume fraction increase can be observed at high temperatures (from 200°C up to 280°C) in the case of slow heating rates. Finally the volume fraction decreases again up to complete dissolution of the newly formed particles.

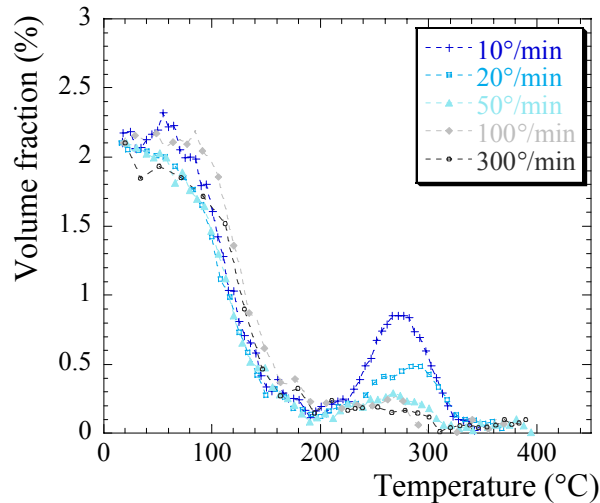


Figure IV.19: Evolution of the volume fraction of T4 initial state during continuous heating from 10°/min up to 300°C.

This increase in volume fraction between 200°C and 280°C can be attributed to the precipitation of the stable η -phase. This is confirmed by the fact that the T4 curve at 10°/min follows the same dissolution behaviour as the T6 and T7 states for temperatures higher than 270°C (see Figure IV.20). When the heating rate is increased, the precipitation of η from the solid solution gradually disappears, because of a decreasing nucleation rate.

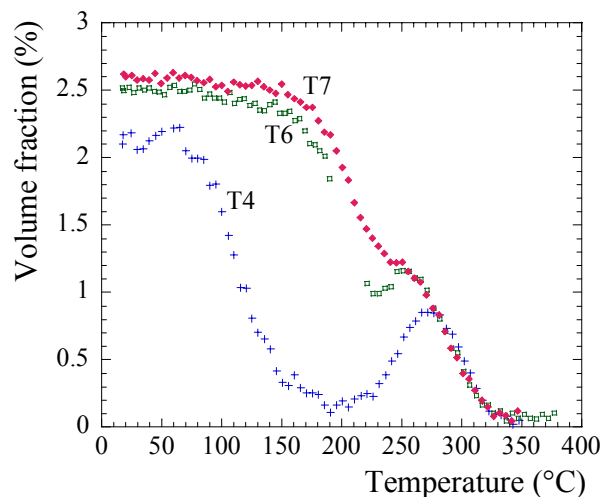


Figure IV.20: Comparison of T4, T6 and T7 volume fraction evolution during continuous heating at 10°/min.

IV.4.2. DSC investigation

Similar continuous heating experiments have been carried out by differential scanning calorimetry (DSC) for heating rates varying from $5^{\circ}/\text{min}$ up to $100^{\circ}/\text{min}$ (maximum heating rate). This technique is particularly adapted to the determination of the nature of the precipitates involved in various reactions.

Figure IV.21 shows the heat flow measured during continuous heating of T6 and T7 materials at a slow heating rate ($5^{\circ}/\text{min}$). Three characteristic peaks can be observed in the T6 scan. Peak I around 210°C is associated with the dissolution of η' -particles and small η -precipitates contained in the initial state. Peak II at 240°C is the signature of the η' to η transformation. Peak III in the temperature range $270\text{--}350^{\circ}\text{C}$ corresponds to the dissolution of stable phases.

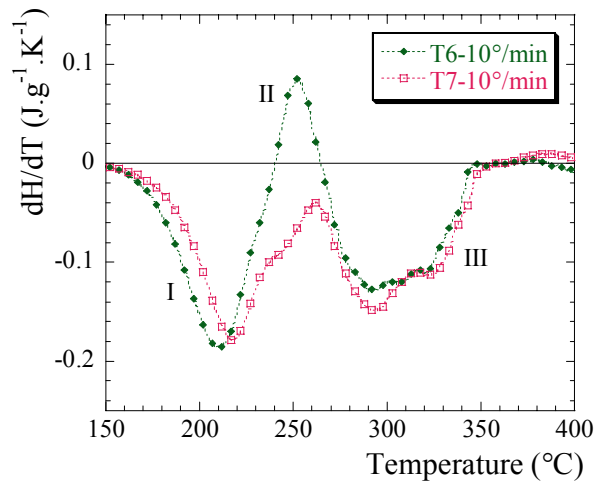


Figure IV.21: DSC scans of T6 and T7 initial states at $5^{\circ}/\text{min}$.

It can be seen that the T7 scan presents a well-defined peak I, at a slightly higher temperature than the T6 peak I. This means that the T7 material also contains a large amount of η' -precipitates, with a larger particle size (shift to higher temperature corresponds to a higher stability of the particles). However, the peak II, characteristic for the phase transformation $\eta' \rightarrow \eta$, as previously observed by SAXS, is not observed in the T7 material. This is certainly related to the pre-existence of numerous η -particles in the initial state. However some η' to η transformation may also occur in the T7 material but its extent is certainly not sufficient to result in an exothermic peak.

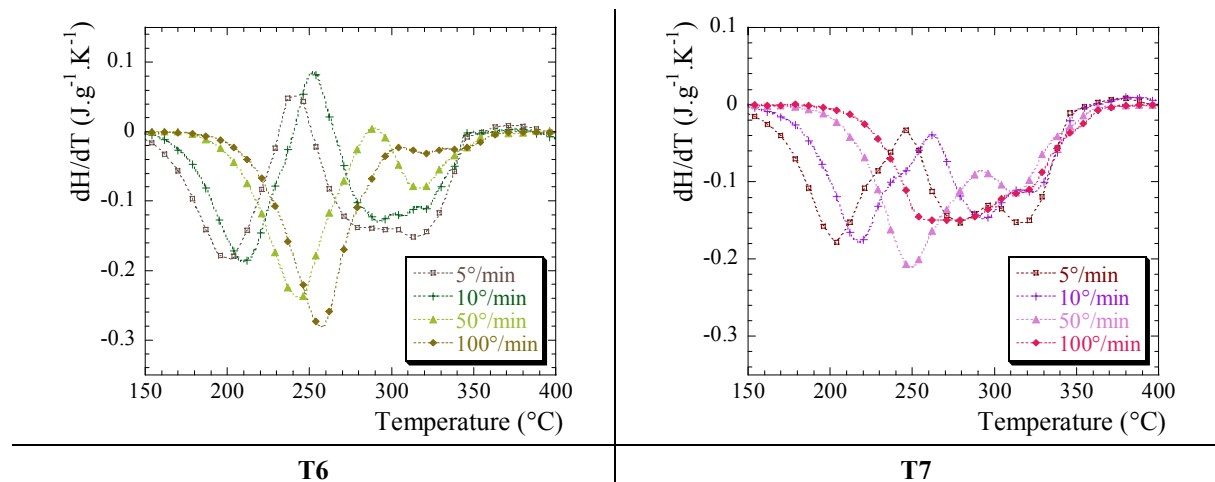


Figure IV.22: Evolution of the DSC scan with heating rate varying from $5^{\circ}/\text{min}$ up to $100^{\circ}/\text{min}$ for T6 and T7 initial states.

The influence of the heating rate on the microstructural evolution is shown in Figure IV.22. As already observed by SAXS, peak II tends to disappear when increasing the heating rate. Moreover the peaks are shifted towards higher temperatures as the heating rate is increased due to kinetic effects. As a result, dissolution peaks obtained during continuous heating at high heating rates are characteristic of the phases initially present in the material (no phase transformation is allowed). As observed by SAXS measurements the critical heating rate for phase transformation is around 50°/min.

The general shape of the T4 scans is completely different to those of the T6 or T7 states, as it can be seen in Figure IV.23. At fast heating rates ($\geq 50^\circ/\text{min}$), only one main peak can be observed at temperatures around 120°C-150°C corresponding to the dissolution of initially present GP zones. For the slow heating rate, 10°/min, the response of the material is much more complex. Actually it presents the whole decomposition process $\text{GP} \rightarrow \eta' \rightarrow \eta$ followed by the final dissolution of the η -phase. Once again this is in good agreement with previous SAXS results.

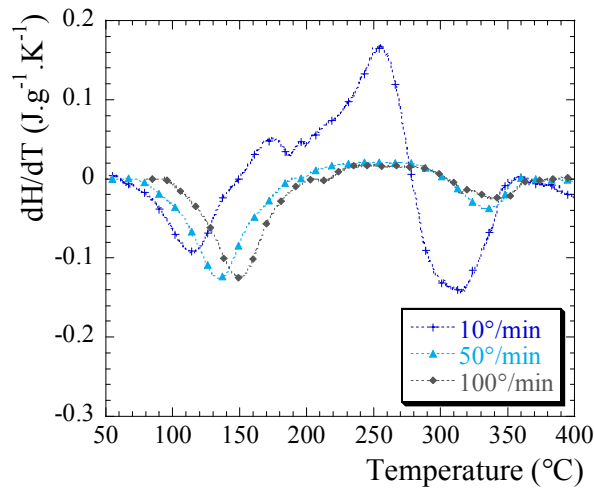


Figure IV.23: DSC scans of the T4 state at heating rate varying from 10°/min up to 100°/min.

Peak temperature analysis

The variation of the peak temperature with the heating rate can give an indication of the activation energy ΔE for dissolution by means of a peak temperature method developed by Kissinger [Kissinger, 1957]. This method was used by García-Cordovilla *et al.* [García-Cordovilla, 1990] and Dorward [Dorward, 1999]. Following this method, the experimental results of the variation of the peak temperature (T_p) with heating rate (h) are described by the equation:

$$\ln \frac{h}{T_p^2} = -\frac{\Delta E}{RT_p} + K \quad (IV.1)$$

where R is the gas constant,
 K is a constant.

This method has been applied to the determination of the activation energy for dissolution of GP zones in the T4 material and for the dissolution of the η' -phase in the T6 and T7 states. Dissolution of the η -phase has not been studied due to the complexity of the corresponding dissolution peak (superposition of several peaks).

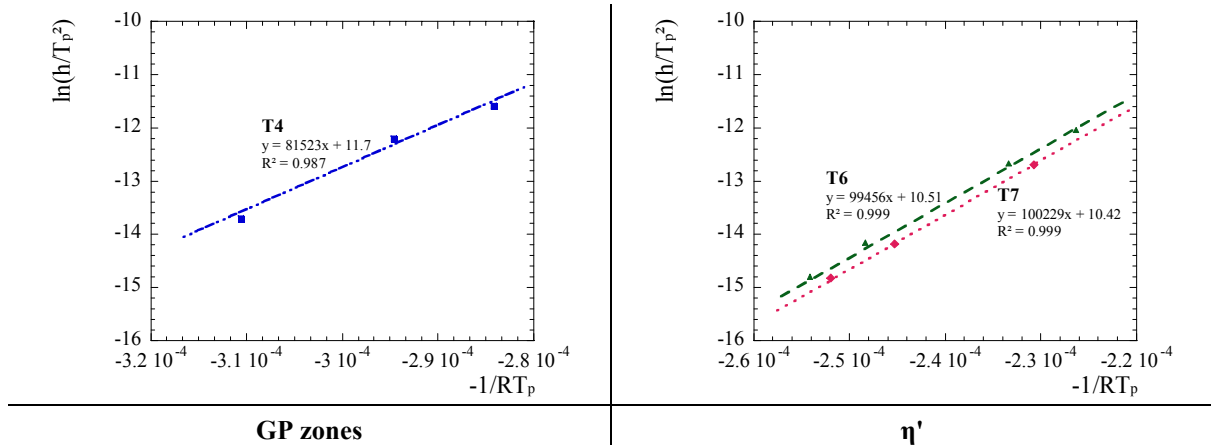


Figure IV.24: Peak temperature method applied to GP zones (T4) and η' (T6 and T7) dissolution.

The activation energies estimated from this procedure for dissolution of GP zones and the η' -phase are displayed in Table IV.2, together with the reported values from the literature. Our results are within the range of magnitude reported by Donoso and García-Cordovilla. For GP zones the activation energy is in good agreement with the migration energy for magnesium-vacancy complexes, whereas, for the η' -phase, the activation energy is in reasonable agreement (slightly lower) with values for diffusion of zinc and magnesium in aluminium ($115\text{-}130\text{ kJ.mol}^{-1}$) [Dorward, 1999; Donoso, 1985].

	Activation energy obtained from experimental data (kJ.mol^{-1})	Reported activation energy in the literature (kJ.mol^{-1})	
GP zones	81.5	75	[Donoso, 1985], Al-4.5at%Zn-1.75at%Mg aged at 25°C
η'	99.5 (T6)	88.4	[García-Cordovilla, 1990], 7075-T6
	100.2 (T7)	116	[Donoso, 1985] Al-4.5at%Zn-1.75at%Mg aged at 120°C

Table IV.2: Tabulation of activation energy for dissolution of GP zones and η' -phase, as obtained from peak temperature analysis and compared with reported values in the literature.

Comparison of DSC and SAXS

DSC and SAXS results obtained on T4 and T6 materials have been compared for a heating rate of $10^\circ/\text{min}$ in Figure IV.25. The correspondence in terms of temperature ranges between both experiments is particularly good.

The volume fraction of precipitates involved in reactions can be related to the area under the curve of the DSC scan, ΔH_r . This relationship can be written:

$$\Delta H_r = C f_v \quad (IV.2)$$

The maximum volume fraction is thus expected to correspond to the end of a positive peak. This can be observed in Figure IV.25.

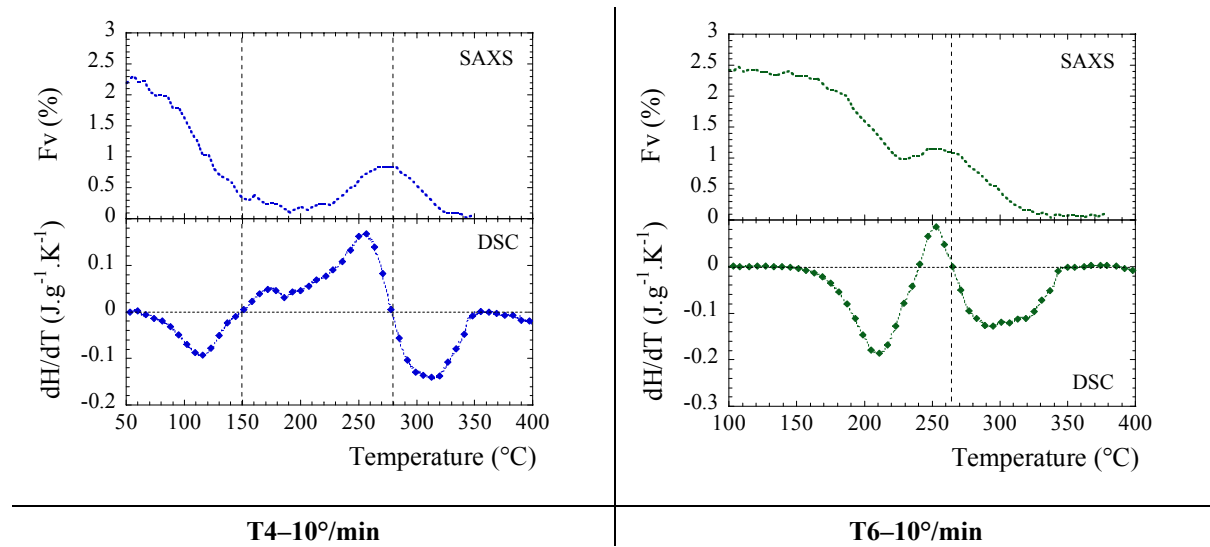


Figure IV.25: Comparison of continuous heating results obtained by SAXS and DSC on the T4 and T6 tempers at 10°/min.

Assuming that the constant C in equation (IV.1) does not depend on the nature of the particles, the integral curve of the DSC signal can be plotted *versus* the temperature and can be compared to the evolution of the volume fraction during continuous heating. The hypothesis is expected to be reasonable when considering phases like η' and η which are thermodynamically close together. The treatment has been applied to T6 and T7 tempers for slow heating rate (10°/min). Actually T6 and T7 materials only present during continuous heating reactions involving η' and η -precipitates. This figure clearly shows an excellent agreement between the DSC and SAXS experiments during continuous heating.

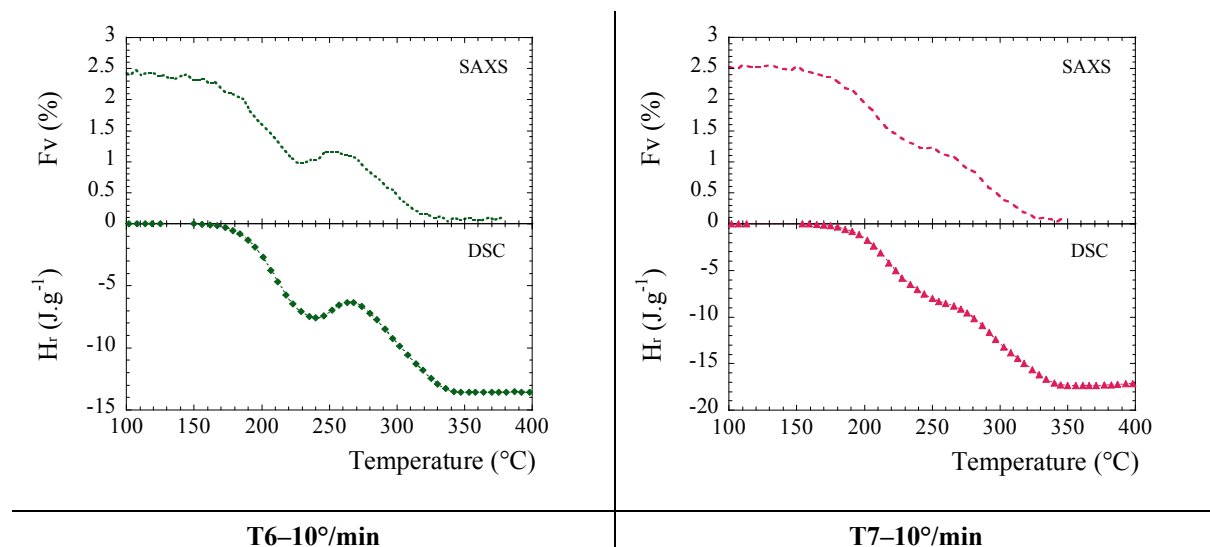


Figure IV.26: Resulted heat of reaction calculated as the integral curve of the DSC signal of T6-10°/min and T7-10°/min, compared with volume fraction estimated by SAXS.

IV.5. Summary

Two main features can be concluded from the analysis of this in-situ study:

- Temperature is the key parameter controlling the dissolution and coarsening mechanisms,
- The heating rate is the important parameter determining the phase transformation, from η' to η or for precipitation of η from the solid solution.

Since the heating rate is very high during welding (even in the transition zone of the T4 welds), no phase transformations are expected to occur during the heat input of the welding thermal cycle.

If we assume that the thermal cycle at each point of the heat-affected zone can be approximated by a heating part at a constant heating rate up to the peak temperature, followed by quenching, the resulting volume fraction and radius can be estimated using the results of continuous heating at high heating rate ($300^\circ/\text{min}$). During continuous heating the microstructure is known at each temperature and the peak temperature is known at each point in the heat-affected zone. Such a reconstruction is displayed in Figure IV.27. Even if some differences remain due to the assumptions concerning the simplified thermal profile, the dissolution events are correctly represented. Then, if we are able to model the precipitation behaviour during continuous heating, then the model will be expected to represent satisfactorily the as-welded precipitation microstructure.

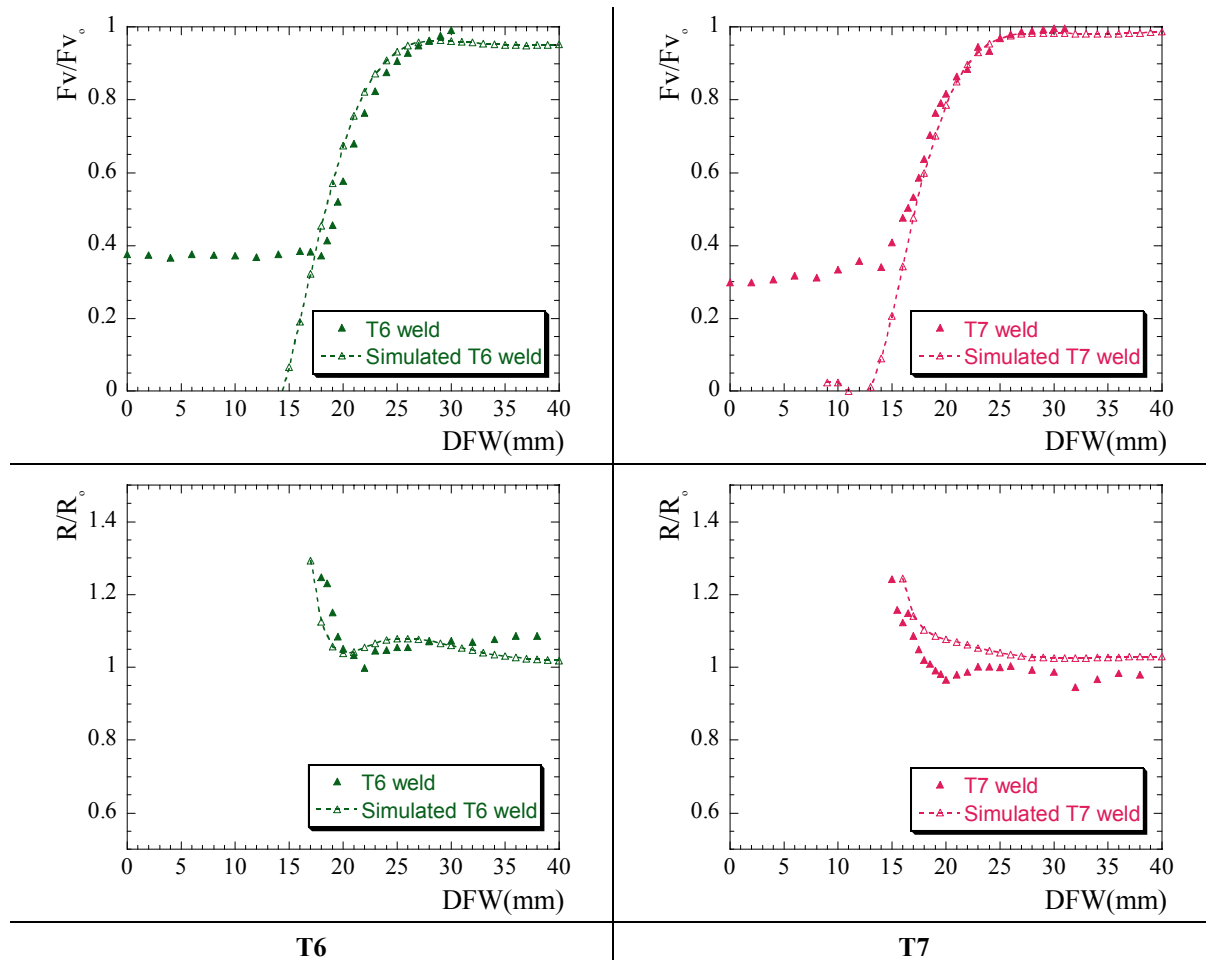


Figure IV.27: Reconstruction of the response of T6 and T7 materials during the heating part of the welding process from continuous heating at 300°C , comparison with measured relative volume fraction just after welding.

F_{v_0} and R_0 are respectively the volume fraction and radius of the initial T6 and T7 states.

Chapter V. Modelling of precipitation evolution during non-isothermal heat treatments

The goal of this section is to describe the evolution of a given precipitate distribution submitted to various heat treatments by the way of simple modelling. This modelling is based on the Myhr-Grong process model developed for Al-Mg-Si alloys adapted to the case of alloys of the 7xxx series. After a short literature review on pre-existing modelling approaches of the precipitation evolution through nucleation, growth and coarsening, the modelling of precipitation evolution in ternary alloys used in this study will be presented and finally applied to our system and compared to experimental data for both in-situ experiments and welding.

V.1. Literature review: precipitation modelling

Precipitation modelling is generally described by three different mechanisms taking place in the evolution history of a precipitate family: nucleation, growth and coarsening. They correspond to three extreme cases, as illustrated in Figure V.1.

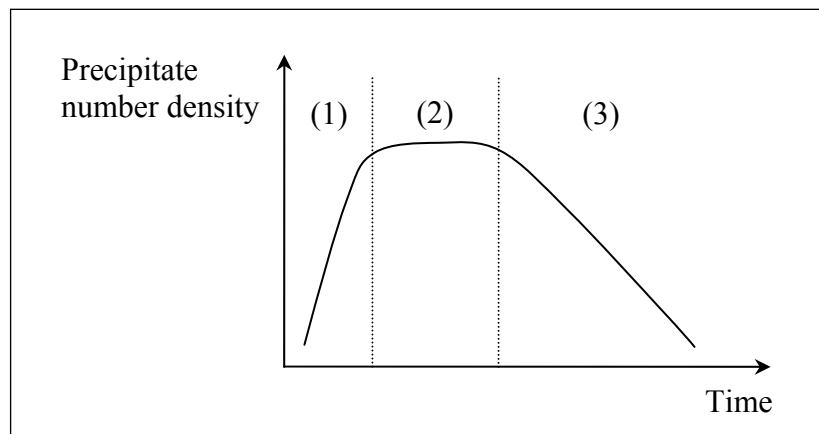


Figure V.1: Schematic variation of the precipitate number density with ageing time.

In zone (1), nucleation, increasing the particle number, is the predominant mechanism, followed by the growth of the resulting particles (zone (2)). Finally, coarsening of the precipitates, favouring large particles at the expense of the smaller ones, becomes predominant in zone (3), leading to a decrease of the particle number density.

For simplicity, some authors describe the time-dependence of the volume fraction using a power law, the Johnson-Mehl-Avrami approach. Some others tend to establish physical laws to describe nucleation, growth and coarsening. In this classical approach, the three mechanisms are considered as separate processes [Martin, 1997; Wagner, 1991]. More recent approaches aim to consider the three processes as concomitant and to handle them simultaneously, in particular by way of numerical modelling.

V.1.1. The JMA approach

To describe the overall microstructural evolution with time during an isothermal heat treatment, some authors like Staley [Staley, 1987], Bratland *et al.* [Bratland, 1997] or Myhr *et al.* [Myhr, 1991] assumed that the fraction transformed X follows a Johnson-Mehl-Avrami equation:

$$X = 1 - \exp(-kt^n) \quad (V.1)$$

where t is the ageing time,
 k is a kinetic constant,
 n is a time exponent.

For diffusion-controlled processes, the time exponent n is varying between 0.5 and 2.5, depending on the assumptions of the model (nucleation rate, morphology of the precipitates, etc.). In practice, the value of n is not constant and varies along the precipitation reaction. During the early stages of decomposition, the time exponent is low due to transient effects. Towards the end of the nucleation regime, the time exponent achieves its maximum value, indicative of diffusion-controlled growth of the particles. It remains constant along the growth regime. At long ageing times, the microstructure tends to the coarsening regime characterised by a lower time exponent.

V.1.2. The classical nucleation, growth and coarsening laws

V.1.2.1. Early stages of decomposition

Two main processes are still in debate to describe the early stage of precipitation of a new phase from the supersaturated solid solution: the classical nucleation and the spinodal decomposition. The normal precipitation reaction involves a thermally activated nucleation step, whereas spinodal decomposition is caused by small fluctuations in composition and decomposes spontaneously (it is also thermally activated but does not require an incubation time). In the following of this work, we will focus on the classical theory of nucleation, generally accepted to describe correctly the early stage of decomposition in metallic systems.

The driving force for microstructural changes during precipitation of a new phase from the supersaturated solid solution is the reduction of the chemical free energy. The free energy changes associated with nucleation are illustrated in Figure V.2. The α matrix at an alloy composition of C_0 is supersaturated with respect to the equilibrium solubility C_α while the stable β phase has a composition of C_β . The reduction of chemical free energy per mole of precipitate is ΔG (see Figure V.2).

Per unit volume of β , the free energy can be written (assuming that activities can be approximated by concentrations, ideal – dilute – solution approximation):

$$\Delta G = -\frac{RT}{V_\beta} \left[C_\beta \ln \frac{C_0}{C_\alpha} + (1 - C_\beta) \ln \left(\frac{1 - C_0}{1 - C_\alpha} \right) \right] \quad (V.2)$$

where V_β is molar volume of β .

If β is almost pure B, then $C_\beta \approx 1$, the chemical driving force can be approximated as:

$$\Delta G = -\frac{RT}{V_\beta} \ln \frac{C_0}{C_\alpha} \quad (V.3)$$

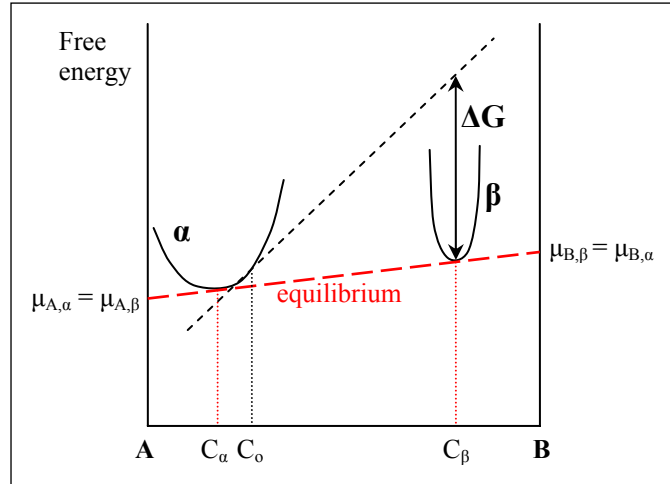


Figure V.2: Free energy as a function of composition for a binary alloy. ΔG illustrates the driving force for nucleation.

The nucleation kinetics have frequently been described in terms of cluster dynamics models. The cluster dynamics approaches are mainly due to Volmer and Weber [Volmer, 1925], Becker and Döring [Becker, 1935] and Zeldovich [Zeldovich, 1949]. Developed models treat solute fluctuations as droplets of β -phase embedded into the α matrix; the interface between α and β is assumed to be sharp (see Figure V.4).

The change in free energy for precipitation of a new β -precipitate is associated with the change in volume free energy Δg_v (<0) and the interfacial energy σ required to form the new interface. With solid systems a strain energy term Δg_{el} (>0) may also be introduced. For a spherical cluster of radius r , the change in free energy can be written:

$$\Delta G(r) = (\Delta g_v + \Delta g_{el}) \frac{4}{3} \pi r^3 + 4\pi r^2 \sigma \quad (V.4)$$

The first term (<0) accounts for the gain of free energy on forming the particle whereas the second (>0) corresponds to energy to form the interface.

The resulting formation energy ΔG versus the size of the cluster r passes through a maximum at $r=r^*$ (see Figure V.3):

$$r^* = \frac{2\sigma}{-(\Delta g_v + \Delta g_{el})} \quad (V.5)$$

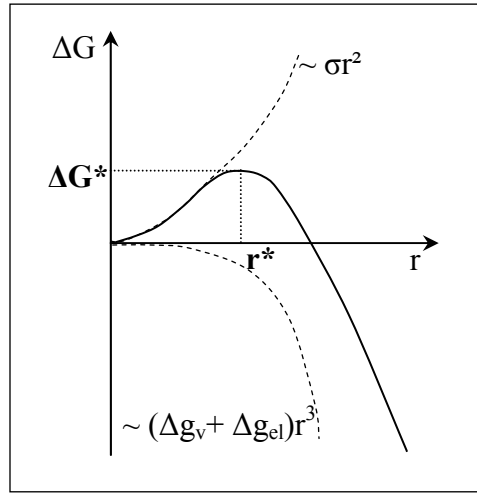


Figure V.3: Schematic representation of free energy changes associated with cluster formation as a function of cluster radius (r).

Clusters of radius r^* are in unstable equilibrium with the solid solution. Therefore only clusters with radii which exceed the radius r^* of the critical nucleus are predicted to grow. The associated critical activation free energy (called activation barrier for nucleation) is:

$$\Delta G^* = \frac{16\pi}{3} \frac{\sigma^3}{(\Delta g_v + \Delta g_{el})^2} \quad (V.6)$$

Here different approaches diverge in the way to describe the probability that a critical cluster will become supercritical. Either, once one atom is added to the cluster, this one become stable [Volmer, 1925]; or some probability to dissolve remains for a cluster slighter bigger than the critical size [Becker, 1935] leading to the introduction of the Zeldovich factor Z [Zeldovich, 1949]. In both cases, nucleation is a thermally activated process with the activation energy being equal to ΔG^* . The steady-state nucleation rate J_s (number of nuclei formed per unit time and unit volume) as proposed by the Becker-Döring theory is:

$$J_s = Z\beta^* N_0 \exp\left(-\frac{\Delta G^*}{kT}\right) \quad (V.7)$$

where β^* is the atomic impingement rate, assumed to be proportional to the cluster area

$$(\beta^* = \frac{4\pi r^{*2} DC_0}{a^4}),$$

Z is the Zeldovich factor (in the order of 1/20 to 1/40; its reciprocal value corresponds approximately to the width of the potential barrier at a distance (kT) below the maximum),

N_0 is the number of potential nucleation sites.

Steady-state is reached immediately. To take into account the time dependence of the nucleation rate $J^*(t)$, an incubation period τ is introduced:

$$J^*(t) = J_s \exp\left(-\frac{\tau}{t}\right) \quad (V.8)$$

with

$$\tau = \frac{1}{2\beta^* Z} \quad (V.9)$$

V.1.2.2. Growth kinetics

All structural changes in the solid state require atomic movement. This movement can occur over short range (order of the atomic spacing) or long range (inter-particles distances) length scales. Precipitation reactions involve both short range atomic movement at the interface (because the matrix and the precipitate have different crystal structures) and long range transport (diffusion) to change the local solute concentrations. The rate controlling step (interface mobility or diffusion) will determine the kinetics of the precipitation reaction.

The interface reaction is likely to be the slower step during the early stage of precipitation since the diffusion distances are very small, while at larger particles sizes diffusion is likely to be the rate controlling step since large amounts of solute need to be brought to or removed from the interface. It is then generally accepted that growth is dominated by diffusion.

A spherical particle of radius r embedded in a supersaturated matrix will grow at a rate [Zener, 1949; Aaron, 1971; Wagner, 1991] (see Figure V.4):

$$\frac{dr}{dt} = \frac{\bar{C}(t) - C_i}{C_p - C_i} \frac{D}{r} \quad (V.10)$$

where $\bar{C}(t)$ is the mean concentration of the matrix, far away from the precipitate,
 C_i is the interfacial concentration,
 C_p is the concentration of the precipitate,
 D is the diffusion coefficient.

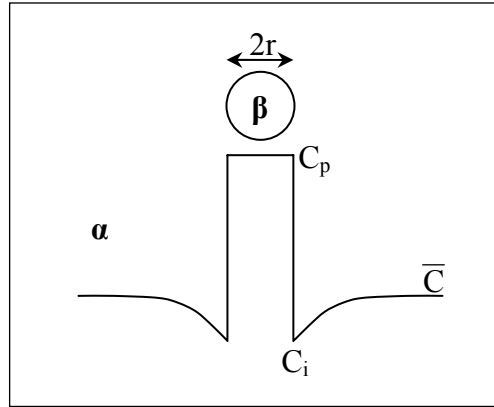


Figure V.4: Spatial variation in solute distribution during nucleation and growth of a β -precipitate embedded in the α matrix. \bar{C} is the concentration far away from the interface; C_p is the concentration of the β -precipitate; C_i is the interfacial concentration.

The concentration $C_i(r)$ at a curved interface can be related to the interface concentration at a flat interface C_i^∞ using the Gibbs-Thompson equation. Moreover C_i^∞ can be assimilated to the equilibrium solute concentration of the matrix at the temperature considered. In the case of a binary alloy, assuming a regular solution behaviour, the Gibbs-Thompson equation can be written:

$$C_i(r) = C_i^\infty \exp\left(\frac{2\sigma V_m}{rRT C_p}\right) \quad (V.11)$$

where σ is the interfacial energy,
 V_m is the molar volume of precipitates,
 T is the absolute temperature.

V.1.2.3. Second-phase dissolution

When precipitates are held at temperatures above their solvus temperature, dissolution of the particles takes place under the chemical driving force arising from their instability at high temperatures. This process has not received the attention accorded to precipitate growth, even though this process is also of great interest, in particular during the welding process.

Aaron and Kotler [Aaron, 1971] studied in detail the dissolution of precipitates and showed that dissolution can not be simply treated as the reverse of growth, due to the different initial radii (approximately zero for growth and non-zero for dissolution) and to the different manners in which solute concentration varies with time (see Figure V.5).

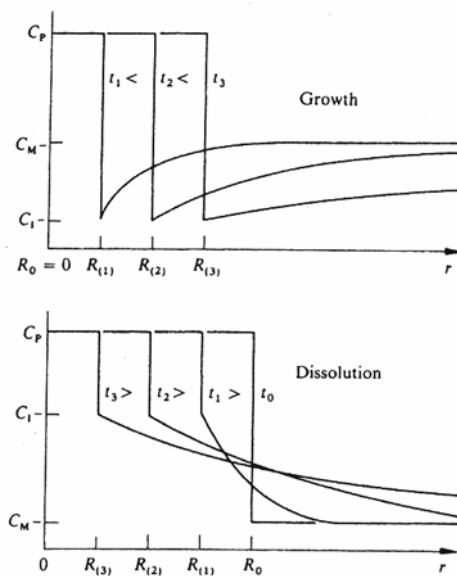


Figure V.5: Schematic comparison between precipitate growth and dissolution showing the differences in the time evolution of the concentration fields around the precipitate resulting from the difference in initial radius R_0 [Aaron, 1971].

However, for small supersaturations [Wagner, 1991], the rate law proposed for growth can also be used to describe by dissolution (see equation V.10). Either C_i exceeds the mean concentration \bar{C} , then particles tend to dissolve, or C_i is smaller than \bar{C} and precipitation growth proceeds.

V.1.2.4. Coarsening of precipitates

At long ageing times the precipitates coarsen to larger sizes in order to release their excess surface energy. According to the Gibbs-Thompson equation (see equation V.11), small particles have a larger ratio of surface area to volume, increasing their solubility as compared to larger particles. This leads to a size-dependent growth rate (see equation V.10), which is positive for larger particles with $\bar{C} > C_i(r)$ and negative for smaller ones with $\bar{C} < C_i(r)$. The growth rate becomes zero for particles with $\bar{C} = C_i(r^*)$. The corresponding critical radius r^* is derived from equation (V.10) as:

$$r^* = \frac{2\sigma V_m}{RTC_p} \frac{1}{\ln \frac{\bar{C}}{C_i^\infty}} \quad (V.12)$$

Hence, driven by the release of excess interfacial free energy, larger particles will grow at the expense of smaller ones. This process is commonly referred as coarsening or Ostwald ripening. Usually, the coarsening process is considered to be confined to the latest stages of the precipitation process.

To describe coarsening, the simple model of diffusional growth of isolated non-interacting particles with uniform size is no longer relevant. Actually, coarsening is a multi-particle diffusion problem. Lifshitz and Slyozov [Lifshitz, 1961] and Wagner [Wagner, 1961] developed a model, called the LSW-coarsening theory, taking into account the interaction between particles of different sizes. The LSW analysis showed that an initially narrow Gaussian distribution of precipitate sizes relaxes to a steady distribution of precipitate sizes. The steady-state LSW size distribution is shown in Figure V.6.

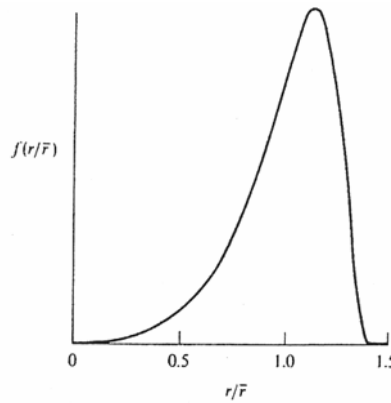


Figure V.6: Shape-invariant distribution function expected from the LSW theory during the steady-state regime. $f(r/\bar{r})$ is the frequency of occurrence of particles of reduced radius (r/\bar{r}) [Martin, 1997].

The LSW equation for the coarsening rate, after this steady distribution has been achieved, is:

$$\bar{r}(t)^3 - \bar{r}_0^3 = \frac{8 D \sigma V_m}{9 RT} \frac{1 - C_i^\infty}{C_p - C_i^\infty} t \quad (V.13)$$

V.1.3. Nucleation, growth and coarsening as coupled processes

Numerical approaches are attempting to consider nucleation, growth and coarsening as concomitant processes.

Some of them are for the moment dedicated to the early stages of decomposition processes. The cluster-dynamics approach is based on the exchange of solute atoms (monomers) between i-mers and is for the moment restricted to binary alloys and requires the knowledge of the initial cluster distribution and of the reaction rates. Monte-Carlo computer simulations consider nucleation as a stochastic process and are based on the nearest-neighbour interaction on a 3-dimensional lattice. For practical computational limitations the maximum size of the model alloy is restricted to the study of early stages of precipitation.

Other approaches apply the classical laws for nucleation and growth to particle distributions. As a consequence, coarsening is automatically included and does not require the introduction of a new equation. This allows us to follow the evolution of the particle distribution during various heat treatments. After first attempts by Langer and Schwarz [Langer, 1980], modified by Kampmann and Wagner [Kampmann, 1984], a complete numerical resolution of the

classical laws applied to particle distribution has been proposed by Wagner and Kampmann [Wagner, 1991]. This type of modelling has been successfully applied to welding of aluminium alloys of the 6xxx series by Myhr and Grong [Myhr, 2000].

V.2. Modelling of particle distribution

A model based on the Myhr-Grong model [Myhr, 2000], initially developed for Al-Mg-Si alloys, has been adapted for this study to the precipitation evolution in Al-Zn-Mg alloys during non-isothermal heat treatments. The model is based on the classical laws of precipitate evolution [Wagner, 1991] and its originality lies in the fact that these laws have been applied to each size class of the particle distribution. The model has been implemented for 7xxx series in the same way as described by Myhr and Grong [Myhr, 2000]. The only difference stems from the determination of the interfacial concentration (see V.2.1.2. Determination of the interfacial concentration). No nucleation or phase transformations have been considered.

V.2.1. Two basic equations

V.2.1.1. Growth/Dissolution equation

The model is based on a classical law governing both dissolution and growth (equation V.10):

$$v = \frac{dr}{dt} = \frac{\bar{C} - C_i(r)}{C_p - C_i(r)} \frac{D}{r}$$

where r is the radius at time t ,

\bar{C} is the mean solute concentration in the matrix (at%),

$C_i(r)$ is the solute concentration at the particle/matrix interface (at%),

C_p is the solute concentration of the precipitate (at%),

D is the volume diffusion coefficient in the matrix ($\text{m}^2 \cdot \text{s}^{-1}$).

All concentrations are relative to the limiting species regarding diffusion (here magnesium solute atoms). \bar{C} is obtained by a mass balance, C_p is known, considering only pure intermetallics (MgZn_2).

$C_i(r)$ remains to be estimated.

V.2.1.2. Determination of interfacial concentration

The interfacial concentration $C_i(r)$ is the solute concentration at the particle/matrix interface. In the case of a diffusion-controlled process, $C_i(r)$ can be approximated by the equilibrium concentration of the matrix in presence of a particle of radius r at the considered temperature. In the case of a binary alloy, the temperature determines this equilibrium concentration, using the Gibbs-Thompson equation (equation V.11) to consider the radius dependence:

$$C_i(r) = C_i^\infty \exp\left(\frac{2\sigma V_m}{rRT C_p}\right)$$

where C_i^∞ is the equilibrium concentration of solute across a planar interface (at%) (given by the phase diagram),

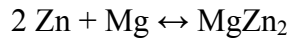
σ is the particle/matrix interfacial energy ($\text{J} \cdot \text{m}^{-2}$),

V_m is the molar volume of the precipitate $MgZn_2$ ($m^3 \cdot mol^{-1}$),
 C_p is the atomic fraction of solute in the precipitate,
 T is the absolute temperature (K),
 R is the universal gas constant ($8.314 J \cdot K^{-1} \cdot mol^{-1}$).

Considering a ternary alloy, the equilibrium diagram is not sufficient to determine univoquely $C_i(r)$ (any tie-line can give a local equilibrium interface condition). Therefore, another equation is needed. Two hypotheses are commonly used: the pseudo-binary assumption [Bratland, 1997] or the flux equality equation [Maugis, 2002].

Determination of the solvus boundary

Let us consider the chemical reaction:



According to the general law of chemical equilibrium, the Gibbs free energy ΔG° is:

$$\Delta G^\circ = \Delta H^\circ - T\Delta S^\circ = -RT \ln K = -RT \ln \frac{a_{Zn}^2 a_{Mg}}{a_{MgZn_2}} \quad (V.14)$$

where K is the solubility product and a_k the respective activity of Zn, Mg and $MgZn_2$.

According to classical thermochemistry:

$$\begin{aligned}
 a_k &= 1 \text{ for a precipitate,} \\
 \text{and } a_k &= C_k^\circ \text{ for a dilute solid solution}
 \end{aligned}$$

where C_k° is the atomic fraction of atom k .

Consequently the solubility product can be written:

$$\ln K = \ln((C_{Zn}^\circ)^2 C_{Mg}^\circ) = \frac{\Delta S^\circ}{R} - \frac{\Delta H^\circ}{RT} \quad (V.15)$$

where C_{Zn}° and C_{Mg}° are the equilibrium atomic fractions of Zn and Mg respectively.

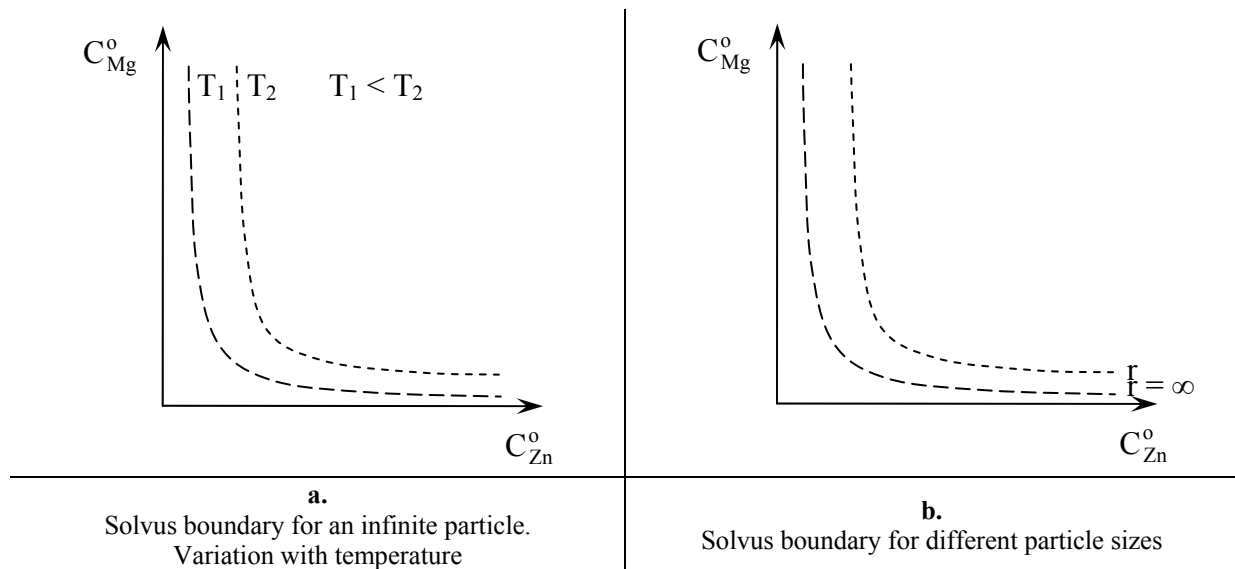


Figure V.7: Schematic representation of the equilibrium solubility limit derived from the solubility product. Influence of temperature (a) and particle curvature (b).

Figure V.7 is a schematic representation of the obtained solubility limit as obtained from the solubility product. These considerations can be used in the determination of the equilibrium concentration of an infinite (or planar) precipitate. When considering a particle of radius r , the stability is decreased by the Gibbs-Thompson effect due to curvature. Thus the solvus boundary is given by the Gibbs-Thompson relationship generalised to the solubility product:

$$K(r) = K_{\infty} \exp\left(\frac{2\sigma V_m}{rRT}\right) \quad (V.16)$$

where $K(r)$ is the solubility product of a particle of radius r ,

K_{∞} is the solubility product corresponding to an infinite (or planar) particle as discussed above.

Pseudo-binary equilibrium

The pseudo-binary equilibrium [Bratland, 1997] assumes that diffusion of solute elements is the same, therefore the equilibrium concentration $C_i(r)$ follows the stoichiometry of the reaction, as illustrated in Figure V.8. The location of $C_i(r)$ is the intersection between the solubility limit for a particle of radius r and the stoichiometric line corresponding to the precipitation reaction. Moreover the mean concentration in matrix \bar{C} is determined by the stoichiometry of the reaction.

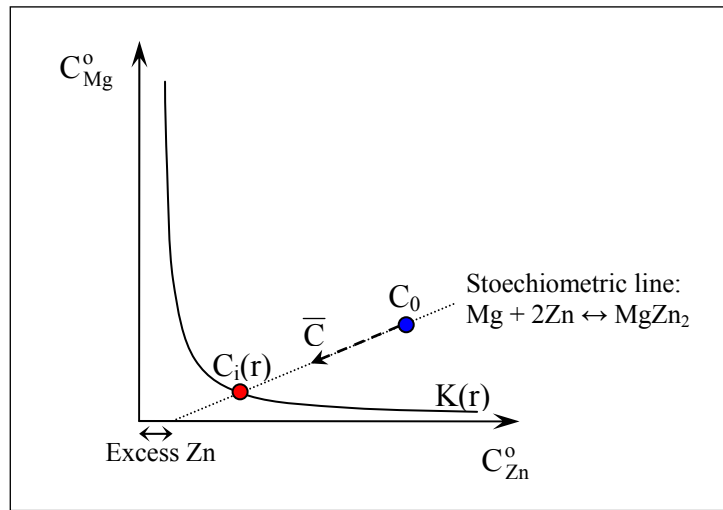


Figure V.8: Pseudo-binary equilibrium defining $C_i(r)$. Mean concentration (\bar{C}) displacements during the precipitation reaction of $MgZn_2$ are also displayed.

The assumption of pseudo-binary equilibrium implies that the equilibrium concentration remains constant for a given temperature. We will see that it is not the case when considering the two different diffusion rates for Mg and Zn.

Flux equality equation

To take into account the difference in diffusion of the different elements, the equality of interfacial fluxes of Zn and Mg can be written [Maugis, 2002]:

$$D_{Zn}(C_{i,Zn}(r) - \bar{C}_{Zn}) = 2D_{Mg}(C_{i,Mg}(r) - \bar{C}_{Mg}) \quad (V.17)$$

where D_{Zn} and D_{Mg} are the respective diffusion coefficients of Zn and Mg,

$C_{i,Zn}(r)$ and $C_{i,Mg}(r)$ are the interfacial concentration of Zn and Mg of a particle of radius r ,

\bar{C}_{Zn} and \bar{C}_{Mg} are the mean concentration in Zn and Mg in the matrix far from the particle.

$C_i(r)$ (referring to the specie limiting the diffusion) is then determined by the intersection between the solubility limit $K(r)$ and the flux equality equation. The flux equality equation is in practice a line going through the point corresponding to the mean concentration in matrix and which slope is $\frac{D_{Zn}}{2D_{Mg}}$. This is illustrated in Figure V.9.

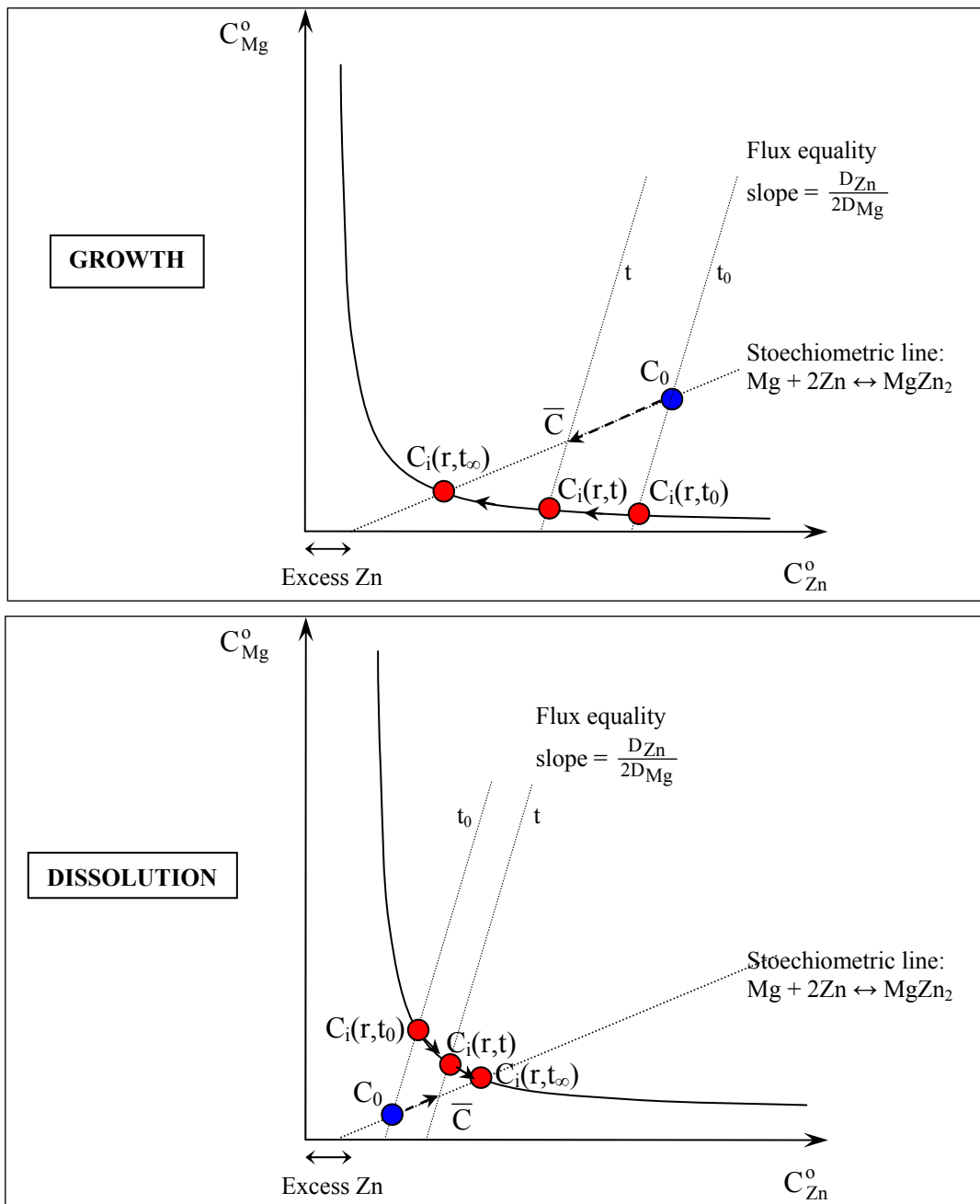


Figure V.9: Flux equality defining $C_i(r)$ and corresponding displacements during the growth or dissolution reaction of $MgZn_2$. Mean concentration (\bar{C}) displacements are also displayed.

In the present case, at a given temperature, the interfacial concentration is moving during the precipitation or dissolution reaction. At long times $C_i(r)$ tends towards the stoichiometric value. Note that the mean radius is increasing (by coarsening) during a precipitation reaction to tend towards the absolute equilibrium (corresponding to an infinite particle).

One should note that pseudo-binary equilibrium is a particular case of flux equality assumption in the case of identical diffusion coefficients for Zn and Mg.

V.2.2. Particle size distribution

As proposed by Myhr and Grong [Myhr, 2000], the control volume approach is used to describe the evolution of a distribution of particles. The particle distribution is discretized into a series of classes of particles whose size ranges between r and $r+\Delta r$. Each class contains $N(r)$ particles per unit volume. The evolution of each size class is controlled by the basic equations presented in the latter section.

Determination of the number density

To better understand this approach, let us consider two size classes whose growth rates $v = \frac{dr}{dt}$ are positive, i.e. $r > r^*$. These two classes are in the growth regime. This case is illustrated in Figure V.10. The calculation of the particle density within each control volume is highly dependent on the sign of the growth rate defined at the limit of the control volume $v_{i-1/2}$ and $v_{i+1/2}$.

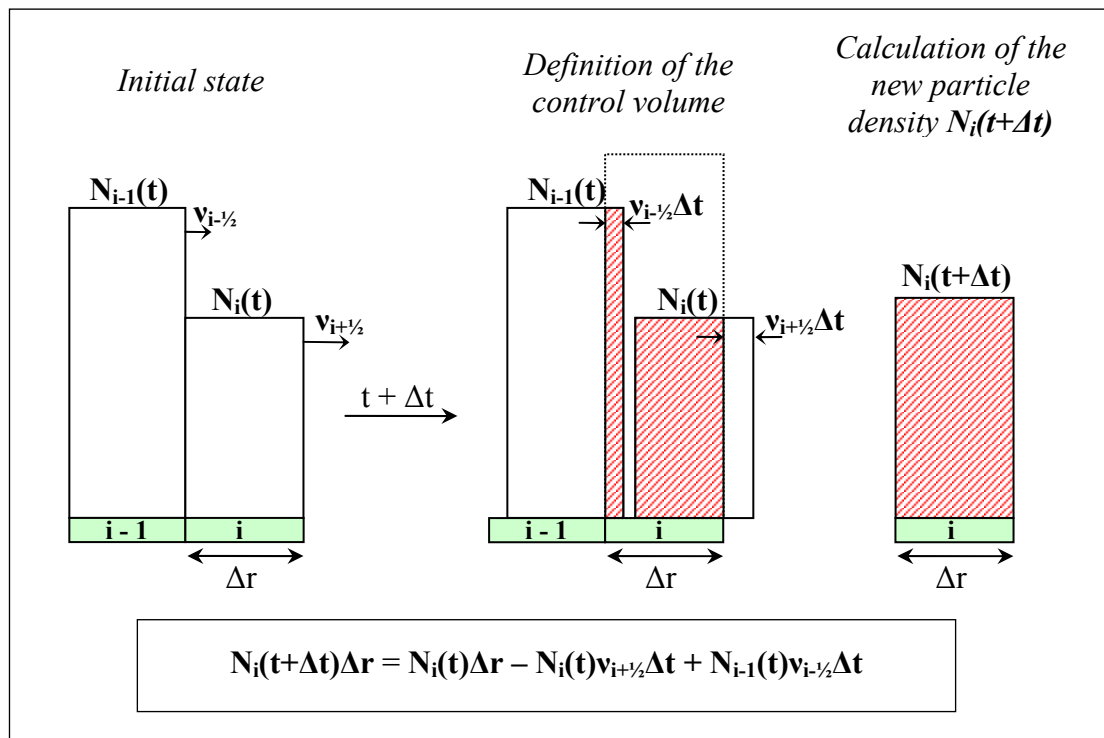


Figure V.10: Calculation of the particle density after an increment of time Δt . Case where two adjacent classes are in growth, i.e. $v_{i-1/2}$ and $v_{i+1/2}$ are positive.

The particle densities corresponding to the different combinations are displayed in Table V.1.

Calculation of the mean-values

The mean radius \bar{r} of the precipitates is defined as:

$$\bar{r} = \frac{\sum_i N_i r_i}{\sum_i N_i} \quad (V.18)$$

where N_i is the density of particles (in $\#/m^3$) in the size class i and r_i is the radius corresponding to the size class i .

Velocity conditions	Number density $N(t+\Delta t)$
$v_{i-1/2} > 0$ and $v_{i+1/2} > 0$	$N_i(t+\Delta t) = N_i(t) - N_i(t) v_{i+1/2} \frac{\Delta t}{\Delta r} + N_{i-1}(t) v_{i-1/2} \frac{\Delta t}{\Delta r}$
$v_{i-1/2} < 0$ and $v_{i+1/2} < 0$	$N_i(t+\Delta t) = N_i(t) - N_i(t) v_{i-1/2} \frac{\Delta t}{\Delta r} + N_{i+1}(t) v_{i+1/2} \frac{\Delta t}{\Delta r}$
$v_{i-1/2} < 0$ and $v_{i+1/2} > 0$	$N_i(t+\Delta t) = N_i(t) - N_i(t) v_{i-1/2} \frac{\Delta t}{\Delta r} - N_i(t) v_{i+1/2} \frac{\Delta t}{\Delta r}$

Table V.1: Determination of the number density in a control volume after an increment time Δt under the different velocity conditions. Note that the condition ($v_{i-1/2} > 0$ and $v_{i+1/2} < 0$) is not considered because not met in the reality.

The volume fraction of particles f_v is:

$$f_v = \sum_i \frac{4}{3} \pi r_i^3 N_i \quad (V.19)$$

The total number of particles N is given by:

$$N = \sum_i N_i \quad (V.20)$$

From mass balance, the mean concentration \bar{C} in the matrix is:

$$\bar{C} = \frac{C_0 - C_p f_v}{1 - f_v} \quad (V.21)$$

Time and boundary conditions

An auto-adapting time increment is calculated at each step of the process to avoid any size class moving more than one size element. Δt is calculated in such a manner that the class presenting the highest velocity v_{\max} will move $\frac{1}{2}\Delta r$. It should be noted that in practice v_{\max} is experienced by the smallest size class of the distribution, which is dissolving.

For very small precipitates, infinite velocities can be calculated due to limitations of the assumptions involved in the growth-rate equation. Therefore a cut-off value of the size distribution is chosen to avoid the interfacial concentration becoming higher than the precipitate composition.

At the opposite end of the distribution, if the largest size class is in the growth regime, i.e. $v(i_{\max}+1/2)$ is positive, then at each time step a new size class will be created, even if $v(i_{\max}+1/2)$ is very small. At the next step this new size class ($i_{\max}+1$) which may contain very few particles/ m^3 (often less than 1 particle/ m^3) will create another size class ($i_{\max}+2$), and so on...

Thus the number of classes would impractically grow without limit. To avoid this type of behaviour inherent to the control volume approach, a new size class can be created exclusively when the corresponding particle density is higher than 1 particle/m^3 . Otherwise the particles are left in their previous size class.

V.3. Calibration of the model

The model parameters, defined in the following section, have been calibrated using experimental data obtained from reversion treatments.

V.3.1. Model parameters

The parameters which need to be calibrated in the model are thermodynamic in nature (the solubility product), the interfacial energy of the η -phase and the diffusion coefficients for both zinc and magnesium. The Gibbs free energy (ΔG°) and the diffusion coefficients are temperature-dependent whereas the surface energy of the precipitates σ is considered as constant.

The Gibbs free energy is:

$$\Delta G^\circ = \Delta H^\circ - T\Delta S^\circ \quad (V.22)$$

where ΔH° is the formation enthalpy of the η -phase and

ΔS° is the entropy variation relative to the formation of the η -phase.

For the sake of simplicity, ΔH° and ΔS° are considered to be constant with temperature.

The diffusion coefficients are described by an Arrhenius law:

$$D = D_0 \exp\left(-\frac{Q_{\text{diff}}}{RT}\right) \quad (V.23)$$

where D_0 is the frequency factor and

Q_{diff} is the activation energy barrier.

Model parameters		Reference values reported from the literature
ΔG°	$\Delta H^\circ \text{ (J.mol}^{-1}\text{)}$	to compare with phase diagrams (see Chapter II.1.1.1) [Petrov, 2000; Pandat]
	$\Delta S^\circ \text{ (J.mol}^{-1}\text{.K}^{-1}\text{)}$	
D_{Mg}	$D_{0,\text{Mg}} \text{ (m}^2\text{.s}^{-1}\text{)}$	[Bakker, 1990]: $D_{0,\text{Mg}} = 1.24 \text{ cm}^2\text{.s}^{-1}$; $Q_{\text{diff,Mg}} = 130.4 \text{ kJ.mol}^{-1}$ Generally accepted: $D_{\text{Mg}} < D_{\text{Zn}}$
	$Q_{\text{diff,Mg}} \text{ (J.mol}^{-1}\text{)}$	
D_{Zn}	$D_{0,\text{Zn}} \text{ (m}^2\text{.s}^{-1}\text{)}$	[Bakker, 1990]: $D_{0,\text{Zn}} = 0.25 \text{ cm}^2\text{.s}^{-1}$; $Q_{\text{diff,Mg}} = 119.6 \text{ kJ.mol}^{-1}$ [Takahashi, 2000]: $D_{0,\text{Zn}} = 0.68 \text{ cm}^2\text{.s}^{-1}$; $Q_{\text{diff,Mg}} = 124.8 \text{ kJ.mol}^{-1}$
	$Q_{\text{diff,Zn}} \text{ (J.mol}^{-1}\text{)}$	
$\sigma \text{ (J.m}^{-2}\text{)}$		[Martin, 1997]: $0.02 < \sigma < 0.6 \text{ J.m}^{-2}$ for metallic precipitates in a metallic matrix (smallest σ correspond to fully coherent precipitates and largest to incoherent precipitates) [Guyot, 1996]: $\sigma = 0.35 \text{ J.m}^{-2}$ for η'

Table V.2: Summary of model parameters and reported reference values from the literature.

All the parameters to be calibrated are summarised in Table V.2, together with reference values reported from the literature.

V.3.2. Calibration for the T7 temper

Experimental data obtained from reversion treatments performed in the temperature range 200-300°C have been used to calibrate the model parameters. The T7 temper contains mainly η -precipitates whose solvus boundary is now well established (see Chapter II.1.1.1).

ΔH°	ΔS°	$D_{0,Mg}$	$Q_{diff,Mg}$	$D_{0,Zn}$	$Q_{diff,Zn}$	σ
75 (kJ/mol)	21.4 (J/mol/K)	$1.3 \cdot 10^{-8}$ (m ² /s)	88.3 (kJ/mol)	$1.3 \cdot 10^{-7}$ (m ² /s)	88.3 (kJ/mol)	650 (mJ/m ²)

Table V.3: Calibrated model parameters for the T7 temper using experimental reversion treatments.

The best set of parameters obtained for the T7 temper are displayed in Table V.3.

The capacity of the model to describe precipitation evolution during a reversion treatment for a T7 initial temper at various temperatures is shown in Figure V.11. The agreement is very satisfying particularly in terms of the evolution of the volume fraction.

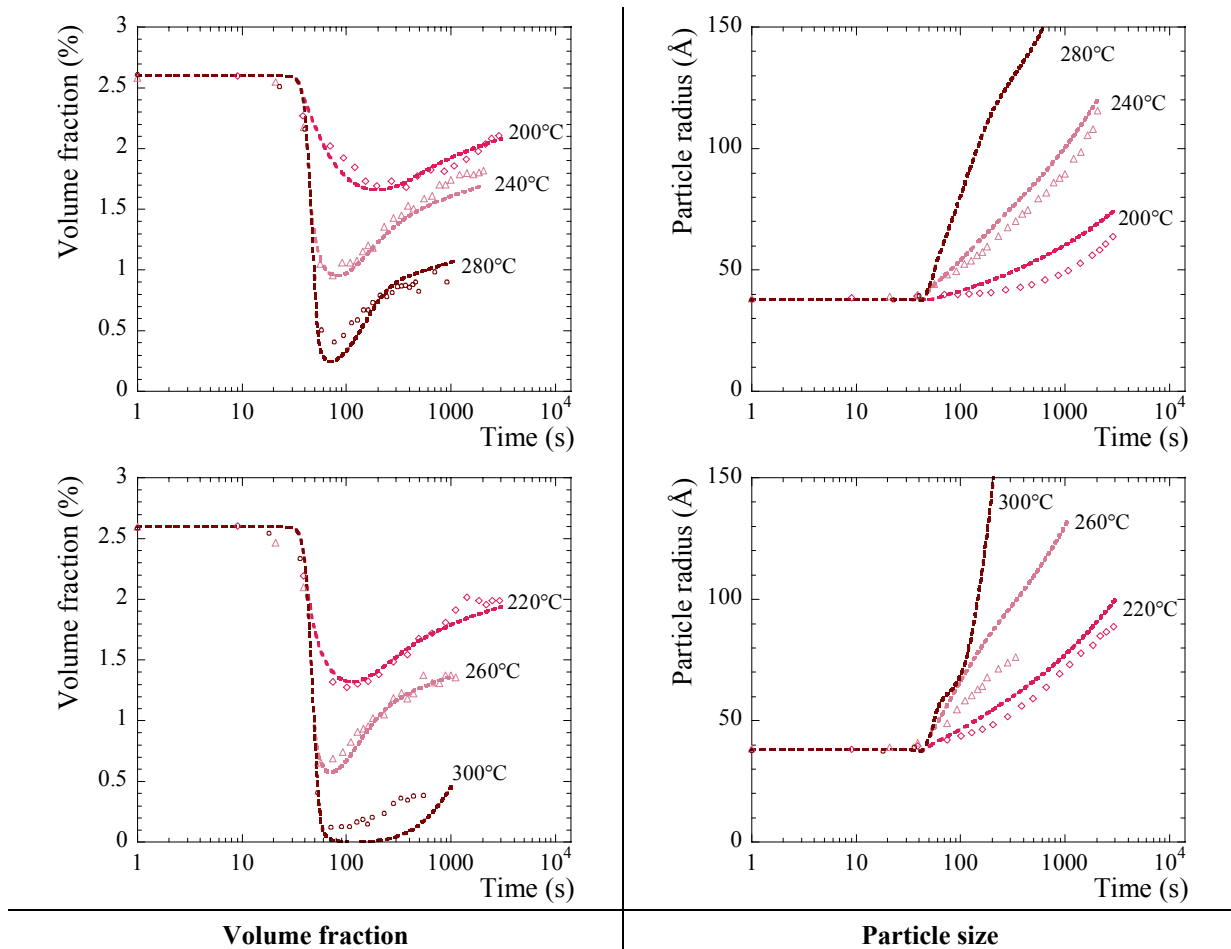


Figure V.11: Modelled precipitation evolution (in dashed line) as compared with experimental results (symbols) during reversion treatments varying from 200°C to 300°C for the T7 temper.

Relevance of the calibrated parameters

Concerning the interface energy, the calibrated value is somewhat higher than the expected value ($\sim 0.3\text{-}0.4\text{ J/m}^2$) for incoherent precipitates. This can be due to composition effects which are one of the limits of this program since an MgZn_2 composition is assumed for all precipitates. However it has been seen in Chapter II that the Zn/Mg ratio is smaller than the equilibrium value for all precipitates, including the η -phase. This can explain the overestimated σ value.

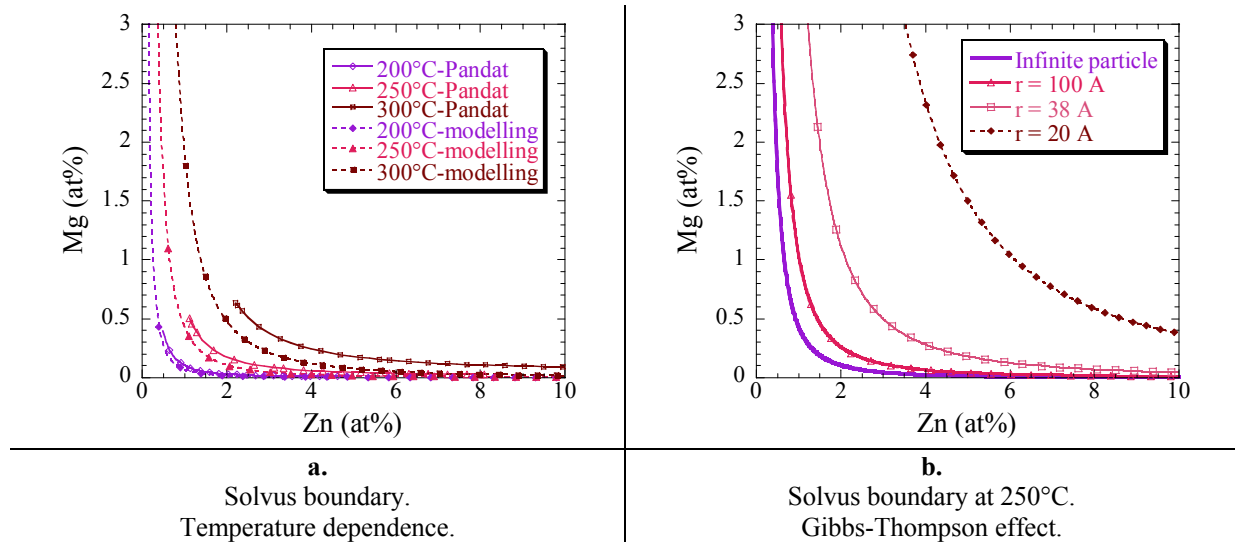


Figure V.12: Calculated solvus boundary of the η -phase using the solubility product approach; comparison with the solvus boundary as given by the Pandat software (a) and Gibbs-Thompson effect at 250°C for particles of different sizes (from 20 Å to 100 Å) compared with an infinite particle.

Using the resulting Gibbs free energy, the solvus boundary of the η -phase can be calculated for different temperatures using the solubility product approach (see equation V.15) and compared with the phase diagram proposed by Pandat (see Chapter II.1.1.1). This is done in Figure V.12.a. The agreement is reasonable. Moreover the influence of the curvature on the stability of the particle is shown in Figure V.12.b at 250°C using the Gibbs-Thompson effect. Even at low temperatures, small particles may be unstable due to size effects.

The diffusion coefficients are relatively far from those reported in the literature. The difference can be explained by the fact that generally the determination of diffusion coefficients is carried out using binary alloys. The possible interaction between the diffusion of zinc and magnesium atoms is not taken into account. Moreover the temperature range studied in our case is relatively small and thus we may not well describe the temperature dependence of the diffusion coefficients far from this temperature range (see Figure V.12).

One should note that the values obtained in the temperature range studied (200-300°C) as compared to the diffusion coefficients given by Bakker [Bakker, 1990] are relatively close. For example, at 250°C for the magnesium: $1.2 \cdot 10^{-17}\text{ m}^2/\text{s}$ for [Bakker, 1990] and $2 \cdot 10^{-17}\text{ m}^2/\text{s}$ in our case.

Sensitivity to parameters

We will discuss here the effect of the different parameters (ΔG° , σ , D_{Mg} , ratio $D_{\text{Mg}}/D_{\text{Zn}}$) on the precipitation evolution (see Figure V.13).

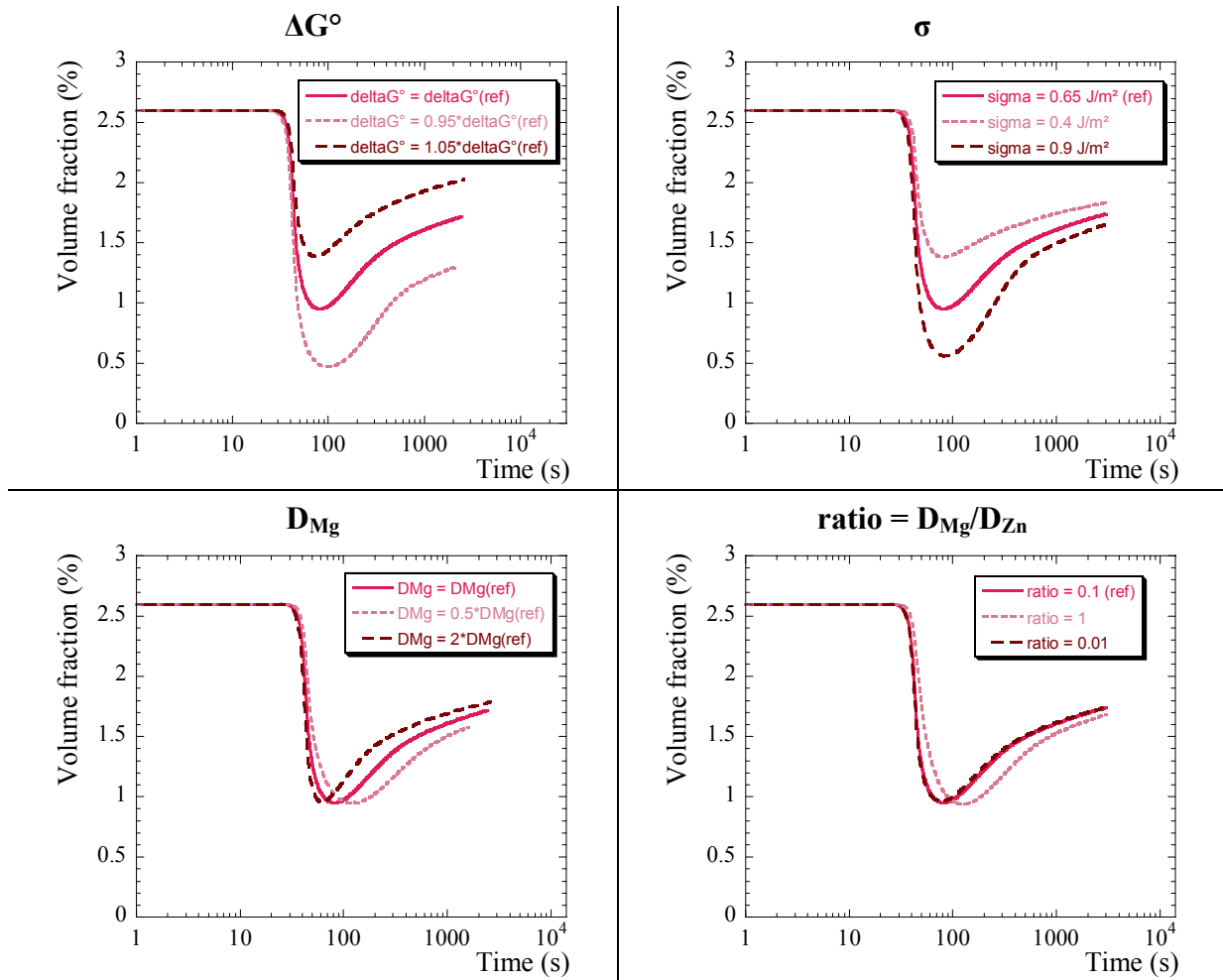


Figure V.13: Sensitivity to parameters. Variation of the precipitation evolution by changing ΔG° , σ , D_{Mg} and ratio D_{Mg}/D_{Zn} as compared to the calibrated reference values during a reversion treatment at 240°C.

The Gibbs free energy affects the competition between dissolution and growth and as expected is the only factor controlling the equilibrium volume fraction (volume fraction at long ageing times). As a consequence, for calibration, ΔG° can be determined for each temperature, independently of the other factors.

Once ΔG° is determined, the interfacial energy σ can be calibrated since these two parameters control the competition between growth and dissolution, in other terms the minimum of volume fraction. A larger interfacial energy tends to favour dissolution.

The last two parameters deal with diffusion coefficients of zinc and magnesium. They affect only the kinetics and not significantly the general behaviour of the precipitation evolution during the heat treatment.

The evolution of the particle distribution and characteristic features like the critical radius r^* will be discussed later in detail (see V.5. Discussion).

V.3.3. Calibration for the T6 and T4 tempers

T6 temper

The same procedure has been employed to determine model parameters for the T6 temper. Finally the same set of parameters as those obtained from the calibration for the T7 temper fits for the calibration of the T6 temper. Figure V.14 shows the results obtained for the T6 temper during reversion treatments in terms of volume fraction and particle size.

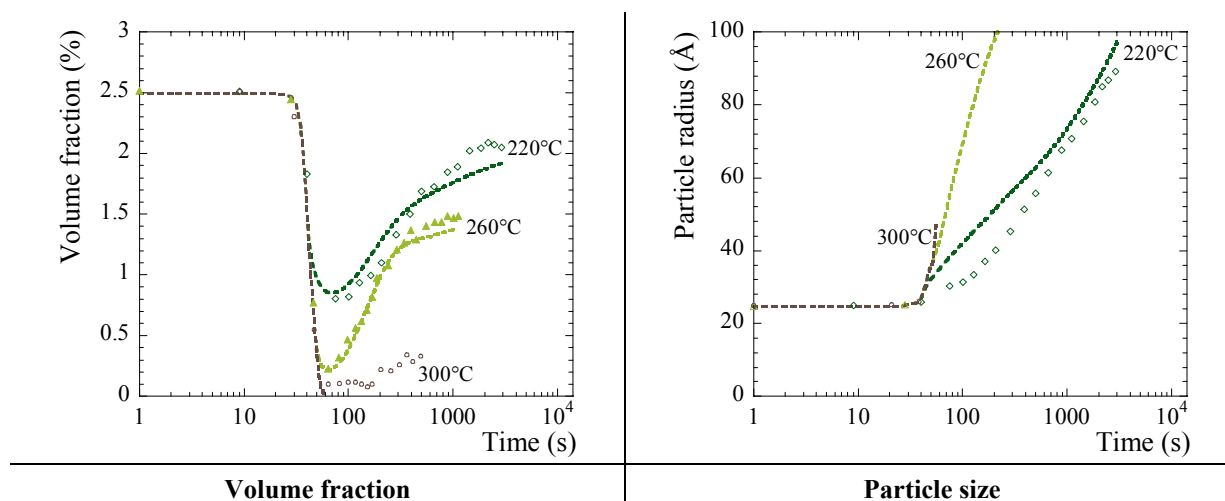


Figure V.14: Modelled precipitation evolution (in dashed line) as compared with experimental results (symbols) during reversion treatments at 220, 260 and 300°C for the T6 temper.

Of course, the diffusion coefficients have been kept equal to those obtained from the T7 calibration. Surprisingly the interfacial energy for η -precipitates also fits for η' -precipitates, even if it is expected that the interfacial energy for metastable precipitates should be smaller than that for stable precipitates. Moreover the T7 Gibbs energy values is also suitable for the T6 material. This means that the precipitates contained in the T6 and T7 tempers are very similar in nature and differences in reversion behaviour mostly arises from size effects (T6 contains smaller precipitates than T7). However we should be careful in such an interpretation: in fact, the model considers both η' and η -precipitates with an MgZn_2 composition. Even if this can be considered as true for the η -phase, it has been shown in Chapter II that the η' -phase does not respect this ratio. The introduction of this special composition in the model would modify the calibration and may result in a smaller interfacial energy and a different solvus boundary. Because of compositional uncertainties concerning the η' -phase, this has not been done.

Despite these compositional assumptions, the model predicts in a satisfying manner the general reversion behaviour.

T4 temper

Adjusting the model to the T4 temper is more adventurous since we have no reversion treatments available. However a set of parameters is proposed here, which has been directly fitted to the welding profiles. The set of parameters is displayed in Table V.4.

ΔH°	ΔS°	$D_{0,Mg}$	$Q_{diff,Mg}$	ratio = D_{Mg}/D_{Zn}	σ
48 (kJ/mol)	10 (J/mol/K)	$1.3 \cdot 10^{-8}$ (m ² /s)	75 (kJ/mol)	0.1	100 (mJ/m ²)

Table V.4: Calibrated model parameters for the T4 temper using welding profiles.

The diffusion coefficients for magnesium and zinc have been kept from the T7 calibration. Moreover the interfacial energy is 6 times smaller than that corresponding to η -precipitates. This is in general agreement with data reported from the literature for fully-coherent precipitates.

The thermodynamic parameters lead to a solvus boundary for GP zones located at lower temperatures than for the η -phase. The solvus temperature corresponding to an alloy composition can be calculated as:

$$T_{eq} = \frac{\Delta H^\circ}{\Delta S^\circ - R \ln((C_{Zn}^0)^2 C_{Mg}^0)} \quad (V.24)$$

The resulting solvus temperature in the case of our alloy is then 160°C. This is a reasonable value as compared to the generally observed temperature range corresponding to the reversion of GP zones [Radomski, 1979].

In summary, the model was calibrated for the three tempers using experimental data obtained from reversion heat treatments (except for the T4 temper). This calibration leads to physically reasonable parameters. This model will be now applied to the other non-isothermal heat treatments.

V.4. Application to non-isothermal heat treatments and welding

Using the parameters defined in the previous section, the model has been first applied to continuous heating and then to the more complex non-isothermal welding process. This section is dedicated to the comparison between experimental data and the results from modelling. The next section will discuss in detail the results and the interest of modelling in the understanding of precipitation evolution during isothermal or non-isothermal heat treatments.

V.4.1. Continuous heating

In order to estimate the capacity of the model to describe the precipitation evolution during non-isothermal heat treatments, the model has been applied to continuous heating.

T7 temper

The results obtained from the simulation for the T7 initial state submitted to continuous heating at 10°/min and 100°/min as compared with experimental data obtained from SAXS in-situ experiments are displayed in Figure V.15. Figure V.16 compares the volume fraction evolution from experimental SAXS investigations and from the simulation for all the experimented heating rates (from 10°/min to 300°/min).

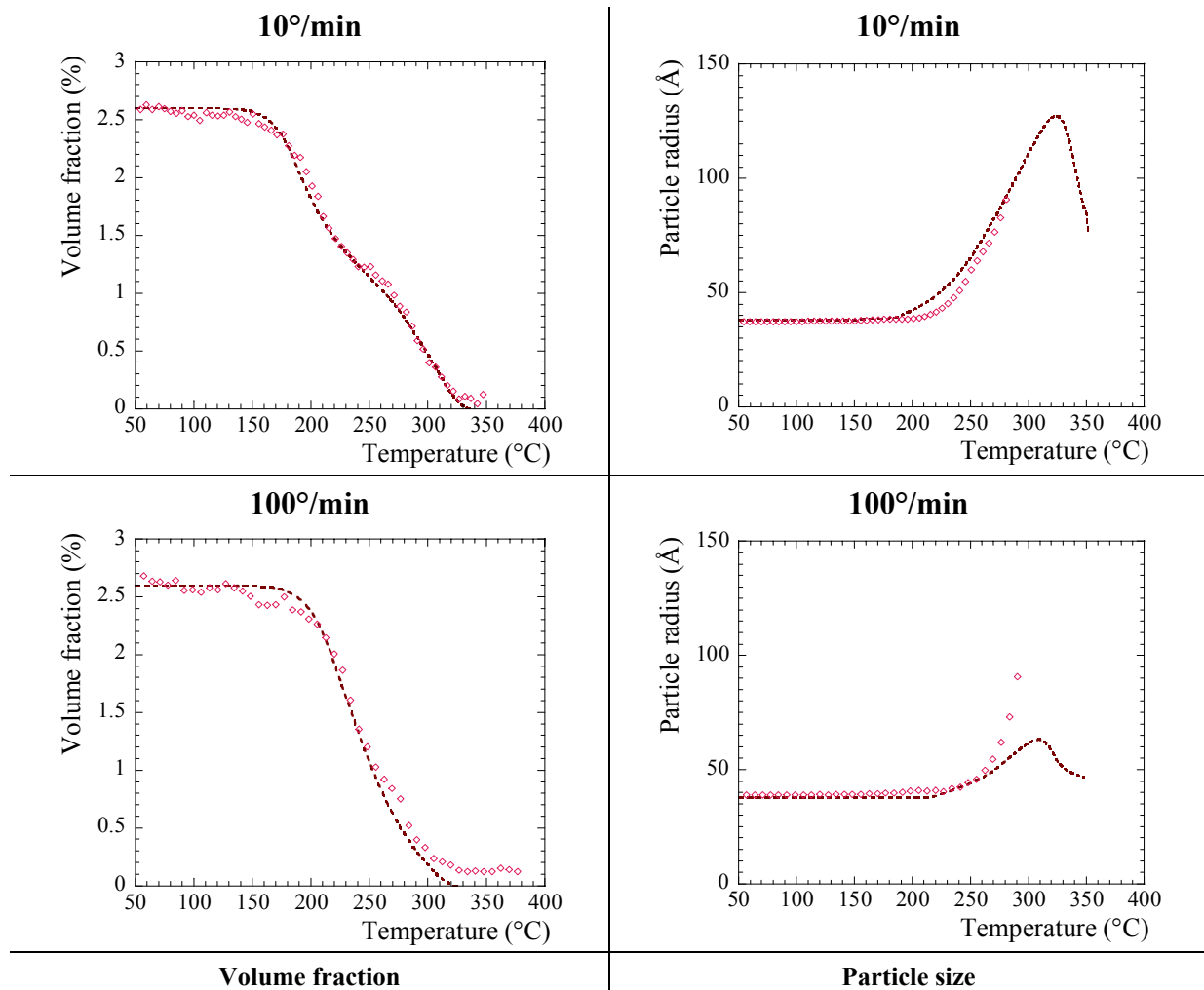


Figure V.15: Modelled precipitation evolution (in dashed line) as compared with experimental results (symbols) during continuous heating at $10^\circ/\text{min}$ and $100^\circ/\text{min}$ for the T7 temper.

One should note the excellent agreement between experimental results and simulation, notably in terms of volume fraction evolution. The model is able to reproduce the heating rate dependence of the dissolution profile by shifting the dissolution curve towards higher temperatures (see Figure V.16). Moreover, the modelled dissolution profile at the low heating rate ($10^\circ/\text{min}$) presents an inflexion point which exactly corresponds to the experimental curve (see Figure V.16). This inflexion point slightly disappears as the heating rate increases. This is in excellent agreement with what has been observed experimentally. In the former chapter, this phenomenon has been attributed to a phase transformation from η' to the η -phase (T7 is a mixture of $\eta'+\eta$). However the model does not take into account phase transformations. It considers only the evolution of the particle distribution of the η -phase. We will discuss this point in detail in the next section (V.5. Discussion).

Concerning the size evolution, the coarsening effect is well represented. For high heating rates the size evolution is slightly underestimated. It appears that high heating rates tend to inhibit coarsening.

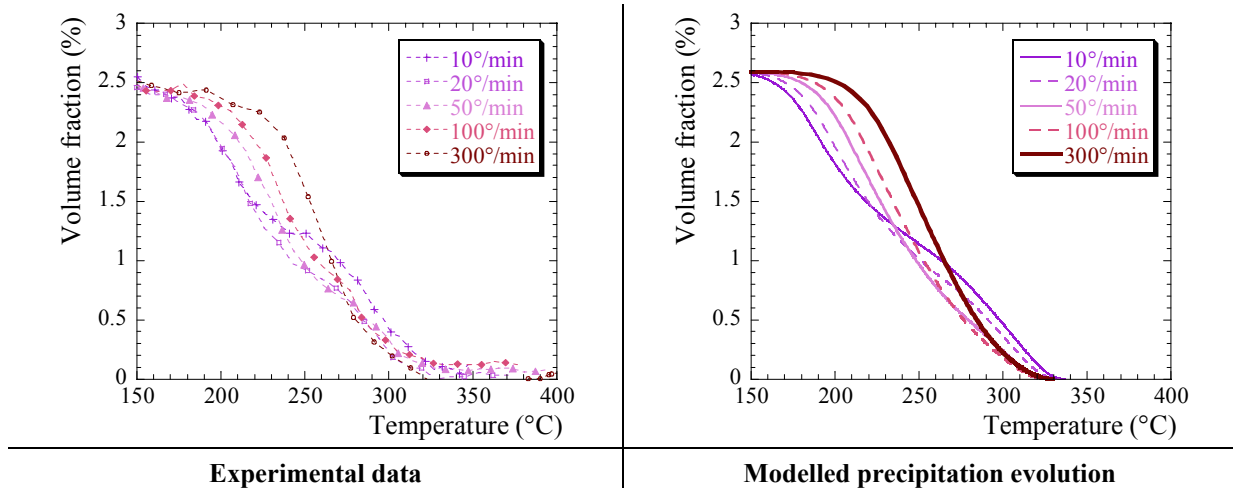


Figure V.16: Comparison between experimental data and modelled precipitation evolution of the T7 temper during continuous heating for heating rates varying from 10°/min to 300°/min.

T6 and T4 tempers

The results obtained from the simulation for the T6 temper are displayed in Figure V.17 and compared with the experimental data for heating rates varying from 10°/min to 300°/min.

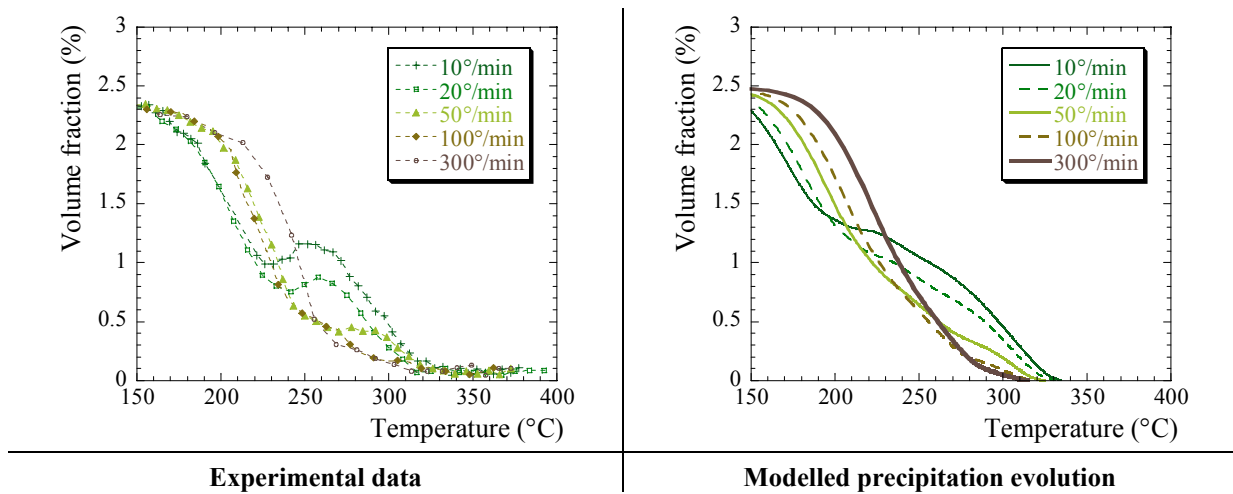


Figure V.17: Comparison between experimental data and modelled precipitation evolution of the T6 temper during continuous heating for heating rates varying from 10°/min to 300°/min.

As was the case for the T7 temper, the agreement between experiment and modelling is very satisfactory for the T6 temper. The temperature range of dissolution and the heating rate dependence are well reproduced. However the model is unable to reproduce the interruption and re-increase of the volume fraction around 250°C observed on the experimental curve. This is probably due to the phase transformation $\eta' \rightarrow \eta$.

Figure V.18 shows the evolution of the volume fraction of an initial T4 state during a continuous heating at 10°/min. The general shape of dissolution is reproduced. The model does not reproduce the re-precipitation of η -precipitates at high temperatures (~280°C) since nucleation is not included.

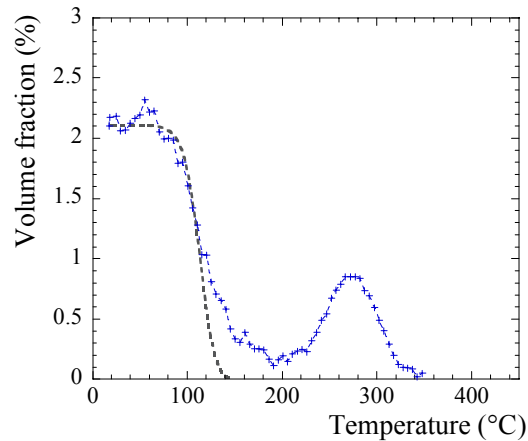


Figure V.18: Comparison between experimental data and modelled precipitation evolution of the T4 temper during continuous heating at 10°/min.

In summary the model very satisfactorily reproduces the experimental results obtained during reversion treatments and continuous heating. The agreement is particularly excellent for the T6 and T7 materials and is more questionable in the case of the T4 initial state due to a lack of experimental data and the fact that nucleation is not considered.

V.4.2. Welding

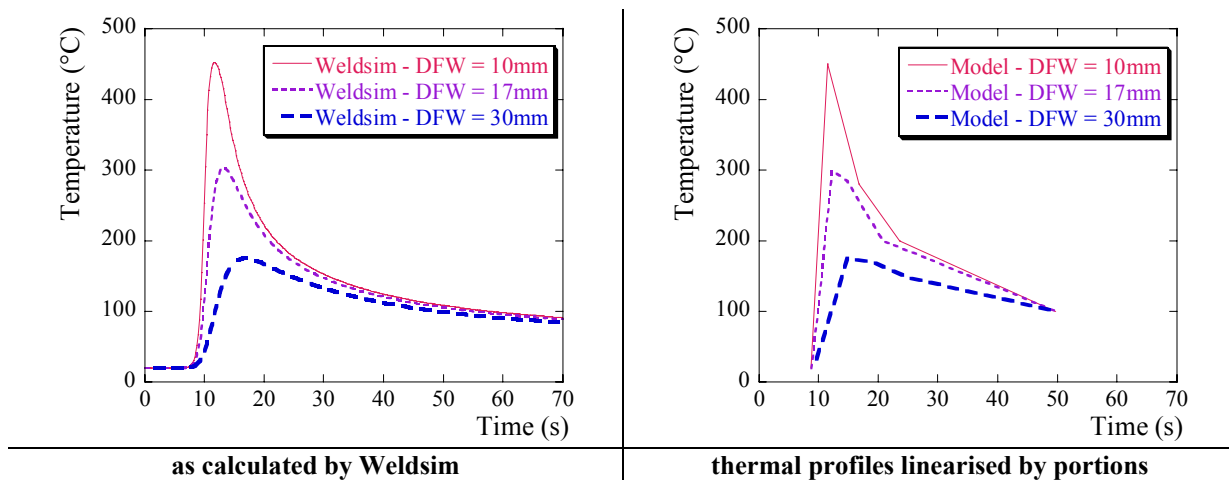


Figure V.19: Comparison between thermal profiles calculated by Weldsim and linearised by portions to be used in the model.

The model is now applied to the thermal profiles experienced in the heat-affected zone of welded materials. Each point of the heat-affected zone corresponds to a particular thermal cycle. This thermal profile is decomposed into several linear portions characterised by an initial and final temperature and its heating rate. This is illustrated in Figure V.19.

Experimental data (volume fraction and particle size) obtained from SAXS correspond to the resulting microstructures at the end of the thermal profile. In

Figure V.20 are presented results of the simulation as compared with experimental data at the end of the welding process.

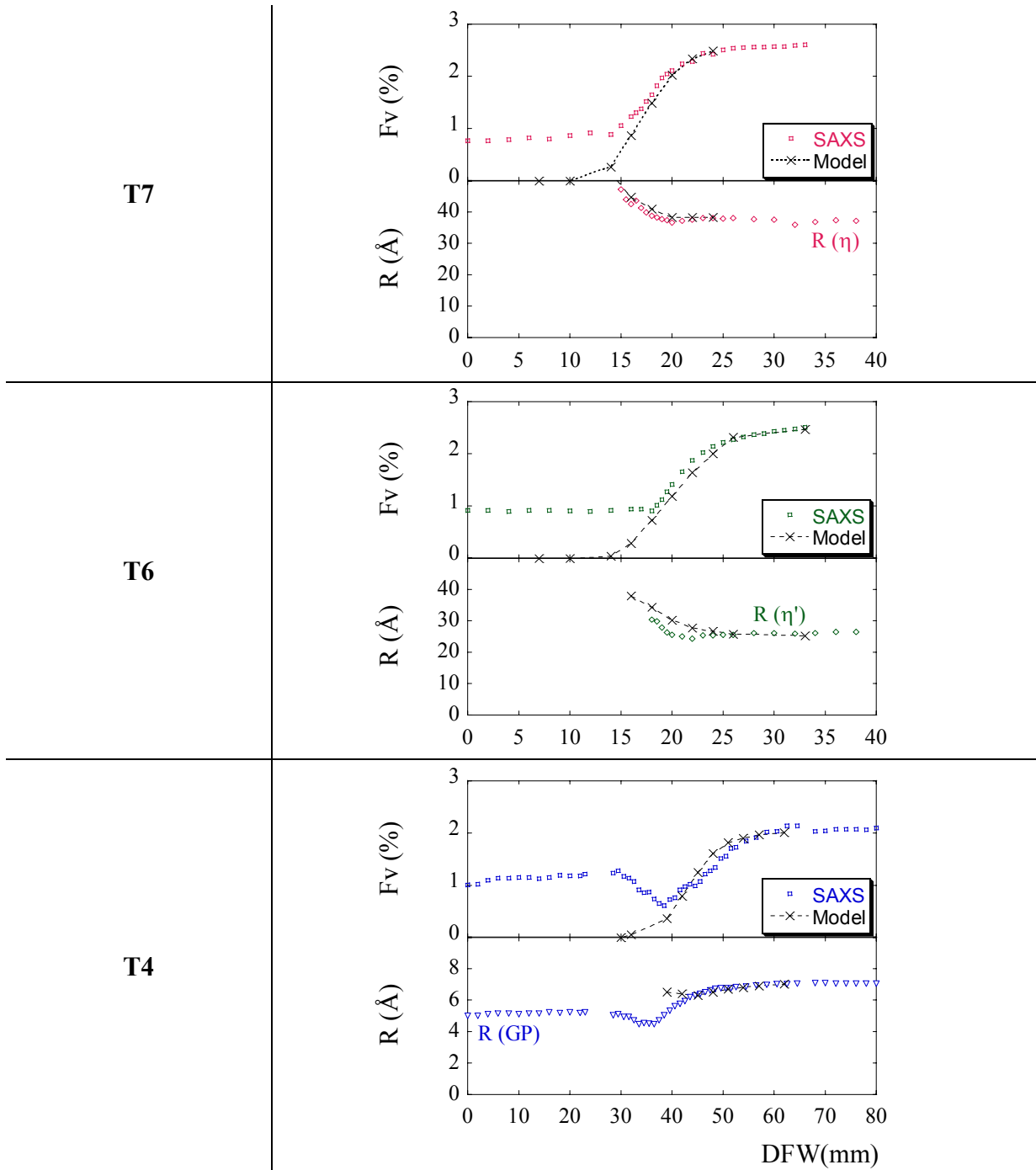


Figure V.20: Welding profiles in terms of volume fraction and particle size resulting from the modelling of the particle size distribution evolution submitted to welding thermal cycles for the three initial states.

The results of the model reproduce in a satisfactory manner the experimental results, in particular for the T6 and T7 tempers in terms of volume fraction and particle size. As the model does not integrate nucleation of GP zones from the solid solution, the precipitation of new GP zones during cooling and storage at room temperature can not be reproduced.

In the case of the T4 temper, a slight decrease in the particle size is described by the model in the transition zone but it is smaller than that experimentally observed. Some elastic effect should certainly be considered to model GP zones.

In summary, the model is very accurate in describing the experimental results for isothermal heat treatments, continuous heating and also the thermal history corresponding to welding. The model has been shown to be sufficiently versatile to be used in the future for the estimation of the microstructure after welding in different situations: effect of a pre-heating, different welding heat input, thermal contact with the outside, etc. Moreover it can also provide information for different compositions.

V.5. Discussion

Furthermore the interest of the model is not only to reproduce experimental results but also to aid in an understanding of the mechanisms controlling the evolution of the particle distribution during such heat treatments.

The model provides access to various internal variables which control the general precipitation evolution and which are not easily measured experimentally like the particle size distribution, the particle density, the mean concentration in solid solution, etc. The objective of this section is to determine the controlling parameters and to contribute to an understanding of how a particle distribution behaves during various heat treatments.

V.5.1. Precipitation evolution during isothermal heat treatments

We will begin this study with a simple heat treatment, i.e. isothermal reversion treatment. We will see how the particle distribution evolves and which parameters are controlling the dissolution to growth transition.

First, one should note that the minimum in the volume fraction observed during isothermal heat treatments is not due to a phase transformation but to the solute redistribution between the particles and the matrix. Of course some phase transformation may occur during the heat treatment and may modify the precipitation evolution but such a phase transformation is not necessary to explain the re-increase of the volume fraction.

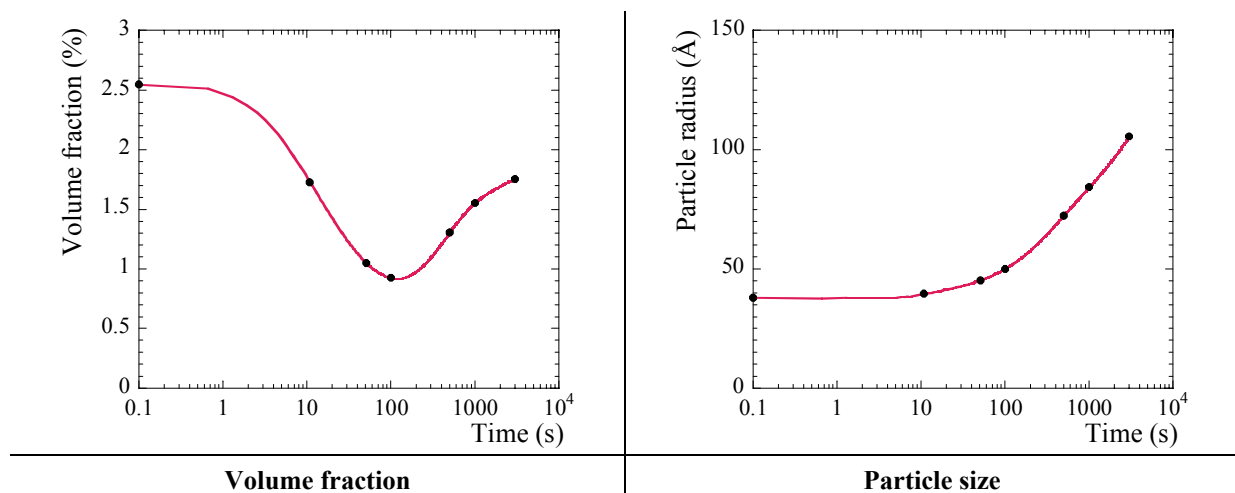


Figure V.21: Modelled evolution of the volume fraction and particle size of a T7 temper during an isothermal heat treatment at 240°C.

In this section dealing with isothermal heat treatments, we will take as an example a pure isothermal treatment (without prior heating) at 240°C on a T7 temper. The results in terms of

volume fraction and radius are displayed in Figure V.21. This example reproduces quite well the experimental observations:

- the volume fraction decreases down to a minimum and re-increases,
- the particle size remains constant at the beginning of the dissolution and then increases (coarsening).

Evolution of the particle distribution

The evolution of the particle distribution during the isothermal heat treatment at 240°C of the T7 temper is displayed in Figure V.22. The initial distribution corresponds to the experimental distribution as obtained from TEM observations.

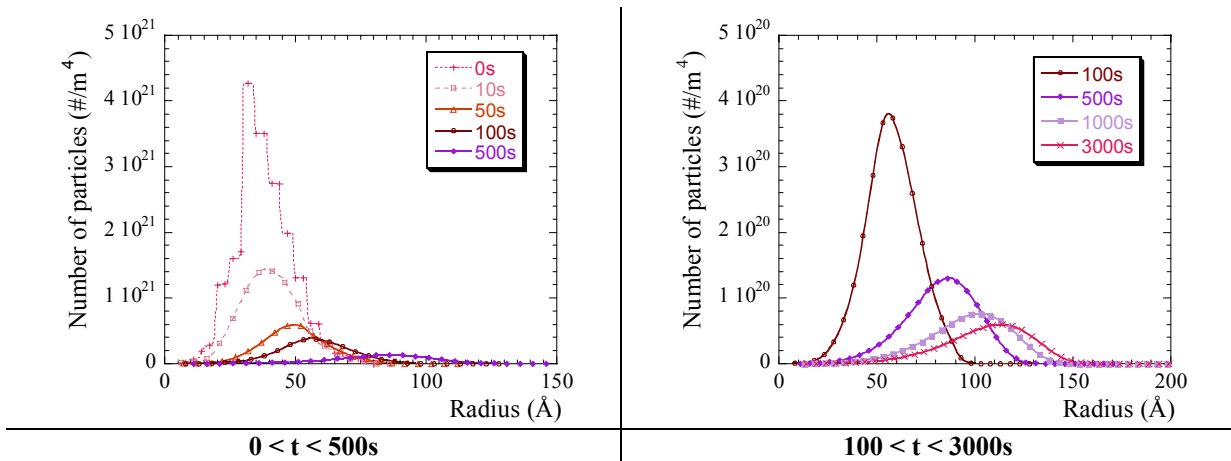


Figure V.22: Modelled evolution of the particle distribution of a T7 temper along the isothermal heat treatment at 240°C at different times corresponding to dots in Figure V.21.

At early stages (up to 10s), the area under the particle distribution is decreasing, illustrated by a reduction of the total number density by a factor of ~2 in 10s (see Figure V.23). However, the size range remains unchanged, giving rise to a large decrease of the volume fraction at a constant mean radius. For longer times, the distribution continues to decrease: the number density decreases by a factor of ~30 at 3000s as compared with the initial state (see Figure V.23). This time, the distribution enlarges towards higher particle sizes, leading to a progressive increase of the mean radius.

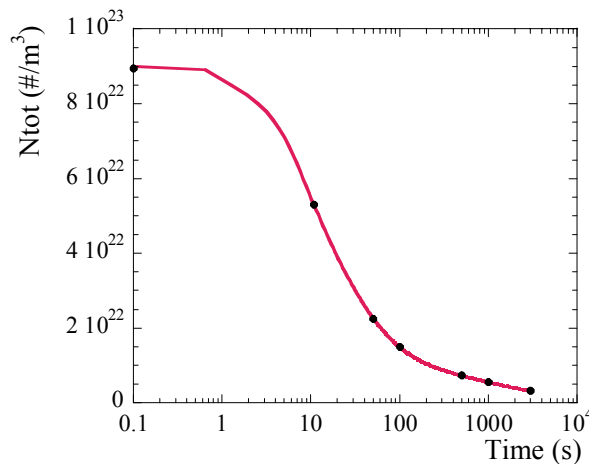


Figure V.23: Modelled evolution of the total number density along the isothermal heat treatment at 240°C of a T7 temper.

For long ageing times the particle distribution is expected to reach a stationary regime described by the LSW theory. The comparison between modelled size distribution and LSW steady-state distribution is made in Figure V.24. One can see that the agreement is not satisfying in particular concerning the cut-off value of the size distribution for $r = 1.5.r^*$ predicted by the LSW theory, which is not respected in our case. This may arise from the fact that general equations of the LSW theory are written in the case of binary alloys under mean-field assumptions.

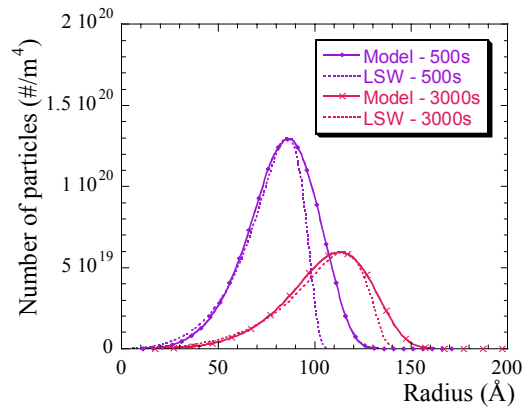


Figure V.24: Comparison between the modelling and the LSW theory for a T7 temper aged at 240°C for 500 and 3000s.

Evolution of the critical radius r^*

The critical radius r^* is the factor controlling the dissolution/growth competition [Myhr, 2000]. Its evolution at different ageing times is shown in Figure V.25, as compared to the particle distribution and the mean radius.

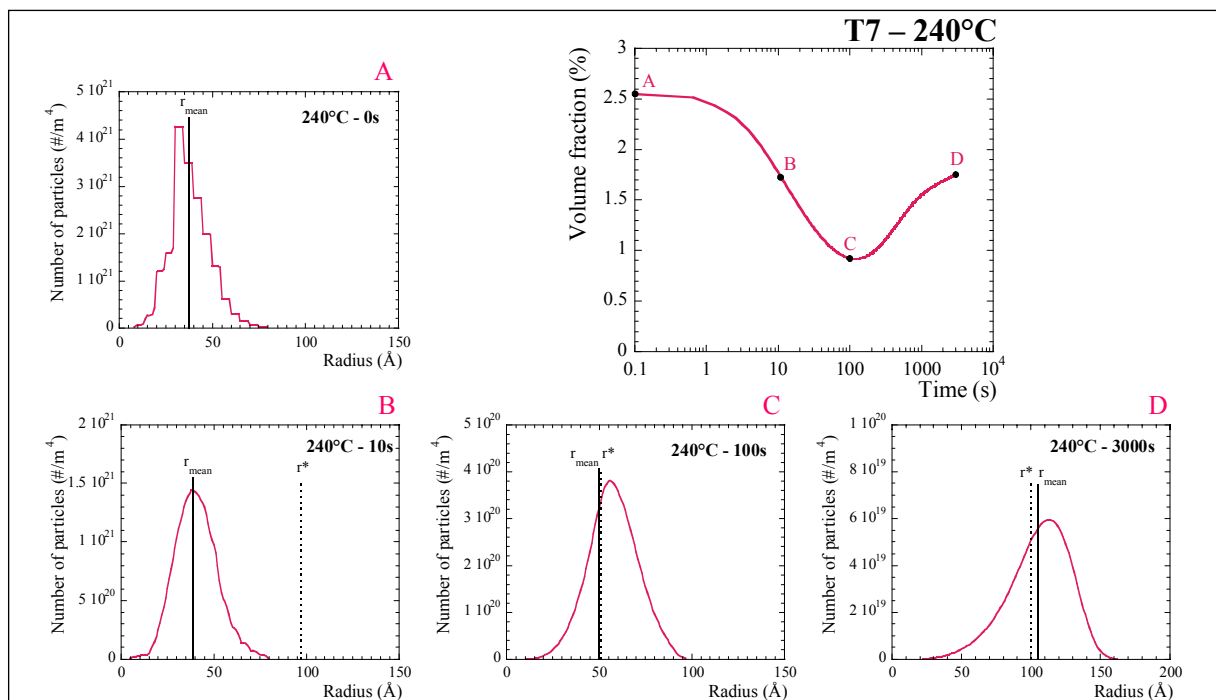


Figure V.25: Critical and mean radius evolution and particle distribution evolution during an isothermal heat treatment at 240°C on a T7 state.

Figure V.26 displays the evolution of the critical radius with time at 240°C for an initial T7 state. When the temperature is rapidly increased, all particles become unstable (r^* is higher than all particle radii) and tend to dissolve, the dissolution rate being higher for small particles. This gives rise to general dissolution affecting all the particles with small variations of the mean radius. Then, due to the enrichment of the matrix in solute atoms, the critical radius decreases and encounters again the remaining distribution. When the critical radius becomes equal to the mean radius, the growth becomes predominant rather than the dissolution which previously dominated. Afterwards the critical radius becomes slightly lower than the mean radius and then coarsening occurs.

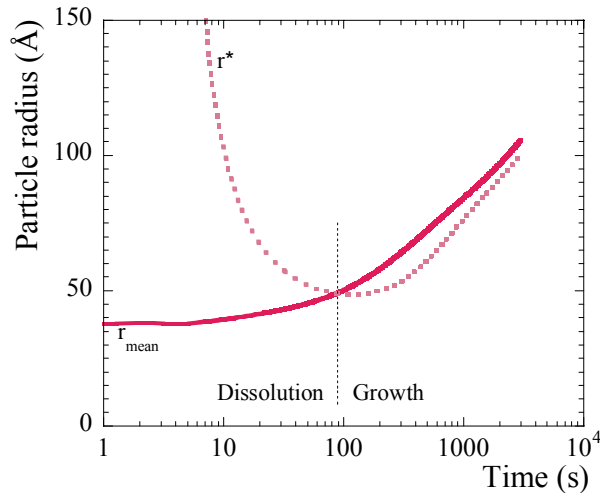


Figure V.26: Variation in the critical radius and mean radius with time at 240°C of a T7 temper.

The evolution of r^* is directly related (refer to equation V.11) to the interfacial energy (when σ increases, r^* increases) and to the interfacial concentration determined by the solubility limit and the ratio D_{Mg}/D_{Zn} .

Note that a classical model which does not take into account the size distribution effect could not reproduce or explain the dissolution at constant mean radius. Actually, in the classical theory, dissolution will automatically involve a decrease of the mean size, as the system is considered as monodisperse.

In summary, the model displays outputs useful in the understanding of the behaviour of a precipitation microstructure submitted to an isothermal heat treatment. Especially we can now understand:

- that the parameter controlling the dissolution/growth coarsening is the r_{mean}/r^* ratio,
- how a distribution of particles can dissolve at constant mean radius.

V.5.2. Precipitation evolution during continuous heating

Concerning continuous heating, one point remains to be clarified: what is the origin of the inflexion point observed at low heating rates (see Figure V.27) which disappears when increasing the heating rate. This inflexion point observed experimentally (refer to Figure V.16) has been first attributed to a phase transformation. However the model is able to reproduce such an inflexion without including a phase transformation in the modelling. Therefore, the inflexion is more probably due to a particle distribution effect.

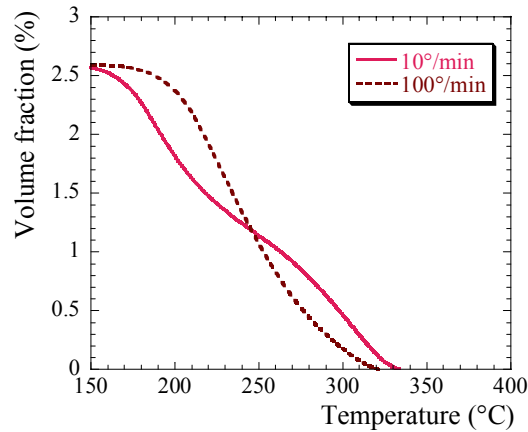


Figure V.27: Modelled evolution of the volume fraction during continuous heating of a T7 temper at low heating rate (10°/min) and high heating rate (100°/min).

This inflexion can be explained by the competition between dissolution and growth, as illustrated in Figure V.28 by the variation in critical radius as compared to the mean radius during continuous heating of a T7 temper. It can be seen that the r^* variation is completely different for the two heating rates. For temperatures higher than 140°C, dissolution becomes the dominant mechanism ($r^* > r_{\text{mean}}$). However at 100°/min, the critical radius remains much higher than the mean radius (all particles are dissolving) whereas at 10°/min the critical radius becomes fairly equal to the mean radius around 250°C. Therefore the dissolution path is slowed down, inducing the observed inflexion point.

Moreover this explains that the coarsening is much more effective for low heating rates, as observed in Figure V.15. Actually as the critical radius encounters the particle distribution, growth of coarse particles ($r > r^*$) occurs, leading to an increase of the particle size.

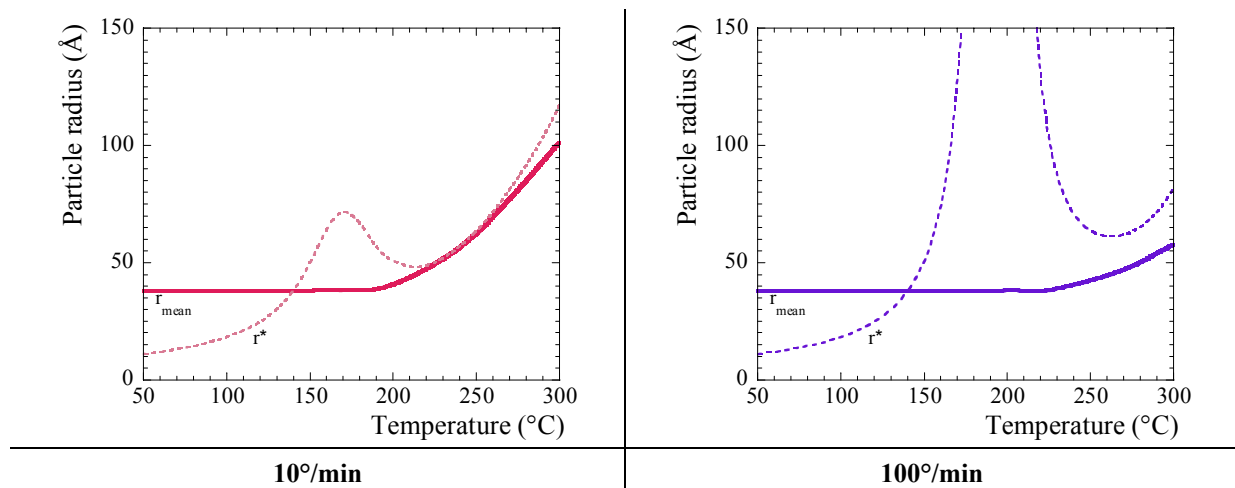


Figure V.28: Comparison of the evolution of the critical and mean radii during continuous heating at a low (10°/min) and high (100°/min) heating rate for a T7 temper.

V.5.3. Precipitation evolution during welding

One interesting feature of the model is to follow the microstructural evolution during the whole welding process and not only at the end of the welding cycle, as is the case for experimental characterisation. This is illustrated in Figure V.29.

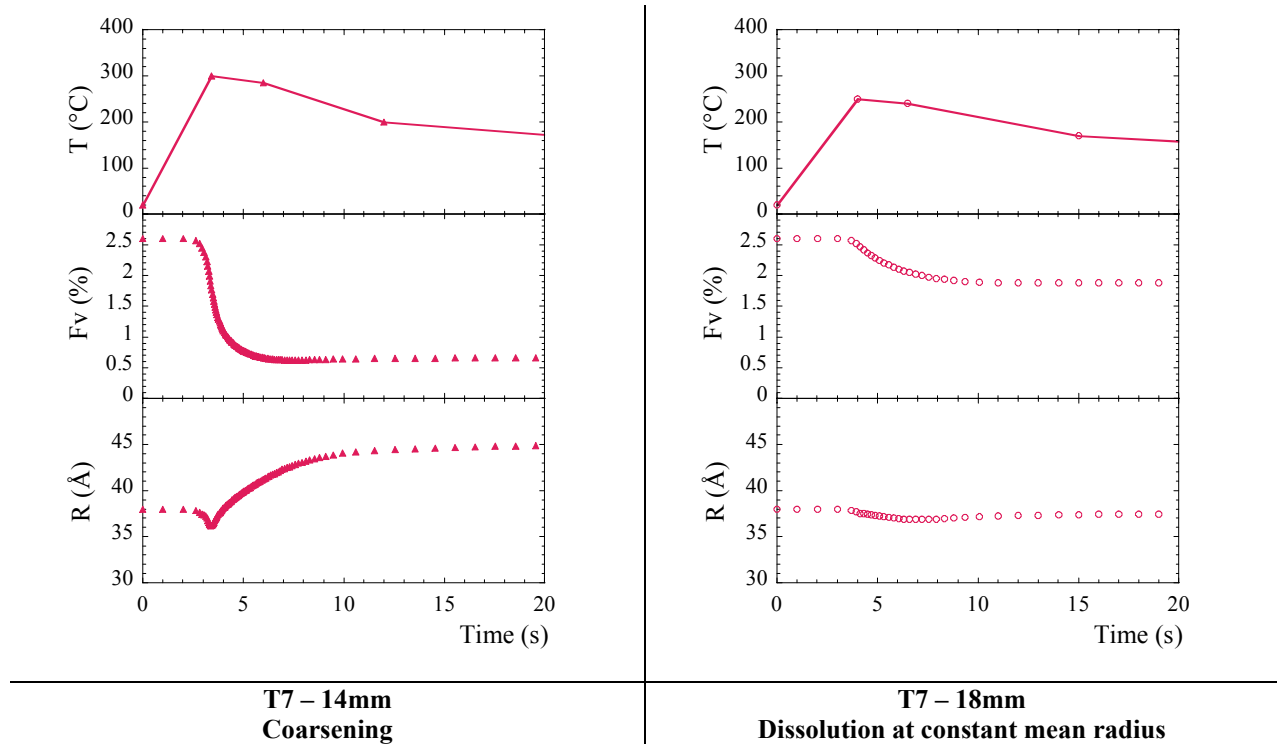


Figure V.29: Modelled evolution of the precipitate microstructure during the welding process for the T7 temper at 14mm and 18mm from the fusion boundary.

We can see for example that in the case of the welded T7 sample located at 14mm and at 18 mm from the fusion boundary, all modifications of the volume fraction and particle size occur at temperature higher than 200°C. At lower temperatures the welding process is too fast to induce precipitate changes.

Moreover the resulting volume fraction is mainly controlled by the initial part of the welding cycle, i.e. the peak temperature and the initial heating rate. The cooling part does not notably affect the volume fraction evolution. However both heating and cooling will determine the final mean particle size.

V.6. Modelling of the yield stress in the heat-affected zone

Volume fraction and mean radius of the particles are experimentally known just after welding and for various natural ageing times. The aim of this section is to propose a simple model able to correlate the microstructural features and the yield stress/microhardness.

V.6.1. General considerations

The estimation of the total yield stress from microstructural features is a combination of different strengthening modes:

- σ_0 : the response of pure aluminium,
- $\Delta\sigma_{HP}$: the grain structure contribution following the Hall-Petch law,
- $\Delta\sigma_{ss}$: the solid solution contribution,
- $\Delta\sigma_p$: the precipitation strengthening.

$\Delta\sigma_{SS}$ is dependent on the concentration of the different solute elements and can be written [Cahn, 1996]:

$$\Delta\sigma_{SS} = \sum_i k_i c_i^{2/3} \quad (V.25)$$

where k_i is a constant and

c_i is the atomic concentration of the element i .

Strengthening arising from a dispersion of particles [Lendvai, 1996] essentially depends on their nature, size and volume fraction. At usual temperatures, there are two main strengthening mechanisms characterised by two different dislocation/precipitate interactions. In fact in front of a particle distribution, two ways to pass through the obstacle are available for dislocations:

- the shearing mechanism when particles are small and coherent,
- the Orowan mechanism when dislocations by-pass unshearable particles.

The increment in yield strength corresponding to these two processes is basically dependent on the volume fraction, f_v , and the average size, R , of the particles [Gerold, 1979]:

$$\Delta\sigma_{cutting} = 0.7M\alpha^{3/2}\mu\sqrt{\frac{Rf_v}{b}} \quad (V.26)$$

$$\Delta\sigma_{Orowan} = 0.6M\mu\frac{b}{R}\sqrt{f_v} \quad (V.27)$$

where M is the Taylor factor (~ 3),

α is a numerical factor describing the specific strength of the particle,

μ is the shear modulus of the matrix (MPa),

b is the Burgers vector,

R is the radius of the particle,

f_v is the volume fraction of particles.

The peak-aged state corresponds to the transition from the cutting mechanism to the by-passing process, when it becomes more favourable to by-pass rather than to shear particles.

V.6.2. Simple modelling of the yield stress

GP zone strengthening is naturally attributed to shearing of the particles (equation V.25). For other particles (η' and η), the mean size of the particles should be considered to determine the controlling mechanism. In Al-Zn-Mg alloys, the critical radius corresponding to the transition from shearing to by-passing is around 35\AA [Lendvai, 1996]. As a consequence for simplicity the strengthening arising from the η' -particles will be attributed to shearing and to by-passing for the η -precipitates.

The contribution of other terms (σ_0 , $\Delta\sigma_{HP}$ and $\Delta\sigma_{SS}$) has been estimated from experimental measurements of the yield stress in solid solution for various alloys. The resulting parameters are displayed in Table V.5, together with the shear modulus used for GP zones, η' and η .

$\sigma_0 + \Delta\sigma_{HP}$	k_{Mg}	k_{Zn}	M	μ	α_{GP}	$\alpha_{\eta'}$	α_{η}
60 (MPa)	16	9	2	25000 (MPa)	0.07	0.06	0.05

Table V.5: Parameters of the yield stress modelling.

To obtain the final yield stress, a classical mixture law has been employed [Koppenall, 1964]:

$$\sigma_{\text{tot}} = \sigma_0 + \Delta\sigma_{\text{HP}} + \Delta\sigma_{\text{ss}} + \sqrt{\Delta\sigma_{\text{GP}}^2 + \Delta\sigma_{\eta'/\eta}^2} \quad (V.28)$$

V.6.3. Application to microhardness evolution in the heat-affected zone

The resulting yield stress predictions have been converted into hardness values through a simple proportional relationship generally accepted between the two mechanical properties:

$$\text{HV} = \frac{1}{3}\sigma \quad (V.29)$$

The different components of the yield stress are shown in Figure V.30. The major contribution arises from precipitates, the contribution from solid solution being negligible.

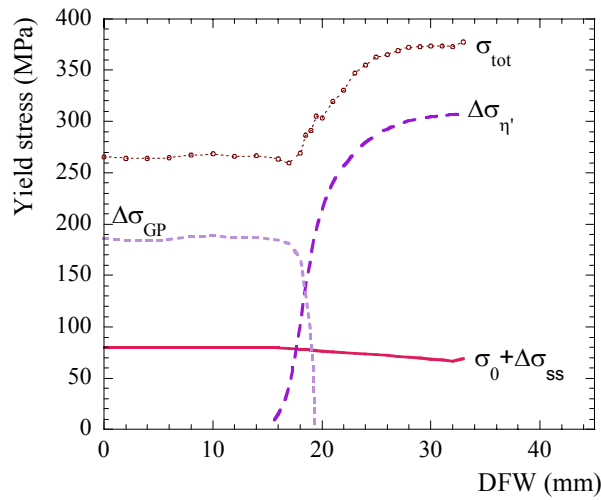


Figure V.30: Different components of the calculation of the yield stress for the T6 materials along the heat-affected zone after 3 days at room temperature.

The results of the modelling are shown in Figure V.31 for T6 and T7 welds for different natural ageing times. The agreement is satisfactory for the three investigated natural ageing times.

Using a simple approach, the model is able to reproduce the evolution of the yield stress/hardness resulting of the welding process and subsequent natural ageing. Once nucleation of GP zones will be considered in the precipitation model, this simple yield stress modelling can be introduced in the process modelling.

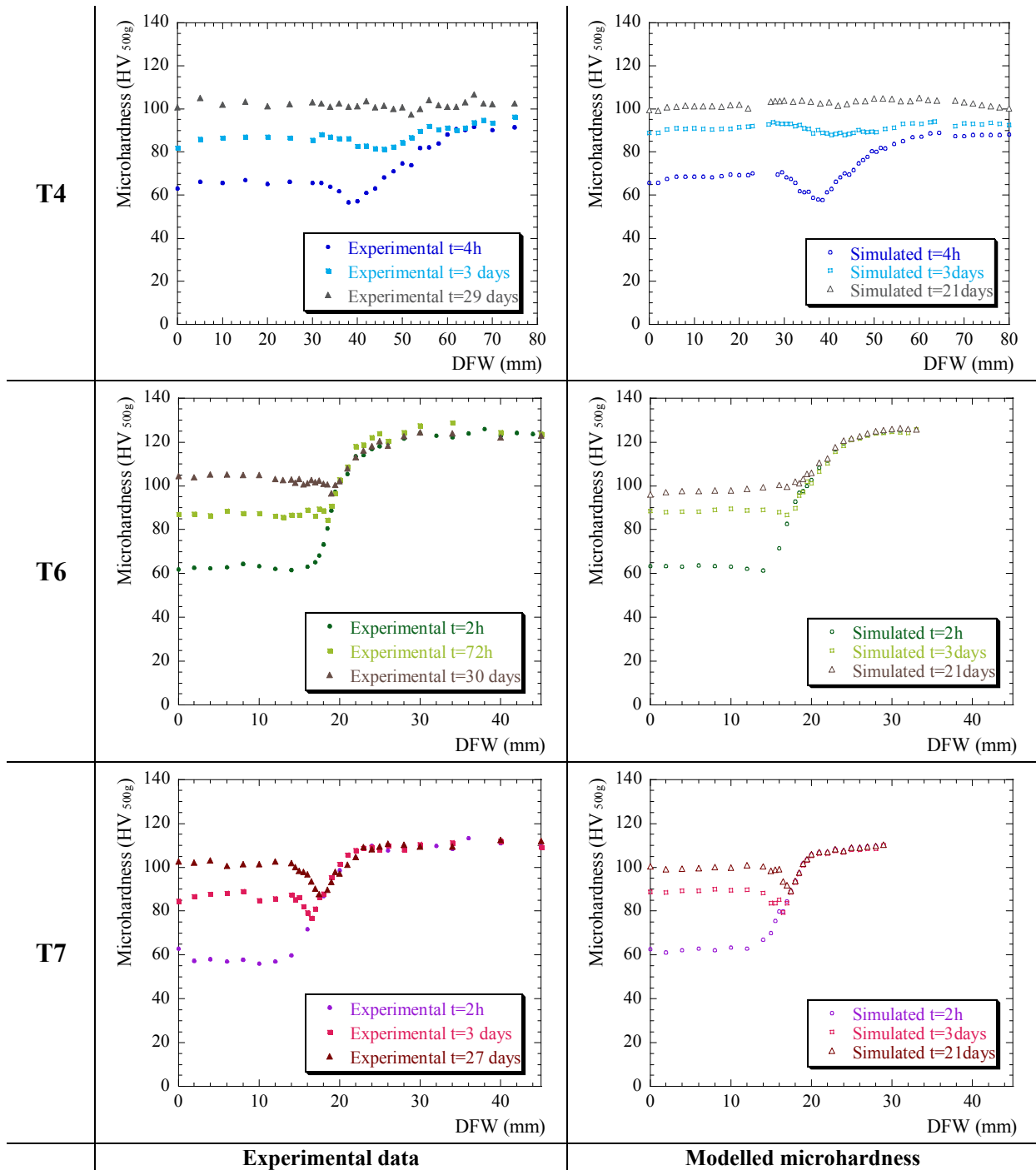


Figure V.31: Comparison of modelled yield stress obtained from experimental volume fraction and particle radii and experimental measurements of the microhardness along the heat-affected zone for various natural ageing times.

V.7. Future developments

In the present state, the model is able to describe the evolution of a given particle distribution of precipitates submitted to temperature cycles. It takes into account a single phase and does not include nucleation. To be able to reproduce the behaviour of the material in terms of precipitation in any situations, the modelling should include:

- homogeneous nucleation in ternary alloys of the different phases from the solid solution, described by the classical laws, characterised in particular by an activation barrier for nucleation $\Delta G_{\text{homogeneous}}$; this has been included in a class modelling for alloys of the 6xxx series by Myhr and Grong [Myhr, 2001].
- phase transformation like $\eta' \rightarrow \eta$: it is then necessary to handle two particle distributions, exchange laws from one to the other; different approaches may be considered:
 - 1) homogeneous nucleation of the second phase, the two phases are only bound by the solid solution,
 - 2) heterogeneous nucleation of η on η' with $\Delta G \ll \Delta G_{\text{homogeneous}}$ and $N_{\text{sites}}=N_{\eta'}$,
 - 3) massive transformation of $\eta' \rightarrow \eta$; in this case the η' -particles become η -precipitates, the η' -distribution becomes progressively the η -distribution; the key point is the determination of the exchange laws to be used.

After implementation, the modelling would be able to describe for example the two-step ageing, i.e. how to get a T6 or T7 precipitate distribution, the reprecipitation of GP zones at room temperature after welding, the phase transformation $\eta' \rightarrow \eta$ during the continuous heating of a T6 temper.

Moreover the modelling of the yield stress could be directly integrated in the model. The modelling can then consider the size effect on the mechanism (shearing or by-passing of the obstacles).

V.8. Summary

In summary, using simple laws controlling dissolution and growth, the modelling dealing with a particle size distribution is able to handle non-isothermal heat treatments in a satisfactory manner, including complex thermal cycles involved in the welding process provided that no nucleation step is involved (when nucleation can take place, our model is unable to reproduce experimental data). Moreover it is able to reproduce experimental phenomena like dissolution at constant mean radius or coarsening during continuous heating at low heating rates that classical models dealing with only the average particle size are not expected to reproduce easily.

Conclusions and future work

In this work, the combination of a quantitative study of precipitate microstructures, completed by a simple modelling approach, has been successful in predicting the evolution of a particle distribution submitted to complex non-isothermal heat treatments. The main results of the experimental and modelling work will be summarised, as well as the methodology that has been developed for the study of precipitation hardening alloys during welding. The perspectives of the work will be given, with special emphasis on the possibilities of welding optimisation.

Main results of the study

Characterisation of the initial states

A quantitative and qualitative characterisation of the initial states has allowed :

- to determine the nature, size and volume fraction of the precipitates present in each temper (GP zones in the T4 temper, η' in the T6 temper and a mixture of $\eta' + \eta$ in the T7 temper),
- to evaluate the composition of the precipitates by coupling SAXS and quantitative TEM: $(\text{Mg,Al})_1\text{Zn}_1$ for η' and $(\text{Mg,Al})_1\text{Zn}_{1.4}$ for η

Experimental statement concerning welding

From the microstructural characterisation of welds, three zones can be distinguished:

- the fully reverted zone where re-precipitation of GP zones at low temperatures occur,
- the transition zone where reversion is only partial and coarsening is observed for the T6 and T7 tempers and
- the unaffected material.

Concerning the T6 and T7 tempers in which coarsening has been observed, we have determined that coarsening does not affect the entire transition zone but only the region where reversion is important. The loss of mechanical properties after post-welding heat treatments,

stems from partial dissolution in the case of natural ageing and from coarsening in the case of artificial ageing.

In the case of the T4 temper, no coarsening has been observed; on the contrary, a decrease of the mean size of the GP zones has been observed in the transition zone. This state presents a good potential for recovery of the base material mechanical properties (\sim T6) through post-welding heat treatments (under appropriate conditions of storage time).

Experimental statement concerning controlled heat treatments

During reversion treatments, three stages can be distinguished:

- first the volume fraction sharply decreases whereas the mean radius remains fairly constant,
- then the volume fraction reaches a minimum,
- finally the volume fraction increases together with the mean particle size (coarsening).

As expected, the more stable the precipitates, the less efficient the dissolution.

Moreover we have determined that at long ageing times, the T6 and T7 materials show identical microstructures. This suggests that a phase transformation $\eta' \rightarrow \eta$ occurs during the ageing treatment in the T6 material.

During continuous heating of the three initial states, dissolution is the main mechanism. When increasing the heating rate, the dissolution curve is shifted towards higher temperatures, due to kinetics effects.

At low heating rates, an anomaly of dissolution (re-increase of the volume fraction) is observed in the T6 material. When increasing the heating rate, the anomaly is shifted towards higher temperatures and tends to disappear. This phenomenon is attributed to a competition between dissolution and phase transformation.

During continuous heating of the T7 temper, no such anomaly has been observed but an inflexion point. It may be due to phase transformation or to size effects.

Continuous heating of the T4 temper is characterised by a full reversion at low temperatures followed by precipitation of the η -phase at higher temperatures. This last phenomenon is strongly rate-dependent.

Regarding the welding process as a complex non-isothermal heat treatment different in each point of the heat-affected zone, the study of controlled heat treatments brings some elements in its understanding.

- As observed during controlled heat treatments, dissolution can occur at constant mean radius: this explains that coarsening is not observed in the whole transition zone.
- No phase transformation (in particular $\eta' \rightarrow \eta$ or GP zone $\rightarrow \eta$) are expected to occur during the welding process due to the very high heating rates experienced during welding.

Process modelling: a complement to understanding

The model developed in this study is based on simple laws of radius evolution of an existing particle size distribution. Nucleation is not of concern as it is expected to be a minor phenomenon in all cases studied. No phase transformation has been included since it is not expected to occur during welding.

The model is able to reproduce:

- the reversion behaviour in terms of volume fraction and mean radius evolution, including the temperature dependence,
- dissolution at constant mean radius during the early stage of reversion,
- the temperature range for dissolution during continuous heating,
- the heating rate dependence for dissolution during continuous heating,
- the inflexion point in the T7 material observed for low heating rates,
- the volume fraction and particle size distribution along the heat-affected zone after welding for the three initial states (except in the fully reverted zone).

The model can explain:

- why dissolution can occur at constant mean radius: the key parameter is the critical radius displacement with regards to the particle size distribution,
- that the minimum of volume fraction during reversion treatments is not necessarily due to phase transformations,
- that the T7 inflexion point during continuous heating at low heating rates is not due to phase transformation but to competition between dissolution and coarsening.

The model is not able to reproduce:

Since nucleation is not included in the model:

- the re-precipitation of GP zones at room temperature after welding in the fully reverted zone,
- the precipitation of the η -phase during continuous heating of the T4 temper.

Since phase transformation is not included in the model:

- the T6 dissolution "anomaly" during continuous heating at low heating rates.

Methodology for the study of welding

A complete methodology for the study of the precipitate evolution during welding has been developed under four axes:

- the detailed characterisation of the precipitation in the as-welded state and during controlled heat treatments,
- Simple modelling of the evolution of a particle size distribution submitted to non-isothermal heat treatments,

- calibration and verification of the robustness of the model on controlled heat treatments,
- prediction of the precipitation evolution during the welding process.

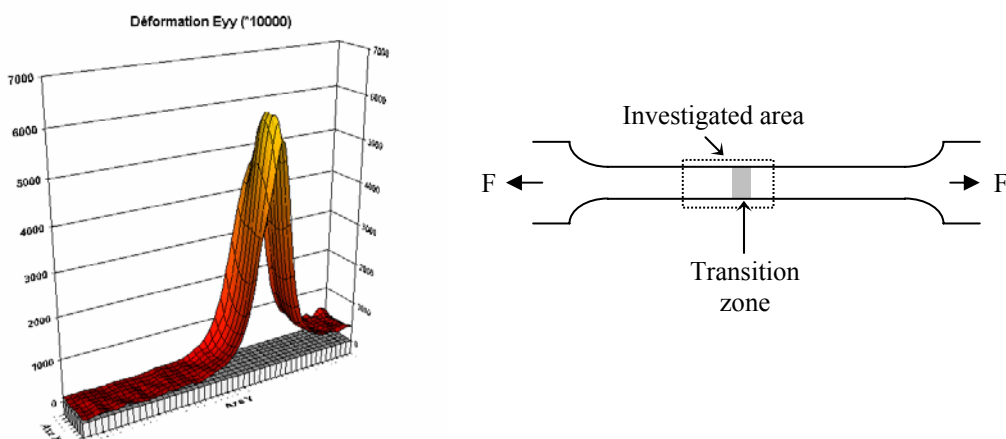
This methodology has been successful in giving recommendations in terms of state of ageing before welding and post-welding heat treatments for obtaining optimal end use mechanical properties.

Future developments

Complements to the present work

Concerning the determination of the initial microstructural states, we have obtained interesting results concerning the composition of nanometric phases. In order to confirm these results, it would be worth to carry out a Tomographic Atom Probe investigation of the same samples. Such a study is under way with the Groupe de Métallurgie Physique of the University of Rouen (France).

Concerning the quantitative description of the weld microstructures and mechanical properties, we have mostly concentrated on the microstructure investigation. Certainly the determination of mechanical properties could be carried out with more precision (with micro-tensile specimens for instance), and the microstructure and hardness could be related by a more complete mechanical model than that has been used in the present work. Further developments of interest could for instance include the study of the distribution of plastic deformation when mechanically testing a weld (see figure below), or the effect of the heterogeneity of precipitate microstructures in the heat affected zone on the service properties of the weld (ductility, fracture, and corrosion resistance). Moreover, the present study on the heat-affected zones should be completed by a study on the weld nugget, which currently is the weak link in the weld assembly.



Measurement of the distribution of longitudinal deformation in the transition zone of a T7 + W + T7 material during a tensile test (the nugget zone is not included in the gage length of the sample). The technique used is imaged correlation from a random pattern deposited on the sample. Maximum deformation occurs in the transition zone, at a value of approximately 55%, as compared to the average deformation of ~5% outside the transition zone.

Concerning the modelling work, we have developed a model which has proven to be very versatile in terms of temperature histories. Its versatility should be further improved by including nucleation, and the possibility for competitive precipitation of several phases. In order to be closer to the reality, the model should be also able to include phases which contain matrix atoms (aluminium in the present case), and most importantly of varying composition (non-stoichiometric phases). This last point is particularly difficult, since the theoretical framework necessary for its implementation in multi-constituent alloys is still lacking. Finally, at least in theory this model is able to predict the effect of alloy composition (supersaturation and Zn/Mg ratio) on the thermal stability of precipitates. However this potential should be checked by studying the response to welding and non-isothermal heat treatments of other alloys.

A similar methodology as has been developed in this work could be successfully applied to other welding techniques, which present other difficulties. Two welding techniques are particularly relevant for precipitation hardening materials: laser welding and friction stir welding. Laser welding is mostly used with 6000 series aluminium alloys, which are not suitable to SAXS investigation due to low contrast. Friction stir welding, however, would be worth studying in the lines defined by this work. The main difference between the MIG and FSW processes will be the addition of intense deformation to the heat input in the thermo-mechanically affected zone. Therefore, one has to be aware that the complexity of this process, involving coupling between precipitation, deformation, recovery and recrystallisation, is much greater than the phenomena occurring in the MIG process.

Alloy design for welding

The model developed in this work has been shown to be predictive for various non-isothermal heat treatments and therefore can be safely used to test other welding situations, by coupling it with the thermal analysis software WELDSIM. For instance, the influence of pre-heating the sheets before welding, changing the welding power, or changing the thermal contact with the outside, could be predicted, in order to minimise actual experimental trials.

The model has been developed specifically to be able to describe other alloy compositions. Of course, this should be carefully checked, since many phenomena can impede the applicability of the parameters of the model to other compositions (for instance, change in precipitate composition). Thus one could explore a number of alloy compositions and test their tendency for precipitate coarsening and for recovery of homogeneous microstructures after post-welding heat treatments, and once again minimise the experimental trials, which are particularly expensive when numerous alloy compositions have to be tested.

Combining these two steps, influence of welding parameters and alloy composition, gives a framework for optimising the end use properties of welds made out of precipitation hardening alloys, and more precisely optimising in a single procedure the couple material / process.

Bibliographic references

- [**Aaron, 1971**] Aaron HB; Kotler GR: Second phase dissolution. *Metallurgical Transactions*, Vol. 2, Feb. 1971, p.393-408.
- [**Adler, 1977**] Adler PN; DeIasi R: Calorimetric studies of 7000 series aluminium alloys : II. Comparison of 7075, 7050, and RX720 alloys. *Metallurgical Transactions A*, Vol. 8A, July 1977, p.1185-1190.
- [**Allen, 1981**] Allen SM: Foil thickness measurements from convergent-beam diffraction patterns. *Philosophical Magazine*, Vol. 43, 1981, p.325-335.
- [**Asano, 1976**] Asano K; Abe M; Fujiwara A: Nucleation of precipitates in Al-Zn-Mg alloys. *Materials Science and Engineering*, Vol. 22, 1976, p.61-70.
- [**Auger, 1974**] Auger P; Raynal JM; Bernole M; Graf R: Etude aux rayons X et par microscopie électronique de la précipitation dans les alliages Al-Zn-Mg et Al-Zn-Mg-Cu revenus entre 100 et 300°C. *Mémoires Scientifiques Revue de Métallurgie*, no. 9, 1974, p.557-568.
- [**Auld, 1974**] Auld JH; Cousland SMck: The structure of the metastable η' phase in aluminium-zinc-magnesium alloys. *Journal of the Australian Institute of Metals*, Vol. 19, 1974, p.194-201.
- [**Bakker, 1990**] Bakker H: *Diffusion in Solid Metals and Alloys*, Landolt-Börnstein, Springer-Verlag, Berlin, 1990, Vol. 26.
- [**Baldantoni, 1985**] Baldantoni A: On the microstructural changes during the retrogression and re-aging of 7075 type aluminium alloys. *Materials Science and Engineering*, Vol. 72, 1985, p.L5-L8.
- [**Becker, 1935**] Becker R; Döring W: *Ann. Phys.*, Vol. 24, 1935, p.719.
- [**Benedetti, 2000**] Benedetti AV; Cabot PL; Garrido JA; Moreira AH: Effect of welding on the microstructure and electrochemical corrosion of Al-Zn-Mg-Fe alloys. *Electrochimica Acta*, Vol. 45, 2000, p.2187-2195.
- [**Berg, 2001**] Berg LK; Gjønnnes J; Hansen V; Li XZ; Knutson-Wedel M; Waterloo G; Schryvers D; Wallenberg LR: GP-zones in Al-Zn-Mg alloys and their role in artificial aging. *Acta Materialia*, Vol. 49, 2001, p.3443-3451.
- [**Bjørneklett, 1996**] Bjørneklett B; Grong Ø; Kluken AO; Jensrud O: Embrittlement phenomena in the HAZ of Al-Zn-Mg weldments. *Materials Science Forum*, Vol. 217-222, 1996, p.1527-1532.
- [**Bjørneklett, 1999**] Bjørneklett BI; Grong Ø; Myhr OR; Kluken AO: A process model for the heat-affected zone microstructure evolution in Al-Zn-Mg weldments. *Metallurgical and Materials Transactions A*, Vol. 30A, Oct. 1999, p.2667-2677.
- [**Blaschko, 1982**] Blaschko O; Ernst G; Fratzl P; Bernole M; Auger P: A neutron scattering investigation of the early stages of Guinier-Preston zone formation in Al-Zn-Mg-(Cu) alloys. *Acta Metallurgica*, Vol. 30, 1982, p.547-552.
- [**Bratland, 1997**] Bratland DH; Grong Ø; Shercliff H; Myhr OR; Tjøtta S: Modelling of precipitation reactions in industrial processing. *Acta Materialia*, no. 1, 1997, p.1-22.
- [**Brenner, 1991**] Brenner SS; Kowalik J; Hua Ming-Jian: FIM/atom probe analysis of a heat treated 7150 aluminum alloy. *Surface Science*, Vol. 246, 1991, p.210-217.
- [**Cahn, 1996**] Cahn RW; Haasen P: *Physical Metallurgy*, 4th edition, Vol.3, 1996.

- [Cina, 1974] Cina B: *U.S. Patent 3856584*, December 24, 1974.
- [Cordier, 1977] Cordier H; Schippers M; Polmear I: Microstructure and intercrystalline fracture in a weldable Al-Zn-Mg alloy. *Zeitschrift für Metallkunde*, Vol. 68, no. 4, April 1977, p.280-284.
- [Danh, 1983] Danh NC ; Rajan K ; Wallace W. A TEM study of microstructural changes during retrogression and reaging in 7075 aluminum. *Metallurgical Transactions A*, Vol. 14A, Sep. 1983, p.1843-1850.
- [Danh, 1985] Danh N; Krishna R; Wallace W: Discussion of "Effect of retrogression and reaging treatments on the microstructure of Al-7075-T651". *Metallurgical transactions A*, Vol. 16, Nov. 1985, p.2068.
- [De Ardo, 1973] De Ardo AJ; Simensen JR CHRJ: A structural investigation of multiple aging of Al-7 wt pct Zn-2.3 wt pct Mg. *Metallurgical Transactions*, Vol. 4, Oct. 1973, p.2413-2421.
- [Degisher, 1980] Degisher HP; Lacom W; Zahra A; Zahra CY: Decomposition processes in an Al-5%Zn-1%Mg alloy. Part II : Electronmicroscopic investigations. *Zeitschrift für Metallkunde*, Vol. 71, 1980, p.231-238.
- [De Iasi, 1977] De Iasi R; Adler PN: Calorimetric studies of 7000 series aluminium alloys : I. Matrix precipitate characterization of 7075. *Metallurgical Transactions A*, Vol. 8A, July 1977, p.1177-1183.
- [Deschamps, 1997] Deschamps A: *Influence de la prédéformation et des traitements thermiques sur la microstructure et les propriétés mécaniques des alliages Al-Zn-Mg-Cu*, Ph.D., 1997.
- [Deschamps, 1998] Deschamps A; Bréchet Y: Influence of quench and heating rates on the ageing response of an Al-Zn-Mg-(Zr) alloy. *Materials Science and Engineering A*, Vol. A251, 1998, p.200-207.
- [Deschamps, 1999] Deschamps A; Livet F; Bréchet Y: Influence of predeformation on ageing in an Al-Zn-Mg alloy I: microstructure evolution and mechanical properties. *Acta Materialia*, Vol. 47, no. 1, 1999, p.281.
- [Deschamps, 2001] Deschamps A; Bigot A; Livet F; Auger P; Bréchet Y; Blavette D: A comparative study of precipitate composition and volume fraction in an Al-Zn-Mg alloy using tomographic atom probe and small-angle X-ray scattering. *Philosophical Magazine A*, Vol. 81, no. 10, 2001, p.2391-2414.
- [Donnadiou, 1999] Donnadiou P; Roux-Michollet M; Chastagnier V: A quantitative study by transmission electron microscopy of nanoscale precipitates in Al-Mg-Si alloys. *Philosophical Magazine A*, Vol. 79, no. 6, 1999, p.1347-1366.
- [Donoso, 1985] Donoso E: Calorimetric study of the dissolution of Guinier-Preston zones and η' phase in Al-4.5at%Zn-1.75at%Mg. *Materials Science and Engineering*, Vol. 74, 1985, p.39-46.
- [Dorward, 1999] Dorward RC: Precipitate coarsening during overaging of Al-Zn-Mg-Cu alloy. *Materials Science and Technology*, Vol. 15, Oct. 1999, p.1133-1138.
- [Easterling, 1992] Easterling K: *Introduction to the Physical Metallurgy of Welding*, 2nd edition, 1992, edited by Butterworth-Heinemann.
- [Ferragut, 1996] Ferragut R; Somoza A; Dupasquier A: On the two-step ageing of a commercial Al-Zn-Mg alloy; a study by positron lifetime spectroscopy. *Journal of Physics : Condensed Matter*, Vol. 8, 1996, p.8945-8952.
- [Ferragut, 1999] Ferragut R; Somoza A; Tolley A: Microstructural evolution of 7012 alloy during the early stages of artificial ageing. *Acta Materialia*, Vol. 47, no. 17, 1999, p.4355-4364.
- [García-Cordovilla, 1990] García-Cordovilla C; Louis E: Kinetics of retrogression in Al-Zn-Mg-(Cu) alloys. *Metallurgical Transactions A*, Vol. 21A, Aug 1990, p.2277-2280.
- [Gazda, 1997] Gazda A; Warmuzek M; Wierzchowski W: DTA investigation of the retrogression and re-ageing in some AlZnMgCu alloys. *Thermochimica Acta*, Vol. 303, 1997, p.197-202.
- [Gerold, 1979] Gerold V: Precipitation hardening. *Dislocations in solids*, Vol. 4, edited by North-Holland publishing company, 1979, p.219.
- [Gjønnnes, 1970] Gjønnnes J; Simensen CHR J: An electron microscope investigation of the microstructure in an aluminium-zinc-magnesium alloy. *Acta Metallurgica*, Vol. 18, Aug. 1970, p.881-890.
- [Glatter, 1982] Glatter O; Kratky O: *Small-Angle X-Ray Scattering*. Academic Press, London, 1982.
- [Godard, 1999] Godard D: *Influences de la précipitation sur le comportement thermomécanique lors de la trempe d'un alliage Al-Zn-Mg-Cu*, Ph.D, 1999.

- [Gomiero, 1990] Gomiero P: *Microstructure et propriétés mécaniques de l'alliage Al-Li-Cu-Mg(Zr) (2091)*. Ph.D., 1990.
- [Gomiero, 1994] Gomiero P; Reeves A; Pierre A; Bley F; Livet F; Vichery H: An in-situ small-angle X-ray scattering (SAXS) study of precipitation in an Al-Zn-Mg-Cu alloy. *Proceedings of the 4th conference on Aluminum alloys: their physical and mechanical properties*, Atlanta, Georgia USA, Sept. 11-16 sep 1994, Vol. 1, 1994, p.644-651.
- [Graf, 1956] Graf R: The ageing of ternary aluminium-zinc-magnesium alloys. *Journal of the Institute of Metals*, Vol. 86, 1956, p.535-536.
- [Grong, 1996] Grong Ø: *Metallurgical Modelling of Welding*. 2nd edition, 1996, edited by Bhadeshia HKDH.
- [Gueffroy, 1981a] Gueffroy B; Löffler H: On the reversion behaviour of an Al-Zn(4.5at%)-Mg(2.0at%) alloy. *Physica Status Solidi (a)*, Vol. 66, 1981, p.585-590.
- [Gueffroy, 1981b] Gueffroy B; Löffler H: On the influence of the pre-ageing temperature on the reversion behaviour of an Al-4.5at%Zn-2.0at%Mg alloy. *Crystal Research and Technology*, Vol. 16, no. 9, 1981, p.1079-1085.
- [Guyot, 1996] Guyot P, Cottignies L: Precipitation kinetics, mechanical strength and electrical conductivity of AlZnMgCu alloys. *Acta Materialia*, Vol. 44, no. 10, 1996, p.4161-4167.
- [Habiby, 1987] Habiby F; Ul Haq A; Hashmi FH; Khan AQ: Some remarks on the hardness and yield strength of aluminum alloy 7075 as a function of retrogression time. *Metallurgical transactions A*, Vol. 18, Feb. 1987, p.350-353.
- [Hepples, 1992] Hepples W; Thunton MC; Holroyd NJH: Microstructural characterization of "white zones" in weldable 7000 series alloys. *Journal of Materials Science*, Vol. 27, 1992, p.5720-5726.
- [Hilliard, 1962] Hilliard JE: The counting and sizing of particles in transmission microscopy. *Transactions of the Metallurgical Society of AIME*, Vol. 224, Oct. 1962, p.906-917.
- [Hono, 1992] Hono K; Sano N; Sakurai T: Quantitative atom-probe analysis of some aluminum alloys. *Surface Science*, Vol. 266, 1992, p.350-357.
- [Hwang, 1998] Hwang RY; Chou CP: The study on microstructural and mechanical properties of weld heat affected zone of 7075-T6 aluminum alloy. *Scripta Materialia*, Vol. 38, no. 2, 1998, p.215-221.
- [Jiang, 2000] Jiang XJ; Noble B; Holme B; Waterloo G; Tafto J: Differential scanning calorimetry and electron diffraction investigation on low-temperature aging in Al-Zn-Mg alloys. *Metallurgical and Materials Transactions A*, Vol. 31A, Feb 2000, p.339-348.
- [Kampmann, 1984] Kampmann R; Wagner R: *Decomposition of alloys: first stages*, edited by Haasen P, 1984, p. 91-103.
- [Kelly, 1975] Kelly PM; Jostsons A; Blake RG; Napier JG: The determination of foil thickness by scanning transmission electron microscopy. *Physica Status Solidi (a)*, Vol. 31, no. 2, 1975, p.771-780.
- [Kim, 1996] Kim HT; Nam SW: Solidification cracking susceptibility of high strength aluminium alloy weldment. *Scripta Materialia*, Vol. 34, no. 7, 1996, p.1139-1145.
- [Kissinger, 1957] Kissinger HE: *Anal. Chem*, Vol. 29, 1957, p.1702.
- [Koppenall, 1964] Koppenall TJ; Kuhlmann-Wilsdorf D: *Appl. Phys. Lett*, Vol. 4, 1964, p.59.
- [Lacom, 1980] Lacom W; Degischer HP; Zahra A; Zahra CY: Calorimetric investigation of precipitation processes in aluminium alloys. *High temperatures – High Pressures*, Vol. 12, 1980, p.549-554.
- [Lacom, 1982] Lacom W; Degischer HP; Zahra A; Zahra CY: Decomposition processes in an Al-5%Zn-1%Mg alloy. Part III : Reversion of GP-zones. *Zeitschrift für Metallkunde*, Vol. 73, no. 12, 1982, p.781-785.
- [Langer, 1980] Langer JS; Schwarz AJ: Kinetics of nucleation in near-critical fluids. *High Physical Review A*, Vol. 21, no. 3, 1980, p.948-958.
- [Lech-Grega, 2001] Lech-Grega M; Hawrylkiewicz S; Richert M; Szymański W: Structural parameters of 7020 alloy after heat treatment simulating the welding process. *Materials Characterization*, Vol. 46, 2001, p.251-257.
- [Lendvai, 1979] Lendvai J; Honyek G; Kovács I: Dissolution of second phases in an Al-Zn-Mg alloy investigated by calorimetric method. *Scripta Metallurgica*, Vol. 13, 1979, p.593-594.

- [Lendvai, 1996] Lendvai J: Precipitation and strengthening in aluminium alloys. *Materials Science Forum*, Vol. 217-222, 1996, p. 43-56.
- [Li, 1999] Li XZ; Hansen V; Gjønnes J; Wallenberg LR: HREM study and structure modeling of the η' phase, the hardening precipitates in commercial Al-Zn-Mg alloys. *Acta Materialia*, Vol. 47, no. 9, 1999, p.2651-2659.
- [Li, 2000] Li X; Starink MJ: Analysis of precipitation and dissolution in overaged 7xxx aluminium alloys using DSC. *Materials Science Forum*, Vol. 331-337, 2000, p.1071-1076.
- [Lifshitz, 1961] Lifshitz IM; Slyozov VV: *J. Phys. Chem. Solids*, Vol. 19, 1961, p.35.
- [Löffler, 1983] Löffler H; Kovács I; Lendvai J: Decomposition processes in Al-Zn-Mg alloys. *Journal of Materials Science*, Vol. 18, 1983, p.2215-2240.
- [Lorimer, 1966] Lorimer GW; Nicholson RB: *Acta Metallurgica*, Vol. 14, 1966, p.1009.
- [Lu, 1996] Lu ZJ; Evans WJ; Parker JD; Birley S: Simulation of microstructure and liquation cracking in 7017 aluminium alloy. *Materials Science and Engineering A*, Vol. A220, 1996, p.1-7.
- [Ma, 1999] Ma T; den Ouden G: Softening behaviour of Al-Zn-Mg alloys due to welding. *Materials Science and Engineering A*, Vol. A266, 1999, p.198-204.
- [Maloney, 1999] Maloney SK; Hono K; Polmear IJ; Ringer SP: The chemistry of precipitates in an aged Al-2,1Zn-1,7Mg at% alloy. *Scripta Materialia*, Vol. 41, no. 10, 1999, p.1031-1038.
- [Martin, 1997] Martin JW; Doherty RD; Cantor B: *Stability of microstructure in metallic systems*, 2nd edition, edited by Cambridge University Press, 1997.
- [Maugis, 2002] Maugis P; Gouné M: A computer model of carbonitride precipitation in steel. *Proceedings of the International Alloy Conference*, July 2002, Estoril.
- [Mayer, 1996] Mayer C: *Optimisation du soudage bord à bord par faisceau laser CO₂ de tôles d'alliages Al-Mg: étude de la microstructure et du comportement mécanique des soudures*. Ph.D, 1996.
- [Meng, 1990] Meng C; Wang Y: A SAXS study on microstructural changes in Al-Zn-Mg alloy during retrogression and reaging. *Scripta Metallurgica et Materialia*, Vol. 24, 1990, p.1521-1524.
- [Meng, 1997] Meng C; Houwen Long; Yong Zheng: A study of the mechanism of hardness change of Al-Zn-Mg alloy during retrogression and reaging treatments by small angle X-ray scattering (SAXS). *Metallurgical and Materials Transactions A*, Vol. 28A, Oct 1997, p.2067-2071.
- [Mondolfo, 1956] Mondolfo LS; Gjostein NA; Lewinson DW: Structural changes during the ageing of an Al-Zn-Mg alloy. *Transactions AIME*, Vol. 206, 1956, p.1378-1385.
- [Morniroli, 1998] Morniroli JP: *Diffraction électronique en faisceau convergent à grand angle (LACBED)*, edited by Société Françaises des Microscopies, 1998.
- [Mukhopadhyay, 1994] Mukhopadhyay AK; Yang QB; Singh SR: The influence of zirconium on the early stages of aging of a ternary Al-Zn-Mg alloy. *Acta Metallurgica et Materialia*, Vol. 42, no. 9, 1994, p. 3083-3091.
- [Myhr, 1991] Myhr OR; Grong Ø: Process modelling applied to 6082-T6 aluminium weldments-I.Reaction kinetics. *Acta Metallurgica et Materialia*, Vol. 39, no. 11, 1991, p.2693-2702.
- [Myhr, 1998] Myhr OR; Klokkehaug S; Fjaer HG; Grong Ø; Kluken AO: Modelling of microstructure evolution and residual stresses in processing and welding of 6082 and 7108 aluminium alloys. *Proceedings of the 5th International Conference on Trends in Welding Research*, Georgia, USA, 1-5 June 1998.
- [Myhr, 1999] Myhr OR; Fjaer HG; Klokkehaug S; Holm EJ; Grong Ø; Kluken AO: Weldsim – An advanced simulation model for aluminium welding. *Proceedings of the 9th International Conference on Computer Technology in Welding*, Sep. 28-30 1999, Detroit, Michigan, USA.
- [Myhr, 2000] Myhr OR; Grong Ø: Modelling of non-isothermal transformations in alloys containing a particle distribution. *Acta Materialia*, Vol. 48, no. 7, 2000, p.1605-1615.
- [Ortner, 1988] Ortner SR; Grovenor CRM; Shollock BA: On the structure and composition of GP zones in high purity AlZnMg alloys. *Scripta Metallurgica*, vol. 22, 1988, p.839-842.
- [Papazian, 1986] Papazian JM: Differential scanning calorimetry evaluation of retrogressed and re-aged microstructures in aluminum alloy 7075. *Materials Science and Engineering*, Vol. 79, 1986, p.97-104.

- [**Park, 1983**] Park JK; Ardell AJ: Microstructures of the commercial 7075 Al alloy in the T651 and T7 tempers. *Metallurgical transactions A*, Vol. 14, oct. 1983, p. 1957-1965.
- [**Park, 1984**] Park JK; Ardell AJ: Effect of retrogression and reaging treatments on the microstructure of Al-7075-T651. *Metallurgical Transactions A*, Vol. 15A, Aug. 1984, p.1531-1543.
- [**Park, 1986**] Park JK; Ardell AJ: Precipitation at grain boundaries in the commercial alloy Al 7075. *Acta Metallurgica*, Vol. 34, no. 12, 1986, p.2399-2409.
- [**Park, 1988**] Park JK: Influence of retrogression and reaging treatments on the strength and stress corrosion resistance of aluminium alloy 7075-T6. *Materials Science and Engineering A*, Vol. A103, 1988, p.223-231.
- [**Park, 1989**] Park JK; Ardell AJ: Correlation between microstructure and calorimetric behavior of aluminum alloy 7075 and Al-Zn-Mg in various tempers. *Materials Science and Engineering A*, Vol. A114, 1989, p.197-203.
- [**Petrov, 2000**] Petrov D: *Ternary alloys : Aluminium-Magnesium-Zinc*. edited by G. Effenberg, published by MSI, Stuttgart (Germany), Vol.16, 2000, p.456-472.
- [**Polmear, 1957-1958**] Polmear IJ: The ageing characteristics of ternary aluminium-zinc-magnesium alloys. *Journal of the Institute of Metals*, Vol. 86, 1957-1958, p.113-120.
- [**Polmear, 1995**] Polmear IJ: *Light alloys: metallurgy of the light metals*. Metallurgy and Materials Science Series, edited by Honeycombe R, Hancock P, 3rd edition, 1995.
- [**Porter, 1981**] Porter DA; Easterling KE: *Phase transformations in metals and alloys*. edited by Van Nostrand Reinhold (UK), 1981.
- [**Radomsky, 1979**] Radomsky M; Kabisch O; Löffler H; Lendvai J; Ungár T; Kovács I; Honyek G: On the decomposition behaviour of Al-4.5at%Zn-2 to 3at%Mg alloys during continuous heating. *Journal of Materials Science*, Vol. 14, 1979, p.2906-2912.
- [**Raghavan, 1980**] Raghavan M: Microanalysis of precipitate free zones (PFZ) in Al-Zn-Mg and Cu-Ni-Nb alloys. *Metallurgical Transactions A*, Vol. 11A, June 1980, p.993-999.
- [**Ringer, 2000**] Ringer SP; Hono K: Microstructural evolution and age hardening in aluminium alloys : atom probe field-ion microscopy and transmission electron microscopy studies. *Materials Characterization*, Vol. 44, 2000, p.101-131.
- [**Russell, 1988**] Russell TP; Lin JS; Spooner S; Wignall GD: Intercalibration of small-angle X-ray and neutron scattering data. *Journal of Applied Crystallography*, Vol. 21, 1988, p.629-638.
- [**Ryum, 1969**] Ryum N: Precipitation and recrystallization in an Al-0.5 wt.% Zr-alloy. *Acta Metallurgica*, Vol. 17, 1969, p.269-278.
- [**Ryum, 1975**] Ryum N: Precipitation kinetics in an Al-Zn-Mg alloy. *Zeitschrift für Metallkunde*, Vol. 66, no. 6, 1975, p.339-343.
- [**Søreng, 1997**] Søreng A: *Localized deformation and mechanical anisotropy in aluminium and AlZnMg alloys*. Ph.D., 1997.
- [**Staley, 1987**] Staley JT: Quench factor analysis of aluminium alloys. *Materials Science and Technology*, Vol. 3, Nov. 1987, p.923-935.
- [**Stiller, 1999**] Stiller K; Warren PJ; Hansen V; Angenete J; Gjønnnes J: Investigation of precipitation in an Al-Zn-Mg alloy after two-step ageing treatment at 100° and 150°C. *Materials Science and Engineering A*, Vol. A270, 1999, p.55-63.
- [**Takahashi, 2000**] Takahashi T; Hirayama K; Minamino Y; Yamane T; Koizumi Y: Quaternary diffusion in 7000 aluminum alloys. *Journal of the Japan Institute of Light Metals*, Vol. 50, no. 10, 2000, p.499-504.
- [**Thomas, 2002**] Thomas WM; Nicholas ED; Watts ER; Staines DG: Friction based welding technology for aluminium. *Materials Science Forum*, Vol. 396-402, 2002, p.1543-1548.
- [**Ungár, 1979a**] Ungár T ; Lendvai J ; Kovács I: Metastable phase diagram of the Al-Zn-Mg alloy system in the low concentration range of Zn and Mg. *Aluminium 55. Jahrg.*, Vol. 10, 1979, p.663-668.
- [**Ungár, 1979b**] Ungár T: The formation of Guinier-Preston zones in the Al-4.8wt%Zn-1.2wt%Mg alloy studied by X-ray small angle scattering. *Zeitschrift für Metallkunde*, Vol. 70, no. 11, 1979, p.739-745.

[Vasudévan, 1987] Vasudévan AK; Doherty RD: Grain boundary ductile fracture in precipitation hardened aluminum alloys. *Acta Metallurgica*, Vol. 35, no. 6, 1987, p.1193-1219.

[Viana, 1999] Viana F; Pinto AMP; Santos HMC; Lopes AB: Retrogression and re-ageing of 7075 aluminium alloy : microstructural characterization. *Journal of Materials Processing Technology*, Vol. 92-93, 1999, p.54-59.

[Volmer, 1925] Volmer M; Weber A: *Z. Phys. Chem.*, Vol. 119, 1925, p.277.

[Wagner, 1961] Wagner C: *Z. Elektrochem.*, Vol. 65, 1961, p.581.

[Wagner, 1991] Wagner R; Kampmann R: Homogeneous second phase precipitation. *Materials Science and Technology: a comprehensive treatment*, Vol. 5, edited by Haasen, VCH, Weinheim, 1991.

[Warren, 1992] Warren PJ; Grovenor CRM; Crompton JS: Field-ion microscope / atom-probe analysis of the effect of RRA heat treatment on the matrix strengthening precipitates in alloy Al-7150. *Surface Science*, Vol. 266, 1992, p.342-349.

[Welding and Brazing, 1971] *Metals Handbook: Welding and Brazing*, Vol. 6, 1971, edited by the American Society for Metals, 8th edition.

[Williams, 1996] Williams DB; Carter CB: *Transmission electron microscopy, Tome II. Diffraction*, edited by Plenum press, 1996.

[Wolverton, 2001] Wolverton C: Crystal structure and stability of complex precipitate phases in Al-Cu-Mg-(Si) and Al-Zn-Mg alloys. *Acta Materialia*, Vol. 49, 2001, p.3129-3142.

[Yamamoto, 1998] Yamamoto A; Minami K; Ishihara U; Tsubakino H: Calorimetric and resistivity study of formation and redissolution of precipitates in 7050 aluminium alloy. *Materials Transactions JIM*, Vol. 39, no. 1, 1998, p.69-74.

[Zahra, 1981] Zahra A; Zahra CY; Lacom W; Degischer HP: Etude des phénomènes de précipitation dans un alliage Al-5%Zn-1%Mg par calorimétrie et microscopie électronique. *Mémoires et Etudes Scientifiques Revue de Métallurgie*, Janv. 1981, p.17-23.

[Zeldovich, 1949] Zeldovich JB: *Acta Physicochim.*, Vol. 18, 1949, p.1.

[Zener, 1949] Zener C: *J. Appl. Phys.*, Vol. 20, 1949, p.950.